Mechanical simulation using a semi analytical method : from elasto-plastic rolling contact to multiple impacts

Thibaut Chaise

Order 2011-ISAL-0076 Year 2011

PhD. THESIS

Mechanical simulation using a semi analytical method: from elasto-plastic rolling contact to multiple impacts

Presented at

l'Institut National des Sciences Appliquées de Lyon

to obtain

the TITLE OF DOCTOR

Doctoral formation:

Mécanique, Énergétique, Génie Civil, Acoustique

Speciality :

MÉCANIQUE - GÉNIE MÉCANIQUE - GÉNIE CIVIL

by

Thibaut CHAISE
Engineer INSA Lyon

Defended on september 5^{th} 2011 on examination Commission

Jury

PROF. JEAN-LOUIS CHABOCHE (ONERA)
PROF. DAVID HILLS (UNIVERSITY OF OXFORD)
PROF. ETIENNE BARTHEL (CNRS - SAINT GOBAIN)
DR. PHILIPPE GILLES (AREVA)
PROF. FARSHID SADEGHI (PURDUE UNIVERSITY)
DR. RÉGIS KUBLER (AMPT AIX-EN-PROVENCE)
DR. FRÉDÉRIC HASNAOUI (EDF)
PROF. DANIEL NÉLIAS (INSA LYON)

LaMCoS - UMR CNRS 5514 - INSA de Lyon
20, avenue Albert Einstein, 69621 Villeurbanne Cedex (FRANCE)

INSA Direction de la Recherche - Ecoles Doctorales – Quinquennal 2011-2015

SIGLE	ECOLE DOCTORALE	NOM ET COORDONNEES DU RESPONSABLE
CHIMIE	CHIMIE DE LYON http://www.edchimie-lyon.fr Insa : R. GOURDON	M. Jean Marc LANCELIN Université de Lyon – Collège Doctoral Bât ESCPE 43 bd du 11 novembre 1918 69622 VILLEURBANNE Cedex Tél : 04.72.43 13 95 directeur@edchimie-lyon.fr
E.E.A.	ELECTRONIQUE, ELECTROTECHNIQUE, AUTOMATIQUE http://edeea.ec-lyon.fr Secrétariat : M.C. HAVGOUDOUKIAN eea@ec-lyon.fr	M. Gérard SCORLETTI Ecole Centrale de Lyon 36 avenue Guy de Collongue 69134 ECULLY Tél : 04.72.18 60 97 Fax : 04 78 43 37 17 Gerard.scorletti@ec-lyon.fr
E2M2	EVOLUTION, ECOSYSTEME, MICROBIOLOGIE, MODELISATION http://e2m2.universite-lyon.fr Insa : H. CHARLES	Mme Gudrun BORNETTE CNRS UMR 5023 LEHNA Université Claude Bernard Lyon 1 Bât Forel 43 bd du 11 novembre 1918 69622 VILLEURBANNE Cédex Tél : 04.72.43.12.94 e2m2@biomserv.univ-lyon1.fr
EDISS	INTERDISCIPLINAIRE SCIENCES-SANTE http://ww2.ibcp.fr/ediss Sec : Safia AIT CHALAL Insa : M. LAGARDE	M. Didier REVEL Hôpital Louis Pradel - Bâtiment Central 28 Avenue Doyen Lépine 69677 BRON Tél : 04.72.68 49 09 Fax :04 72 35 49 16 Didier.revel@creatis.uni-lyon1.fr
INFOMATHS	INFORMATIQUE ET MATHEMATIQUES http://infomaths.univ-lyon1.fr	M. Johannes KELLENDONK Université Claude Bernard Lyon 1 LIRIS – INFOMATHS- Bâtiment Nautibus 43 bd du 11 novembre 1918 69622 VILLEURBANNE Cedex Tél : 04.72. 43.19.05 Fax 04 72 43 13 10 infomaths@bat710.univ-lyon1.fr
Matériaux	MATERIAUX DE LYON	M. Jean-Yves BUFFIERE INSA de Lyon - École Doctorale Matériaux Secrétariat Mériem LABOUNE Bâtiment Antoine de Saint-Exupéry 25bis Avenue Jean Capelle 69621 VILLEURBANNE Tel : 04 72 43 71 70 Fax : 04 72 43 72 37 ed.materiaux@insa-lyon.fr
MEGA	MECANIQUE, ENERGETIQUE, GENIE CIVIL, ACOUSTIQUE (ED n°162)	M. Philippe BOISSE INSA de Lyon - École Doctorale MEGA Secrétariat Mériem LABOUNE Bâtiment Antoine de Saint-Exupéry 25bis Avenue Jean Capelle 69621 VILLEURBANNE Tel : 04 72 43 71 70 Fax : 04 72 43 72 37 mega@insa-lyon.fr Site web : http://www.ed-mega.com
ScSo	ScSo* M. OBADIA Lionel Sec : Viviane POLSINELLI Insa : J.Y. TOUSSAINT	M. OBADIA Lionel Université Lyon 2 86 rue Pasteur 69365 LYON Cedex 07 Tél : 04.78.69.72.76 Fax : 04.37.28.04.48 Lionel.Obadia@univ-lyon2.fr

*ScSo : Histoire, Geographie, Aménagement, Urbanisme, Archéologie, Science politique, Sociologie, Anthropologie

Acknowledgment

Je tiens à remercier en premier lieu les personnes qui ont suivi mon travail ces trois dernières années de thèse. Je remercie donc les membres d'AREVA et EDF : Philippe Gilles, Vincent Robin, Jean-Marie Carrez, Nicolas Toutée, Franck Pawlack, Frédéric Hasnaoui, Gérard Douchet et Sahid Taheri qui ont suivi ce travail et ont permis de lui apporter une intéressante dimension industrielle. De vifs remerciements vont aussi à Jun Li pour les compléments que son travail a pu apporter au mien.

Je remercie aussi très sincèrement Marc Desvignes et Régis Kubler du laboratoire Mécasurf des Arts et Métiers Aix-en-Provence pour m'avoir offert la possibilité d'ajouter une dimension expérimentale à mes travaux de thèse et pour m'avoir régulièrement accueilli ces dernières années. Je remercie aussi Adrien Arret pour l'aide qu'il m'a apporté dans la réalisation de ces expérimentations et le long traitement des données qui a suivi. Il m'est impossible de parler d'expérimentations sans remercier Philippe Chaudet pour son aide précieuse, ainsi que Jean-Pascal Guilhermond et Paul Valverde pour leur rassurante présence dans les sous-sols obscurs du LaMCoS.

I wish to thank greatly Farshid Sadeghi for receiving me in his METL lab. I am sincerely grateful of the time and trust he offered me. I truly thank the METL guys: Nick, Ankur, Ben, Anurag, John, Pankaj, Andy, Trevor, Chin-Pei, Acit, Roshan, Dave, Matthew, Behrouz and Additiya for their welcome, their friendship and for accepting the "french guy" among them in shorter time than it took me to remember their names.

Je remercie Étienne Barthel et David Hills pour avoir accepté de rapporter ce travail et pour leur contribution à son amélioration. Mes remerciements vont aussi à Jean-Louis Chaboche pour sa participation à mon jury de thèse.

I wish to thank Étienne Barthel and David Hills for reporting my work and for their contribution to its improvement. My thanks also go to Jean-Louis Chaboche for his participation to my jury.

Toute ma gratitude va aux personnes que j'ai connu au LaMCoS. Mes premiers remerciements vont aux membres de la team SAM : Benjamin, Julien et Caroline avec qui j'ai eu plaisir à travailler et à m'arracher les cheveux. Je remercie particulièrement Cédric, Alexandre, Gauthier et Daniel pour leur présence toujours agréable, pour les plantes vertes et pour leur amitié. Je remercie aussi Michel, Fabrice, Nahiène, Tarek, Thomas, Anthony pour leur aide et leurs discussions ainsi que les autres doctorants Yancheng, Jikai, Jing, Benoît, Émilien, Lucas, Romain, David, Paul, Loane, Aline et Fabien. Enfin, je n'oublie pas tous les autres membres, passés et présents du labo, que certes je ne cite pas par lassitude des tristes listes énumératives mais dont la contribution aux bons souvenirs que j'ai de ces trois années n'est pas moindre.

Je porte une attention tout particulière à remercier Daniel Nélias pour l'encadrement de ces trois années de thèse, pour avoir su trouver des disponibilités au sein d'un emploi du temps dont la seule évocation me fait trembler et pour les formidables opportunités de

conférence, d’échanges et d’avenir qu’il a su m’offrir.

Mes derniers et plus sincères remerciements vont à mes parents pour leur soutien permanent et inconditionnel, à ma soeur qui se doit d’accepter que je sois docteur avant elle et surtout à Myriam, toujours à mes côtés dans les mauvais mais surtout et plus souvent dans les bons moments.

Abstract

La durée de vie en fonctionnement des pièces mécaniques peut être augmentée par la présence de contraintes résiduelles de compression. Inhérentes à la plupart des procédés de fabrication, les contraintes résiduelles jouent un rôle sur la tenue en service des éléments mécaniques. La connaissance et la maîtrise de ces contraintes résiduelles et des procédés associés sont donc fondamentales. La mise en place de méthodes numériques performantes pour prédire ces contraintes résiduelles permettra à terme d'éviter de nombreux et coûteux essais et d'étudier l'influence des principaux paramètres.

Cette thèse présente le développement et l'application de méthodes de calcul semi analytiques (SA) à la modélisation de procédés mécaniques de mise en compression des surfaces. Les méthodes SA, initialement développées pour la simulation des contacts élasto-plastiques, ont l'avantage de temps de calcul très significativement réduits par rapport aux méthodes numériques conventionnelles. Cette méthode est d'abord utilisée pour la simulation d'un procédé connu sous le nom de galetage, avec un chargement de type contact roulant. Enfin elle est utilisée pour la simulation d'impacts uniques puis répétés, et les développements associés présentés.

Le contact roulant entre deux massifs élasto-plastiques, représentant une pièce traitée par galetage et l'élément roulant est d'abord étudié. Une première approche, sans considération du frottement, est effectuée. L'influence de plusieurs paramètres déterminants est analysée :

- modèle de comportement de l'élément roulant : purement élastique ou élasto-plastique de propriétés égales à celles de la surface traitée
- modèle d'écrouissage de la surface traitée : les deux cas limites d'un massif à écrouissage purement isotrope et purement cinématique sont abordés
- géométrie des massifs en contact : sphères ou ellipsoïdes
- type de chargement : indentation ou roulement.

Trois types de résultats sont analysés :le déplacement résiduel en surface après application de la charge, la valeur maximale de la pression de contact, à mettre en regard de la pression hertzienne d'un contact élastique de charge équivalente, et la déformation plastique maximale. Trois conclusions principales sont déduites de cette analyse :

- la géométrie des éléments en contact a une influence significative sur le niveau de charge obtenu et par conséquent le niveau de déformation plastique atteint
- pour un contact considéré comme purement élastique, le type de chargement n'a aucune influence sur les résultat mais la différence devient critique lorsque l'un des éléments en contact est plastique

- le modèle d'écrouissage (isotrope ou cinématique) n'a qu'une influence négligeable sur les résultats d'indentation. Au contraire, dans le cas d'un contact roulant, le modèle d'écrouissage joue fortement sur les résultats et particulièrement sur la stabilisation du niveau de déformation plastique avec le nombre de cycles de roulement.

La simulation d'impacts est ensuite abordée. La méthode développée est tout d'abord validée numériquement. Deux benchmarks sont effectués entre la méthode SA et différents codes éléments finis sur les cas d'un impact unique et de trois impacts successifs à vitesse constante. Les résultats des benchmarks permettent d'assurer la validité de la méthode SA tout en détectant les limites des hypothèses constitutives du modèle. Des améliorations notables de la méthode, notamment sur la prise en compte des grands déplacements, permettent de repousser les limites de validité du modèle et de prendre en compte des déformations de l'ordre d'une dizaine de pourcents.

La méthode développée est appliquée à la prédiction du coefficient de restitution. Dans le cas de l'impact d'une bille rigide sur un massif élastique parfaitement plastique, les résultats issus de la méthode S.A. sont tout d'abord confrontés aux modèles analytiques issus de la littérature ainsi qu'à d'autres modèles numériques. Une extension à des impacts sur massif élasto-plastique à écrouissage isotrope est faite, servant de base au développement de formules analytiques. En se basant sur les travaux de Jackson et al. [JAC 10] et Weir et Tallon [WEI 05], des formules analytiques permettant une expression directe du coefficient de restitution sont proposées. Ces nouvelles formules permettent ainsi de décrire l'influence :

- de la vitesse d'impact, au delà des limites classiquement décrites par les formules issues de la littérature

- des propriétés des matériaux : élastiques mais aussi plastique en prenant en compte le taux d'écrouissage dans l'hypothèse où celui-ci est isotrope.

La méthode SA est ensuite confrontée à l'expérience. Trois matériaux ont été plus particulièrement étudiés : 316L, AA 7010, et l'Inconel 600. Les impacts sont réalisés à partir d'un canon à air comprimé développé par le laboratoire Mécasurf. Les dimensions des impacts ainsi que les déformations générées, mesurées par stéréo corrélation sont comparéés aux résultats issus de la méthode. Ces premiers résultats encouragenants permettent notamment d'étudier l'importance du frottement sur les résultats ainsi que les limites de l'hypothèse de petites perturbations prises à la base du développement de la méthode. Les vitesses d'impact et de rebond sont utilisées pour calculer les coefficients de restitution puis confrontés aux formules analytiques développées, permettant de noter l'importance de la prise en compte de l'écrouissage dans la prédiction des vitesses de rebond.

Une méthodologie est développée pour la prise en compte d'impacts multiple. L'état de contrainte et de déformation dans une pièce ayant subi un traitement de grenaillage est supposée homogène dans des plans parallèles à la surface impactée. Une répartition

triangulaire des impacts est supposée à partir de laquelle une zone de référence est définie comme étant le triangle formé par le centre des trois premiers impacts. Les résultats sont ensuite moyennés sur cette surface de référence, la valeur représentative obtenue étant indépendante de l'ordre des impacts et, dans une certaine mesure, de la répartition des impacts. La rapidité d'exécution des calculs par méthode SA est mise à contribution pour étudier l'influence de différents paramètres des procédés de type grenaillage :

- taux de recouvrement. Il est montré qu'un effet de saturation apparait au delà d'une valeur donnée de taux de recouvrement, dépendant des propriétés des matériaux concernés
- vitesse d'impact : la vitesse moyenne des différents impacts apparait comme le paramètre déterminant du procédé, permettant de simplifier les simulations d'impacts multiples
- nombre d'impacts : au delà de trois impacts, l'évolution de la déformation plastique dans la zone de référence est négligeable et ce même dans les configurations les plus critiques (forts taux de recouvrement).

Il est ainsi montré que la simulation de trois impacts répartis de manière triangulaire avec une vitesse d'impact représentative de l'énergie cinétique moyenne fournie au cours du procédé est suffisante pour décrire la déformation plastique moyenne générée par plusieurs impacts. La différence entre les valeurs moyennées et observées simplement au centre de l'impact montre l'importance du post-traitement des résultats pour la comparaison aux données expérimentales.

Le procédé de billage ultrasonore a été tout particulièrement étudié. Dans un premier temps nous nous sommes attachés à décrire la cinématique des billes dans une chambre fermée, mises et maintenues en mouvement par une sonotrode. L'utilisation de formules analytiques pour l'estimation des coefficients de restitution, lors des nombreux chocs entre les billes ou avec les parois de la chambre, a permis d'affiner le calcul des vitesses moyennes d'impact en fonction des paramètres du procédé. La méthode SA est ensuite utilisée pour déterminer le champ de déformations plastiques induits par les impacts. Trois impacts à vitesse constante sont simulés. Le comportement du matériau appliqué est issu d'essais cycliques de traction-compression réalisés préalablement. Enfin une méthode de projection est proposée pour permettre in fine la prédiction des contraintes résiduelles pour des structures fines ou épaisses. Le champ des déformations plastiques moyennées issu de la méthode semi analytique est utilisé comme donnée d'entrée pour un modèle éléments-finis de la structure grenaillée. Une première série de validations expérimentales de la méthodologie est proposée. La déformée d'une éprouvette fine de type Almen ainsi que les champs de contraintes résiduelles générés par les impacts sont comparés avec succès aux résultats issus de la méthode.

KEYWORDS: Modélisation numérique, Méthode semi analytique, plasticité, impact, grenaillage

Contents

List of Figures

List of Tables

Nomenclature

A	Acceleration of the sphere
A_c	Contact area
A_d	Surface area for the calculation of the semi infinite body surface pressure for the residual stresses calculation
A_r	Reference area for multiple impacts
B	First swift isotropic hardening law parameter
B^{∞}_{ijkl}	Influence coefficient of the kl component of a cuboid of uniform plastic strain on the ij component of residual stresses in an infinite body
$B^{\infty/2}_{ijkl}$	Influence coefficient of the kl component of a cuboid of uniform plastic strain on the ij component of residual stresses in a semi infinite body
C	Second swift isotropic hardening law parameter
C^{p}_{ij}	Influence coefficient of a surface pressure on the ij component of the elastic stresses
$C^{q_x}_{ij}$	Influence coefficient of a surface shear in the x direction on the ij component of the elastic stresses
$C^{q_y}_{ij}$	Influence coefficient of a surface shear in the y direction on the ij component of the elastic stresses
C_1	First parameter of the Armstrong-Frederick kinematic hardening law
C_2	Second parameter of the Armstrong-Frederick kinematic hardening law
D^p	Effect of a uniform pressure applied on a rectangular patch on the normal surface elastic displacement u^e_z
D_{kij}	Influence coefficient of the ij component of a plastic strain cuboid on the residual displacement in direction k
E	Young's modulus of the impacted body
E^*	Equivalent Young modulus
E_T	Tangent modulus of the isotropic hardening law
E_i	YoungŠs modulus of body i
E_k	Kinetic energy of the sphere
F_c	Contact force resulting from the integral of pressures
F	Normal applied load
F_y	Threshold contact force leading to plastic flow
G	Elastic shear modulus
$\underline{\underline{H}}$	Function definition of the back stress in the return mapping algorithm
J_2	Von Mises equivalent tensor
K	Conventional shear yield stress

M_R	Rolling moment
N_i	Number of points in the computation domain in the direction i
N_{plast}	Number of points in the plastic zone
N_r	Number of points in the reference area A_r
P	Contact pressure
P_{hertz}	Hertzian contact pressure
P_{max}	Maximum contact pressure
P_0	Total normal load applied to the surfaces
P^*	Maximum contact pressure for an elastic impact
R	Sphere radius
R_{eq}	Equivalent radius for two spherical bodies in contact
R_i	Radius of body i
R_0	Radius of impact dent at $z = 0$ altitude
T_c	Elastic impact duration
X_1	First hardening variable tensor
X_2	Second hardening variable tensor
a	Contact radius for a circular point contact, semi-minor axis for an elliptical one
a^*	Maximum area of contact radius for an elastic plastic impact
a_e^*	Maximum area of contact radius for an elastic impact
$a_{ei\,j}$	Parameters giving the evolution of f_{ei} in Eq. 4.13 (i=1,3 ; j=1,3)
a_{mi}	Parameters giving the evolution of f_m in Eq. 4.17 (i=1,2)
a_x	Mesh grid in the x direction
a_y	Mesh grid in the y direction
c	semi-major axis of the contact ellipse for elliptical contacts
	Coverage for multiple impacts
d	Reference distance between multiple impacts
e	Coefficient of restitution
e_N	Normal coefficient of restitution when considering normal and tangential velocities
e_T	Tangential coefficient of restitution when considering normal and tangential velocities
e	Coefficient of restitution for a single impact
e_n	Coefficient of restitution of the n-th repeated impact
e_p	Von Mises equivalent plastic strain
f	Yield function
f_{ei}	Parameters of the proposed law for the coefficient of restitution
	of a single impact in Eq. 4.12 (i=1,3)
f_m	Parameter of the proposed law for the coefficient of restitution
	for repeated impacts in Eq. 4.14
g	Gravitational acceleration
h	Surface separation
h_d	Maximum impact dent height
k	Ellipticity ratio
m	Mass of the sphere
n	Third swift isotropic hardening law parameter

p	Accumulated plastic strain
p_{ISO}	Isotropic part of the hardening in the software Systus
q_i	Shear in the i direction $(i = x, y)$
r	Isotropic hardening variable
$\underline{\underline{s}}$	Difference between total and back stress tensors
t	Time
u^{tot}	Total surface displacement in the z direction
u_z^e	Elastic surface displacement in the z direction
u_z^{res}	Residual surface displacement in the z direction
u^{tot_z}	Thermal surface displacement in the z direction
v	Initial velocity of the sphere - Impact velocity
$\vec{v}$	In volume velocity of shots in the ultrasonic shot peening model
v_r	Final velocity of the sphere after impact (rebound)
v_y	Initial velocity of the sphere leading to plastic flow during impact
x	Along the surface axis direction
$\vec{x}$	In volume position of shots in the ultrasonic shot peening model
y	Along the surface axis direction
z	In depth axis direction
z_{min}	Minimum altitude/maximum depth of an impact dent
z_{trans}	Depth of transition from the 2D to 3DFFT residual stress calculation method
Δi	Mesh size in the x direction $(i = x, y, z)$
Δt	Time step
α_i^{th}	Thermal expansion coefficient in the i direction
δ_z	Rigid body approach in the direction normal to the surface
δ_z^*	Maximum rigid body approach for an elastic impact
δ_y	Rigid body approach leading to plastic flow during impact
γ_2	Third parameter of the Armstrong-Frederick kinematic hardening law
$\underline{\underline{\varepsilon^e}}$	Elastic strain tensor
$\underline{\underline{\varepsilon^p}}$	Plastic strain tensor
ε_{eq}^p	Von Mises equivalent plastic strain
$\underline{\underline{\varepsilon^{tot}}}$	Total strain tensor
ε_{eq}^p	Von Mises equivalent plastic strain
ε_{y0}	Initial yield strain
$\underline{\underline{\mu}}$	Normalized stress tensor
ν_i	PoissonŠs ratio of body i
Ω_p	Plastic zone
ρ	Density of the sphere
σ_{CIN}	Kinematic part of the yield limit
σ_{ISO}	Isotropic part of the yield limit
$\underline{\underline{\sigma^e}}$	Elastic stress tensor
σ^n	Normal stress applied on the semi infinite body for the residual stress computation
$\underline{\underline{\sigma^r es}}$	Residual stress tensor

$\underline{\underline{\sigma}}^{t}$	Thermal stress tensor
$\underline{\underline{\sigma}}^{tot}$	Total stress tensor
σ_Y	Conventional yield stress at 0.2% plastic strain
σ_y	Current yield limit
σ_{y0}	Initial yield limit
θ_i	relative angle of the surfaces in contact in the direction i

Introduction

Mechanical components can be subjected during their lifetime to large loads, cyclic loadings or overloading. Cyclic loadings can cause fatigue and reduce the lifetime of mechanical parts even if the material behaves purely elastically. If the applied load overcome a certain threshold, plastic flow will occur in the body and change radically its behaviour.

The occurring of plasticity in a part can have both positive and negative effects. By changing significantly the distribution and amplitude of stress, the presence of plastic strain can extend the lifetime of a part but it also generates permanent deformation of the surfaces that can change the load distribution and cause preliminary failure. The generation of plastic strains into a component is widely done to introduce residual stresses. Residual stresses, by opposing the stresses generated by the load, will extend the duration of the concerned part by artificially reducing the internal stresses during operation.

Residual stresses are delicate quantities to measure and most methods of measurements are destructive and costly. Numerical simulation allows to fully and accurately analyse fields of residual stresses and their generation. There is thus a strong interest in developing fast and efficient methods to simulate and predict residual stress amplitude and distribution. A fine definition of residual stresses links with an accurate definition of the loads generating these stresses. Most loads being carried through contacts, a correct modelling of the contacts is fundamental. Semi analytical methods are numerical methods that have gain more attention in the past few years for their speed and reliability to simulation mechanical contacts, including plasticity among other effects.

The purpose of this work is the development and extension of the Semi Analytical Method (SAM) for the simulation of mechanical contacts generating plasticity and residual stresses. Among the various industrial processes used to generate residual stresses, several are using impacts. The emphasis has been put on shot peening processes and thus on the extension of the SAM to the modelling of impacts. Low plasticity burnishing is also studied through the simulation of rolling contacts. Most application of the SAM being concentrated on rolling elements simulation or fretting contacts, the level of plastic strain involved, when existing, are usually low, up to a few percents. Residual stresses generation involves usually higher levels of plasticity and focus was put on the efficiency of the SAM at relatively high strain levels while still keeping significant improvements in computation time.

The first chapter presents the industrial context. Processes used to generate residual

stresses are presented and a focus is made on peening processes, the parameters and phenomena they involved. A literature review on the following key points for our analysis is then made: impacts and multiple impacts models and contact mechanics. An accurate history of the development of the SAM is presented. Classical but useful formulae from the literature are recalled and a final point on rolling contact mechanics is addressed.

The second chapter presents the numerical model. The SAM has been deeply studied and developed by former workers, this chapter focuses only on the specificities of the method and on points of enhancements addressed in this work. A first set of validations on simple cases is proposed to confirm the modifications brought to the method.

The effects of plasticity and hardening in rolling contacts is presented in the third chapter as a first step of low plasticity burnishing simulation. This analysis completes former studies on rolling contact and introduces the consideration of kinematic hardening in the SAM.

Following chapters are dedicated to the study of impacts. The numerical simulation of single impacts is first addressed in the fourth chapter. Numerical validation through a benchmark is proposed and the model is then applied to the determination of the coefficient of restitution. Several formulae derived from the literature and numerical results are proposed to predict in various cases this macroscopic measure of an impact.

Interesting collaboration allowed to perform experiments of single impacts. Results from these experiments are presented in the fifth chapter and used to validate the formulae proposed previously and the numerical model developed.

The last chapter focuses on the modelling of multiple impacts processes. A method is proposed for the simulation of multiple impacts and the processing of the results to obtain a representative picture of the reality. A benchmark with several other computational methods validates the SAM that is then applied to various cases. Complementary models are proposed to perform simulation of a full ultrasonic shot peening process, from the original process parameters to the final residual stress state in any kind of structures.

State of the art

In this first chapter, a bibliographic study of the fields addressed in this analysis is made. Industrial processes generating compressive residual stresses are first recalled, focusing on processes involving impacts and ultrasonic shot peening. A presentation of the methods of simulation and common results on impact and multiple impacts is then made. A large part is dedicated to the history of contact modelling, from the historical Hertzian contact to the more recent developments of semi analytical methods. Finally, a brief focus is made on rolling contact.

Contents

1.1 Introduction

The aim of this study is the development of a semi analytical method for the modelling of various industrial processes and especially for the consideration of impacts at low velocities. Low velocities here includes velocities at which the residual strain of the impacting body is negligible. The semi analytical method has been shown efficient to compute residual strains and stresses in various and complex cases.

Industrial processes generating residual stresses are thus first observed. Major part of this study focuses on the extension of the method to impact modelling and processes using impacts have so been studied. The main parameters governing the impacts processes, that consequently will show the model parameters, physical phenomena and processes to concentrate on, are indicated.

Various hypothesis and model existing for impacts are observed, the effect of inertia is first studied. Focus is then put on numerical models, for single impacts first for matters of simplicity. The physical phenomena involved are approached even those that won't be considered in this study.

A simplified analysis of many processes and phenomena can be made with the analysis of the coefficient of restitution, and a study of all existing models and several applying hypothesis is made. Then the techniques and methods to consider multiple impacts are addressed.

Finally more general contact mechanics are studied, starting from the original Hertzian elastic theories used as references, case validation and normalisation values. The analytical results for circular and elliptical point contacts are fully recalled. The extensions and progress to non Hertzian and non elastic contacts is then studied, leading finally to the most achieved numerical models and a history of the semi analytical methods.

At last the motivations leading to studies of rolling contacts are presented.

1.2 Generating compressive residual stresses

1.2.1 Industrial context

The duration of mechanical components is fundamental in nowadays industrial applications. The premature failure of components can lead to very large costs in repairing, replacement or in the worst cases damages to industrial installations or injuries. The knowledge and prediction of such failure is thus of great importance. The behaviour of mechanical components over a long period of time is studied through fatigue analysis and is a full field of study by itself. Yet to obtain a consistent description of fatigue effect and consequently anticipate the failure of mechanisms, a correct knowledge of the initial state of the components is necessary. Mechanical parts are never stress free. They contain so called residual stresses, i.e. stresses remaining once all kind of loading has been removed from the mechanical part. These stresses can have various origins. They can be originated from thermal effects, mechanical loadings, phase transformation or chemical effects. In all these cases, a part of the piece is subjected to a permanent deformation that generates

adaptation strains in the deformed part and around it. These elastic strains logically generate stresses according to the elastic behaviour of materials and these are called residual stresses.

It is known that introducing compressive residual stresses in the most solicited parts allows to delay the appearance of cracks and their propagation. Several processes are then used to introduce stresses in the material, the compressive part of theses stresses should concentrate on the most solicited zones. One way to do so is to generate a superficial plastic deformation on the treated part.

Where the problem becomes even more complex is that the forming of mechanical parts does not produce stress free elements. Welding, machining, casting, and their numerous variations are able to generate complex shapes but they introduce complex stress fields, which depth in the elements can vary, that can be damageable to the parts. A first step is to control these processes and know the stresses they produce. In a second step, it can be planed to reduce the generated stresses by better mastering the processes. However, when the generated stresses are too high, or present large surface tensile zones, i.e. a huge risk of crack propagation, it is often necessary to apply surface treatments to reduce these stresses or at best switch surface tensile residual stresses to compressive residual stresses, to optimize the life of the component.

1.2.2 Industrial processes

Processes like expanding or roller-burnishing are some of the ways to generate surface plasticity. They consist in applying a tool (like a roll or a punch) on the surface with a load high enough to generate a plastic flow. Depending on the number of passes and the size of the tool theses processes can be called under different names, like low plasticity burnishing. The mechanical phenomena governing the process remain globally the same. The simulation of such processes is derived from the simulation of rolling contact, a field that is well known through the study of rolling elements, like bearings.

A second family of processes generates similar effect but the treated surface is here impacted to produce a plastic flow. Hammering is one of these techniques, for which several hammers are put in movement by the effect of a high frequency sonotrode and applied to the surface, some recent work on high frequency hammering can be found in [LEQ 10] and [LEQ 11].

Laser peening is another process in which a laser impulse is produced on the surface of the piece. The treated surface might be coated or covered with a thin film of water. The energy produced by the laser generates a small blast at the surface. When water is used, the loading of the surfaces is purely mechanical and consequently the process is very close to hammering, except that the pressure distribution and intensity are different. For some applications, the surface might be uncoated or treated without water, in which case a thermal loading is to be considered which will largely affect the sequence of events.

Furthermore, peening type processes use the impact of small spheres on the surface to generate plasticity and introduce residual stresses. The diameter of the balls or shots can vary from some fractions of millimetres to several millimetres. The shot velocity

ranges usually from a few meters per second to around a hundred meter per second. The main difference between the processes is the method used to put the shots in movements. Traditional methods use air blasting systems or centrifugal blast wheels to throw the shots up against the treated part. Such methods are rather simple but present large difficulties in controlling the velocity at which the balls impact the surface and bringing together the shots to recycle them afterwards.

An other method, called roto peening, uses a rotating wheel to which the shots are connected by a flexible part. The advantage of this technique is that the impacting shots stay fixed to the device. Yet, one needs to control the fixing of the shots to the flexible parts and to consider the mechanical behaviour of this flexible part on the loading conditions of the piece. Furthermore, the impact is not free any more and sliding may occur during the impact which would largely modify the behaviour of the process compared to more classical impacts methods.

One last common method is ultrasonic shot peening. A schematic diagram of the method is provided in Fig. 1.1. The shots are here confined in a closed chamber, which allows to use a limited number of shots. The shots are of a few millimetres in diameter. An electric generator is used to generate a sine ultrasonic signal, which is amplified and transmitted to a sonotrode that puts the ball in movement by contact. The impact velocity of the shots on the surface thus depends on the sonotrode frequency and movement amplitude but usually approaches $10m/s$. The treated piece can be located in the chamber if it's small enough, as in Fig. 1.1. In this case complicated shapes pieces can be treated. The actual impact velocity, impact angle and effective covering rate of the piece are then difficult to control. For larger pieces, the chamber presents an opened side and the device is simply applied on the area to treat. The peening treatment is then applied for a given time and then translated to the next area. This treatment can easily be automatised if the process parameters are correctly known.

Finally, cold spray is a process worth mentioning here. The principle is quite similar to conventional shot peening but the impact velocity is one order of magnitude higher, with velocities ranging from $100m/s$ to $1000m/s$. Consequently the shot deformation is considerable and very large deformations are involved. When the impacts present a very large angle with the normal of the treated surface, this process can be used as abrasion, while for almost normal impacts, the shots keep stuck to the surface. When the material of the shots is different than the material of the surface, cold spray can be used to created coatings, while it can be used for refill operations when the shots and the surface are made out of the same material. This process has gain large interest in the past few years and several studies try nowadays to understand better the physics of this problem, both experimentally, see for example [STO 06], and numerically [YIL 11].

1.2.3 Peening processes efficiency and parameters

In all peening processes, the process is governed by the following parameters: shot mechanical properties, shot diameter, duration of peening treatment, number of shots, velocity of impacts and angle of impacts. The angle of impacts effect is often neglected in

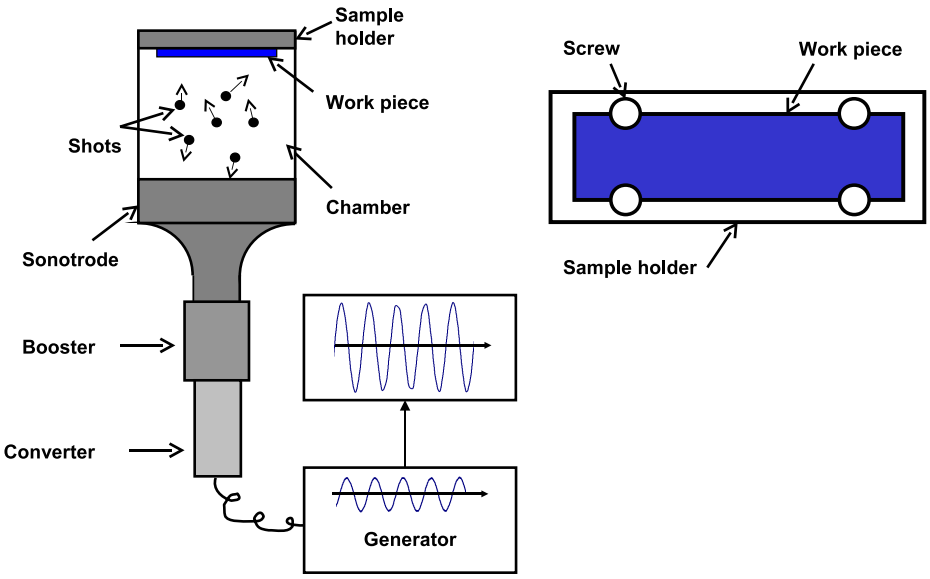

Figure 1.1: Ultrasonic shot peening process schematic diagram showing the shot peening chamber, ultrasounds generator system and the sample holding system.

the studies. For many peening applications the projection of shots towards the surface is controlled enough so that the angle made between the trajectory and the normal to the surface is low enough so that the effect of the tangential velocity can be neglected. So usually, impacts are considered normal to the surface.

Baskaran [BAS 10] recently provided a remarkable review of shot peening simulations and of shot peening effects. Figure 1.2 presents a schematic diagram of shot peening and of the basic dimensions involved. The work piece and several shots are represented. Each shot produces a dent which dimensions are close to the contact radius, classically denoted a^*. An affected zone is produced in the work piece, this zone can roughly be considered as the plastically deformed volume, yet it should be noted that the area affected by residual stresses can be significantly larger than the plastic zone.

The residual stress distribution in the depth of the work piece is represented in fig 1.3. The plastic zone being concentrated just below the surface, compressive residual stresses are located in a small sub surface zone, thus leading to the delay of crack propagation. The tensile stresses are rejected far below the surface and a rough estimation of the equilibrium provides the ratio between the compressive and tensile stress zones ($A_1 = A_2$). The size of the compressive zone is mainly related to the size of the plastic zone, which depends on the peening parameter, while the compressive stress zone will expand in the depth of the work piece with a notable effect of the length of the piece if the dimension in depth is of the same order of the affected zone.

The residual stress distribution, i.e. mainly their depth and their maximum amplitude

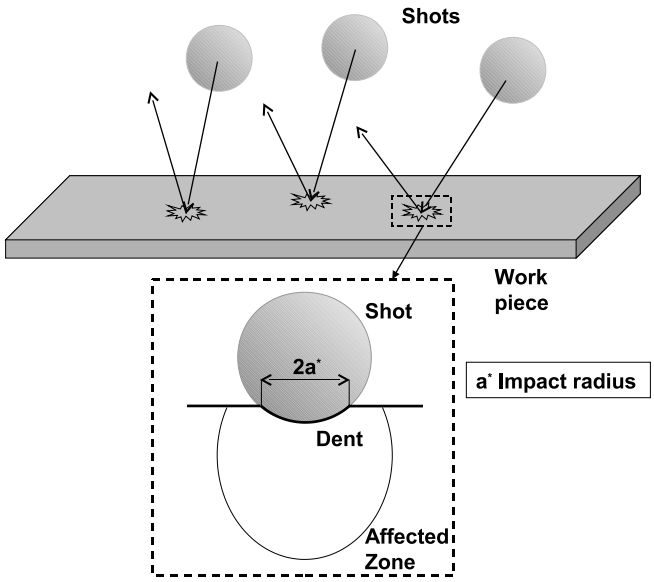

Figure 1.2: Schematic diagram of shot peening. Shot peening involves multiple and progressively repeated impacts, resulting in plastic deformation of the surface layer. Once the shot leaves the work piece, the adjoining layer of material resists any further deformation thus causing Residual Compressive Stresses [BAS 10].

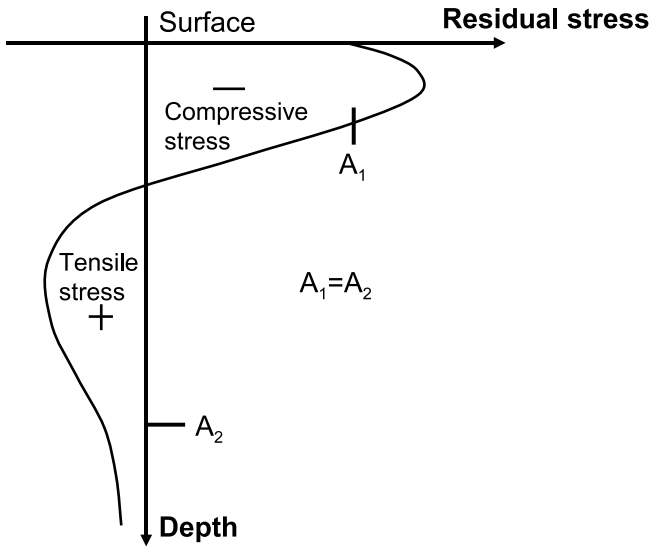

Figure 1.3: Residual stress distribution after peening treatment. The large compressive stresses acting on a small thickness (Area A1) are balanced by small tensile stresses acting on a large thickness (Area A2) [BAS 10].

is governed by the peening parameters. Figure 1.4 resumes the main process parameters and their effect on the residual stress distribution. The air nozzle pressure, which is to be linked with conventional air blasting systems, is here indicated but can be directly linked to the velocity of the shots. It appears that increasing impact velocity, shot diameter and time of treatment directly increase the amplitude of residual stresses and the depth of the compressive zone. The hardness of both material plays a direct role in the increase of the subsurface maximum stress amplitude and at the same time of the surface residual stress. Finally, an increasing hardness of the shots tends to increase the depth of stresses, while the hardness of the piece's material logically has the opposite effect.

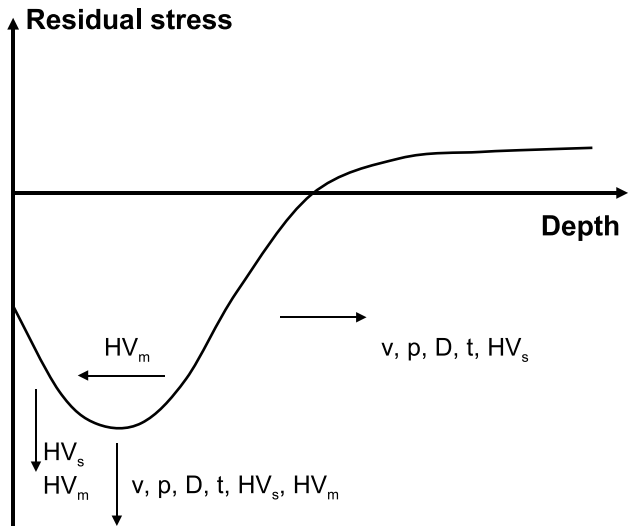

Figure 1.4: Effects of input parameters on Residual Compressive Stresses (RCS). HV represents the hardness, v the shot velocity, D the diameter of the shots, p the air pressure from nozzle and t the time of treatment. The subscripts s and m denote the shot and the target material respectively [BAS 10].

In a more macroscopic view, a shot peening treatment will have effects on several aspects of the work piece. It will modify the residual stress state of the piece and introduce new plastic strains, but it will also influence the initial crack distribution, being able to close some existing cracks but also to generate new ones if the treatment is too long. The plastic strains involved can lead to a change in the material's properties. The surface roughness and topography will also change due to the dents produced by the impacts [SAN 10], and the global geometry of the piece can be changed if the residual distortions generated have amplitudes close to the piece dimensions. Figure 1.5 resumes the different changes that can be cause to a material by a peening treatment as defined by Schulze [SCH 02].

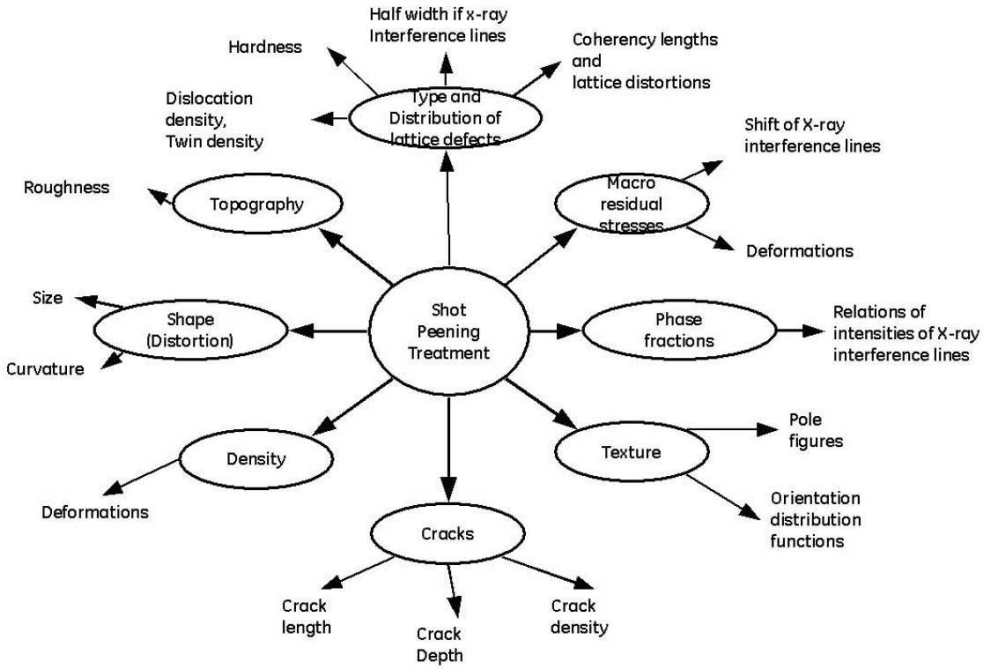

Figure 1.5: Changes in the material due to peening [SCH 02].

1.3 Mechanics of impacts

1.3.1 Single impact modelling

1.3.1.1 Inertial effects

When considering the impact of spherical bodies, several expressions can be used to describe the mechanics of the problem. Several phenomena may be considered

- the normal problem
- the tangential problem,
- inertia effects and dissipation through elastic wave propagation
- inelastic effect and dissipation through plasticity

The inertia effect are widely considered to be negligible for low to moderate velocities, i.e. up to a few hundreds of m/s. This hypothesis was first claimed by Johnson [JOH 85]. Following Love's criterion [LOV 52], this hypothesis is valid as long as the body dimensions are such that they allow the elastic waves to reflect many times during the impact. In this case, the quasi-static hypothesis is correct, which leads to the condition $v < 0.002c_0$ where c_0 is the elastic wave velocity in the bodies. For steel, this velocity is equal to $5200m/s$ which leads to a limit velocity of $10.4m/s$. This might seem quite low compared to the announced range of studied velocities. It is to notice that the impact behaviour ceases to be elastic far beyond this limit. Thus the onset of yield occurs before the condition on inertia effects. Still purely elastic behaviour is largely considered since it gives reference values. Especially, the duration of an elastic plastic impact differs slightly from the elastic duration of an impact.

Authors have proven that inertial effects have no influence on the elastic plastic impact problem, see [DES 00, YAN 05] for example. Some authors have studied the effect of inertial effects on the very first step after contact, such as Thompson and Robinson [THO 77] or Lee and Komvopoulos [LEE 10]. They showed that just at the onset of contact the indentation velocity can overcome the elastic wave velocity, thus creating a 'super-seismic regime'. The duration of this phase is largely negligible compared to the duration of the impact.

1.3.1.2 Analytical models

The simulation of impacts is a critical step in the knowledge of compressive residual stress generating processes. From the highly classical Hertz theory [HER 82], simple models for elastic impact modelling were derived by Davies [DAV 48] and Johnson [JOH 85]. These analytical models allow a perfect prediction of the phenomenon of an elastic impact but show drastically insufficient when plasticity is involved. For processes like shot peening, the impact velocities are far beyond the yield velocity, that is to say very large plastic flow occurs during the impacts.

Some analytical models exist to predict the results of shot peening processes. Franchim et al [FRA 09] proposed an analytical model based on experimental observations that allows to predict roughly residual stresses produced by a shot peening process. Tirosh [TIR 08] proposed a full analytical model to estimate the residual stresses. The plastic zone generated by an impact is approximated as a penny-shape inclusion for which residual stresses can be analytically calculated. This model involves very strong hypothesis on the material behaviour. The shape of impacts is necessarily governed by strong assumptions to obtain simple geometrical shapes from which analytical solutions can be derived and multiple impacts and close influence between impacts has to be neglected for the simplified theory to apply. Yet this model allows a fast and interesting estimation of the stresses and is extended to the fatigue life and shakedown analysis. More recently, Bhuvaraghan et al. [BHU 10a] proposed an analytical model for a single impact based on the work of Shen and Atluri [SHE 06] that accounts for strain rate in an isotropic material.

1.3.1.3 Numerical models

Analytical or simplified models present interesting applications for fast estimation and first steps but they are insufficient when a deeper understanding is necessary. More accurate numerical models are necessary to describe the plastic zone, residual stresses and other physical phenomena that may occur during impacts. The huge majority of the work made on impact modelling is made with the finite element method (FEM). Several can here be cited [KLE 09, ROU 09, VUQ 99, YAN 05, MAJ 05], the FE models are usually quite similar when only one impact is to be considered but differ highly when considering several impacts.

The precise effect of some physical phenomena can be better understood on single impacts. Impact models logically consider plasticity and sometime extend it to visco plastic effects, see for example Klemenz et al. [KLE 09]. It was shown by Rouhaud et al. [ROU 02] that the residual stresses are usually overestimated in shot peening simulations. A first contribution by Ould et al. [OUL 06, MAH 07] showed that kinematic hardening contributes to reducing the residual amount of stresses. Rouquette et al. [ROU 09] added thermal effects to their FE model. They showed that the heat produced by plasticity decreases the amount of residual stresses although the temperature remains below $200C$ for a metal under typical conditions of the peening process. These recent examples show that shot peening involves multiple physical phenomena each of which needs to be considered for a full global understanding of the problem.

1.3.1.4 Predicting the coefficients of restitution

An interesting way to analyse the energy stored by the impacted surface resides in the analysis of the coefficient of restitution. This dimensionless parameter is used to describe/predict the rebound velocity such as in ultrasonic shot peening [PIL 05, COC 06], sand-blasting [CHA 09] or cold spraying [ASS 03]. The coefficient of restitution is also of interest in many applications where overloads or damage are linked to impacts, such as

for read-write heads in hard-drives [KAT 09, KAT 10], mechanical seals or elements of roller bearings [SOC 06]. Considering an impact purely normal to the surface, the coefficient of restitution, usually denoted e is defined as the ratio between the rebound velocity and the initial velocity.

$$e = \left| \frac{v_r}{v_i} \right| \tag{1.1}$$

Several authors have studied the coefficient of restitution through analytical models, numerical models, mostly based on the Finite Element Method (FEM) or experiments. Johnson [JOH 85] first studied the elastic impact between two spheres or between an equivalent sphere and a plane, providing an analytical formula when an elastic-perfectly plastic behaviour is considered. Based on the simplified assumption that the contact pressure is constant and equal to three times the dynamic yield strength when plasticity occurs, he provided an analytical expression for the impact of an elastic sphere over an elastic perfectly plastic body. This expression can be extended to isotropic strain hardening when the strain-stress curve is assumed to follow a power law.

These expressions are usually derived from the simulation of indentation thus neglecting inertia effects, which is assumed to be valid for impact velocities up to $500 m/s$ for steels. Yang and Komvopoulos [YAN 05] studied the impact of a rigid sphere on an elastic half-space. They showed that inertial effects may have a significant effect during the very first load increments but become negligible beyond.

Thornton [THO 97] defined an analytical expression of the coefficient of restitution for the contact between two elastic-perfectly plastic spheres. The coefficient of restitution e is described as a function of the normalized velocity v/v_y where v is the initial relative velocity of the two bodies in contact and v_y the lowest initial relative velocity that leads to plastic flow in one of the bodies in contact. Note that the coefficient of restitution by Thornton is found very different than the one by Johnson. This could be attributed to the fact that both bodies are elastic-plastic instead of only one for Johnson.

Zhang and Vu-Quoc [VUQ 99, ZHA 02] studied the impact of a an elastic perfectly plastic sphere on a rigid body, using FEM to model plasticity in the sphere. They compared three different FE models' results to the Thornton's expression of the restitution coefficient. Based on their results, it can be concluded that the Thornton's formula underestimates the value of the coefficient of restitution at least for values of initial velocity up to a hundred times the yield velocity. From our point of view it means that the Thornton's equation is probably valid when the materials of the two bodies are identical and for impact velocities much higher than the yield threshold.

More recently, Jackson and co-workers [JAC 10] derived several equations from a mixed analysis between FE results and contact equations to describe the loading and unloading of a rigid sphere on an elastic perfectly plastic body. They quite successfully compared their results to published models and experiments. They provided accurate and reliable so called "empirical equations" to predict the coefficient of restitution. They also studied the influence of the Poisson's ratio and showed its strong impact on the coefficient of restitution. They also mentioned that the influence of strain hardening is rather

low, referencing Kogut and Etsion [KOG 02]. However these authors studied the normal indentation of a rigid sphere on an elastic plastic body with linear isotropic hardening but with a tangent modulus limited to 10% of the Young modulus leading to a difference for the contact parameters lower than 20% compared to the perfectly plastic case. It will be shown later that this difference should not be considered negligible for impacts with stronger strain hardening.

Weir and Tallon [WEI 05] studied the impact of small particles at low velocity (around $1m/s$). They developed an analytical model taking into account the size of the elastic-perfectly plastic particles to model granular flows. They also displayed results for multiple impacts at the same point with a constant initial velocity. Theses results exhibited an asymptote equal to 1 for the coefficient of restitution when the number of impacts is high enough. Finally they proposed some equations to model the evolution of the coefficient of restitution with the number of impacts as a function of the initial coefficient of restitution.

Multiple repeated impacts at constant velocity have also been studied by Seifried et al. [SEI 05]. They have shown an increase of the coefficient of restitution with the number of impacts up to a saturation. However, the saturation value is here found different from 1 since the sphere impacts a rod in which part of the initial kinetic energy is lost through inertial effects. This work was extended to study the effect of visco-plasticity that can be critical depending on the impacted material [SEI 10]. Using a pendulum-type experimental set-up, they validated their results for velocities up to $3.5m/s$. Repeated impacts with visco-plasticity was also studied numerically and a good correlation with experiments was observed [MIN 10]. Finally Minamoto and Kawamura [MIN 11] extended this work for "moderately high speed" i.e. up to $20m/s$ using an air-gun type set-up. Interesting comparisons can be made with the impact of a sphere on a semi-infinite body, yet considering the differences due to inertial effects in the rod.

Li et al. [LI 02, WU 05, LI 09] studied impact on a slightly different case. They developed models to take into account the deformation of an elastic-plastic sphere on a rigid half-space. They observed a transition velocity above which the sphere reaches a quasi-viscous state and starts to fully smash against the impacted surface. Note than in these models and related experiments the deformation takes place only (models) or mostly (experiments) within the impacting sphere. Moreover the sphere is highly deformed. The rebound behaviour is largely different from the cases where the flat is elastic-plastic and the impacting sphere is rigid or elastic, which leads to maximum strains of lower magnitude and so lower plasticity.

1.3.2 Multiple impacts modelling

Various authors have provided multiple impacts schemes based on FE models. Baskaran [BAS 10] recently provided a very relevant review of several existing models. The large number of impacts to simulate and large computation domain are a critical limit factor for efficient and relevant computations. The increase of computation capabilities allows today to perform simulations and some multiple impacts simulations can be performed, see for example the work by Klemenz [KLE 05, KLE 09], that worked with combined

hardening models with viscous effects.

A large effort is put on the decrease of the computation domain to obtain realistic calculation times. The use of symmetries is of course common, often modelling only one quarter of the impact domain. This is mainly possible since only impacts normal to the surface are simulated, a tangential velocity components would reduce the number of symmetries. Several impacts are sometimes performed at the same time at fixed distance and with a given sequence of impacts to represent the fully shot peened state. The model adopted by Klemenz et al. is given in Fig. 1.6.

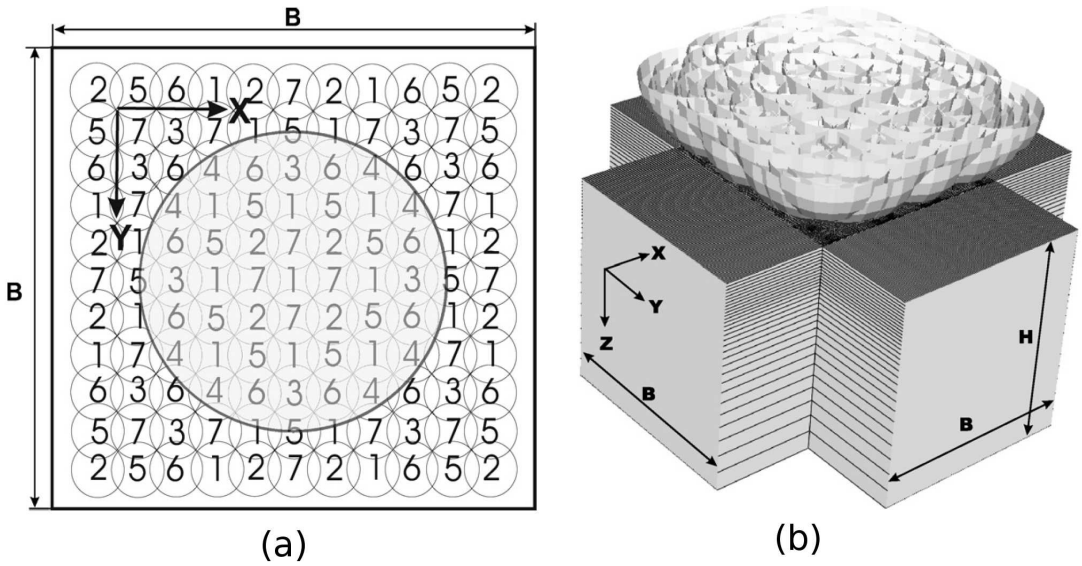

Figure 1.6: Impact order and arrangement with full coverage and marked evaluation area (a) and 3D-FE shot peening model (b) from [KLE 09].

Unit representative cells are chosen to represent the impacts sequence and to analyse the results. As seen in fig 1.6, impacts are chosen to be occurring in a square repartition by various authors. For Klemenz et al., the results are evaluated in large area containing several impacts. Majzoobi et al. [MAJ 05] chose a similar square repartition of the impacts, considering all impacts happening at the same time and using the symmetries along all sides of the square to reproduce the unit cell, see Fig. 1.7. They observe the residual stresses in depth at several locations of the model. They observe a quite large dependency of the point of observation for results just below the surface.

Schiffner et al. [SCH 99] proposed an extension of 2D model to a 3D model using a triangular shot repartition by exploiting the symmetries of the problem. Their work probably lacked the calculation power but provided an interesting insight to other shot repartition models. Kim et al. [KIM 10] proposed an analysis of residual stresses produced by multiple impacts with a square repartition similar to that proposed by Klemenz

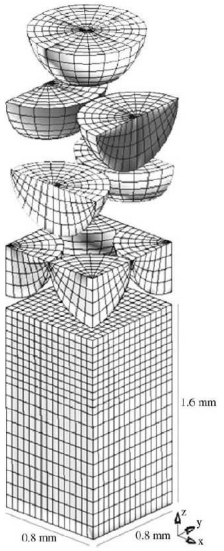

Figure 1.7: Nine-shot impact model from [MAJ 05].

et al. They proposed an averaging method of the results for comparison with the experimental residual stresses measures made by x-rays that are necessarily averaged. Two methods were proposed: averaging the results over four nodes situated at each corner of the reference square unit cell or averaging the results over the full reference area. They showed that the averaging of results over the full reference area gives good correlation with experimental results thus showing the importance of focusing on averaged results and not only on the profile in depth at a given position. Other similar models can be found in [MEG 07, LI 07]. Other authors chose to focus on a randomized impact repartition, see for example Miao et al. [MIA 09] or Bhuvaraghan [BHU 10b] who proposed a coupled FEM-DEM model. The DEM model allows to predict the position and velocities of impacts while the FEM model is used for the effective impact calculation and the prediction of residual stresses and strains.

1.4 Contact mechanics

1.4.1 Hertzian contact

1.4.1.1 Hertz hypotheses

The mechanics of contacts was first really developed by Hertz [HER 82] who presented what is called nowadays the Hertzian contact. The Hertzian contact describes the contact between two elastic bodies of spherical or elliptical geometries subjected to a static load

or displacement. The Hertzian theory is based on some important hypothesis:

- the contact zone has an elliptical shape
- the problem is considered frictionless
- the elastic bodies are considered semi-infinite

This last hypothesis is of crucial importance for the theory to apply. The bodies can be considered semi-infinite under two conditions :

- the contact area dimensions are small in comparison with the bodies dimensions. In this case the stresses are concentrated around the contact zone and the influence of the bodies' boundaries on the stress repartition is negligible. This condition is ensured by the non-conformity of the surfaces:
- the radii of curvature of the bodies in contact are large compared to the dimensions of the contact. This condition validates the previous one. Consequently the angles made by the surfaces in contact have to remain small. The contact area can then be approximated by a plane and the stress level remains compatible with the theory of elasticity.

These hypothesis are quite restrictive and thus the theory does not apply for finite dimension bodies and when the behaviour is no longer elastic. Yet they give satisfactory solutions for a large number of applications and offer a fast first step estimation for more complicated applications. Many particular analytical solutions have been developed over the years and can be found in Johnson's reference book [JOH 85]. The solutions for a circular contact are recalled here as well as the approximated solutions for an elliptical contact, recently developed by Antoine et al. [ANT 06]. Extension of this theory can be made for the consideration of an elastic impact. Consequent formulae are here recalled as well.

1.4.1.2 Circular contact

The analytical solution for the elastic contact of two solids of revolution is described by Johnson [JOH 85]. The main equations resulting from this solution are recalled here. The two bodies in contact, denoted 1 et 2, have radii of curvature denoted respectively R_1 and R_2. The relative curvature of the bodies in contact is given by Eq. 1.2. The problem is represented in Fig. 1.8

$$\frac{1}{R_{eq}} = \frac{1}{R_1} + \frac{1}{R_2} \tag{1.2}$$

The elastic properties of body i are given by its Young modulus of elasticity E_i and Poisson's ratio ν_i. The equivalent Young modulus of the two surfaces in contact E^* is described by Eq. 1.3. It is important to note here that E^* is the only material parameter governing the results.

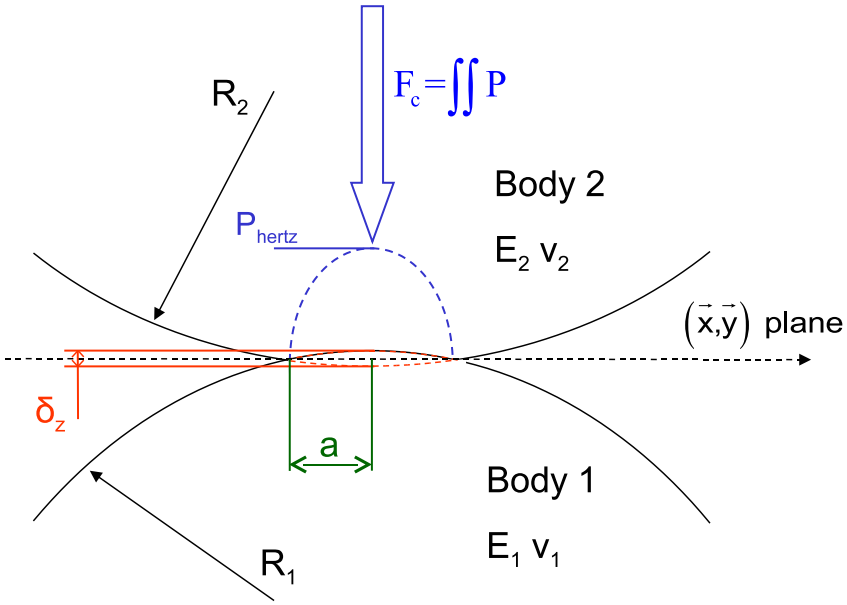

Figure 1.8: Schematic representation of the Hertzian contact of solids of revolution: main parameters of the theory.

$$\frac{1}{E^*} = \frac{1-\nu_1^2}{E_1} + \frac{1-\nu_2^2}{E_2} \tag{1.3}$$

Considering an applied load F to the bodies in contact, all other contact parameters are deduced. The area of contact radius a, the rigid body displacement δ_z and maximum contact pressure P_{hertz} are deducted from the applied load. Similar formulae can easily be deduced with a, δ_z or P_{hertz} as input value.

$$a = \left(\frac{3FR}{4E^*}\right)^{1/3} \tag{1.4}$$

$$P_{hertz} = \frac{3F}{2\pi a^2} = \left(\frac{6FE^{*2}}{\pi^3 R^2}\right)^{1/3} \tag{1.5}$$

$$\delta_z = \frac{a^2}{R} = \left(\frac{9F^2}{16RE^{*2}}\right)^{1/3} \tag{1.6}$$

Finally the pressure profile in the area of contact which is parabolic is also defined as a function of the distance r from the center of the contact.

$$P = P_{hertz}\left(1 - \left(\frac{r}{a}\right)^2\right)^{-1/2} | r \leq a \tag{1.7}$$

1.4.1.3 Elliptical contact

The Hertzian contact of elliptical bodies leads to the formulation of elliptic integrals of the first F_F and second F_ε kinds, defined in Eqs. 1.20 and 1.21. Antoine et al. [ANT 06] proposed approximate functions for the elliptic integrals that allow excellent evaluations of the contact parameters. As for the contact of bodies of revolution, the contact of two elastic elliptical bodies 1 and 2 of radii R_{ix} and R_{iy} respectively in the x and y directions that are directions parallel to the contact surface. The curvatures of the bodies are defined as the inverse of the radii $\rho_i = 1/R_i$. The geometrical parameters of the problem are represented in Fig. 1.9.

The elastic properties of the bodies are defined similarly to the previous case with the equivalent Young modulus of the bodies in contact defined in Eq. 1.3. The load applied on the bodies is denoted F_c and the rigid body displacement δ, δ^* is a dimensionless form of the displacement.

The curvature is defined with the curvature sum $\sum\rho$ and curvature difference F_ρ.

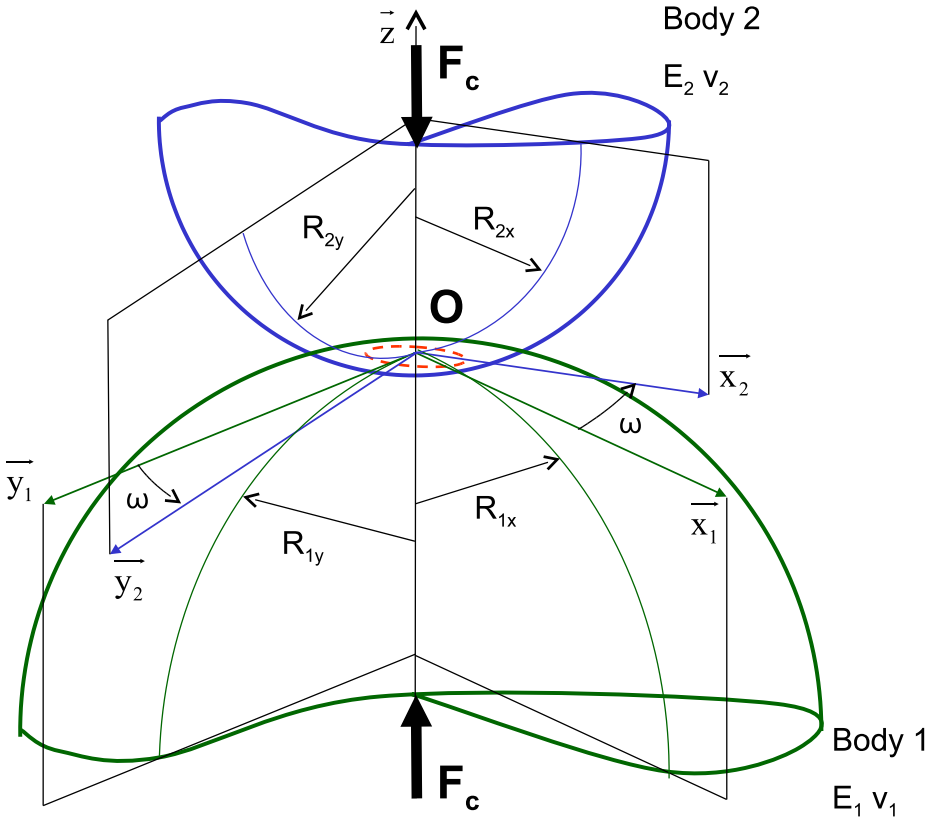

Figure 1.9: Schematic representation of the Hertzian contact of elliptical solids: bodies 1 et 2, planes of principal curvatures, geometrical parameters and applied force F_c from [ANT 06].

$$\sum \rho = \rho_{1x} + \rho_{1y} + \rho_{2x} + \rho_{2y} \tag{1.8}$$

$$F_\rho = -\frac{\sqrt{R_1^2 + R_2^2 + 2R_1R_2cos2\omega}}{\sum \rho} \tag{1.9}$$

Where $R_1 = \rho_{1x} - \rho_{1y}$ and $R_2 = \rho_{2x} - \rho_{2y}$ and ω is the angle between planes of relative principal curvatures of both bodies in contact. The relative curvatures of the bodies A and B are defined as:

$$A = \frac{\sum \rho}{4}\left(1 + F_\rho\right) \tag{1.10}$$

$$B = \frac{\sum \rho}{4}\left(1 - F_\rho\right) \tag{1.11}$$

These parameters are necessary to define the area of contact. This area is elliptical with its semi major axis denoted a and semi minor axis denoted b. The axis of the contact ellipse are defined as functions of their dimensionless form a^* and b^*.

$$a = a^* \left(\frac{3F_c}{2\left(A+B\right)E^*}\right)^{1/3} \tag{1.12}$$

$$a^* = \left(\frac{2\kappa^2 F_\varepsilon\left(\kappa\right)}{\pi}\right)^{1/3} \tag{1.13}$$

$$b = b^* \left(\frac{3F_c}{2\left(A+B\right)E^*}\right)^{1/3} \tag{1.14}$$

$$b^* = \left(\frac{2F_\varepsilon\left(\kappa\right)}{\pi\kappa}\right)^{1/3} \tag{1.15}$$

The rigid body approach δ, its dimensionless value δ^* are defined as follows.

$$\delta = \delta^* \left(\frac{3F_c}{2E^*}\right)^{2/3} \frac{\left(A+B\right)^{1/3}}{2} \tag{1.16}$$

$$\delta^* = \frac{2F_F\left(\kappa\right)}{\pi}\left(\frac{\pi}{2\kappa^2 F_\varepsilon\left(\kappa\right)}\right)^{1/3} \tag{1.17}$$

Consequently, the force displacement relationship can be expressed.

$$F_c = \left(\frac{2^{5/2}}{3}\frac{E^*}{\left(\delta^*\right)^{\frac{3}{2}}\left(A+B\right)^{\frac{1}{2}}}\right)\delta^{3/2} \tag{1.18}$$

All this formulae are function of the ellipticity parameter κ defined as a/b which is to the geometrical parameter F_ρ according to the hertzian contact theory.

$$F_\rho = \frac{B/A-1}{B/A+1} = \frac{\left(\kappa^2+1\right)F_\varepsilon(\kappa) - 2F_F(\kappa)}{\left(\kappa^2-1\right)F_\varepsilon(\kappa)} \tag{1.19}$$

The elliptic integrals of the first and second kind, respectively F_F and F_ε are defined as follows:

$$F_F(\kappa) = \int_0^{\pi/2} \left(1-\left(1-\frac{1}{\kappa^2}\right) sin^2\phi\right)^{-1/3} d\phi \tag{1.20}$$

$$F_\varepsilon(\kappa) = \int_0^{\pi/2} \left(1-\left(1-\frac{1}{\kappa^2}\right) sin^2\phi\right)^{1/2} d\phi \tag{1.21}$$

The problem of the theory resides in the expression of theses integrals which is not analytically known. Approximate functions are thus given for the integrals, as function of parameter $m_1 = 1/\kappa^2$. They are only valid for $0 \leq m_1 \leq 1$ (i.e. $\kappa \geq 1$). From the approximate expressions 1.22 and 1.23, the contact parameters a, b and δ defined previously can be deduced.

$$F_F(\kappa) = \left(\alpha_0+\alpha_1 m_1+\alpha_2 m_1^2\right) - \left(\alpha_3+\alpha_4 m_1+\alpha_5 m_1^2\right)\ln m_1 \tag{1.22}$$

$$F_\varepsilon(\kappa) = \left(\beta_0+\beta_1 m_1+\beta_2 m_1^2\right) - \left(\beta_3 m_1+\beta_4 m_1^2\right)\ln m_1 \tag{1.23}$$

The numerical constants in eqs 1.22 and 1.23 are defined in table 1.1.

α_0	1.3862944	α_4	0.1213478	β_2	0.1077812
α_1	0.1119723	α_5	0.0288729	β_3	0.2452727
α_2	0.0725296	β_0	1	β_4	0.0412496
α_3	0.5	β_1	0.4630151		

Table 1.1: Coefficients for the polynomial approximations 1.22 and 1.23 of the elliptic integrals of first and second kinds from [ANT 06].

1.4.1.4 Frictionless Elastic Normal Impact

The theory of Hertz for the normal contact between two spheres can be used to calculate the maximum rigid body approach δ^* for an elastic impact knowing the equivalent radius and initial relative velocity v of the two bodies in contact.

At any point of the impact, the relationship between the rigid body displacement δ and the load F is given by Eq. 1.6. The elastic energy in the body can then easily be calculated. At the climax of the impact, δ is equal to δ^*, the maximum rigid approach. The elastic energy is then equal to the initial kinetic of the ball E_k as indicated in Eq. 1.24.

$$E_k = \frac{1}{2}mv^2 = \int_0^{\delta^*} F \, d\delta \tag{1.24}$$

This allows to calculate δ^*, as proposed by Davies [DAV 48]. The value of δ^* can then be expressed as a function of the sphere radius R and its initial velocity v, as given by Eq. 1.25.

$$\delta^* = \left(\frac{15}{8} \frac{E_k}{E^* \sqrt{R}} \right)^{\frac{2}{5}} \tag{1.25}$$

$$\delta^* = R \left(\frac{5}{4} \rho \pi \frac{v^2}{E^*} \right)^{\frac{2}{5}} \tag{1.26}$$

This equation can be applied more generally to the impact of spherical bodies of radii R_1 and R_2 by substituting the equivalent radius R_{eq} (see Eq. 1.2) to R.

No full analytical expression exists for the time-displacement curve of an elastic impact problem. However, a numerical integration of the time-displacement curve was made by Deresiewicz [DER 68] which allows then to determine the total time of impact:

$$T_c = 2.94 \frac{\delta^*}{v} = 2.87 \left(\frac{m^2}{R E^{*2} v} \right)^{\frac{1}{5}} \tag{1.27}$$

An extension of this theory can be made to account for plasticity and thus consider plastic dissipation during the impact. This more generally leads to the studies on the coefficient of restitution and is described in 1.3.1.4. A similar approach has been applied by Maw et al. [MAW 76, MAW 81] to oblique impacts. Considering the elastic properties and friction coefficients of the surfaces in contact and the initial angle of impact, three regimes can be defined: (i) complete sticking regime for angle of impacts that are small compared to the friction angle, (ii) partial slip regime during the impact with complete slip at the beginning and the end of the impact and finally (iii) full sliding for high incidence angles.

1.4.2 Non Hertzian contact

When the geometries in contact cannot be approximated as ellipsoids or when the behaviour of the body is no more elastic, numerous analytical solutions exist as well. Most of these theories still assume contact between semi infinite bodies but various solutions exist as well for contact between plates or shells. More complex geometries, including angles or corners have also been studied. Various solutions exist for two dimensional bodies and are often extended to three dimensional problems when an axisymmetric condition can be assumed. The book by Gladwell [GLA 80] resumes two of these methods: the "singular integral equations" (see also [MUS 53, GAL 53]) and the Fourrier transform, see [SNE 51].

The contact of rough surfaces, that allows to consider true manufactured surfaces in opposition with the perfect surfaces considered by the Hertzian contact, has also been part of numerous studies. Westergaard [WES 39] provided a solution for the contact of surfaces presenting a sinusoidal roughness. Greenwood and Williamson [GRE 66] have developed solutions of rough surfaces using a statistical method describing the distribution of spherical asperities based on a gaussian distribution.

When the body is no longer homogeneous, solutions exist for the contact on a coated body. The coating and the underlying body are both considered elastic but with different properties. Solutions for coatings of constant thickness have been described by Meijers [MEI 68] using the integral methods from Gladwell [GLA 80].

Analytical solutions exist also for plasticity. They usually consider rigid perfectly plastic bodies. Johnson [JOH 85] proposed several solutions for the contact and indentation of plastic bodies and for various geometries. Similar solutions for elastic perfectly plastic contacts exists for the indentation of spheres, pyramids or cones. The extension of this theory coupled with the impact considerations allows to calculate analytical solutions for the coefficient of restitution of the impact of elastic perfectly plastic bodies.

Finally, lot of work has been made on the study of combination of normal and tangential contacts. For full sliding situations, the normal contact problem is all-sufficient since the shear generated is directly the product of the friction coefficient by the contact pressure. Cattaneo [CAT 38] and Mindlin [MIN 49] provided the solution for mono dimensional partial slip problems. A spherical contact is considered, on which a normal and tangential loading are applied. The ratio between the loads has to stay below the full slip condition given by Coulomb law. Mindlin and Deresiewicz [MID 53] went further considering a tangential loading proportional to the normal loading. At last, this problem was generalised to bi-dimensional geometries and more complex geometries by Ciavarella [CIA 98a, CIA 98b].

1.4.3 Mechanical modelling using semi analytical-methods

For general problems, including complex or finite geometries, influence of plasticity, inhomogeneities or general tangential loading, the use of numerical methods comes necessary. The most widely used method is of course the Finite Element method. The discretization of bodies into finite elements allows to consider all kind of problems and physical phenomena, including dynamics, thermal effects, plasticity, ... This method is largely mastered and contact problems can be solved this way. Yet numerical problems often occur and the fine meshing needed in the critical areas, especially the high stress gradient zones around the contact, sometimes lead to prohibitive computation times. An alternative to this method is the boundary elements method (BEM). This method is quite similar to the FEM except that only the boundaries of surfaces of the bodies are meshed. From this method, analytical solutions can be derived that led to the development of the semi analytical methods (SAM). When analytical solutions can't be found for complex problems, it is possible to discretize the problems in a sum of basic known solutions for which analytical solutions are known. This basic principle is the foundation of the SAM.

1.4.3.1 Development of the semi analytical techniques

The first semi analytical models were proposed by Bentall and Johnson [BEN 67] and Paul and Hashemi [PAU 81] for contact problems under a static load. Kalker proposed a first formalisation of this method [KAL 90] using a Newton-Raphson algorithm. Nowell then studied fretting problems using similar methods but restricted to bi-dimensional problems [NOW 98, DIN 04]. Other numerical techniques were proposed, for example Jaeger [JAE 04] uses a Gauss-Seidel algorithm.

Acceleration techniques were then proposed and widely used. Multi-grid techniques were first used [BRA 90, LUB 91] and more recently Fast Fourrier Transforms techniques (FFT) [JU 96, NOG 97, POL 00] that are today accepted as the most suitable technique for semi analytical models. The use of FFT allows a huge gain in the computation time compare to direct calculation methods but requires an extension of the domain of 8 times in each dimension problem. This extension was reduced to two times in each computation direction by the use of DC-FFT technique proposed by Liu et al. [LIU 00]. The zero-padding and wrap-around order techniques applied to the analytical solutions reduce to a negligible part the computation error made during the FFT transformation. The coupling of these computation methods with powerful algorithms like the conjugate gradient method (CGM) [POL 99] allows today the use of very fine mesh in contact areas.

The extension in recent years to plasticity added the consideration of 3D semi analytical solutions. Bi-dimensional FFTs were first applied at each depth of the solids in contact [JAC 02]. An acceleration of the technique was proposed by Zhou et al. [ZHO 09], called the 3D-FFT technique in opposition with the plane by plane 2D-FFT technique that allows a significant decrease of the computations times.

A significant condition of the use of FFT technique is the necessity of having a regular mesh. Thus semi analytical models are always composed of cuboidal elements which dimensions are constant. Other methods exists, like the Galerkin vectors technique [YU 91a, YU 91b, LIU 05] for the computation of 3D problems but have not been applied yet to complete semi analytical models.

1.4.3.2 Towards more physical phenomena

The use of SAM was first developed for solving contact problems of elastic complex shape bodies [BEN 67, PAU 81, KAL 90]. The models were then extended to coatings of constant thickness behaving elastically [TIA 96, PEN 00, PEN 01, PEN 02, CAI 05] and thermo-elastic problems [LIU 01, LIU 03]. The extension of SAM always relies on the knowledge of the reference analytical solutions needed to discretize the problem into known problems. Most of these analytical solutions are derived from the BEM. It is important to recall that the SAM always apply to semi infinite bodies.

Chiu [CHI 77, CHI 78] developed analytical solutions for the residual stresses generated by a cuboid of uniform strain included in a semi infinite body. These solutions were implemented to SAM to consider the effect of plasticity by Jacq et al. [JAC 01, JAC 02]. This opened the way to elastic plastic contact problems formulation. Problems of contact of fractal surfaces were then studied by Willner [WIL 04].

The elastic plastic contact SAM model was applied to the study of various phenomena. The interaction between plastic behaviour and frictional heating was developed by Boucly et al. [BOU 04, BOU 05]. At the same time, plasticity computation was improved using a return mapping algorithm as defined by Simo and Taylor [SIM 85]. The analysis of frictional heating in contacts, with the influence of heat partition and sliding speed was studied by Chen et al. [CHE 08b]. The method was also applied to the case of electrical sliding contacts, to study the effect of thermal softening and melting inception [CHE 09a].

The fine discretization of the contact domain allowed by the SAM lead to the study of the contact of rough surfaces [SAI 02]. Similar models were applied for wear and to the running-in of surfaces [NéL 06] and more recently by Bosman et al [BOS 11a], Wang et al. [WAN 10b] or Chen et al. [CHE 09b]. Fast computation were also used to perform studies on multiple loadings and unloadings [CHE 08c].

Antaluca et al. applied a tangential loading in the case of full sliding contact to study the application over dented surfaces [ANT 04, ANT 05] and studied the case of a rolling loading over an elastic-plastic flat studying also the influence of the ellipticity ratio of the surfaces in contact, ranging from circular contacts to almost cylindrical contacts [NéL 07a] with application to conventional roller bearings and up to cylindrical bearings. Boucly et al. applied similar models to the study of rolling and sliding contact between asperities [BOU 07].

Beyond the simplification of full slipping regime, Gallego et al. proposed a full contact model for elastic bodies under stick-slip conditions [GAL 07a]. This model was applied to the prediction of wear of fretting surfaces [GAL 06] and under partial slip condition [GAL 07b]. The model is able to handle all three fretting modes [GAL 10b] and was coupled with FEM simulation of blades turbines to study the fretting wear at the blade/disk interface [GAL 10a]. This model was applied to the case of elastic layered materials [WAN 10a]. In this method, the normal and tangential contact problems are solved alternatively. A fully coupled method was proposed by Willner [WIL 88].

Analytical solutions to account for plasticity in the tangential problem were determined by Fulleringer et al. [FUL 10] and applied to model fretting and wear models of elastic plastic bodies [FUL 11].

Most recent works were made to couple the dry contact semi analytical models with lubricated contacts. The transition from mild to severe wear lubricated contacts, still with the effect of plasticity was studied by Bosman et al. [BOS 11b]. The coupling between elastic hydrodynamic lubrication (EHL) models and elastic plastic contact models to lead to PEHL models was made by Ren et al. [REN 10].

At last a huge effort is made today to consider the effect of inclusions or inhomogeneities in the contact bodies, model that can be applied to the contact of solids with defects or irregular coatings. Indentation on elastic bodies containing inhomogeneities [LER 10] or on elastic plastic indentation on layered materials [CHE 10] has been studied using the inclusion method and the field is still in full development.

1.5 Rolling contact mechanics

Rolling contact mechanics and especially fatigue induced by rolling contacts is a wide field of study. This phenomenon is involved in many industrial applications such as bearings, gears, cams or mechanical transmissions. The fatigue behaviour of material is a known field and evaluation of the life duration of a component under cyclic loading can be estimated. Certain material present a endurance limit load below which no fatigue phenomenon and thus no ruin of the system will occur. Yet the knowledge of the stress history in the material, both considering the residual stress state and applied stress is necessary for this analysis.
For high reliability industrial applications, systems are dimensioned to word under their yield limit so that their behaviour stays fully elastic. A simple analytical approach, such as the Hertzian contact is then all-sufficient to analyse the stress history inside the body, but the fatigue behaviour under multiple cycles still needs to be analysed. This approach might show insufficient when the system is submitted to punctual peak loads that may overcome the yield limit and thus generates defects in the components. The passing of the load over such created or pre-existing defects will generate higher pressures that may lead to further plastic flow or crack generation and propagation.

The study of rolling over dents has been studied for example by Nelias et al. [NéL 05, VIN 06]. The development of semi analytical models applied to indentation [JAC 02, JAC 01] has led to their extension to the study of rolling contacts over dented surfaces [ANT 04]. The pressure fields generated by the contact of two elastic plastic bodies with contact load higher that the limit the load has been studied by Antaluca et al. [NéL 07a] and the study was generalized to spherical and elliptical contact geometries. The residual imprint generated by plasticity and the effect of several load passes was made, leading towards a better understanding of rolling contact under high loads.

1.6 Conclusions

This PhD aims at establishing a method for the simulation of impact and especially multiple impact processes using a semi analytical method. A large knowledge on elastic plastic contact model based on SAMs will be used as a basis. This method should then be applied to the study of the shot peening process as part of a collaboration work [LI 11]. The study of the state of the art showed first that there exists a large number of industrial phenomena that can be modelled simply by impacts and thus pointed at the interest in developing a general tool that can be applied to multiple processes.

Numerous parameters involved in this processes were identified, reinforcing the interest in having a fast and efficient method to study the effect of all these parameters that are shot radius or velocity and material properties among others.

It was observed that impact simulation does not need to consider inertia effects which will be significant in the development of the method. Several physical phenomena are to be considered to capture the full physics of the problems. Obvious part of these phe-

nomena, like plasticity and several material hardening laws will be considered. More complicated phenomena like thermal effects are considered as second order influence and will not be considered.

The main process parameter for shot peening simulation is obviously the number of impacts. The complexity of modelling the full process implies necessarily the definition of a strategy to consider multiple impacts in a reduced model. Several strategies exist but none seems obviously better and a particular care will be applied on the definition of this method. The multiple impact modelling bibliography study also showed a huge domination of finite elements methods. No alternative clearly exists today. A large number of impacts can be considered today due to the increase of computation power but this still can be a limitation. A fast and reliable model seems an interesting alternative. Simple analytical and thus extremely fast models exists and are in development but the application to a full problem with multiple impacts is not reached yet.

FE results comparisons with experiments usually show good correlation if these results are correctly interpreted in terms of area or point where the results are taken. FE can thus be an interesting reference for validation but it is pointed that a correct interpretation and post treatment of the results is necessary. This care will be brought to the multiple impact method definition.

The coefficient of restitution is an interesting field with various applications and several approaches exist. Studies usually are confined to low velocities, which corresponds to the lower velocities of shot peening and no effect of hardening is considered. Furthermore, these studies usually concentrate on a single impact. An extension of these analysis would prove an interesting development for the study of multiple impact phenomena in a simple analytical way.

Finally, the use of SAMs for contact problems is today widely use. Their efficiency has been proven, their accuracy as well. And they attract more and more interests. The number of physical phenomena considered increases and thus they offer varied possibilities for mechanical simulation. Their computation speed is recognized and they present as a good candidate to model multiple impact phenomena.

A Semi Analytical method for contact and impact simulations

A semi analytical contact method was formerly developed to study the contact of non conformal elastic-plastic bodies. The aim of this work is to extend this method to the consideration of impacts. This chapter presents the major improvements made to the method for the consideration of impacts. These improvements fulfil two aims: the adaptation of the method to relatively large strain levels and the consideration of impact loadings.

The general algorithm and contact solvers are first briefly depicted. A brief explanation of numerical improvements is made. This chapter then concentrates on two major parts of the code: the stress calculation, on which enhancements have been brought for the computation speed and the large displacement consideration, and the plastic strain computation that has been extended to the consideration of kinematic, and thus, mixed hardening. Focus is made then on the specificities of impact consideration and the subsequent additions made to the method. At last validations of the model are presented.

Contents

2.1 Introduction

The study of the state of the art in chapter 1 showed the interest of semi analytical methods (SAMs) for mechanical modelling. Based on a large experience on SAMs and their advantages it was chosen to extend the SAM to the consideration of impacts. The use of SAM is mainly interesting for the computation speed it offers. The ease it presents for the resolution of contact problems is also an advantage compared to conventional methods. Finally, the state of the art also showed that the study of impacts is widely ruled by the Finite Element Method and SAMs can turn up as an interesting alternative.

The model presented here is derived from the model developed by Jacq [JAC 01] and Boucly [BOU 08]. A semi analytical method was thus developed to model the contact of elastic-plastic bodies of random shape. Thermal effects as well as the modelling of wear was included in the model that considered only isotropic hardening. Several other physical mechanisms, such as tangential stick-slip effects or inclusion modelling, have also been included to SAMs by various authors. The reader may refer to section 1.4.3 for an accurate description of the existing SAMs and modelled phenomena.

Thermal and tangential effects were not included. The study of the literature showed that these effects are of second order for the studied phenomena. The SAM was firstly developed for the simulation of contacts between mechanical components. Under normal load conditions, these components are usually designed to run under their yield limit or slightly above it. Consequently the study may consider only elasticity [GAL 07a] a low plasticity level [JAC 01, BOU 08], typically around 1 or 2% or residual strain. The main goal of the current study is the analysis of industrial processes generating compressive residual stresses. These processes involve larger strain levels and thus the use of the method was extended.

The use of SAM at level of deformation of a few percents of plastic strain involves some care in the definition of the size of the mesh. Actually, numerical instabilities can occur in SAM, similarly to effects occurring with the discrete element method. The resolution of these instabilities is presented in section 2.2.5. The convergence criteria used in the former were inappropriate for large strain consideration and have been corrected, see sec. 2.2.4.

The semi analytical solutions used in the SAM used a small-strain formulation as defined in Eq. 2.1, where u^e denotes the elastic displacements and ε^e the elastic strain.

$$\varepsilon^e_{ij} = \frac{1}{2}\left(u^e_{i,j} + u^e_{j,i}\right) \tag{2.1}$$

The consideration of cross-terms in the strain formulation is thus not included in SAM and cannot be part of the model, except for considering other semi analytical solutions. Another important feature of the model is the fact that the plastic strains are calculated incrementally, which is crucial for large strain consideration. The semi analytical solutions used in this method are derived from the Hertzian contact theory, see sec. 1.4.1.1 and so consider that the angles made by the surfaces in contact remain small. When the bodies in contact encounter large deformation, this hypothesis is no longer valid and improve-

ments were brought to the method to account for this effect in the calculation of stresses generated by the contact pressure, see sec. 2.3.1. At last, an important part of the strain considerations is the incompatibility equations, that ensure the continuity of the strain and displacement fields. The non respect of this hypothesis generates an error that can be neglected at low strain levels, but increases with the strain. This feature is not included in the current method and might be a source of error in the presented results as well as an important improvement for upcoming work.

The residual strain computation is a second critical step in the SAM. First, it is the feature that will determine the influence of plasticity and thus determine the difference with the analytical elastic solutions and second it is the most time consuming step of the model. For these reasons, a particular care was brought to this part of the model. The so called 2DFFT method, used by Jacq and Boucly [JAC 01, BOU 08] was replaced by the 3DFFT method, which allows faster computation and a decrease in the amount of memory used by the model. Despite the significant benefit in computation time, this method shows intrinsically rather inaccurate to calculate residual stresses generated by strains located very close to the surface. A combination of the two methods is thus proposed to decrease this error while still keeping large benefits in speed.

The computation of plastic strains, that generate the residual stresses, is made by a classical return-mapping algorithm, first described by Simo and Taylor [SIM 85]. Former studies concentrated on isotropic hardening, the current study added the consideration of the kinematic hardening and so the return-mapping algorithm was extended to these considerations. The various hardening laws used throughout this work are presented subsequently.

As the state of the art showed, the influence of inertial effects in low velocity impacts is negligible. This feature was thus not included in the model which is then a quasi-static model for which the load path is not known a priori. To consider impact, it is needed to determine the loading path at each step as a function of the initial impact velocity. The determination of the impact loading is described in sec. 2.5.

The last part of this chapter is dedicated to the numerical validation of the method. Former validations made on the elastic-plastic analytical contact model are quickly recalled. The modifications brought to the plastic strain calculation, including the 3DFFT methods and convergence criteria modification are validated through comparisons with FEM results. Elastic analytical solutions are used to validate the impact loading calculation loop. At last, benchmarks of the simulation of impacts at large strain levels (about 10%) have been made with several finite elements codes and will be presented in the following chapters.

Finally, some important aspects of the SAMs are worth recalling here. As indicated further, Fast Fourier Transforms (FFT) are used for the computation of mechanical quantities. The model must then have a mesh of constant size in all three space directions. Consequently, no mesh reduction in critical areas is possible. A second important aspect is the use of the semi analytical solutions that are defined for semi infinite bodies. The consideration of the boundary conditions is thus intrinsic to the used solutions. Consequently, only the area of interest is to be meshed, which allows large gains in computation

time since no meshing of the boundaries is necessary. The drawback to this aspect is that the method is only able to model semi infinite bodies. That is to say the dimensions of the simulated bodies have to be large with respect to the area of interest (i.e. the plastic zone) as described by Saint Venant's principle.

2.2 General algorithm and contact solver

2.2.1 General algorithm

The general algorithm of the SAM is described here and plotted in Fig. 2.1. In addition to the common steps of the model, the most important steps for the simulation of impact are presented. Optional steps, i.e. the tangential contact solver and the consideration of large displacements, are also indicated.

The initial state is first defined. The geometries of the two bodies in contact as well as their material properties are given. Only one body is considered elastic-plastic in this study but two elastic plastic bodies could easily be considered. Initial strains and stresses can be included in the elastic-plastic body. Strains can be consequence of former plasticity or eventual non homogeneous inclusions, though not part of this work. Stresses can be of two kinds: residual stresses, consequence of the formerly described strains, or so-called initial stresses. Initial stresses, denoted σ^{init}, can come from material phase transformation, surface treatment or strains located outside the simulated zone. At last, the loading path has to be defined: contact force or rigid body displacement history for classical contact problems, additional rolling distance and rolling step for rolling loads and initial velocity for impacts. For impact simulations, the current velocity is used at each step to calculate the rigid body displacement δ_z or contact force F_c.

In all cases, the force or displacement is used as input to the contact solver. The contact is solved using a conjugate gradient method (CGM), see Normal Contact Problem in Fig. 2.1. When considering tangential effects, an additional contact solver is used. The normal and tangential contact problems are solved alternatively, the other being consider constant, until convergence of both problems, see [GAL 07a]. From the contact solver, the surface pressure field (plus eventual shear fields) is calculated. The normal contact solver is briefly described in section 2.2.3.

In the case of large displacements, this pressure field is considered applied on the deformed surface and projected on the initial reference surface to account for the angles made by the surfaces. Consequently, the initial pressure field is resolved into a pressure normal to the initial surface and shears in the two directions parallel to the surface. This operation is descibed in section 2.3.1.

The contact being solved, the loading of the body is described and the stresses are

then computed. From the pressure, and eventual shear fields, so called elastic stresses σ^e are calculated using classical elementary analytical solutions described in annex A (see section 2.3.1). The residual stresses σ^{res} generated by non homogeneous strains in the body are computed using either the 2DFFT or 3DFFT method, described further in section 2.3.2. Initial stresses σ^{init} are added to obtain the total stress σ^{tot} which is simply the sum of all three stress components according to the small strain hypothesis:

$$\sigma^{tot}(B) = \sigma^{e}(B) + \sigma^{res}(B) + \sigma^{init}(B), B \textit{ being a point in the volume} \tag{2.2}$$

The total stress is used as input to the return-mapping algorithm and used to calculate the increment of plastic strain at each point of the body, see section 2.4. From this increment, new residual stresses are computed along with the increment of surface residual displacement. The new stress and strain state in the bodies being known, the convergence of the problem is checked. The increment of residual stress validates the convergence of the contact problem while the yield function does the same for the plastic problem. The convergence criteria are described in section 2.2.4. In case of convergence, the next load increment is started, determining the new load or displacement. In the opposite case, the geometry is updated with the residual stress and a new iteration is done, starting with the contact solver, with updated stresses and this until convergence is reached.

Three mechanical quantities are to be computed in this method: surface displacements, stresses and plastic strains. The plastic strains are computed at each element using the return mapping algorithm. The displacements and stresses are quantities that can be directly computed at a given time from the source that generates. This source is the loading (pressure and/or shears) for the "elastic" displacements and stresses, and the plastic strains for the "residual" displacements and stresses. Influence coefficients, recalled in annex A, describe the link between the source and the calculated quantity. The influence coefficients are applied using the DC-FFT method to reduce the computation time. This fast computational method, based on the Fast Fourier Transforms is described in the following section.

2.2.2 The DC-FFT Method

Semi-analytical methods are based on the use of elementary analytical solutions. Their use to solve contact problems is well-known, more details can be found in [JAC 01, JAC 02], [BOU 05, BOU 08] or [GAL 07a]. Only the basic principle of the method is recalled here. The summation of analytical solutions to obtain the solution of the complex problem is a time consuming operation. It is accelerated by the use of Fast Fourier Transforms (FFT). This was first introduced by Ju and Farris [JU 96].

The method is illustrated by the computation of the vertical displacement of an elastic surface generated by a pressure distribution. This computation is made at the Normal Contact Problem step, represented in Fig. 2.1. While solving the contact, a pressure field

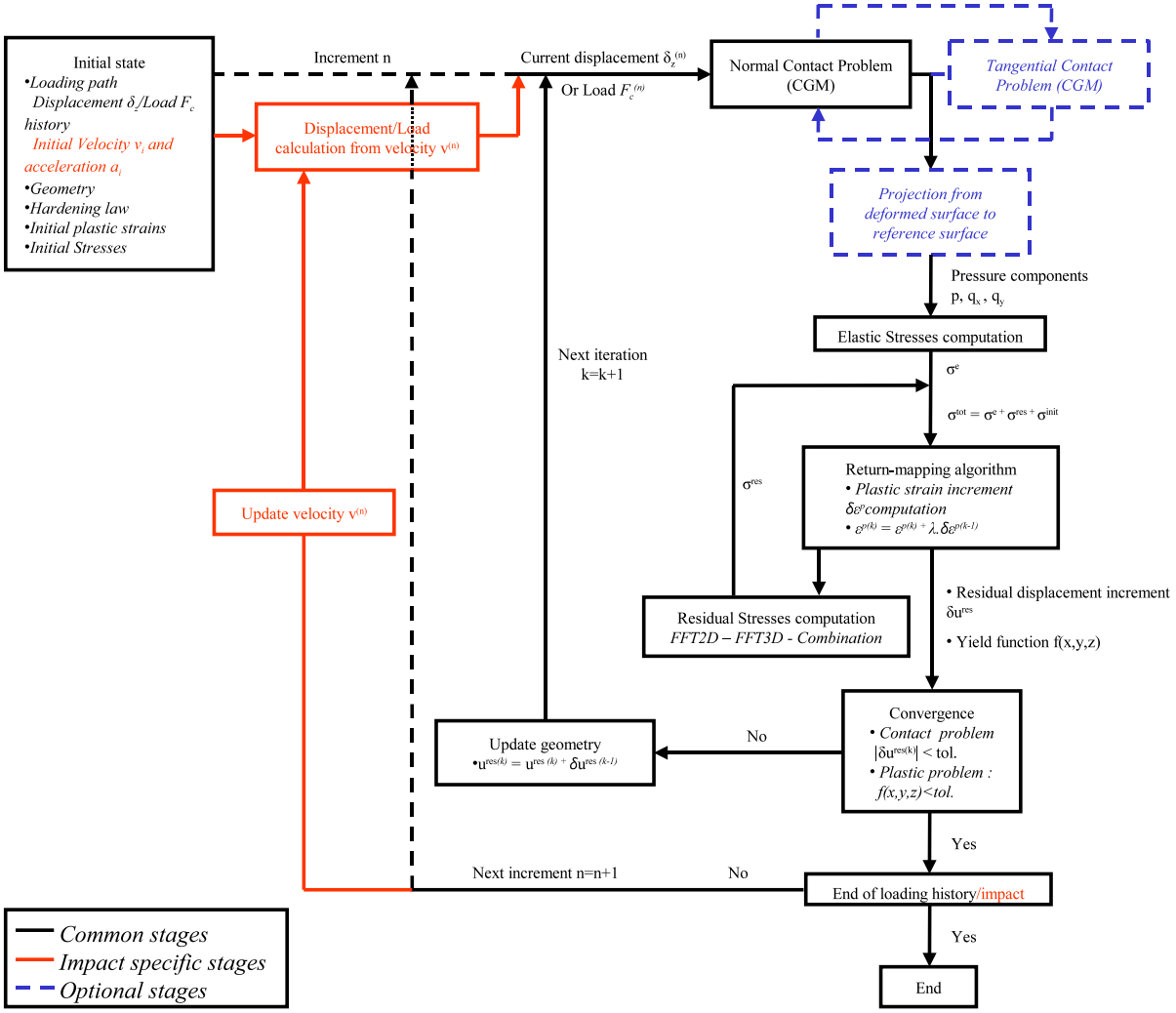

Figure 2.1: General algorithm of the contact-impact semi analytical model.

is determined and the displacement of the surface is then used to compute the gap between the surfaces in contact, as detailed in the following section.

The well-known Boussinesq solution [BOU 85] gives the normal displacement at any point of a surface subjected to a unit force. A similar solution has been provided by Love [LOV 52] for a rectangle on which a uniform pressure is applied. These elementary solutions are known as Green's functions or influence coefficients. By discretizing the pressure distribution into several patches of uniform pressure, one obtains a two-dimensional convolution product to describe the surface normal displacement u_z^e at any point (x,y) of the surface by taking into account the contribution of each patch of uniform pressure p.

$$u_z^e(x,y) = \iint D^p\left(x-x',y-y'\right) p\left(x',y'\right)\ dx'dy' \tag{2.3}$$

The matrix D^p here represents the effect of a uniform pressure applied on a patch located at (x',y') on the normal displacement u_z^e at (x,y). This convolution product is then computed by switching to the frequency domain using the Fast Fourier Transforms (FFT) where it becomes a simple matrix multiplication.

$$\hat{u_z^e}(x,y) = \hat{D^p}(x,y)\,\hat{p}(x,y) \tag{2.4}$$

where $\hat{u_z^e}$ represents the Fourier transform of u_z^e.

Converting data to the frequency domain introduces errors to the solution due to the periodic repetition of data in the frequency domain inherent to the FFT. In standard frequency analysis, an increase of the initial data in a virtual domain by a factor 5 [JU 96] or 8 [POL 00] minimum in all space dimensions is necessary to neglect these errors. Liu et. al. [LIU 00] introduced the discrete convolution method with the FFT (DC-FFT) to reduce this time consuming domain increase. The computation domain is here only extended by a factor two in all directions but particular care is put to the virtual domain definition. The data source, i.e. the pressure in the example given before, is extended by zeros in the virtual domain, this is called the zero-padding. The matrix of coefficients is extended using the wrap-around order technique. This consists in reproducing the coefficients in the virtual domain by respecting their parity. The FFT is then applied to the extended data, multiplication is made in the frequency domain and the inverse FFT allows to determine the final results with negligible error. By the use of this technique the computation of the results is really fast and the extension of the computation domain limited. Details on the method can be found in [LIU 00, GAL 07a].

2.2.3 Contact resolution

The resolution of the contact is a critical step of the model and a strength of the method. The use of SAM for contact problem resolution is well mastered now and only the fundamental steps are recalled here.

The contact of two elastic bodies is here considered. The geometry of both bodies is described by the surface separation h at each point (i,j) of the computation domain.

A total load F_c or rigid body displacement δ_z is applied on the bodies in contact. The equations to be solved simultaneously for the elastic contact problem are as follows:

$$u_z^{tot}(i,j) = h(i,j) + \delta_z, (i,j) \in A_c \tag{2.5}$$

$$p(i,j) > 0, (i,j) \in A_c \tag{2.6}$$

$$u_z^{tot}(i,j) \geq h(i,j) + \alpha, (i,j) \ni A_c \tag{2.7}$$

$$p(i,j) = 0, (i,j) \ni A_c \tag{2.8}$$

$$\Delta x \Delta y \sum_{(i,j) \in A_c} p(i,j) = F_c \tag{2.9}$$

where $u_z^{tot}(i,j)$ is the composite normal displacement of both bodies at point (i,j) of the contact area A_c, $p(i,j)$ is the pressure, Δx and Δy are the grid spacings along the x and y directions, respectively. The main parameters for the problem of a sphere applied on a plane are plotted in Fig. 2.2 (a). Figure 2.2 (b) represents the case of large displacements, where the pressure profile is highly influenced by plasticity and additional shear is considered. The same set of equations is used for elastic-plastic contact, the only difference being the permanent surface deformation u^{res} that is added to the surface geometry.

The elastic-plastic contact formulation is based on Betti's reciprocal theorem. First introduced by Jacq et al. [JAC 02] for elastic-plastic contacts, it has been adapted by Boucly et al. [BOU 05] for thermal-elastic-plastic contacts, who introduced frictional heating based on the work of Liu and Wang [LIU 03] in thermo-elasticity. Thermal effect won't be considered in the current work. Betti's reciprocal theorem allows the calculation of displacements u and stresses $\sigma(i,j)$, as the summation of the contribution of the elastic field, the residual state, and the thermally induced strains, as in Eqs. 2.10 and 2.2 below:

$$u_z^{tot}(A) = u_z^e(A) + u_z^{res}(A), A \textit{ being a point on the surface} \tag{2.10}$$

At each convergence step of the contact problem, a pressure distribution is defined, and the contact conditions described by Eqs. 2.5 to 2.9 are checked. The update of pressures at each step to reach the converged solution is made following the Conjugate Gradient Method (CGM) as described by Polonsky and Keer [POL 99].

In the present investigation only normal effects will be considered and hence impacts will be assumed frictionless. However the coupling between normal and tangential effects has already been implemented in the contact solver - see Gallego et al. [GAL 10c] and Fulleringer and Nelias [FUL 10] - and this will be the subject of future works.

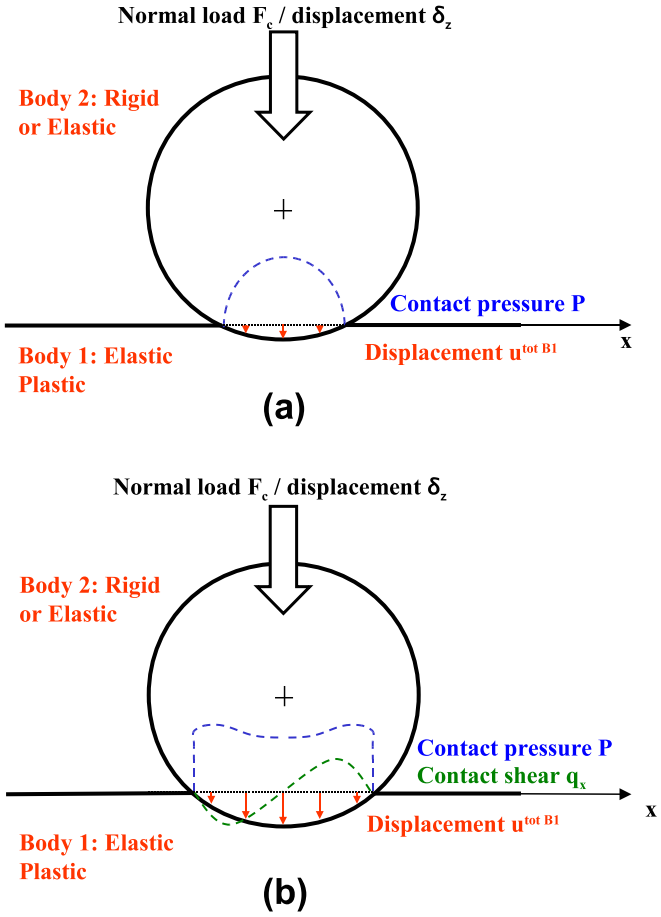

Figure 2.2: Representation of the contact parameters for a rigid or elastic ball applied on an elastic-plastic flat with normal force F_c of displacement δ_z. (a) without consideration of large displacements (b) with large displacements consideration.

2.2.4 Convergence criteria

Former versions of the model [JAC 01, BOU 08] used a criterion based on the increment of residual displacement to ensure the convergence of the current load increment. Considering the residual displacement $u^{res(n)(k)}$ at load increment n and convergence iteration k, and the residual displacement at the former iteration $u^{res(n)(k-1)}$ calculated over the computation domain of size $N_x \times N_y$, N_i being the number of points in direction i, the convergence is ensured if the error calculated as in Eq. 2.11 is lower than a prescribed tolerance tol..

$$\frac{\sqrt{\sum_{i=1,N_x}\sum_{j=1,N_y}\left(u^{res(n)(k)}(i,j)-u^{res(n)(k-1)}(i,j)\right)^2}}{N_xN_yMax\left|u^{res(n)(k)}\right|} \leq tol. \tag{2.11}$$

This criterion ensures the convergence of the contact problem. The force or displacement being prescribed, the residual displacement is the only variable input of the contact problem during a loading increment. Thus the stabilization of the residual displacement guarantees the stabilization of the contact problem.

The residual displacement is only a two-dimensional image of the subsurface three dimensional plastic strains. The convergence of the residual displacement does not guarantee the convergence of the plastic problem, the influence of sub-surface strains being low on the residual displacement. A criteria based on the yield function f at each point of the solid is used as defined in Eq. 2.12. The yield function is defined in Eq. 2.31, $\langle a \rangle$ are the McCauley brackets, denoting the positive part of a and N_plast the number of points not having reached stabilization yet.

$$\frac{\sum_{i=1,N_x}\sum_{j=1,N_y}\sum_{k=1,N_z}\left\langle \frac{f(x,y,z)}{\sigma_y(x,y,z)} \right\rangle}{N_{plast}} \leq tol. \tag{2.12}$$

The new convergence criterion based on the yield function ensures the correct convergence of the plastic problem.

2.2.5 Numerical problems

The SAMs, as other numerical methods, are subjected to problems inherent to the numerical schemes. The most problematic is the concentration of the calculated plastic strain on some elements. This problems, common in the discrete element method (DEM), generates after a few iterations a "chessboard-like" strain pattern, the strains being concentrated on one element over two, thus releasing the surrounding elements and so supporting and propagating the phenomenon. It is interesting to notice that the average obtained solution is close to the effective solution of the problem. This phenomenon generates oscillations around the actual solution, but also often leads to a divergence of the solution. Figure 2.3 shows the residual strain profiles in a plane cutting the surface for two equivalent cases, one presenting localization and the other without numerical problems.

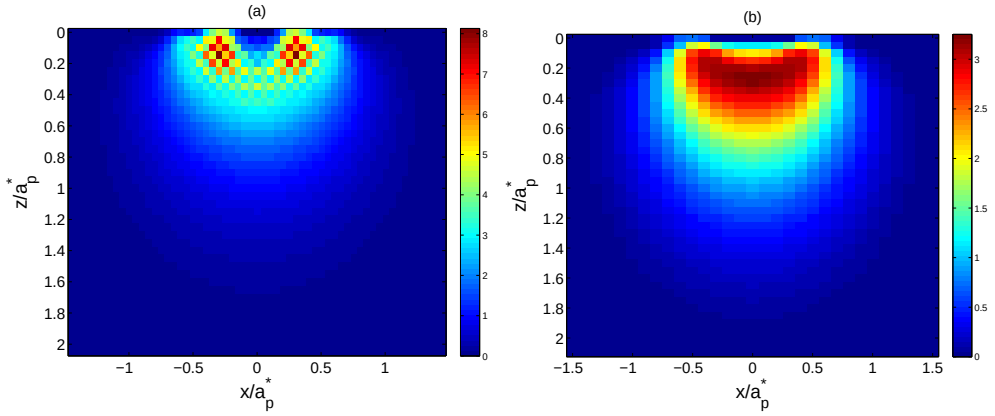

Figure 2.3: Accumulated plastic strain field in the z direction for a typical impact. Cases with (a) and without (b) localisation at equivalent time steps. In case (b) the mesh size in z direction is half the mesh size in the x and y directions.

The use of non-local methods allows a great improvement of this problem. These methods were firstly implemented for the definition of the plastic strain field. Further evaluation of the problems showed that the use of non-local methods only delays the problem while adding parameters of crucial influence of the model and should thus only be used for the most critical cases.

Non local methods lies on the consideration that the plastic strain at a given point A is not only function of the state of this point but also of the state of the surrounding points. The influence of each point B is defined by a weight function $\psi(A,B)$, which values converges to 0 after a given characteristic length l. The value of the strain at point A is then calculated as a weighted mean of the surrounding variables over the whole computation domain Ω, see Eq. 2.13. The efficiency of the method lies in the choice of the weight function ψ and its characteristic length l. A finite Gaussian type weight function with a characteristic length small enough compared to the strain gradients observed in the calculations showed the best results.

$$\underline{\underline{\varepsilon^p}}(A) = \int_\Omega \psi(A,B)\,\underline{\underline{\varepsilon^p}}(B)\,\mathrm{d}\Omega \tag{2.13}$$

The most efficient way to solve this numerical problem, and the one used in Fig. 2.3 is derived from the DEM. This problem being common in DEM is solved by adding extra elements in the concentration zones to increase the mesh density. This method is difficult to apply directly due to the constant mesh size necessary for the SAM as explained in this chapter's introduction. Reducing mesh dimensions in all three directions just reduces the problem to oscillations at a lower frequency. The solution is to reduce the mesh dimension in the depth direction only (z) and thus using cuboids of dimensions $\Delta x \times \Delta y \times \Delta z$ with $\Delta x\times = 2\Delta z$. The ratio between Δx and Δy is taken equal to 1 for axisymmetric problems

but can be modified for problems with a dominant x or y direction.

2.3 Stress calculation

Stresses occurring in the elastic-plastic body considered in this model may have three origins as indicated in Eq. 2.2. Thermal effects not being considered in this study, stresses in the bodies can be generated by: (i) the pressure and/or shears applied on the body's surface, denoted σ^e, (ii) non homogeneous strains in the body, reduced to plastic strain in this study, denoted σ^{res} and (iii) initial stresses, denoted σ^{init} that are generated by other effects (phase transformation, nitriding, non homogeneous strains located outside the computation zone,...) and are constant throughout the computation.

The elastic stresses are calculated using the DC-FFT technique applied to the analytical solutions first derived by Love [LOV 52] for the effect of pressure and extended to the effect of shears by Vergne [VER 85]. When only a normal contact problem is considered, the elastic stresses are generated by a pressure only. If the load is large enough (typically when reaching 10% of total strain), the small displacement assumption is no more valid and additional shears due to the geometry of the surfaces in contact are to be considered. Details on this operation are presented here.

The calculation of residual stresses is the most time consuming step of the method. Its efficiency is thus crucial to the speed of the method. Furthermore, residual stresses being the origin of the difference between an elastic solution and the effective result of an elastic plastic simulation, their accuracy is also fundamental. An acceleration technique for the computation of these stresses and its limitations in terms of results is presented further.

2.3.1 Elastic stresses

An important feature of the model is the assumption of small strains and small displacements that allows the superimposition of the elastic and inelastic contributions. This hypothesis is usually considered valid in finite elements for strains up to approximately 10% . When large strains occur, it is important to consider an update in the geometry of the system. Two characteristics of the SAM allow to consider quite large amplitudes of strains while keeping the small strain hypothesis. First the real surface geometry is fully considered when solving the contact. The SAM results are then similar to that obtained with geometry update in finite elements methods. The second feature to consider is the angle made by the surfaces in contact. In the classical analytical contact formulations, the angle made by the surface is considered small enough to be neglected [JOH 85]. When deformations become large enough, this hypothesis is no longer valid. The contact solver gives a pressure that acts normal to the contact surface. If the angle made by the deformed surface is large enough compared to the reference flat surface, the contact pressure will have both a normal and a tangential effect. A formulation is here proposed to consider this tangential effect in the computation of stresses.

After solving the contact using the CGM, a pressure field p^{CGM}, discretized over the

contact surface is known. This pressure field is assumed to act normal to the effective surface of the bodies in contact. At each point of coordinate (i, j) of the contact surface A_c, the effective angles made by the deformed surfaces are calculated in each of the directions, x and y, parallel to the surface. The residual displacement u^{res} of the surfaces in the only part to consider here, the elastic displacement u^e of the surfaces being implicitly considered by the analytical solutions giving the stresses.

$$\theta_x(i,j) = \frac{1}{2}\left(\theta_{x^+}(i,j) + \theta_{x^-}(i,j)\right) \tag{2.14}$$

Where:

$$\theta_{x^+}(i,j) = atan\left(\frac{u_z^{res\ B1}(i+1,j) - u_z^{res\ B1}(i,j)}{\Delta x}\right) \tag{2.15}$$

$$\theta_{x^-}(i,j) = atan\left(\frac{u_z^{res\ B1}(i,j) - u_z^{res\ B1}(i-1,j)}{\Delta x}\right) \tag{2.16}$$

Where B_1 is the elastic plastic, originally flat, surface impacted by the balls and B_2 the impacting ball.

Similarly, the angle of the surface in the y direction is computed as follows:

$$\theta_y(i,j) = \frac{1}{2}\left(\theta_{y^+}(i,j) + \theta_{y^-}(i,j)\right) \tag{2.17}$$

Where:

$$\theta_{y^+}(i,j) = atan\left(\frac{u_z^{res\ B1}(i,j+1) - u_z^{res\ B1}(i,j)}{\Delta x}\right) \tag{2.18}$$

$$\theta_{y^-}(i,j) = atan\left(\frac{u_z^{res\ B1}(i,j) - u_z^{res\ B1}(i,j-1)}{\Delta x}\right) \tag{2.19}$$

Figure 2.4 (a) illustrates the calculation of the surface's angles.

Consequently, the pressure calculated by the CGM P^{CGM}, assumed to be normal to the real deformed surface, is projected on the reference flat surface to obtain the equivalent pressures P^r and shears, s_x^r and s_y^r. The normal to the real surface is taken as the normal to the two directions defined by θ_x and θ_y. The projection of the calculated pressure over the reference surface is illustrated in Fig. 2.4 (b).

$$P^r(i,j) = P^{CGM}(i,j)\cos(\theta_x)\cos(\theta_y) \tag{2.20}$$

$$q_x^r(i,j) = P^{CGM}(i,j)\sin(\theta_x) \tag{2.21}$$

$$q_y^r(i,j) = P^{CGM}(i,j)\sin(\theta_y) \tag{2.22}$$

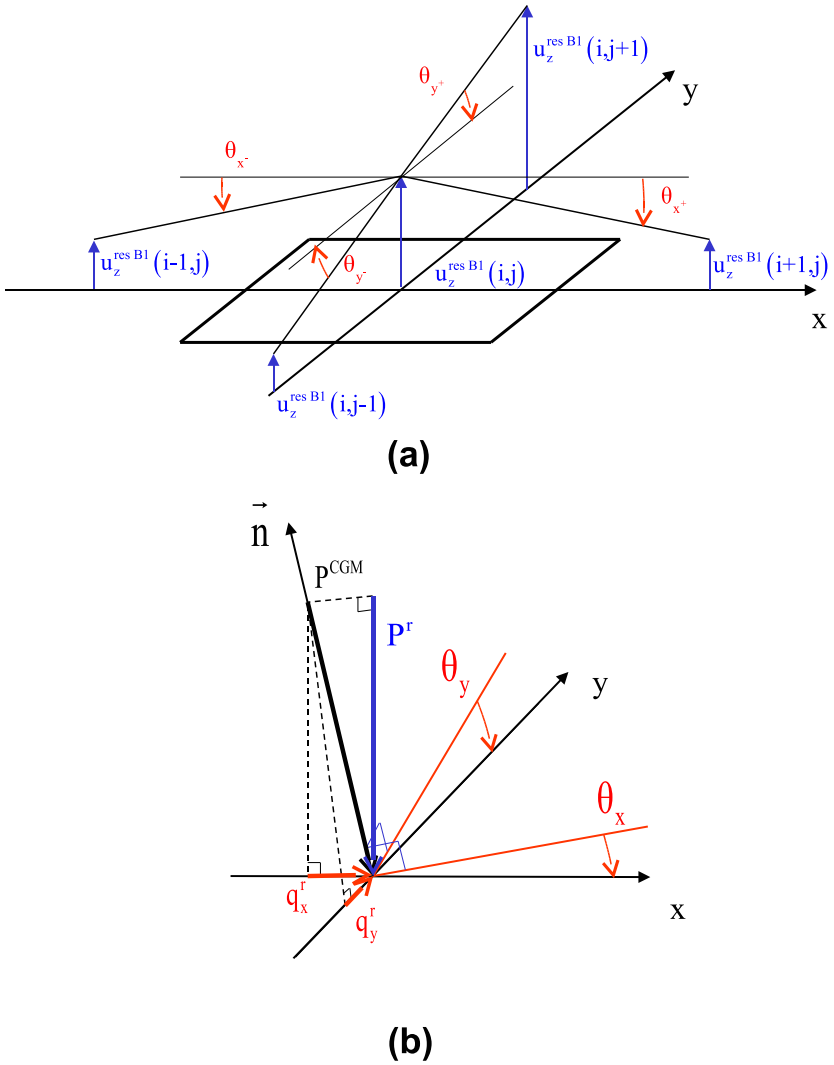

Figure 2.4: (a) Calculation of the surface angle against the reference surface. (b) Projection of the CGM calculated pressure p^{CGM} normal to the deformed surface on to the reference surface.

The total elastic stresses σ^e in the body are calculated from the resulting pressure and shears. The stresses generated by the pressure are calculated using the formulae derived by Love [LOV 52] which have been extended to the case of tangential loading to account for the effect of shears by Vergne [VER 85]. These formulae are recalled in annex A.

This projection of the pressure over the real deformed surface allows to consider large displacements in the stress computation. The SAM implicitly assumes a small perturbation hypothesis. For reasons mentioned above, the contact solver allows to go beyond the classical limits of this hypothesis. A description of the upper limit of strain accepted by the method is tackled in chapter 4. A complete approach of large strain and displacement problems would need three considerations:

- large displacements and slopes: the method proposed in this section ensures a correct consideration of this effect for the stress computation.

- large strains: the Green functions used to compute all stresses and displacement in the SAM assume small strains and neglect the second order terms in the strain tensor definition. The use or development of specific Green functions accounting for these terms is necessary to compute correctly large strains. At high strain levels (typically above 10% of strain) discontinuities in the strain fields might appear and cause instabilities in the convergence process. These discontinuities would be the consequence of the terms neglected in the strain definition. No study of the effect of the small strain assumption in the SAM has been conducted at the author's knowledge, yet the simulations and validations presented in the following show that this effect is negligible for strain level lower than 10%.

- geometry updating: the stresses computation is made on the reference geometry. Large changes of the geometry of the solids in contact will influence the stress distribution. As for the strain definition, no study of the effect of this specific feature has been made but results prove that this effect has no critical influence in the ranges of strains and stresses investigated in the following chapter.

2.3.2 Residual stresses

The computation of the residual stresses is made in a similar way than the computation of elastic stresses. The source of stresses, here the plastic strains, is three dimensional while the pressure generating the elastic stresses is two dimensional. This implies significant differences in the computation and especially it the time length it takes. As the pressure distribution was divided into patches of uniform pressure, the plastic zone is divided into cuboids of uniform plastic strain. The DC-FFT method is then used to calculate the residual stresses at any point of the body as the sum of the contribution of each cuboid of the plastic volume, denoted Ω_p.

The influence coefficients describing the residual stresses σ^{res} generated by a cuboid of uniform strain are calculated based on the superposition principle proposed by Chiu [CHI 77, CHI 78] and first applied by Jacq et al. [JAC 02]. The stresses generated by a

cuboid of uniform residual strain are the sum of three effects: the effect of the cuboid in an infinite body, the effect of a mirror cuboid in an infinite body and a normal stress, applied on the free surface to consider the hypothesis of a semi-infinite body. The mirror cuboid is located beyond the equivalent free surface at a distance along the depth z axis equal to twice the effective depth of the cuboid. The xz and yz shear components of the mirror cuboid have the same amplitude but opposite sign of those of the reference cuboid. The effects of both cuboids allows to remove the shearing effects on the free surface. Finally, the normal traction generated by these two cuboids is then applied on the free surface to obtain the final value in a semi-infinite body. This decomposition is illustrated in Fig. 2.5 and Eq. 2.23.

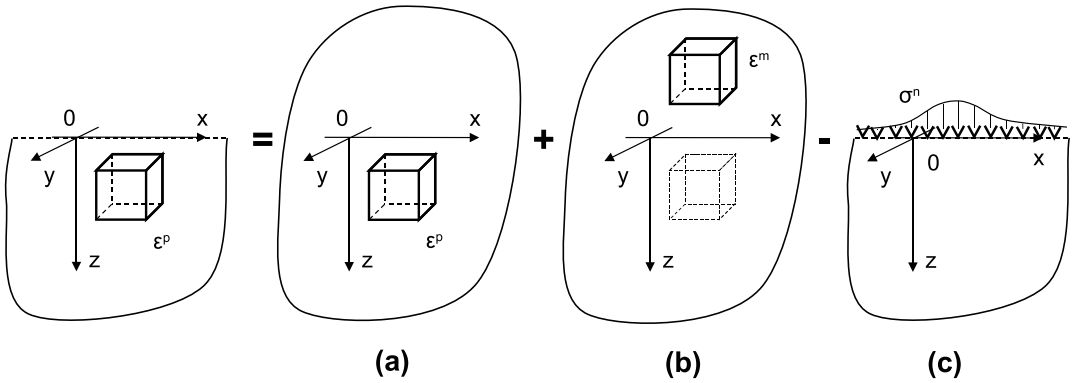

Figure 2.5: Subdivision of the problem of the residual stresses generated by a cuboid of uniform strain ε^p in a semi infinite body into the sum of stresses generated by (a) the same cuboid in an infinite body, (b) a mirror cuboid in an infinite body and (c) a normal pressure applied on the semi infinite body surface.

$$\underline{\underline{\sigma}}^{res}(x,y,z) = \underline{\underline{\sigma}}^{res.\infty}(x,y,z) + \underline{\underline{\sigma}}^{res\ m\ \infty}(x,y,z) + \underline{\underline{\sigma}}^{res\ surf}(x,y,z) \tag{2.23}$$

Jacq et al. [JAC 02] used a direct formulation of the stresses generated by a cuboid in a semi infinite body. The influence coefficients obtained depend on the depth of the cuboid and the calculation point. The DC-FFT must then be applied for each plastic strain depth and calculation point depth. The FFT computations are only two dimensional and the method is so called 2DFFT. Calculating separately the effects of the three sub-problems to finally sum up the total residual stresses allows a significant gain in computation time and was first proposed by Zhou et al. [ZHO 09]. This so called 3DFFT method, for the computation of the stresses in an infinite body generated by the cuboid or its mirror, by 3DFFT, is here used to increase the computation speed. The description of the influence coefficients necessary to perform the 3DFFT method is recalled in annex A.

For the 2DFFT method, the residual stress generated at point (x,y,z) by a cuboid of uniform strain of size $\Delta x \times \Delta y$ located at point (x_0,y_0,z_0) is expressed directly as follows:

$$\sigma_{ij}^{res}(x,y,z) = B_{ijkl}^{\infty/2}(x-x_0,y-y_0,z,z_0)\,\varepsilon_{kl}^{p}(x_0,y_0,z_0) \tag{2.24}$$

In the case of a complete plastic volume Ω_p, the stress any point of the body is obtained as:

$$\sigma_{ij}^{res}(x,y,z) = \sum_{(x_0,y_0,z_0)\in\Omega_p} B_{ijkl}^{\infty/2}(x-x_0,y-y_0,z,z_0)\,\varepsilon_{kl}^{p}(x_0,y_0,z_0) \tag{2.25}$$

A two dimensional FFT is then applied in the x and y directions for each value of z and z_0 to compute the values of the stresses as:

$$\sigma_{ij}^{res}(x,y,z) = \sum_{z_0} FFT^{-1}\left(\hat{B}_{ijkl}^{\infty/2}(z,z_0)\,\hat{\varepsilon}_{kl}^{p}(z_0)\right) \tag{2.26}$$

Where $\hat{B}_{ijkl}^{\infty/2}(z,z_0)$ and $\hat{\varepsilon}_{kl}^{p}(z_0)$ are respectively the two dimensional FFT of $B_{ijkl}^{\infty/2}(x,y,z,z_0)$ and $\varepsilon_{kl}^{p}(x_0,y_0,z_0)$ in the x and y directions.

In the case of the 3DFFT method, the computation is divided into three parts, following the superposition principle. In the case of a plastic volume Ω_d, this leads to:

$$\begin{aligned}\sigma_{ij}^{res}(x,y,z) = \sum_{(x_0,y_0,z_0)\in\Omega_p} \Big[& B_{ijkl}^{\infty}(x-x_0,y-y_0,z-z_0)\,\varepsilon_{kl}^{p}(x_0,y_0,z_0) \\ & + B_{ijkl}^{\infty}(x-x_0,y-y_0,z+z_0)\,\varepsilon_{kl}^{pm}(x_0,y_0,z_0)\Big] \\ & - \sum_{(x',y')\in A_d} C_{kl}^{p}(x-x',y-y',z)\,\sigma_{kl}^{n}(x',y')\end{aligned} \tag{2.27}$$

Where A_d is the discretized area, for precision in computation, A_d is taken to be the calculation domain extended by a given value in x and y directions. Commonly, this value is taken to be equal to 20 in the x^+, x^-, y^+ and y^- directions. σ^n is the stress component normal to the free surface generated by the plastic volume and its mirror in the equivalent semi infinite body :

$$\begin{aligned}\sigma^{n}(x',y') = \sum_{(x_0,y_0,z_0)\in\Omega_p} \Big[& B_{zzkl}^{\infty}(x'-x_0,y'-y_0,z'-z_0)\,\varepsilon_{kl}^{p}(x_0,y_0,z_0) \\ & + B_{zzkl}^{\infty}(x'-x_0,y'-y_0,z'+z_0)\,\varepsilon_{kl}^{pm}(x_0,y_0,z_0)\Big]\end{aligned} \tag{2.28}$$

The FFTs are then applied to perform the convolution products in the frequency domain and the reverse FFTs allow to obtain the final residual stress. The trick is that the two first terms in Eq. 2.27 can be obtained directly by performing a three dimensional FFT and the third term simply one two dimensional FFT:

$$\begin{aligned}\sigma_{ij}^{res}(x,y,z) = & FFT^{-1}\left(\hat{B}_{ijkl}^{\infty}\hat{\varepsilon}_{kl}^{p}\right) \\ & + FFT^{-1}\left(\hat{B}_{ijkl}^{\infty}\hat{\varepsilon}_{kl}^{pm}\right) \\ & - FFT^{-1}\left(\hat{C}_{kl}^{p}(z)\,\hat{\sigma}_{kl}^{n}\right)\end{aligned} \tag{2.29}$$

Where $\hat{B}_{ijkl}^{\infty}$, $\hat{\varepsilon}_{kl}^{p}$ and $\hat{\varepsilon}_{kl}^{pm}$ are the 3DFFT of $B_{ijkl}^{\infty}(x,y,z)$, $\varepsilon_{kl}^{p}(x_0,y_0,z_0)$ and $\varepsilon_{kl}^{pm}(x_0,y_0,z_0)$ respectively and $\hat{C_{kl}^{p}}(z)$ and $\hat{\sigma}_{kl}^{n}$ the 2DFFT of $C_{kl}^{p}(x,y,z)$ and $\sigma_{kl}^{n}(x',y')$ respectively in the x and y directions.

This expression can be generalized to any stress caused by a cuboid of given strain, in the modelling of inclusions or inhomogeneities [LER 10, CHE 10]. It is interesting to note that the 2DFFT technique can be used for the case of plastic strain only due to the incompressibility of the plastic strain. The trace of the plastic strain matrix is nil and thus the analytical calculation of the coefficient is made possible, see [CHI 78, JAC 02] for more details. For strains due to inclusions or inhomogeneities, that are not necessarily incompressible, the calculation of the coefficients for the 2DFFT is not possible and the 3DFFT technique, that uses only Chiu's formulation for an infinite body [CHI 77] and the effect of a surface pressure, has to be used.

The third term is simply the elastic stresses generated by an equivalent pressure on the body surface. This equivalent pressure is calculated as the stress normal to the surface generated in an equivalent infinite body by the considered cuboid and its mirror relatively to the free surface. During the computation, the result of calculation of the two first terms is used to compute the third one.

When using the 3DFFT technique, the computation time is highly reduced for two reasons. First the actual computation time is lower as described in [ZHO 09] due to the number of operations needed to perform the residual stress calculation. This effect is actually of second order, the major effect being that the coefficients matrices are of lower dimension. For the 2DFFT technique, the coefficient matrix has a size $N_x \times N_y \times N_z^2$ where N_i is the number of elements in the i direction, where it is only of size $N_x \times N_y \times 2N_z$ when using the 3DFFT technique. This generates a large gain in computation time for the influence coefficient calculation by itself and for the matrices reading, writing and global manipulation. So the actual effective gain is more a programming effect that an actual gain in the calculation technique. Still, this improvement is considerable and as far as the calculation using the 3DFFT technique is possible, it should be applied.

The calculation of residual stresses using the 3DFFT method is validated on the case of a thermoelastic stress field generated by a spherical inclusion in a half-space. Mindlin and Cheng [MIN 50] derived an analytic solution for this stress field. A cubical domain of size $a \times a \times a$ is modelled. A spherical inclusion of radius $R = 7a/16$ centred in the domain is discretized into cuboids. The inclusion center is located at $z = a/2$ Dilatation properties are attributed to the inclusion so that it has diagonal strains $\varepsilon_{ii} = \alpha T$ where T is a prescribed temperature. Simple thermal strains are here assumed for comparison

with an analytical solution but a complete strain tensor could be modelled by this method. The stresses generated by the thermal strains are calculated using the 3DFFT technique. Results are normalized by $\sigma_0 = E\alpha T/3(1-\nu)$, where E and ν are the elastic properties of the body and the inclusion. Figure 2.6 shows the results along the in-depth z-axis through the center of the inclusion and along the x-axis (parallel to the surface) at the surface of the body and along the same x-axis (denoted here x') at depth z, passing through the center of the inclusion for all three normal stress components.

A very good correspondence between SAM and analytical results is found. Results taken through the center of the inclusion along an axis parallel to the surface and along a similar axis but at the surface give excellent results as well. As indicated by Zhou et al [ZHO 09], the model was discretized with 128 elements in each directions. This is rather fine but necessary in this case to model accurately enough the curvature of the sphere. The sides of the inclusion are rather close to the borders of the computation domain, which, according to Zhou, allows to show the low influence of the surface traction. This is true in this validation case since the distance of the inclusion to the surface decreases as going towards the border of the domain. Concrete application have shown that this conclusion holds no longer for different strain repartitions. The computation domain of the surface traction is thus extended for a better definition as indicated further.

Comparison with SAM results resulting of coarser discretization have been performed, down to a $32 \times 32 \times 32$ elements domain. SAM results are then satisfactory excepted around the curve of the sphere due to a poor representation of the sphere as cuboids.

Validation of the technique is thus satisfactory. Yet the 3DFFT technique for the residual stress calculation presents two drawbacks. First, the surface contribution σ^n has to be integrated over a finite surface. For the 2DFFT technique, the contribution of this pressure was analytically considered and so integrated over an infinite surface. In the 3DFFT technique, this contribution has to be limited to a finite surface A_d. This finite surface is taken to be greater than the calculation domain. Consequently, the effect of σ^n located outside of A_d on the computation domain will be negligible. The increase in computation time due to this domain extension is negligible since the contribution of the plastic domain and its mirror has only to be considered in the $z = 0$ plane.

Secondly, this surface contribution, that was formerly analytically defined is now discretized on the computation mesh. Following Saint Venant's principle, the effect of the discretization will be negligible far enough from the surface but might have a major effect for the surface elements and that just below it. Since the mesh dimensions have to be constant over all the computation domain to apply the FFTs, this problem can not be solved just by refining the mesh.

It is proposed to mix both methods to minimize the effect of the surface discretization when the plastic area reaches the surface. The 2D-FFT technique is used to account for the contribution of plastic strains up to a given transition depth z_{trans}. The 3D-FFT technique is used to compute the effect of the remaining plastic strains. For practical applications, a value of z_{trans} equal to 5 showed the best results in terms of quality of results and computation speed.

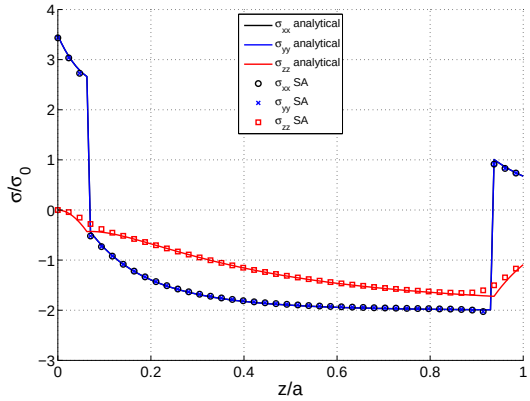

(a) Along z-axis

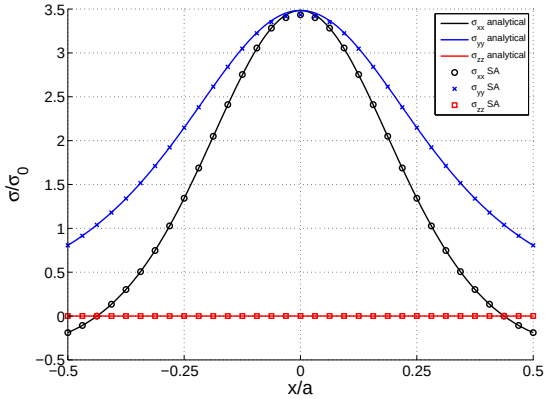

(b) Along x-axis

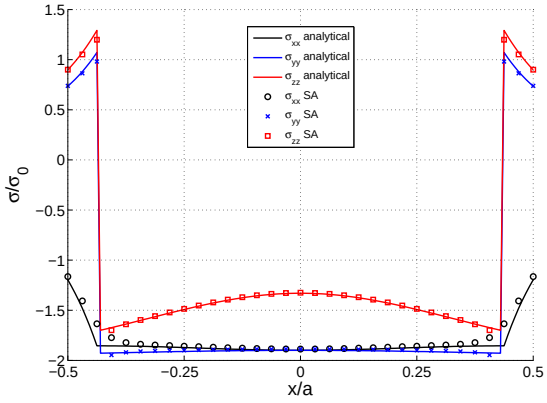

(c) Along x'-axis

Figure 2.6: Validation of the 3DFFT technique. Computation of the stress generated by a spherical inclusion of uniform strain in a half-space, comparison with analytical solution from Mindlin and Cheng [MIN 50]. Stresses along depth axis z passing by the center of the inclusion (a), along the x-axis parallel to the surface (b) and along the x'-axis, parallel to x, passing through the center of the inclusion (c).

$$\begin{aligned}\sigma_{ij}^{res}(x,y,z) = & \sum_{(x_0,y_0,z_0)\in\Omega_p|z\leq z_{trans}} B_{ijkl}^{\infty/2}(x-x_0,y-y_0,z,z_0)\,\varepsilon_{kl}^{p}(x_0,y_0,z_0) \\ & \sum_{(x_0,y_0,z_0)\in\Omega_p|z>z_{trans}} B_{ijkl}^{\infty}(x-x_0,y-y_0,z-z_0)\,\varepsilon_{kl}^{p}(x_0,y_0,z_0) \\ & + B_{ijkl}^{\infty}(x-x_0,y-y_0,z+z_0)\,\varepsilon_{kl}^{pm}(x_0,y_0,z_0) \\ & - \sum_{(x',y')\in A_d} C_{kl}^{p}(x-x',y-y',z)\,\sigma_{kl}^{n}(x',y')\end{aligned} \tag{2.30}$$

In practice, the residual stresses computation method is determined as a function of the expected residual strain distribution, desired accuracy of results and desired computation speed. It should be noted that even the 2DFFT method, although it is slower than the 3DFFT method, gives results in a largely reduced CPU time compared to an equivalent simulation made by the Finite Element Method with equivalent computation power.

2.4 Plastic strain calculation

2.4.1 The return mapping algorithm

Knowing the total stresses applied to the body, the plastic strain increment generated by these stresses is calculated. A classical return mapping algorithm is used. The return mapping algorithm was first proposed by Simo and Taylor [SIM 85] and extended to larger considerations by Fotiu and Nemat-Nasser [FOT 96]. The extension by Fotiu et al. allows to consider rate dependant plasticity and a plastic predictor-elastic corrector for large increments of plastic strain. This second scheme cannot easily be implemented to the semi analytical method and the efficiency of the classical elastic predictor-plastic corrector scheme was considered all-sufficient. The return mapping algorithm was first adapted into the SAM by Boucly et al. [BOU 05]. The extension to kinematic and mixed hardening has been here made and the full algorithm is recalled.

The plastic body is assumed to be under the effect of a total stress tensor $\underline{\underline{\sigma}}$. For the general presentation of the algorithm, the material is assumed to have a mixed hardening behaviour, with kinematic hardening variable or back-stress $\underline{\underline{X}}$ and isotropic hardening variable r. The several hardening laws used will be recalled in section 2.4.2. Assuming Von Mises plasticity, the yield function is calculated as follows :

$$f = J_2\left(\underline{\underline{\sigma}} - \underline{\underline{X}}\right) - r \tag{2.31}$$

Where J_2 represents the Von Mises equivalent stress and is given by 2.32 where the prime denotes the deviatoric part of the corresponding tensor.

$$J_2\left(\underline{\underline{\sigma}}\right) = \sqrt{\frac{3}{2}\underline{\underline{\sigma}}' : \underline{\underline{\sigma}}'} \tag{2.32}$$

The plastic strain rate $\dot{p}$ and the accumulated plastic strain p are also defined.

$$\dot{p} = \sqrt{\frac{2}{3}\underline{\underline{\dot{\varepsilon}^p}} : \underline{\underline{\dot{\varepsilon}^p}}} \tag{2.33}$$

$$p = \int_0^t \dot{p}\,\mathrm{dt} \tag{2.34}$$

The loading-unloading conditions are then governed by the Kuhn-Tucker relations :

$$f \leq 0,\ \dot{p} \geq 0,\ f\dot{p} = 0 \tag{2.35}$$

The isotropic hardening variable is assumed to depend on the accumulated plastic strain p only, i.e. neither temperature nor strain rate dependency is considered. Similarly, the back stress is assumed to have the following dependencies :

$$\dot{\underline{\underline{X}}} = H(p)\,\dot{p}\underline{\underline{\mu}} \tag{2.36}$$

Where $\underline{\underline{\mu}}$ is a normalized stress tensor. For simplicity in the notation, the difference between the total stress and the back stress is noted $\underline{\underline{s}}$ and its Von Mises equivalent is noted σ_{VM}

$$\underline{\underline{\mu}} = \frac{3\left(\underline{\underline{\sigma}} - \underline{\underline{X}}\right)'}{2J_2\left(\underline{\underline{\sigma}} - \underline{\underline{X}}\right)} = \frac{\underline{\underline{s}}}{\sigma_{VM}},\ \underline{\underline{\mu}} : \underline{\underline{\mu}} = \frac{3}{2} \tag{2.37}$$

From a known loading state (a), the total strain increment to the next loading state (b) is first considered purely elastic (elastic predictor scheme), the total stress increment is usually calculated using Hooke's law. In the case of the semi analytical method, the problem is stress driven and the elastic predictor $\underline{\underline{s}}^{(1)}$ is directly calculated. The initial conditions for the return mapping are the given in Eq. 2.38.

$$\begin{aligned}
\sigma_{VM}^{(1)} &= \sqrt{\frac{3}{2}\underline{\underline{s'}}^{(1)} : \underline{\underline{s'}}}^{(1)} \\
\underline{\underline{\mu}}^{(1)} &= \frac{3\underline{\underline{s'}}^{(1)}}{2\sigma_{VM}^{(1)}} \\
p^{(1)} &= p_a \\
\underline{\underline{\varepsilon}}^{p(1)} &= \underline{\underline{\varepsilon}}_a^p \\
r^{(1)} &= r_a \\
H^{(1)} &= H_a \\
\underline{\underline{X}}^{(1)} &= \underline{\underline{X}}_a
\end{aligned} \tag{2.38}$$

At each convergence step (n) of the return-mapping, the yield function is calculated:

$$f^{(n)} = \sigma_{VM}^{(n)} - r^{(n)} \tag{2.39}$$

Then the plastic multiplier, which is here equal to the plastic strain increment Δp is calculated:

$$\Delta p^{(n)} = \frac{f^{(n)}}{3G + r_{,p}^{(n)} + \frac{3}{2}H^{(n)}} \tag{2.40}$$

Where G is the elastic shear modulus of the plastic body defined as $E/(2(1+\nu))$. The stresses, strains and hardening variables are updated :

$$\begin{aligned}
\sigma_{VM}^{(n+1)} &= \sigma_{VM}^{(n)} - \left(3G + \frac{3}{2}H^{(n)}\right)\Delta p^{(n)} \\
\underline{\underline{s'}}^{(n+1)} &= \underline{\underline{s'}}^{(n)} - \frac{2}{3}\left(3G + \frac{3}{2}H^{(n)}\right)\Delta p^{(n)}\underline{\underline{\mu}}^{(n)} \\
p^{(n+1)} &= p^{(n)} + \Delta p^{(n)} \\
\underline{\underline{\varepsilon}}^{p(n+1)} &= \underline{\underline{\varepsilon}}^{p(n)} + \Delta p^{(n)}\underline{\underline{\mu}}^{(n)} \\
r^{(n+1)} &= r\left(p^{(n+1)}\right) \\
H^{(n+1)} &= H\left(p^{(n+1)}\right) \\
\underline{\underline{X}}^{(n+1)} &= \underline{\underline{X}}^{(n)} + H^{(n)}\Delta p^{(n)}\underline{\underline{\mu}}^{(n)}
\end{aligned} \tag{2.41}$$

The convergence of the process is checked with the new yield function.

$$\left|f^{(n+1)}\right| = \left|\sigma_{VM}^{(n+1)} - r^{(n+1)}\right| < tol. \tag{2.42}$$

Where $tol.$ is a prescribed tolerance, usually taken equal to 1.10^{-6}. If the convergence is not reached the next plastic multiplier is calculated, else the final values of accumulated plastic strain, plastic strain tensor, isotropic hardening variables and back stress tensor are equal to that calculated at step $(n+1)$.

2.4.2 Hardening laws

The extension of plasticity to the consideration of all hardening types was made. Kinematic hardening, allowing then to reproduce mixed hardening behaviours was included in the model. Basic hardening behaviours are depicted in Fig. 2.7. Figure 2.7(a) shows the perfectly-plastic case, i.e. with no hardening. This case is very common in many analytical solutions for it simplifies the establishment of equations. Comparison between

numerical and analytical results is thus often made on the case of perfectly-plastic behaviour. This case often results in numerical difficulties in solving the equilibrium. Figure 2.7(b) shows the case of a linear isotropic hardening, i.e. the case where hardening leads to an isotropic increase of the yield surface, and thus of the yield limit. Finally, Fig. 2.7(c) illustrates kinematic hardening, where plastic flow causes a translation of the yield surface, the elastic domain being thus constant in size. The general hardening behaviour of material can be expected to be mixed, with more or less influence of the isotropic and kinematic parts.

Four isotropic hardening laws, depending on the accumulated plastic strain p, the elastic young modulus E and the initial yield limit σ_{y0} are used.

- the perfectly plastic hardening law

$$\begin{aligned} r &= \sigma_{y0} \\ r_{,p} &= 0 \end{aligned} \tag{2.43}$$

- the linear hardening law

$$\begin{aligned} r &= \sigma_{y0} + \frac{E_T}{1-\frac{E_T}{E}} p \\ r_{,p} &= \frac{E_T}{1-\frac{E_T}{E}} \end{aligned} \tag{2.44}$$

- Swift hardening law

$$\begin{aligned} r &= B\left(C + p10^6\right)^n \\ r_{,p} &= 10^6 B\left(C + p10^6\right)^{n-1} \end{aligned} \tag{2.45}$$

- Ramberg Osgood hardening law

$$\begin{aligned} r &= \sigma_{y0} + Kp^n \\ r_{,p} &= Knp^{n-1} \end{aligned} \tag{2.46}$$

For the kinematic hardening law, only the Armstrong-Frederick hardening law is here presented. This law uses two hardening variables $\underline{\underline{X}}_1$ and $\underline{\underline{X}}_2$ and a simple linear hardening can be deduced by keeping only $\underline{\underline{X}}_1$.

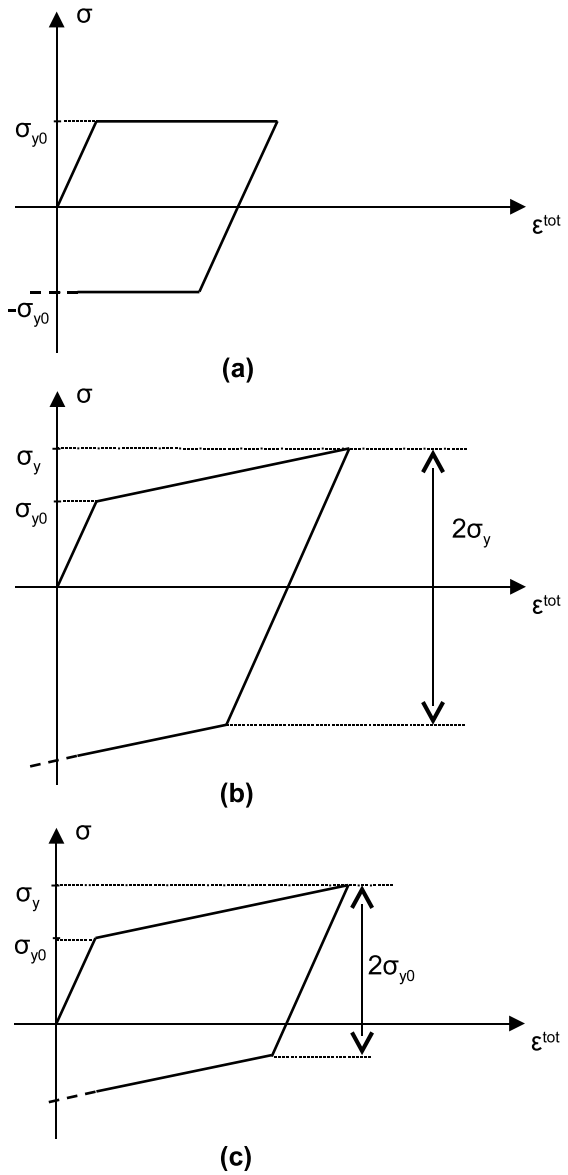

Figure 2.7: Stress-Total strain curves for typical hardening laws. (a) Perfectly plastic hardening law. (b) linear isotropic hardening law. (c) linear kinematic hardening law.

$$\begin{aligned}
\underline{\underline{X}} &= \underline{\underline{X_1}} + \underline{\underline{X_2}} \\
d\underline{\underline{X_1}} &= \frac{2}{3} C_1 d\underline{\underline{\varepsilon^p}} \\
d\underline{\underline{X_2}} &= \frac{2}{3} C_2 d\underline{\underline{\varepsilon^p}} - \gamma_2 \underline{\underline{X_2}} \dot{p} \\
H &= \frac{2}{3}(C_1 + C_2) - \gamma_2 \frac{\underline{\underline{X_2}} : \underline{\underline{s}}}{\sigma_{VM}}
\end{aligned} \tag{2.47}$$

2.5 From contact to impact

The elastic plastic contact solver has been modified for the simulation of impacts. The problem is considered quasi-static, meaning that no inertial effects are taken into account, which is consistent for impact speeds lower than $500 m/s$ for most materials as indicated by Johnson [JOH 85] and deduced from the state of the art study. In other words the proposed method should be valid for impact speeds lower than the sound velocity and when the contact area is small in comparison to the dimensions of the impacted body. The initial velocity is taken to be normal to the impacted surface, the contact is assumed frictionless and so no computation of the tangential problem is made. For impacts involving strains higher than $6-8\%$, the angle between the vertical axis (normal load) and the normal to the deformed surface is considered and equivalent shears are calculated following the methodology described in section 2.3.1.

When considering an impact loading, the load path is not known a priori. The only input data is the initial velocity v^i or more generally the initial kinetic energy E_k^i. At each load step n the load has thus to be evaluated as a function of the current kinetic energy E_k^n. It is then possible to drive the problem with the contact force F_c or the rigid body displacement δ_z.

The rigid body displacement is an interesting option since its calculation is easy when the velocity is known by following simple equations. Yet, when plasticity occurs at prescribed displacement, the calculated contact force decreases at each convergence step of the plastic problem during loading. This scheme can lead to the calculation of non physical plastic strains. A coefficient of relaxation can be applied to the calculated strains but will only reduce the amplitude of the strains and not correct their distribution. The error made through the scheme will be negligible if the time step is small enough. Validations of the model have shown that the error made using a displacement driven scheme is negligible, satisfactory results being obtained.

The second solution is to use a prescribed contact force scheme. The contact force has to be estimated in a more complicated way than the displacement and it should be checked at each load step that the applied force will not overcome the actual maximum load of the problem. This is made by checking the energies involved and is described further. For comparison of the impact loops and potential future improvements of the

method, both problem driving are presented here.

For the displacement driven formulation the time of each load step Δt^{δ_z} is considered constant and taken to be an input fraction of the elastic time step described in Eq. 2.60. For the contact force driven formulation, the time of each load step Δt^n is variable and is calculated a posteriori as a function of the rigid body displacement covered by the ball during the last load step and its velocity.

Knowing the contact force F_c^n, rigid body displacement δ_z^n at load step n, the work E_{F_c} done by the contact force during the last load step is first calculated :

$$\begin{aligned} E_{F_c}^n &= \int_{\delta_z^{n-1}}^{\delta_z^n} F_c \, \mathrm{d}\delta_z \\ &= \frac{F_c^n + F_c^{n-1}}{2} \left(\delta_z^n - \delta_z^{n-1}\right) \end{aligned} \tag{2.48}$$

The kinetic energy of the ball is then updated to account for the work done by F_c

$$E_k^n = E_k^{n-1} - E_{F_c}^n \tag{2.49}$$

The velocity of the sphere v^n is then calculated. Its sign is given by the sign of the work done by the contact force, which is positive during loading, i.e. when the ball's velocity is positive.

$$v^n = \frac{E_{F_c}^n}{\left|E_{F_c}^n\right|} \sqrt{\frac{2E_k^n}{m}} \; \textit{during loading} \tag{2.50}$$

For a displacement driven problem, the next rigid body displacement is directly deducted from the velocity and the known time step value Δt^{δ}.

$$\Delta t^{n+1} = \Delta t^{\delta} \tag{2.51}$$

$$\delta_z^{n+1} = \delta_z^n + \Delta t^{\delta_z} v^n \tag{2.52}$$

For a load driven problem, a hypothetical rigid body displacement δ_z^{hyp} is first estimated as in the displacement driven case, considering that the time step does not vary much :

$$\delta_z^{hyp} = \delta_z^n + \Delta t^{\delta_z} v^n \tag{2.53}$$

The next contact force is then estimated assuming a constant load/displacement ratio for both load steps :

$$F_c^{n+1} = F_c^n + \frac{F_c^n - F_c^{n-1}}{\delta_z^n - \delta_z^{n-1}} \left(\delta_z^{hyp} - \delta_z^n\right) \tag{2.54}$$

To avoid an overloading of elastic plastic body, the work hypothetically done by F_c^{n+1} over a distance $\left(\delta_z^{hyp} - \delta_z^n\right)$ is calculated following Eq. 2.48 and compared to the residual kinetic energy E_k^t. If the difference in these energies overcomes a prescribed tolerance, the applied load F_c^{n+1} is decreased. A similar check is made a posteriori once both contact parameters are given by the elastic plastic contact solver. If the prescribed tolerance on the energies tol_E is overcome, the last load step is cancelled and the input data reduced.

$$\begin{aligned} &If\ \frac{F_c^{n+1}+F_c^n}{2}\left(\delta_z^{n+1}-\delta_z^n\right) < tol_E \\ &then: cancel\ step \\ &\qquad reduce\ prescribed\ load/displacement \end{aligned} \tag{2.55}$$

The time step is then calculated in the load driven scheme :

$$\Delta t^{n+1} = \frac{\delta_z^{n+1} - \delta_z^n}{v^{n+1} - v^n} \tag{2.56}$$

The problem being quasi-static, the time step definition plays no specific role on the convergence of the solver. However an accurate definition of the time step is required to describe accurately the maximum rigid body approach. Large time steps lead to a rough estimate of the plastic strains but this effect is of second order since the plastic strains calculated at the last load steps cover the strains of the previous steps. A parametric study on the time step effect showed that a total of 20 time steps for loading-unloading is sufficient for a fine definition of the maximum loading and give the same results for the rebound velocity and residual plastic strains than when a smaller time step is used. The duration of an elastic impact being analytically known and close to the duration of an elastic-plastic impact, the actual time step is determined from Eq. 2.60.

The time step being constant and the velocity decreasing during loading, the increment of displacement δ_z is large for the first steps and reduces up to the climax of the impact. Consequently, the displacement steps are fine at the maximum load and relatively coarse at the first time steps.

Influence of the load and displacement driven schemes was not completely studied. At low plastic strain amplitude, both methods give equivalent results. For larger plastic strain levels, a greater influence is expected for which more detailed analysis should be considered.

For all impact applications presented, the displacement-driven method was used.

2.6 Model validation

Further validations of the model are proposed here. The plastic strain and residual stresses calculation being modified, a validation of the calculation of plastic strains and residual strains at low plasticity level is first proposed to guarantee the efficiency of the new

method for all former applications of the SAM. This validation is made through comparisons with finite element indentation simulations based on the work by Jacq [JAC 01].

In a second time, a validation of the impact loading calculation for a displacement driven situation is proposed. The displacement versus time curve of an elastic impact is calculated and compared to well-known analytical solutions.

Analysis of the results of impacts at higher plasticity levels, involving the new calculation of elastic stresses will be proposed in the following chapters as benchmarks with several finite elements codes. This will provide detailed validations of the plastic and impact considerations. Validations of the impact model are made at a macroscopic level in chapter 4 by studying the coefficient of restitution and comparing it to several results from the literature.

2.6.1 Low plasticity level indentation - Comparison with FEM results

Former validations of the elastic plastic semi analytical contact code where made for indentation at low plasticity levels [JAC 02] and further carried out to higher plasticity levels (up to 5% plastic strain and values of rigid body displacement δ_z equal to 110 times the critical rigid body displacement δ_y corresponding to the onset of plasticity) [NéL 06]. The validations proposed by Jacq et al. is here reproduced to validate the new convergence criteria and residual strain calculations through the 3DFFT technique.

The quasi static indentation of an elastic plastic flat with Swift isotropic hardening law by a rigid sphere is simulated using the semi analytical model and the commercial finite element code Abaqus. The indentation parameters are recalled in Tab. 2.1. Residual stress and strain components are plotted along the depth axis at two locations: at the center of the contact, see Fig. 2.8 and at $2\mu m$ of the center of the contact, which corresponds here to one half of the contact radius under maximum load, see Fig. 2.9.

	Body 1	Body 2
Geometry	Sphere $R = 105\mu m$	Flat
Elastic properties	Rigid	$E_2 = 210GPa$ $\nu_2 = 0.3$
Plastic properties	Rigid	Swift $B = 1240MPa$ $C = 30$ $n = 0.085$
Load	$190mN$; $P_{Hertz} = 5.5GPa$; $a = 4\mu m$	

Table 2.1: Indentation parameters for the SAM validation at low plasticity level indentation. Comparison between SAM and Abaqus results.

An excellent fit is obtained for the residual strains and stresses, both at the center of the contact and at a close distance between SAM and FEM results. The new plasticity

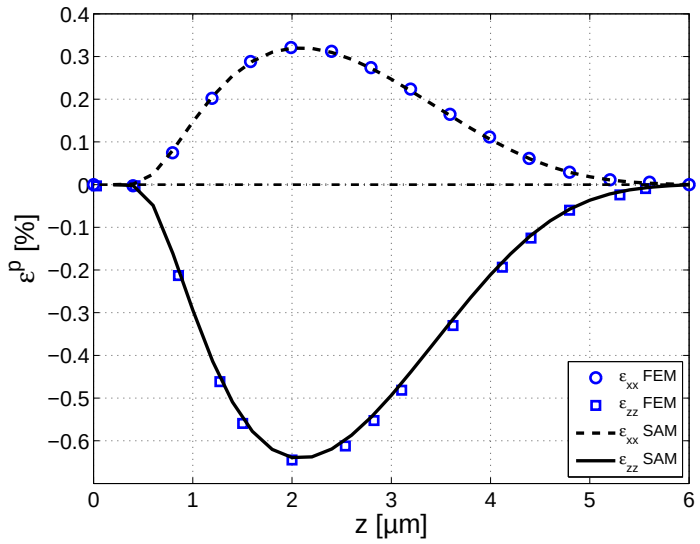

(a) Plastic strains

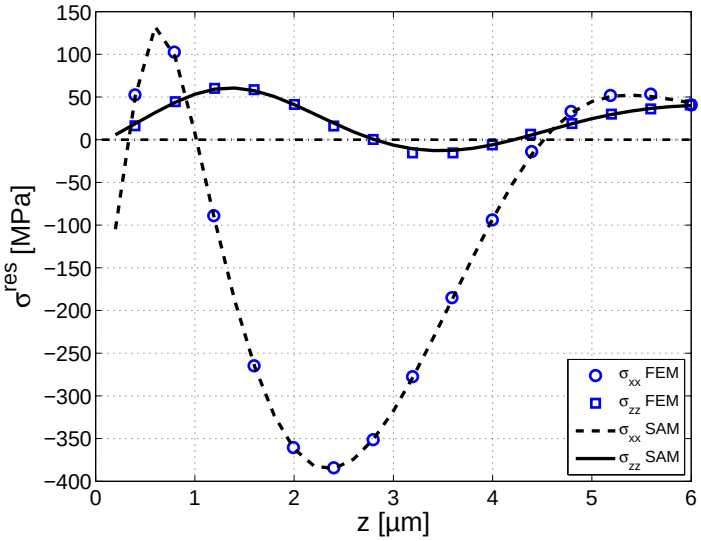

(b) Residual stresses

Figure 2.8: Residual strains and stresses calculated in depth at the center of the indentation of a rigid sphere on an elastic plastic flat. FEM and SAM results comparison.

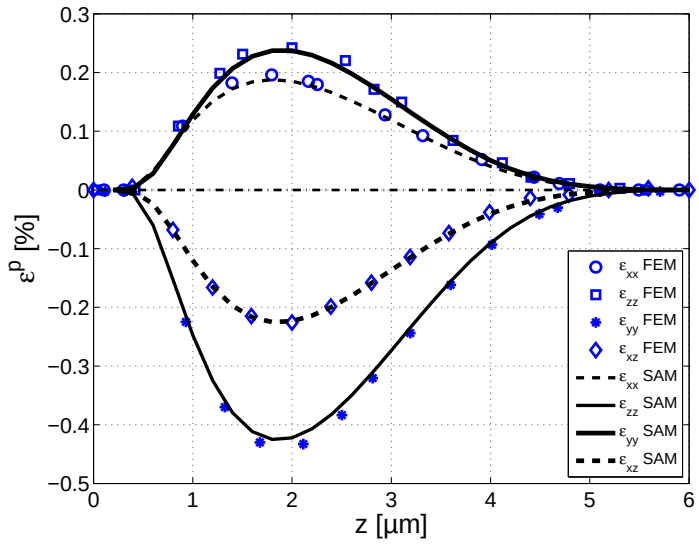

(a) Plastic strains

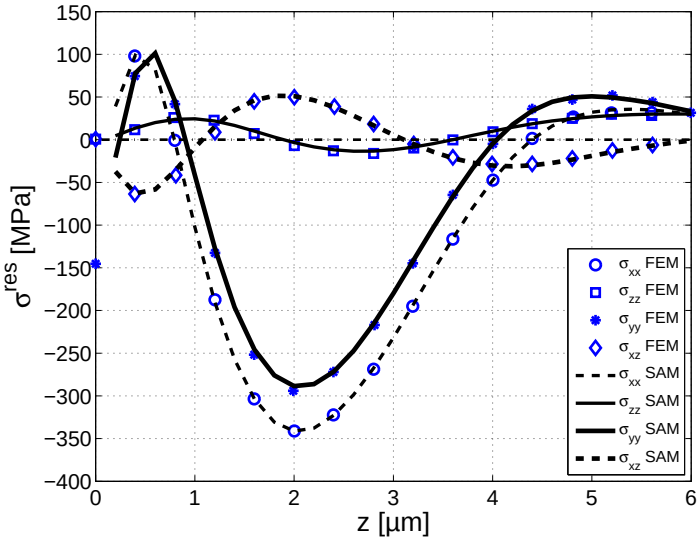

(b) Residual stresses

Figure 2.9: Residual strains and stresses calculated in depth at $2\mu m$ from the center of the indentation of a rigid sphere on an elastic plastic flat. FEM and SAM results comparison.

loop parameters can thus be considered validated with respect to Abaqus and with the former versions of the model.

It can be noticed here that experimental validations of the model where made by comparisons of the residual displacements generated by a sphere rolling on a flat. SAM results showed excellent correlation with the experimental results. Further details are available in [JAC 01].

2.6.2 Impact loop validation

The impact loop is first validated through a simple elastic impact case where analytical solutions are well-known.

The theory of Hertz for the normal contact between two spheres as summarized by Johnson [JOH 85] can be used to calculate the maximum rigid body approach δ^* knowing the equivalent radius and initial relative velocity of the two bodies in contact. This is done by equalizing the initial kinetic energy and the elastic deformation energy stored during the impact, as proposed by Davies [DAV 48]. The value of δ^* can also be expressed as a function of the sphere radius R and its initial velocity v, as given by Eq. 2.57,

$$\delta^* = \left(\frac{15}{8} \frac{E_k}{E^* \sqrt{R}} \right)^{\frac{2}{5}} \tag{2.57}$$

where the kinetic energy E_k is defined by:

$$E_k = \frac{1}{2} m v^2 \tag{2.58}$$

It yields:

$$\delta^* = R \left(\frac{5}{4} \rho \pi \frac{v^2}{E^*} \right)^{\frac{2}{5}} \tag{2.59}$$

No analytical expression exists for the time-displacement curve of an elastic impact problem. However, the total time of impact can be expressed as follows:

$$T_c = 2.94 \frac{\delta^*}{v} = 2.87 \left(\frac{m^2}{R E^{*2} v} \right)^{\frac{1}{5}} \tag{2.60}$$

Using the semi-analytical method, the simulation of an elastic impact is first performed. Figure 2.10 illustrates the rigid body displacement versus time during an elastic impact and for a circular contact (sphere on flat). The maximum rigid body displacement δ^* and the total impact duration T_c given by 2.59 and 2.60 are used to normalize the plot. The numerical results obtained from the current model corroborate well with the analytical results for the maximum values.

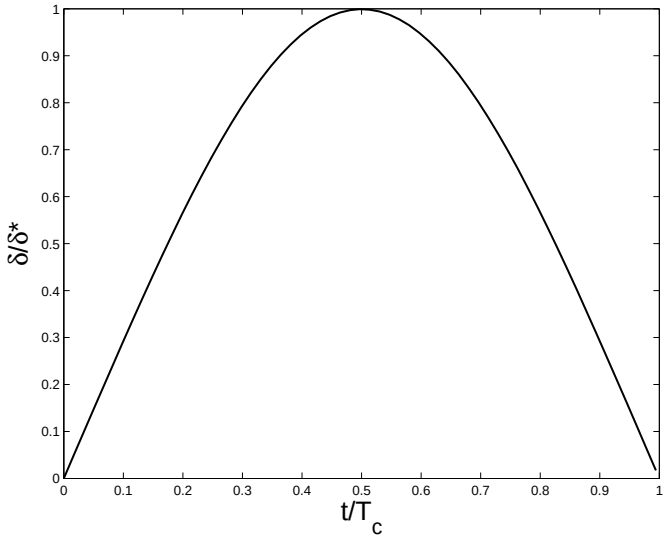

Figure 2.10: SAM Time-Displacement curve for an elastic impact with displacement δ normalized by the analytical maximum rigid body displacement δ^* and time t normalized by the analytical total impact duration T_c

2.7 Conclusions

The semi analytical method was developed and extended to be able to simulate contact at rather high plastic strain levels, up to the limits of the assumed small strain hypothesis.

Several improvements were made on the method to increase its accuracy and computational speed. The modelled mechanical phenomena were enhanced, with the consideration of impact loadings and kinematic hardening. The method is now capable of simulating static or rolling contacts with any kind of plasticity hardening model in reduced computation time compared to the former versions of the model. Applications of these improvements to the simulation of rolling contact will be made in the following chapter.

The validation of impact modelling has been initiated with the validation of the impact loading calculation for a simple elastic case. Based on this, the impacts being considered quasi-static the code can be considered fully efficient to model impacts involving low plastic strain levels (up to about 10%) for which the method was formerly validated.

The behaviour of the method for higher levels of plasticity needs to be investigated. The consideration of plasticity at large strain levels has been improved with the lifting of the small displacement hypothesis. Quality of the obtained results needs to be inquired. Besides, important consideration like compatibility equations are still not considered by the method and validations of the results is to be done. Chapter 4 illustrates several applications in this direction.

Analysis of the results at the macroscopic level with the comparison of the coefficient of restitution will be made and benchmarks with several finite element codes will allow to evaluate the influence of large strains and the efficiency of the method to simulate these phenomena.

From rolling contact...

In this chapter, some applications of the semi analytical model to rolling contact problems are presented. Industrial applications of rolling contacts, typically including bearings are usually loaded below their yield limit or encounter very low plasticity levels. Thus the pressure and stress levels are commonly calculated using analytical elastic solutions. One aim of this chapter is to show limits of this approach by observing the effect of plasticity on the maximum pressure observed during contact.

The study begins with the analysis of the effect of the hardening model on indentation and rolling contacts. The evolution of the residual imprint is studied, the effect of the rolling loading and hardening model on this imprint and its stabilization are analysed. The influence of several parameters on the maximum pressure during contact and maximum residual strain is then observed. Ranging from an elastic contact to a stress level above the yield limit, the influence of the contact geometry (circular or elliptical) and loading type (indentation or rolling) is presented.

Contents

3.1 Introduction

Low plasticity burnishing is an industrial process used to generate compressive residual stresses by the application of a rolling load on the treated surface. The geometry of the loaded body can vary as well as the applied load depending on the desired effect. A study of the rolling of a sphere or an ellipsoid on an elastic plastic semi infinite body is proposed here as a first insight on low plasticity burnishing modelling.

What is often referred to as a Hertzian contact may undergo plasticity either at the macro-scale due to an accidental overload, or at an asperity scale due to the presence of surface defects and/or roughness. Whereas an elastic solution does not explicitly consider the surface velocity or loading history, it is also apparent that a moving (rolling) load will not yield the same residual stress and strain distribution as that of a purely vertical loading/unloading. Three-dimensional (3D) analysis is also more complex than the two-dimensional (2D) problem since it implies a change in the surface conformity. This chapter presents the results of a numerical investigation on frictionless elastic-plastic elliptical point contacts with a moving load, as compared to a purely vertical (indentation) load. In the present analysis, both bodies may behave in an elastic-plastic mode. Both kinematic and isotropic hardening are considered to account for repeated rolling contacts. The contact pressure and the plastic strain are found to be reduced when the two bodies are elastic-plastic, as compared to the case when one of the bodies remains elastic. Numerical results also indicate that, at a given load intensity, the maximum contact pressure and equivalent plastic strain are affected by the contact geometry (circular and elliptical point contacts), and differ significantly when the load is moving compared to purely vertical indentation. Whereas the maximum elastic contact pressure (Hertz solution) is often used as a control parameter for rolling contact fatigue analysis, whatever the geometry of the contact (point, elliptical or line contact), the results presented here show that the effective contact pressure and subsequent residual strains are strongly dependent on the contact geometry in the elastic-plastic regime.

A series of simulations will be briefly presented and analysed in terms of the pressure distribution under load, as well as permanent surface deformation and residual strain after unloading. These Two geometries will be investigated, first a circular point contact and second an elliptical point contact with an ellipticity ratio equal to eight. The contact is considered frictionless, thus no computation of tangential problem is made. The tangential displacement implies only a translation of the geometry and plastic strains of both surfaces in contact.

It is often assumed that plasticity in a contact acts to limit the contact pressure to a threshold value and is only dependant on the material hardness or yield stress, which is also referred to as elastic-perfectly plastic behaviour. Such an approach can be used as a first step, and may yield satisfactory results for a rough surface in terms of real contact area, pressure distribution, and gap between the contacting surfaces. However, it does not allow an adequate description of the subsurface stress state, since it does not consider plasticity which leads to residual stresses and strains.

The incorporation of plasticity in 3D rolling contact analyses has recently gained more

attention due to progress in semi-analytical methods (SAM) [JAC 02, SAI 02, BOU 05, WAN 05, NéL 06, POP 06a, POP 06b, BOU 07, NéL 07a, NéL 07b, ANT 08, CHE 08a, CHE 08c, WAN 10b], which are an alternative to more costly finite element method (FEM) simulations (see for example [BIJ 97, JIA 02, GUO 04, KER 07]). While line contacts and elliptical point contacts may undergo plasticity when the yield stress is exceeded, the 3D case is more complex since it involves an additional mechanism which is an increase in the surface conformity as the ellipsoid generates a groove on the counterface as it translates. Moreover, most mechanical contacts carry their service load not simply once, but potentially for a large number of repeated cycles. Therefore the contact analysis could be repeated to account for cyclic loading of the contacting materials, which can result in large computational overhead when conventional FEM is used. Note that a first attempt to describe the effect of the hardening model (isotropic, kinematic and combined kinematic-isotropic hardening) in repeated frictionless rolling elastic-plastic circular point contact is due to Chen et al. [CHE 08c].

3.2 Hardening Criteria and Numerical Data

There are numerous plasticity models that have been developed - ranging from elastic-perfectly plastic to elastic-plastic with linear or non-linear behaviour with kinematic, isotropic, combined isotropic-kinematic, or anisotropic hardening, each having select capabilities to describe various experimental phenomena. The choice of the yield criterion may also affect the results. Elastic-perfectly plastic flow without hardening corresponds to the case in which the stress remains constant during flow; this is exhibited by mild steels and soft metallic materials as a flat zone in the stress-strain curve. This behaviour does not match that of hardenable alloy steels that have high yield limits. Since it is our desire to develop models that are most appropriate for this class of steels, a hardening law is therefore necessary. For isotropic metals, the experimental points are situated between the von Mises and the Tresca criteria, with very ductile metals closer to the Tresca criterion [LEM 90]. In numerical models, however, the von Mises criterion is the one most commonly used because of its easier implementation in numerical calculations. The Tresca criterion is more difficult to use because of the discontinuity in the normal at the corners of the yield surface. It is why in this investigation, a kinematic and an isotropic hardening models along with the von Mises yield criterion have been chosen for the representation of the yield surface. As a first approximation, it is assumed that the cyclic stress-strain response of the material is identical to that under monotonic tension, neglecting any cyclic softening that may occur due to micro-structural/metallurgical phase changes.

The isotropic hardening law of the EP body is described by the Swift's law, i.e. $\sigma_y = B(C+10^6 p)^n$, which presents the numerical advantage of being continuously differentiable. Parameters describing the hardening of AISI 52100 bearing steel, for which data are available, are selected for illustrational purposes: $B = 945MPa$, $C = 20$, and $n = 0.121$ [BOU 05], with p being the accumulated plastic strain. This gives a conventional shear yield stress $K = \sigma_Y/2 = 1187MPa$ at 0.2% plastic strain. The load level investigated cor-

responds to an elastic contact pressure up to $8GPa$ (Hertzian assumption), which remains in the elastic shakedown regime. The limit between the elastic regime and the elastic shakedown regime corresponds to the onset of yielding. It is well known (since Johnson [JOH 85]) that from the von Mises criterion Ű and a Poisson's ratio of 0.3 Ű the maximum contact pressure to initiate yield is $P_{max} = 2.8K = 1.60\sigma_Y$ at a depth of $0.48a$ for a circular point contact, whilst it begins at a point equal to $0.78a$ below the surface when $P_{max} = 3.1K = 1.79\sigma_Y$ for Hertzian 2D line contact. Note that no upper limit of shakedown exists since isotropic hardening is assumed, in other words, a ratcheting regime is not reached.

The kinematic hardening law of the EP body is described by the Armstrong-Frederick's law. Two kinematic hardening variables $\underline{\underline{X_1}}$ and $\underline{\underline{X_2}}$ are used. Their evolution is described by Eq. 2.47. The yield function is defined by Eq. 2.31:

Parameters C_1, C_2 and γ_2 are obtained by best fitting both hardening laws for a monotonic tensile loading with values of equivalent plastic strain e_p ranging from 0 to 2%. These values cover the range of plastic strain studied here. The initial yield limit σ_{y0} is taken equal to the initial yield limit of the isotropic Swift's law. This leads to $C_1 = 34,591MPa$, $C_2 = 974,304MPa$, $\gamma_2 = 856$ and $\sigma_{y0} = 1,358MPa$. Both hardening curves present a maximum difference of 7.5% with an average of 1.27%. Figure 3.1 illustrates the resulting hardening curves for the isotropic Swift law and the kinematic Armstrong-Frederick law.

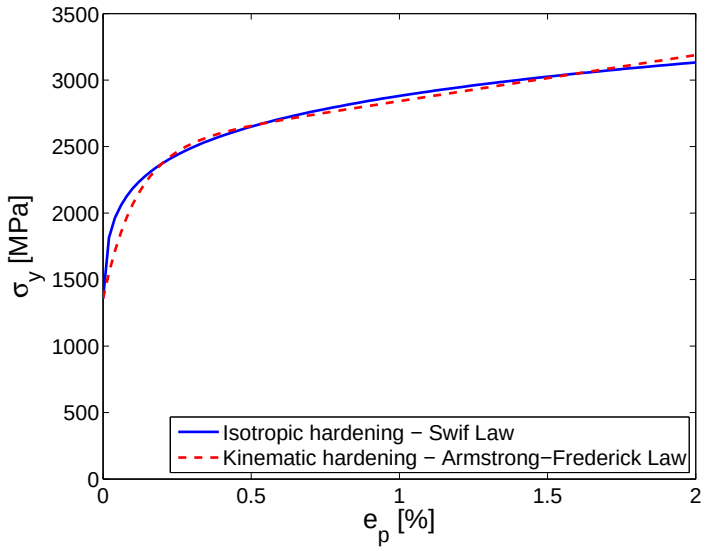

Figure 3.1: Hardening curves for the isotropic Swift's hardening law and the kinematic Armstrong Frederick's law

Throughout this study, pressure results are presented normalized by the Hertzian pressure. The Hertzian pressure is defined as the maximum pressure for a spherical contact.

It is defined as in Eq. 1.5(see [JOH 85]).

For an elliptic contact, approximate analytical equations have been given by Antoine et al. [ANT 06]. The Hertzian pressure for an elliptical contact point loaded with force P_0 is then defined as:

$$P_{hertz} = \frac{3}{2}\frac{P_0}{\pi ac} \tag{3.1}$$

where a and c are the semi-minor and semi-major axes of the contact ellipse defined in Eqs. 1.12 and 1.14.

3.3 Indentation results

The vertical loading and unloading of an elastic ball over an EP flat surface is investigated. A normal force of $1150N$ is applied on the ball. This corresponds, in the elastic case, to a Hertzian pressure of $5.7GPa$. The ball is made of ceramic (Si_3N_4) with diameter $d = 9.525mm$. The flat surface is elastic plastic with either isotropic or kinematic hardening. The contact is considered frictionless, that is to say no computation of the tangential problem is made. The bodies in contact are considered semi infinite which is here consistent with the small contact radius ($a = 311\mu m$ in the elastic case) compared to the dimensions of the bodies. Small strain hypothesis is assumed, this approach has been validated for rigid body displacement δ up to $110\delta_c$ [NéL 06] where δ_c is the critical rigid body displacement at the onset of yielding. In this study, the maximum ratio δ/δ_c is limited to 60.

The dimensionless pressure profiles under the maximum load are given for both hardening behaviours in Fig. 3.2(a) The radius and pressure are normalized by the elastic solution for i.e. the contact radius a and the Hertzian pressure P_{hertz}. Both hardening laws lead to similar pressure profiles which can be explained by the fact that the difference between hardening behaviours takes mostly place during unloading, not loading. Note also that, in this example, the influence of plasticity is rather low. Indeed, the pressure profiles are only slightly flattened and the effective contact radius is very close to the elastic contact radius.

Figure 3.2(b) gives the equivalent plastic strain profiles in depth and at the center of the contact after unloading. Both profiles are very similar. Slight differences appear just below the surface and after the Hertzian depth where the amplitude of strains is the lowest, around 0.1%. This corresponds to the range of plastic strain where the hardening curves slightly differ. As a consequence of plastic strains, a permanent residual displacement appears at the surface of the flat as represented in Fig 3.2(c). The small difference between the two profiles is explained by the integral of the equivalent plastic strain versus depth and after unloading, see Fig. 3.2(b). It can be concluded that, at this load level and for the simulation of indentation with a single vertical loading/unloading, the translation of the hardening surface has no significant effect. This results correlates with recent work by Zait et al. [ZAI 10]. They studied the normal loading of an elastic plastic sphere with

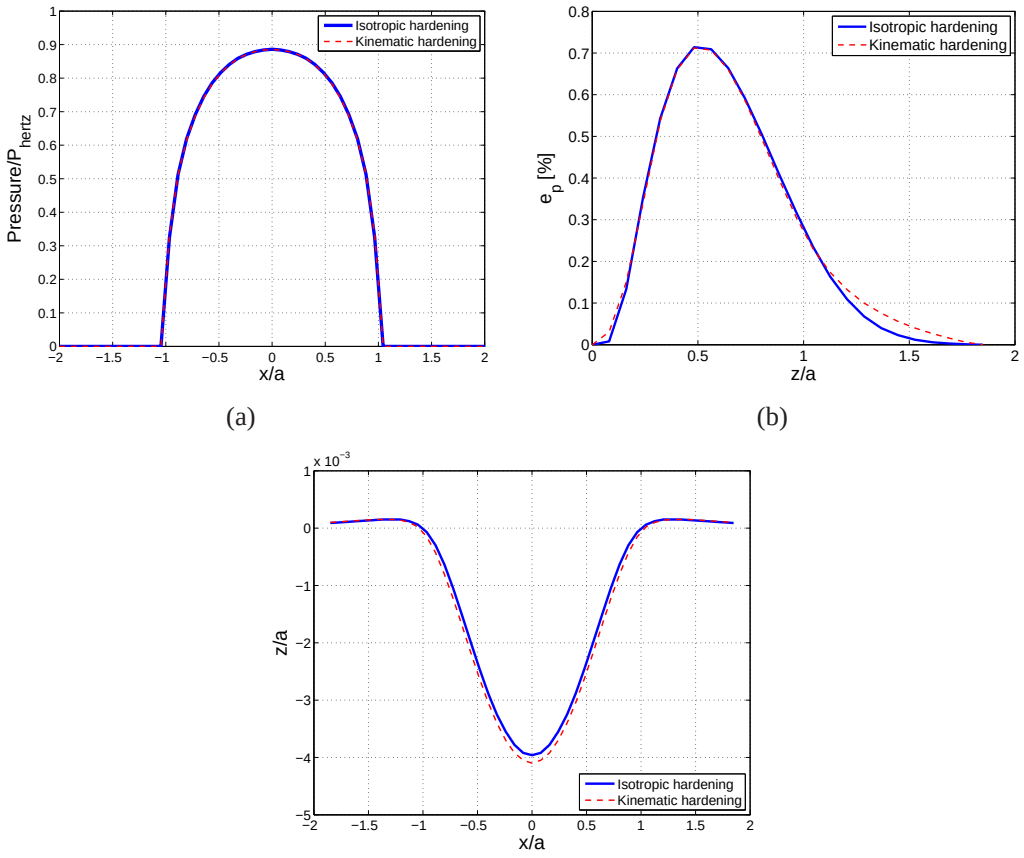

Figure 3.2: Pressure profile under maximum load (a), equivalent plastic strain profile in depth at the center of the contact (b) and longitudinal profile (c) for vertical indentation of an elastic ball on an EP flat surface with either isotropic or kinematic hardening ($k = 1$, $P_{hertz} = 5.7GPa$)

a rigid flat and showed that the hardening model (isotropic or kinematic) has negligible effect on the results.

3.4 Repeated rolling cycles, effect of the hardening model

The frictionless rolling of a ceramic Si_3N_4 (elastic) ball of diameter $9.525mm$ on an elastic-plastic flat (AISI 52100 steel) is then investigated. This includes determining the shape of the permanent imprint found on the surface of the EP flat for the different hardening laws. When a tangential displacement is applied to the ball, the contact pressure profile becomes dissymmetric in the x direction as shown in Fig. 3.3. It leads to a slight shift of the center of the contact force F_c (integral of the pressure distribution) thus generating a moment that balances the rolling moment M_R needed to cause rolling of the ball. The full kinematics of the ball is represented in Fig. 3.4. The presence of a resisting torque to rolling can also be interpreted as an apparent friction coefficient if instead of a rolling torque one considers a tangential force acting at the ball center. This apparent friction coefficient - only due to inelastic effect - is equal to the ratio between the pressure distribution centroid and the ball radius.

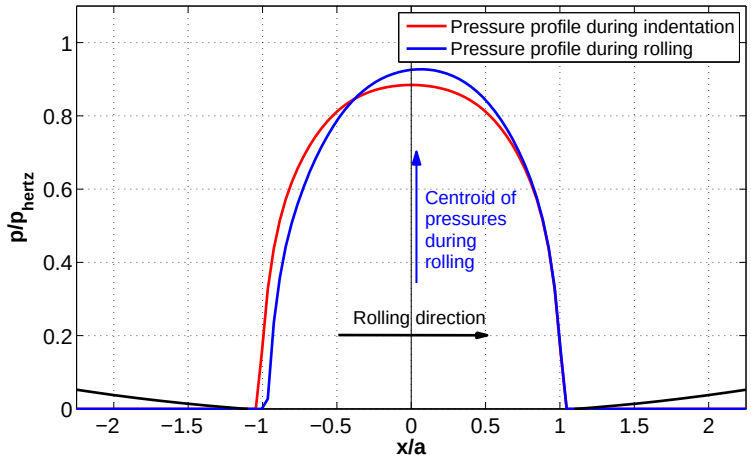

Figure 3.3: Pressure profiles generated by an elastic ball on an elastic plastic flat during indentation and rolling. The dissymmetry of the pressure profile during rolling leads to a swift of the reaction force from the O_z axis.

Figure 3.5 shows the longitudinal profile (permanent) found after the first three loading/unloading cycles with rolling of the ball under a Hertz contact pressure of $5.7GPa$ (elastic solution) for an isotropic hardening law. The curve with triangle symbols corresponds to the axisymmetric imprint found after unloading and without rolling. The solid

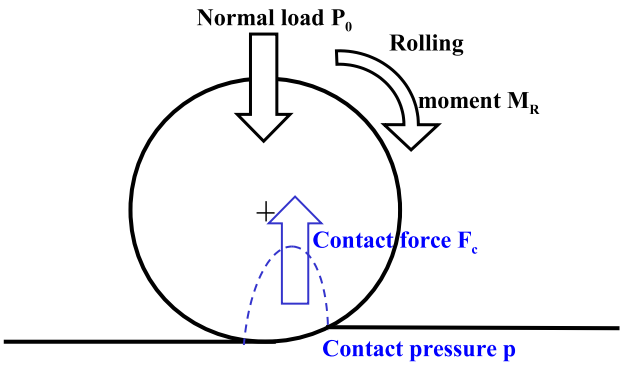

Figure 3.4: Kinematics of a ball rolling on a flat. A normal load P_0 is applied to the ball. The dissymmetry of the contact pressure distribution leads to a swift of the reaction force F_c which generates a moment compensated by the rolling moment M_R.

curves represent the permanent imprint after vertical loading, rolling of $6.6a$ (i.e. $2.05mm$) from left to right, maintaining the normal load constant, and (vertical) unloading. Results are presented in a dimensionless form with the abscissa and ordinate normalized by the contact radius a ($311\mu m$). The parameter k denotes the ellipticity ratio ($k = c/a$; i.e. $k = 1$ for a circular point contact). One may observe a decrease in the imprint depth after a transient period during rolling. This depth reaches an asymptotic value after rolling a few multiples of the contact radius, which corresponds to a steady-state regime. This is explained by the change in conformity when the movement starts, which produces a decrease in the maximum contact pressure and subsequently lower plasticity, as shown in Fig. 8 in [NéL 07a]. A comparison of the surface displacement found at the center of the rolling track after unloading for the first three rolling cycles shows that the permanent imprint quickly reaches a stabilized value after very few cycles, i.e., two or three rolling loading cycles, which is due to the isotropic hardening model assumed here. The evolution between the first and second cycles is explained by the change in the surface conformity due to the plastic imprint that occurs mainly after the first loading cycle. During the first cycle the ball is rolling on a flat surface (but a groove is formed behind), whereas it rolls on a groove for further cycles. It should be noted that the maximum depth is higher for the rolling case compared to the pure vertical loading/unloading case. However, the imprint depth in the steady-state (rolling) area is found to be slightly lower than the depth corresponding to an indent (vertical loading/unloading). Another interesting phenomena is the pile-up at the end, i.e., at the point of unloading, that is found to be higher than the pile-up at the beginning. This can be explained by the fact that the plastic strain is

higher near the starting point than it is at the end. This is also why both the permanent imprint near the starting point is deeper and the pile-up is shallower. This result is in good agreement with scratch simulations via FEM [BUC 05].

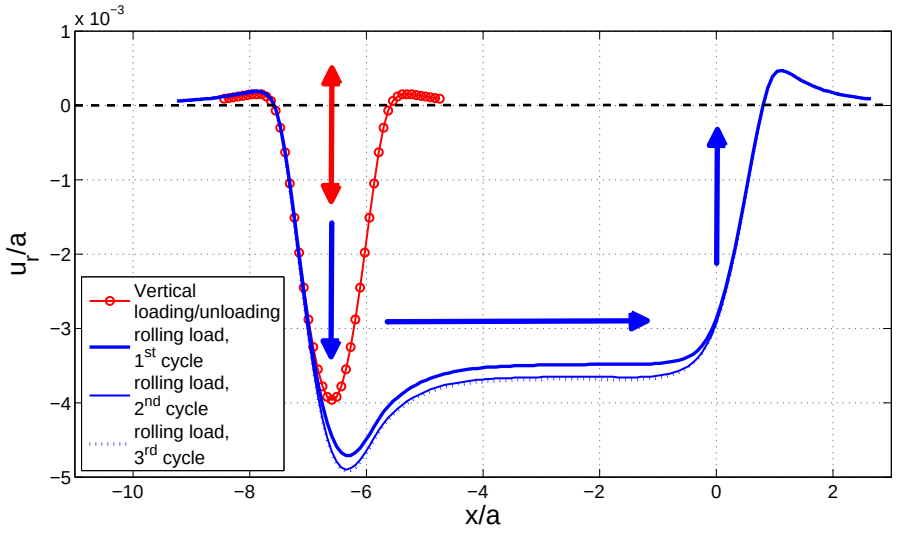

Figure 3.5: Longitudinal profile comparison of a vertical loading/unloading with and without rolling ($k = 1$, $P_{hertz} = 5.7GPa$, elastic ball on an EP flat surface with isotropic hardening; after one, two, and three cycles, rolling distance of $6.6a$). Loading, rolling, and unloading are represented by the heavy arrows.

Equivalent simulations have been performed with an EP flat with an Armstrong-Frederick's kinematic hardening law. Results are presented in Fig. 3.6 similarly to those in Fig. 3.5. While the results for a single indentation were very similar for the different hardening laws, the influence of the kinematic hardening is here significant. First, it can be observed that the imprint after rolling is deeper than for indentation, whereas it was shallower for isotropic hardening. It can be explained by a redistribution of residual plastic strains during rolling (or after unloading). Second, it is found that the imprint presents also an increase in depth at the end of the rolling path which was not visible for isotropic hardening. Finally, after five rolling cycles and this load level, the imprint is not yet stabilized. Going back to the redistribution of plastic strains during unloading it is well-known that for the contact of a ball over a flat, the shear profile is symmetric with a change in sign at the center of the contact. When rolling occurs, the area under the initial contact in the rolling direction undergoes shearing stresses that change sign as illustrated in Fig. 3.7. The elastic shear stress σ_{xz} generated by the contact pressure are represented in the plane ($y = 0$) for two rolling increments separated by a distance $1.75a$. It can be seen that the point at $x/a = -1$, $z/a = 0.5$ will experience a change in shear stress from $0.4\sigma_Y$ to $-0.4\sigma_Y$.

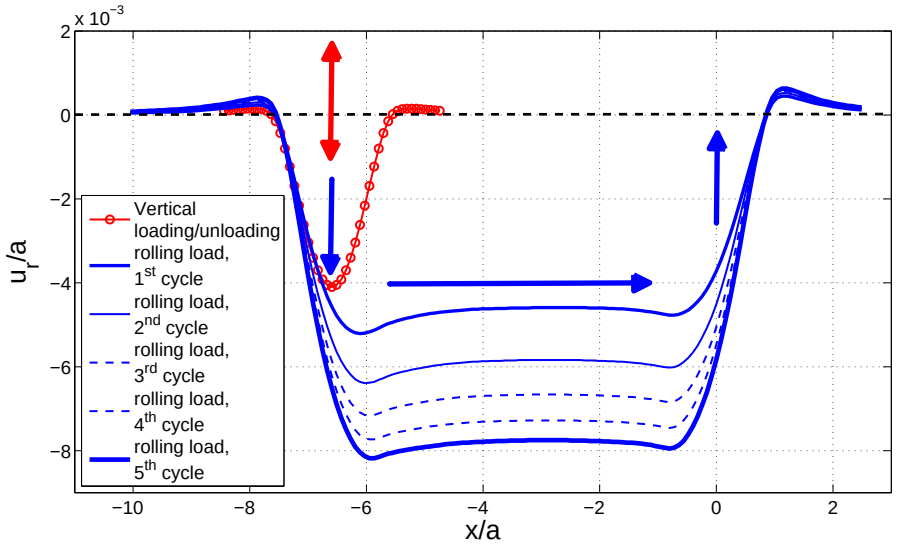

Figure 3.6: Longitudinal profile comparison of a vertical loading/unloading with and without rolling ($k = 1$, $P_{hertz} = 5.7GPa$, elastic ball on an EP flat surface with kinematic hardening; after the five first cycles, rolling distance of $6.6a$). Loading, rolling, and unloading are represented by the heavy arrows.

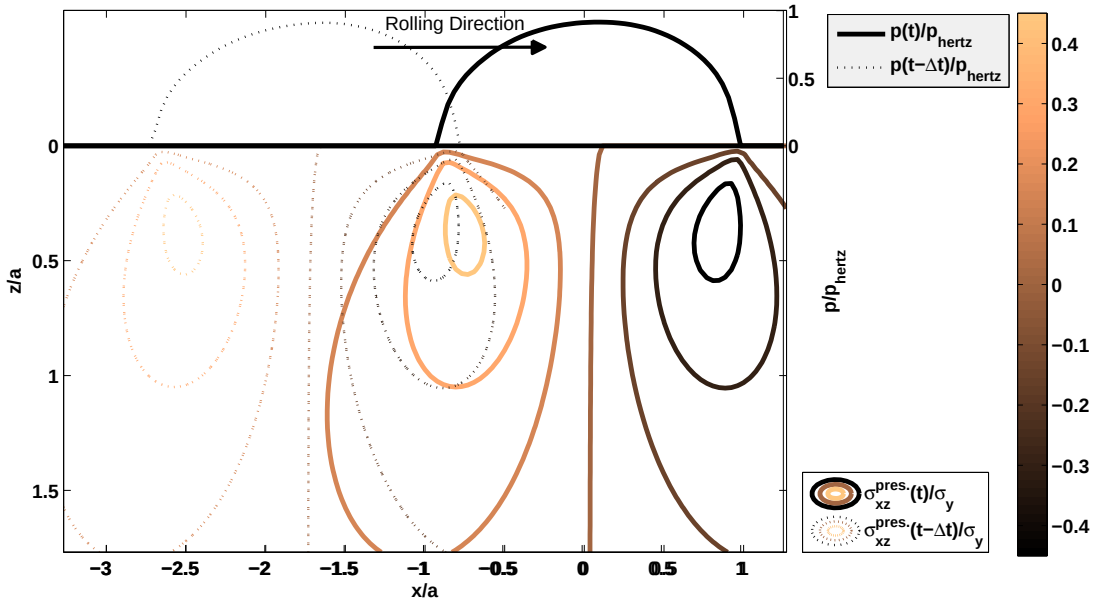

Figure 3.7: Profiles in the plane ($y = 0$) of normalized stresses σ_{xz} generated by the normalized contact pressure at t and $t - \Delta t$ separated by a rolling distance of $1.75a$. First rolling cycle of an elastic sphere over an elastic plastic plane with kinematic hardening. Both represented states correspond to steady-state during the rolling load.

For isotropic hardening, since the yield surface increases symmetrically in all directions, no further plasticization occurs when the load passes. However for a fully kinematic hardening, the yield surface is translated and when the shearing stresses switch sign, reverse plasticity occurs and the component ε^p_{xz} of plastic strain decreases. The influence of this strain component on the residual displacement explains the higher depth of the imprint when the EP flat behaves plastically kinematic. A similar phenomenon occurs for diagonal components ε^p_{xx} and ε^p_{zz}, but in a less pronounced way since their amplitude is lower than for shearing stresses. In kinematic materials, when a load is applied in one direction and plasticity occurs, the yield surface is translated in this "direction". If the load direction changes, another point (could be an opposite point) on the yield surface can be reached in the new direction and thus reverse plasticity will occur. The same trends append after each rolling loading cycle. As a consequence, the residual displacement profile is modified after the each rolling loading cycle, while it converges very quickly to a stabilized profile for isotropic hardening, typically after 2 or 3 cycles depending on the load level. The increase in the residual displacement tends to decrease after each new cycle (see Fig. 3.6). Moreover here far more than 5 cycles are needed to reach the shakedown. The isotropic and kinematic hardening behaviours can be considered as asymptotic and idealized behaviours compared to the response of real materials when submitted to cyclic loading, with a more complex mixed kinematic and isotropic hardening. The fully isotropic behaviour shows a very fast shakedown while the fully kinematic behaviour implies that more cycles are needed (no stabilization after the five first cycles in Fig. 3.6).

3.5 Circular and elliptical indentation of isotropic hardening bodies

The contact between a stationary or rolling ellipsoid and a flat is now investigated. The ellipsoid and the flat can have the same elastic properties, however the ellipsoid may behave either elastically or elastic-plastically, whereas the half-space is always elastic-plastic. This corresponds to the two extreme situations when two EP bodies with identical elastic properties but with different hardening laws are in contact. It is typically the case when two bodies are made of the same alloy but with different heat treatments. In what follows the plastic behaviour is now assumed isotropic.

Next, the indentation of an elastic-plastic half space by a sphere was analysed, with the load intensity, i.e., the Hertz pressure normalized by the conventional uni-axial yield stress P_{hertz}/σ_Y, as the reference configuration. The maximum contact pressure, P_{max}, and the equivalent plastic strain, $e_p = \sqrt{\frac{2}{3}\varepsilon^p_{ij} : \varepsilon^p_{ij}}$, found at the Herztian depth are shown in Fig. 3.8. One may observe a pronounced reduction in the maximum contact pressure when simulating contact between two EP bodies or one EP against one E, up to 30% and 22% at the highest load as compared to the elastic solution ($8GPa$), respectively. In addition, one may observe a significant decrease in the maximum plastic strain found at the Hertzian depth, from 1.92% for one EP body to 1.38% for two EP bodies, the plastic

strain being equally distributed between the two bodies in the latter case.

The above solutions are now compared to the solution found when an elastic or elastic-plastic sphere rolls over an elastic-plastic half space. The same maximum load is applied than for the indentation but once the maximum load is reached, a tangential displacement is applied to the ball thus translating the point of application of the normal load on the flat surface. Figure 3.9 follows the presentation of results in Fig. 3.8 after three frictionless rolling loading cycles, in the steady-state region, i.e., after a rolling distance of at least five times the contact radius. Three interesting features are observed. First, it is found that the decrease in the maximum contact pressure compared to the elastic solution is less important when the load is rolling ($P_{max}/P_{hertz} = 0.864$ and 0.8 for one and two elastic-plastic bodies, respectively) than for indentation ($P_{max}/P_{hertz} = 0.796$ and 0.717, see Fig. 3.8). The reason is that the change in conformity is less important compared to the elastic situation (sphere on flat) when the sphere is rolling within a groove, than when the sphere is loaded against an indented flat. Second, it is observed that there is a very significant increase in the maximum plastic strain, from 1.92 to 3.09% for one EP body and from 1.38 to 2.32% for two EP bodies, which corresponds to an increase of more than 50%. As a general trend, the fact that both bodies are EP implies a reduction in the maximum contact pressure, then decreasing the level of plasticity (plastic strain), and subsequently the depth of the permanent imprint observed at the surface. Third, as mentioned before, neither evolution of maximum pressure nor of maximum plastic strain is observed after the second rolling cycle. The pressure is almost constant for all three rolling cycles, being only slightly modified by the evolution of the contact surface. A large difference is observed for the maximum plastic strain between the first and second rolling cycle but no evolution is observed after the second rolling cycle, the shakedown being reached. As the normal load increases, the amount of plasticity created during the first rolling cycle increases and consequently the difference between the two first cycles increases. The bigger change in surface conformity, the more plasticity is needed to accommodate this change.

In many engineering applications the contact geometry is neither linear (cylinder on flat) nor circular. The maximum contact pressure and the maximum plastic strain when an ellipsoid is vertically loaded/unloaded against an elastic-plastic flat (indentation) using the data for AISI 52100 bearing steel are shown in Fig. 3.10. The same data are plotted in Fig. 3.11 when the ellipsoid is rolling on the half-space. Note that before and during rolling, the ellipsoid is elongated in the direction transverse to the rolling direction, leading to an elliptical contact with an ellipticity ratio $k = c/a = 8$. It appears that the static elliptical contact differs only slightly from the circular contact in terms of the maximum contact pressure and plastic strain, see Figs. 3.8 and 3.10. For the elliptical contact ($k = 8$) the maximum contact pressure decreases to 0.837 and 0.767 times the Hertz pressure (elastic solution) for one and two EP bodies, respectively ($P_{max}/P_{hertz} = 0.796$ and 0.717, respectively, for $k = 1$, see Fig. 3.8). Meanwhile, the maximum plastic strain found at the highest contact load (Hertz contact pressure of $8GPa$) reaches 1.81 and 1.31% for one and two EP bodies, respectively, for $k = 8$, instead of 1.92 and 1.38%, respectively, for $k = 1$.

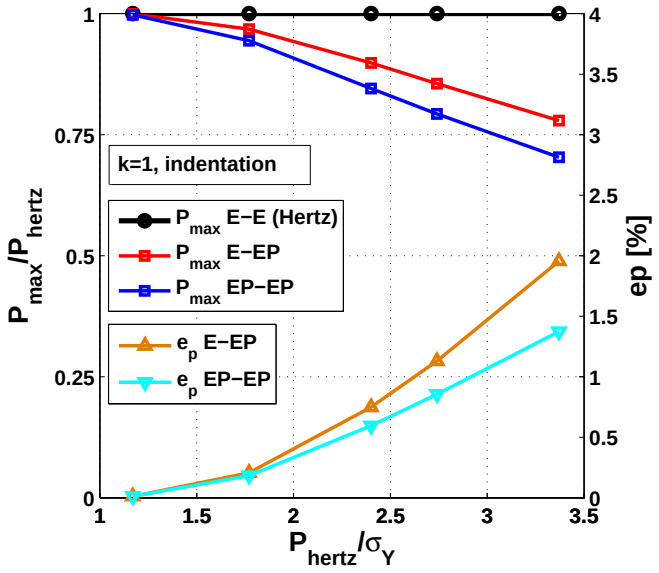

Figure 3.8: Maximum contact pressure, P_{max}, normalized by the elastic solution, P_{hertz} (Hertz pressure), and equivalent plastic strain, e_p (%), vs. the load intensity, P_{hertz}/σ_Y, for two EP spheres pressed against each other. E and EP refer to elastic and elastic-plastic, respectively. The elastic solution (E_E) is the Hertz solution.

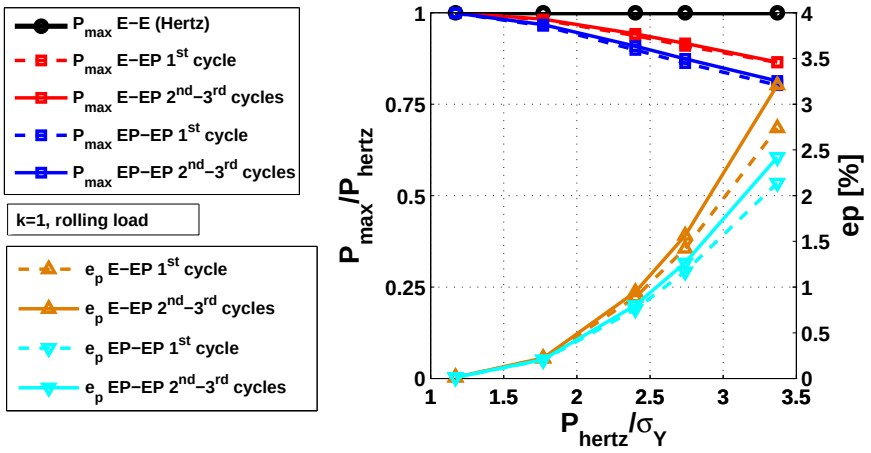

Figure 3.9: Maximum contact pressure, P_{max}, normalized by the elastic solution, P_{hertz} (Hertz pressure), and equivalent plastic strain, e_p (%), vs. the load intensity, P_{hertz}/σ_Y, for the three first frictionless rolling cycles, circular point contact ($k = 1$).

It is worth mentioning that, for a circular point contact ($k = 1$), differences between the vertical and rolling loading (see Figs. 3.8 and 3.9) are less pronounced than for an elliptical contact ($k = 8$), see Figs. 3.10 and 3.11. During rolling, the maximum contact pressure, which is observed in the steady-state region (i.e., when the ellipsoid has rolled a distance several times its semi-minor axis), is only reduced to 0.962 and 0.92 times the Hertz pressure for one and two EP bodies, respectively, whereas the reduction was 0.864 and 0.8 for a rolling circular point contact. This can be explained by the fact that the surface conformity is only slightly altered due to plasticity when a cylinder rolls on a flat. Indeed at the second rolling cycle a ball will roll in a groove formed during the first rolling cycle. For a cylinder or when the ellipticity ratio is quite large no groove is formed and the cylinder will continue to roll on a plane i.e. without geometry accommodation. Complementary elements can be found in [NéL 07a]. Since the contact pressure remains quite high despite plasticity and material hardening, the plastic strain at the Hertzian depth reaches 3.98 and 3.17% for one and two EP bodies, respectively, which is more than twice the values found for the same static elliptical contact. The evolution between the different rolling cycles observed for the elliptic contact case is similar to that of the spherical contact case ($k = 1$), i.e. results for the 2^{nd} and 3^{rd} rolling cycles are very close (within 1% of difference for the highest load).

It is worth mentioning that the onset of yielding, as graphically depicted in Figs. 3.8-3.11, tends to occur below the limits given by Johnson [JOH 85]. This phenomenon is an artefact of the SAM and may be explained as follows. Using Swift's law one may

define different yield limits. The conventional yield stress corresponds to a plastic strain of 0.2%. Some metallurgists prefer to use the micro-yield stress defined by as the stress leading to a plastic strain of 20×10^{-6} which is measurable in experiments. Numerically, the onset of yielding occurs for $e_p = 0$, i.e. for $\sigma_y = B$ which is significantly lower than the conventional yield stress $\sigma_Y = B(C+2000)^n = 2373MPa$ used here to normalize the results.

The numerical results presented here are pertinent to experiments in rolling contact fatigue (RCF). Usually, the choice of the load level for a given RCF experiment is often related to the maximum (Hertz) contact pressure corresponding to the elastic solution, which does not differ when the load is static or moving. It is shown here that, whereas the magnitude of the maximum von Mises equivalent stress normalized by the contact pressure is hardly dependent on the contact geometry for the elastic solution, the plastic strain is strongly affected by the ellipticity ratio and also by whether or not the load is moving. Therefore, it is suggested that experiments should be performed at the same magnitude of plastic strain instead of identical contact pressure when comparing materials from different experimental test configurations, or when trying to extrapolate results from point to line contact or vice-versa.

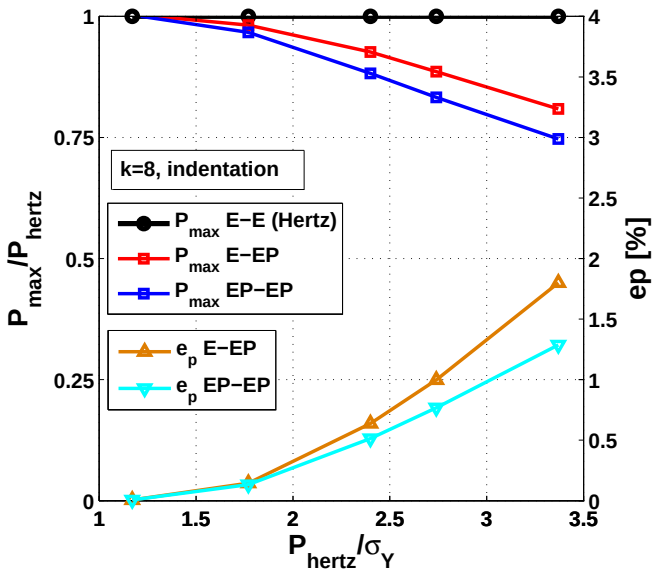

Figure 3.10: Maximum contact pressure, P_{max}, normalized by the elastic solution, P_{hertz} (Hertz pressure); and equivalent plastic strain, e_p (%), vs. the load intensity, P_{hertz}/σ_Y, for frictionless vertical loading, elliptical point contact ($k = 8$).

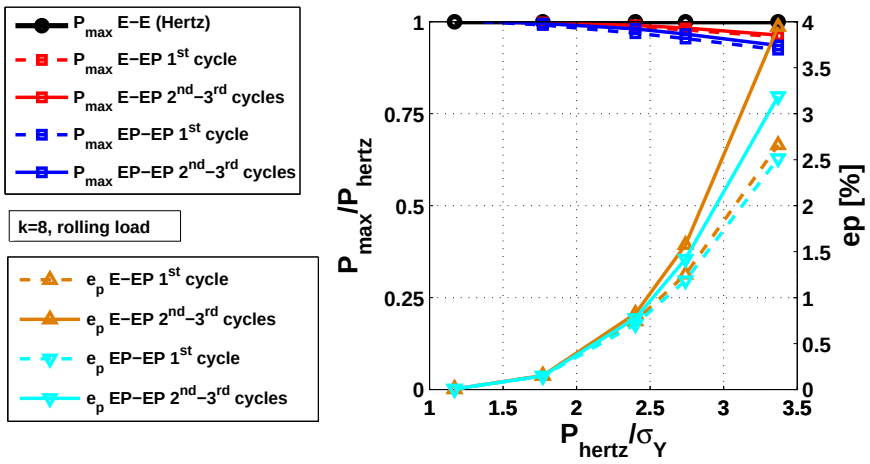

Figure 3.11: Maximum contact pressure, P_{max}, normalized by the elastic solution, P_{hertz} (Hertz pressure); and equivalent plastic strain, e_p (%), vs. the load intensity, P_{hertz}/σ_Y, for the first three frictionless rolling cycles, elliptical point contact ($k = 8$).

3.6 Conclusions

Several conclusions can be deduced from these simulations that provide interesting insights on the effect of plasticity on static and rolling contacts of non-conformal bodies.

- Circular and elliptical point contacts have been investigated, for stationary (indentation) and moving (frictionless rolling) loads, with at least one elastic-plastic body. The numerical results presented here indicate that the maximum contact pressure and the maximum equivalent plastic strain are strongly affected by the contact geometry (ellipticity ratio) and differ significantly when the load is moving as compared to the stationary (indentation) situation.

- For a circular point contact ($k = 1$) the maximum contact pressure reached after a few rolling cycles is found to be slightly higher than for static indentation after the same number of cycles. Subsequently, the maximum equivalent plastic strain increases significantly, by a factor of up to 1.5 for the examples presented.

- For a circular point contact ($k = 1$) the residual imprint is significantly higher for kinematic hardening than for isotropic hardening. It stabilizes after a few cycles for isotropic hardening while it keeps on increasing for kinematic hardening. A change of the residual imprint geometry is also observed at the unloading point after rolling.

- For an elliptical contact ($k = 8$) with the major axis in the direction transverse to the rolling direction, the contact pressure decrease from the Hertzian solution is less pronounced than for a circular point contact, since the conformity is less affected.
- For an elliptical contact ($k = 8$) it is found that the maximum equivalent plastic strain during rolling can be more than twice the value obtained for vertical loading/unloading.

... To the modelling of impact

This chapter presents results of impacts simulations using the semi analytical method. A benchmark with three finite elements codes is first presented to validate the method at high levels of strain. The method is then used to study the influence of the radius of a sphere impacting a semi infinite plane. Computation of coefficients of restitution is then made for a wide range of situations and empirical formulae are proposed to fit the simulation results. Insights are provided for a straight forward estimation of the coefficient of restitution in any general case.

Contents

4.1 Introduction

A semi analytical method for the study of contact and impact problems has been developed. It has been validated for cases of low plastic strain intensity and for elastic impacts. The method was applied to the simulation of rolling contact and will be here applied to the study of impacts involving relatively large strain levels.

A first section of this chapter presents the benchmark conducted with three finite element codes to validate the SAM results on a single impact involving plastic strain overcoming 10%. The influence of the large displacement consideration in the elastic stresses calculation, presented in section 2.3.1 is studied in detail. This section shows the important influence of the evolution brought to the code and its efficiency to study impacts at relatively high velocities. The computation time required by the various codes is quickly examined.

Based on the benchmark results a study of the influence of the mesh size on the quality of results and on the speed of calculation is conducted. This allows to evaluate the best elements size as a function of the problem's dimensions in terms of required speed while still obtaining acceptable results.

After a quick study on the effect of the shot's radius on an impact's results, a large part is dedicated to the study of the coefficient of restitution. As a very macroscopic quantity, the coefficient of restitution is used in various situations, ranging from peening simulations to sports. A comparison with results from several authors is first conducted, thus providing new validations of the code and showing its capability in predicting coefficients of restitution. Formulae are then provided, based on Jackson et al [JAC 10], to predict the coefficient of restitution as a function of the initial impact velocity and of the hardening behaviour of the impacted material, though limited to isotropic linear hardening. An extension of these results is provided for repeated impacts, i.e. impacts occurring at the same point and with constant initial velocity, based on results by Weir et al [WEI 05]. At last, some insights are provided for the evaluation of the coefficient of restitution for impacts occurring at different initial points.

4.2 Single Impact benchmark

4.2.1 Codes and Impact parameters

Results presented in chapter 2 showed the accuracy of the method at low levels of plasticity (below 1% of equivalent plastic strain). Nelias et al. [NéL 06] observed the results at higher plasticity levels for the case of indentation. Indentation results based on the SAM were compared with FEM comparisons from Kogut and Etsion [KOG 02]. The plastic zone evolutions were compared for rigid body displacements δ_z up to $110\delta_{zc}$ where δ_{zc} is the critical rigid body approach at which first yield occurs. For $\delta_z \leq 28\delta_{zc}$, corresponding in this case to an equivalent plastic strain of 5%, an excellent agreement was found between both methods. Above this value of δ_z, fairly good results are obtained, with a small

discrepancy due to the fact that the maximum plastic strain increases (up to 12% in this case) to levels for which the small strain hypothesis holds no longer.

The aforementioned discrepancies are rather small and good confidence is attributed to the SAM, even for rather large plastic strain levels. A benchmark was conducted between the SAM and Finite Element codes used by several partners. The aim of this benchmark is to evaluate the capability of the SAM to predict the residual strain and stress levels generated by the single impact of a sphere on an elastic-plastic flat. This benchmark would allow to estimate the error made by the small strain hypothesis on the SAM results and ensure the capability of the method to calculate the equivalent quasi-static loading from an initial velocity in the case of an elastic-plastic impact, in complement with results from chapter 2.

The impact of a purely elastic ball, with properties equivalent to that of the steel 100Cr6 on an elastic plastic flat with isotropic hardening and material properties similar to titanium alloy Ta6V is studied. The initial impact velocity of the ball is taken equal to $40m/s$ which produces an equivalent plastic strain level around 10% which is in the average of plastic strain levels commonly observed during shot peening. The contact is considered frictionless and the initial velocity is taken to be purely normal to the impacted surface. No inertial effects are considered for the SAM, yet the density of the ball is necessary for the velocity update and thus provided. The simulation parameters are indicated in Tab. 4.1.

	Body 1	Body 2
Geometry	Sphere $R = 0.3mm$	Flat
Material	100Cr6	Ta6V
Density	$\rho_1 = 7800kg/m^3$	N.A.
Elastic properties	$E_1 = 207GPa$ $\nu_1 = 0.3$	$E_2 = 111GPa$ $\nu_2 = 0.29$
Plastic properties	Purely elastic	Ramberg-Osgood $\sigma_{y0} = 478MPa$ $K = 3270.6MPa$ $n = 0.441$
Initial velocity	$v = 40m/s$	

Table 4.1: Material parameters for the single impact benchmark between the Semi Analytical Method, Abaqus, code_ASTER and Systus.

SAM results are compared with results from three FE codes: Abaqus, Systus and Code_Aster. The goal being to compare the results more than the computation speed of the codes, the meshes are taken of equal size in the contact zone and the evolution of the mesh in the rest of the computation domain is adapted to each model. Approximated computation times are noted down for comparison. A fine mesh is selected for accurate comparison of the results: $8.5\mu m$ in the x and y in-plane directions, $4.25\mu m$ in the depth, in the contact area. This corresponds to 10 elements along the contact radius. Relatively

large computation times are resulting from this but a fair representation of the stress and strain gradients is obtained. For all finite element codes, linear elements with reduced integration are used. Such element with a unique Gauss point are the closest to the SAM *elements* that present a unique calculation point.

The finite elements models consider large displacements and geometry update. Inertial effects are implicitly considered as well through the explicit scheme. Benchmark results thus allow to confirm the negligible effect of inertia and to evaluate the influence of the small strain hypothesis and geometry update on the results. The SAM method, as indicated in chapter 2 does consider a small strain formulation for the stresses calculation. Furthermore, large displacements have been implemented and this benchmark will show the influence of this improvement. At last, the SAM does not update the geometry as FE codes do. Nevertheless the effective surface shape is considered while solving the contact and all stresses are calculated in the Lagrangian reference frame. This allow a fair quality of results even for relatively large strains as shown here.

	Finite Element codes			Semi Analytical Method
	Abaqus	Code_Aster	Systus	
Element size in contact area	$\Delta x = \Delta y = 8.5\mu m$ $a^*/\Delta x \approx 10$ $\Delta z = \Delta x/2$ (in depth direction)			
Element type	Linear hexahedra with reduced integration			Cuboids with a central calculation point
Number of nodes	139693	101121	139557	168070[1]
Approximate CPU time	20h	15h	10h	1.7h
[1] Number of cuboids in the largest (final) computation zone				

Table 4.2: Numerical parameters for the single impact benchmark between the Semi Analytical Method, Abaqus, code_ASTER and Systus.

4.2.2 Results and analysis

A rapid analysis can first be made on the computation domain size and time between the different codes. The SAM presents a significantly reduced computation time despite a higher number of elements. This increase number of elements is due to the constant size of the SAM elements, necessary for the FFT calculation. The fine mesh size in the contact area has to be the same over the whole computation domain even in the zones with lower strain and stress gradients. The Systus results were computed in reduced CPU time compared to the other FE codes, yet it should be noticed that only a quarter of the domain was modelled while Abaqus and Code_Aster models describe one half of the problem. The SAM models the full 3D domain, without symmetry simplifications. Despite this drawback, the computation with the SAM is significantly faster (see Tab. 4.2).

Residual surface displacements calculated by the various codes are plotted in Fig. 4.1. Residual stresses and plastic strain results are also compared. The stress and strain components are analysed in depth at the center of the contact (Figs. 4.2 and 4.5). Von Mises equivalent values are also analysed along the z-axis (Figs. 4.3 and 4.6). In each case, the SAM results are presented with and without the large displacement consideration to analyse the effect of this new formulation. The equivalent plastic strain and von Mises residual stress calculated by the SAM in the (x,z) plane are also plotted, respectively in Figs. 4.4 and 4.7. All distances are normalized by the contact radius a^*, calculated equal to $85 + / - 4.25 \mu m$ by the SAM. Stresses are normalized by the initial yield limit σ_{y0} indicated in Tab. 4.1.

One of the first macroscopic results observable is the surface residual displacement. The comparison of SAM and FE results in Fig. 4.1(a) shows a very good agreement. All codes but code_Aster show an equal maximum residual displacement. Abaqus shows irregularities on the residual stress profile which points at one of the advantages of the SAM that is the easy consideration of contact. Other FE codes don't show this problem. The waviness of the Abaqus results are obviously oscillating around the right value. A point of divergence between codes, and especially between the SAM and FEM is the transition point from negative to positive residual displacement, around $x = a^*$. The SAM predicts a larger residual imprint and a notable difference in residual displacement in this zone. This difference might be considered negligible but will especially have some consequences on the comparisons with experimental results in the following chapter. The value of residual displacement around $x = a^*$ is mainly governed by the subsurface plastic strains, that are concentrated at this point and reach the surface as can be seen in Fig. 4.4. It can also be related to the pressure profiles. For such levels of plastic strain, the pressure profile is no longer flat: the center value decreases while the value at the perimeter increases (see Fig. 2.2). A second interesting fact is the almost negligible influence of the large displacement consideration on the residual displacement profile, see Fig. 4.1(b). This indicates first that the large displacement consideration is not fundamental for the comparison of simple surface displacement, at least in the direction normal to the surface ; and in second time that the normal residual displacement is not very sensitive to the model's parameters.

Plastic strains give a better view of the overall results. The plastic strain components being observed at the center of the contact in this case of an axisymmetric problem, the shear terms are nil and only the radial term ($\varepsilon^p_{xx} = \varepsilon^p_{yy}$) and the term in the depth ε^p_{zz} remain. The accumulated plastic strain is, in this case, almost similar to the equivalent plastic strain since the hardening is isotropic and no cyclic loading was applied. The resulting accumulated plastic strain shows logically the same behaviour as the detailed components. It can be noticed that the zz components is the most sensitive and the one for which the largest differences are observed. The maximum value as well as its depth are very similar between all methods. The SAM can then be considered accurate to predict plastic strains even at relatively high strain amplitudes (here about 10%).

The second interesting fact is the influence of the large displacement formulation in the SAM. Figure 4.3(b) shows that without large displacements, the maximum residual value is well predicted although its depth is different. Furthermore, the value at the surface

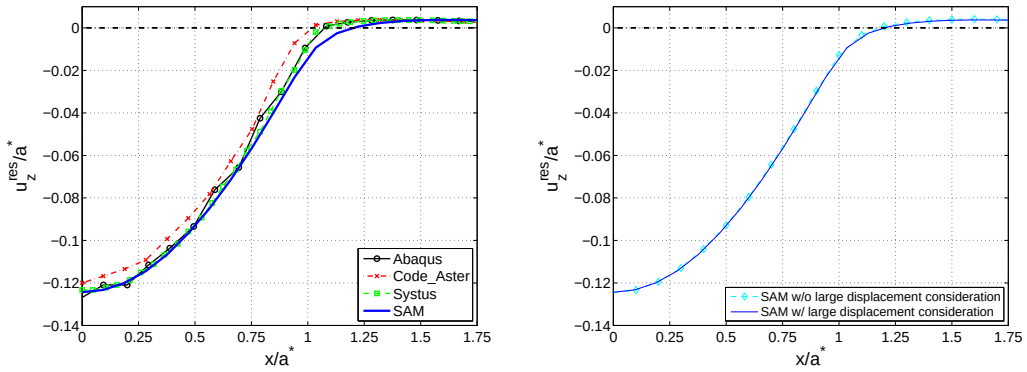

(a) Benchmark results (b) Large displacement effect

Figure 4.1: Residual surface displacement u_z^{res} for the single impact benchmark case. Comparison of several methods (a) (SAM with large displacement effect) and comparison of large displacement effect on SAM results (b).

changes significantly. While it is negative when a purely normal problem is considered, the influence of the modified geometry and thus the adding of shear implies a significant value of plastic strain at the surface of the body, which is predicted by the FEM. The influence of the surface displacement and the angle so generated is quite important here and should be accounted for in the SAM simulations.

Figure 4.4 shows the accumulated plastic strain profiles in the $y = 0$ plane calculated by the SAM with and without large displacement consideration. The shears added by the large displacement consideration generates a reorganization of the plastic strain. The maximum plastic strain level is slightly higher and much more concentrated in a torus located just below the surface under the limits of the contact area.

Residual stresses are a direct consequence of the plastic strain and the final interesting parameter for industrial applications. The residual stress distribution at the center of the impact in Fig. 4.5(a) (the shear components being nil as for the plastic strains) shows a fairly good agreement between all four different methods. The discrepancy between the methods is higher for the stresses than it was for the strains. Once again the zz component is the most sensitive and presents a relatively high discrepancy between all different methods. SAM results are fairly good compared to FEM results. The maximum values and their depths are well reproduced, yet differences appear close to the surface. These differences are not surprising considering the very large difference in contact and stress considerations between the SAM and FEM. Figure 4.5(b) shows the influence of the large displacement consideration. The gap in the zz stress component is relatively low but highly significant for the radial component. The surface value in particular changes significantly when large displacements are considered. An inaccurate estimation of the surface inclination effect can then have large consequences on the residual stresses, especially in the critical subsurface zone. Figure 4.6 shows the same results for the von Mises residual stress. As a direct consequence of the stress terms formerly described,

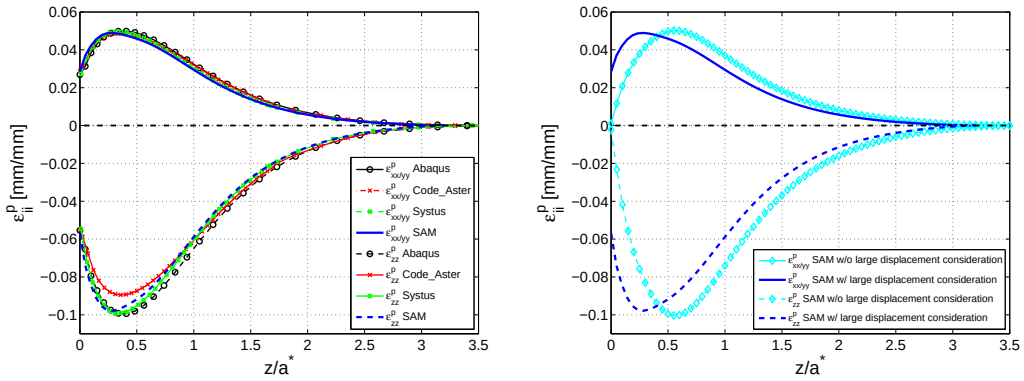

(a) Benchmark results (b) Large displacement effect

Figure 4.2: Plastic strain components ($\varepsilon^p_{xx} = \varepsilon^p_{yy}$ and ε^p_{zz}) along depth z at the center of the contact for the single impact benchmark case. Comparison of several methods (a) (SAM with large displacement effect) and comparison of large displacement effect on SAM results (b).

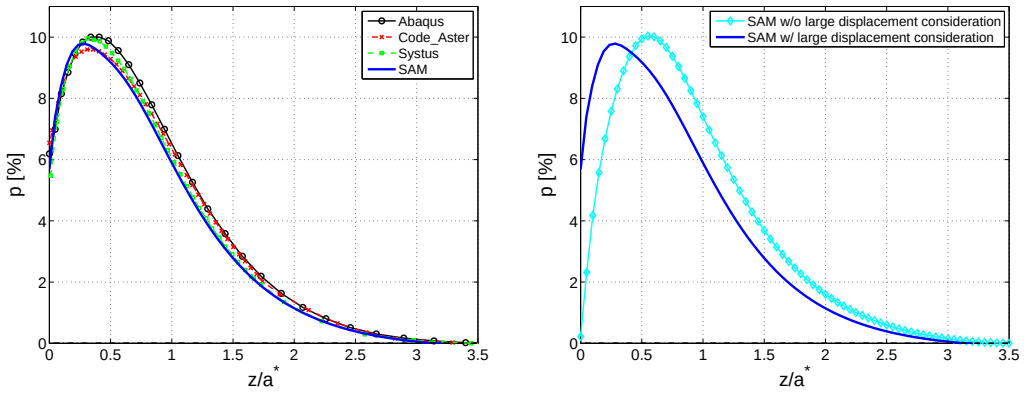

(a) Benchmark results (b) Large displacement effect

Figure 4.3: Accumulated plastic strain p along depth z at the center of the contact for the single impact benchmark case. Comparison of several methods (a) (SAM with large displacement effect) and comparison of large displacement effect on SAM results (b).

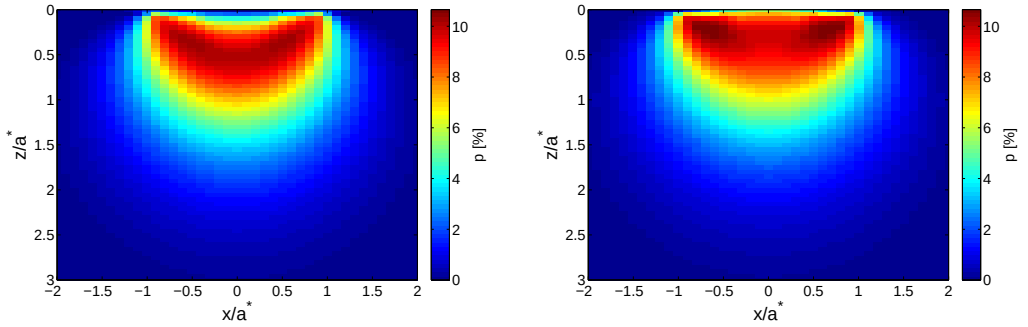

(a) SAM w/o large displacements (b) SAM w/ large displacements

Figure 4.4: Accumulated plastic strain p in the $y = 0$ plane for the single impact benchmark case. SAM results without (a) and with (b) large displacement effect.

the von Mises stress is fairly well reproduced by the SAM. The differences close to the surface cumulate and a gap is noticed between the FEM and the SAM up to a depth equal to $0.5a^*$. Equivalent results without large displacement consideration are significantly different. The evolution of stresses close to the surface is strongly affected by the added shears. The maximum stress value and its depth are also very different. Yet, it can be seem in Fig. 4.7 that the overall stress distribution is not that different between the two methods. Neither are the stress levels. The values at the center of the impact just below the surface are the most affected by the large displacement consideration.

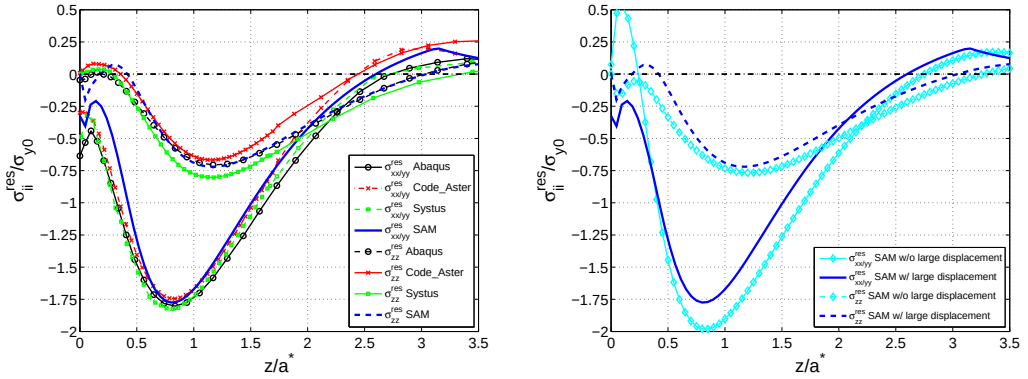

(a) Benchmark results (b) Large displacement effect

Figure 4.5: Residual stress components ($\sigma_{xx}^{res} = \sigma_{yy}^{res}$ and σ_{zz}^{res}) along depth z at the center of the contact for the single impact benchmark case. Comparison of several methods (a) (SAM with large displacement effect) and comparison of large displacement effect on SAM results (b).

At last, Fig. 4.8 shows the residual tensile and compression zones distribution, based on the sign of the residual hydrostatic pressure $p_{hyd}^{res} = (\sigma_{xx}^{res} + \sigma_{yy}^{res} + \sigma_{zz}^{res})/3$. As analysed

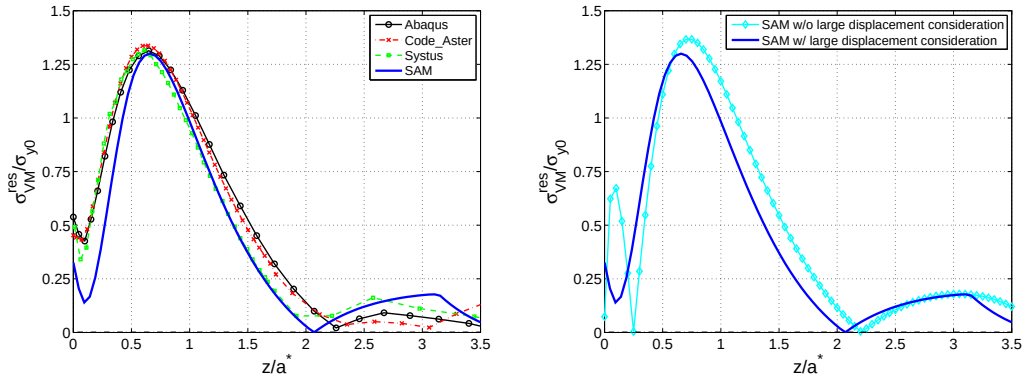

(a) Benchmark results (b) Large displacement effect

Figure 4.6: Residual von Mises stress σ^{res}_{VM} along depth z at the center of the contact for the single impact benchmark case. Comparison of several methods (a) (SAM with large displacement effect) and comparison of large displacement effect on SAM results (b).

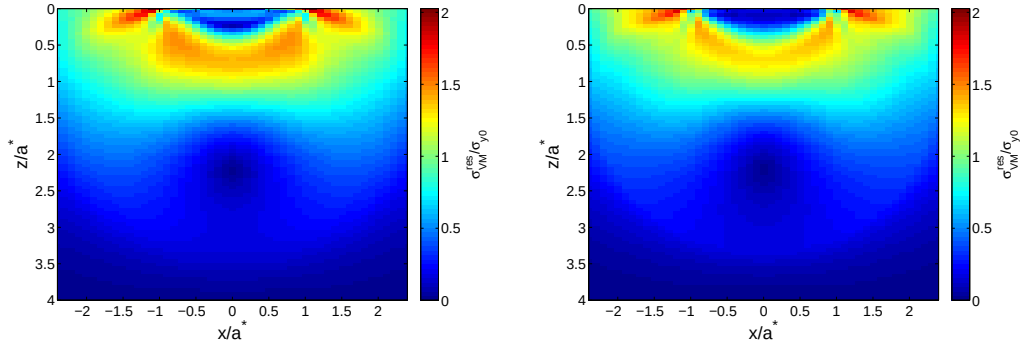

(a) SAM w/o large displacements (b) SAM w/ large displacements

Figure 4.7: Residual von Mises stress σ^{res}_{VM} in the $y = 0$ plane for the single impact benchmark case. SAM results without (a) and with (b) large displacement effect.

before, the residual stress distribution is not largely affected by the large displacement consideration. After one impact, the area below the impact is in compression up to a depth approximately equal to $3a^*$. The depth of this zone reduces with the distance from the center of the impact. The surroundings of this zone endure residual tension. It should be noticed that a very localised torus of tensile zone is observed just around the impact. This zone corresponds to the pile-up in the residual displacement observed at the surface of an impacted material. Interestingly, without large displacement consideration a small tensile zone was determined at the center of the impact that disappears when the surface modification is correctly accounted. This is also an important feature of the large displacement consideration.

It can be expected that the effect of further impacts will delete the surface tensile zone and make the compressive zone uniform. A compressive layer of depth $3a^*$ can be expected as a result from several impact uniformly distributed.

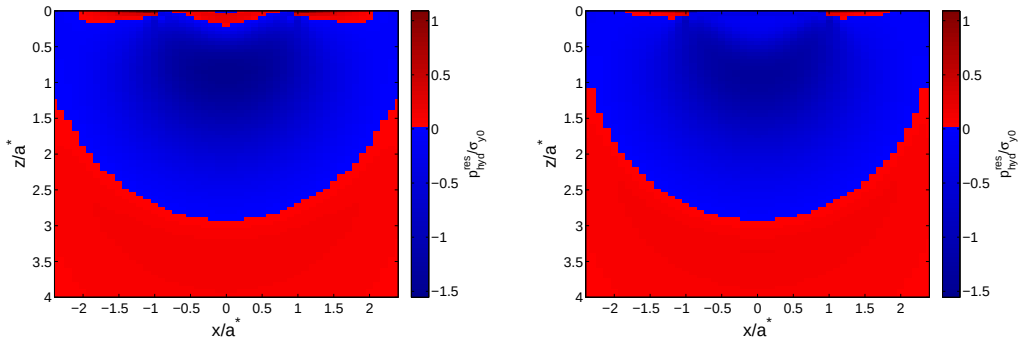

(a) SAM w/o large displacements (b) SAM w/ large displacements

Figure 4.8: Representation of the tensile and compression residual stress zones in the $y = 0$ plane for the single impact benchmark case. SAM results without (a) and with (b) large displacement effect.

4.2.3 Effect of the mesh size on SAM results

Based on the results issued from the benchmark, a study on the effect of the mesh size is done. Simulations with the single impact benchmark parameters are performed with four different meshes. The effect of the large displacement consideration is also observed. The mesh sizes are described by the number of elements along the contact radius a^*. This value ranges from 10 in the benchmark case to 3 in the coarser mesh case.

For all 8 cases, the accumulated plastic strain p and residual von Mises stress are plotted in Figs. 4.9 and 4.10 respectively, at the center of the impact and along the depth axis z. Approximate CPU time (constant whether the large displacement are considered or not) as a function of mesh size are indicated in Tab. 4.3. At last, the coefficient of restitution, defined in Eq. 4.5 is calculated for each simulation. The error between

each result and the reference coefficient of restitution (value for the finer mesh with large displacement consideration) is plotted in Fig. 4.11.

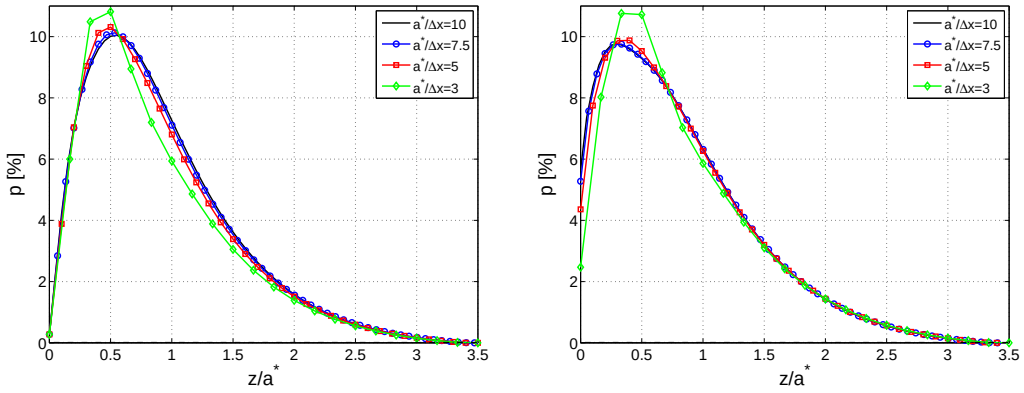

(a) SAM w/o large displacements (b) SAM w/ large displacements

Figure 4.9: Accumulated plastic strain p along depth z at the center of the contact for the single impact benchmark case, evolution of the results with the mesh size Δx. SAM results without (a) and with (b) large displacement effect.

The accumulated plastic strain and residual stress are found almost constant for the two finer mesh cases ($a^*/\Delta x = 10$ and 7.5), this ensures that a critical mesh size has been reached and that the obtained results won't be changed by a further mesh refinement. Results with a relatively coarse mesh (only 5 elements in the contact radius) still present a very good agreement with the benchmark results. Plastic strain profiles at the center of the impact present a negligible difference while the residual von Mises stress differs by less than 6%. For the coarser mesh case, a large difference in the maximum strain and stress level is observed with a rather poor definition of its depth, due to the size of the mesh. The evolution of the stress with the mesh size is more significant than the evolution of strain. A coarse mesh leads to a maximum error of the von Mises residual stress equal to about 20% when large displacement are considered, and up to 35% in the opposite case. This last trend is common to all the results, that is to say that the model without large displacement consideration is a bit more sensitive to the mesh size than the full model (see Figs. 4.9(a) and 4.10(a)). When large displacements are considered, the results distribution is fully reproduced for all mesh sizes, while the coarser mesh results show an important difference in the surface residual stress with the standard model. In all cases, the surface and maximum values are the most modified by the element size, while all intermediate values are fairly well reproduced.

The results on the coefficient of restitution allow a global error consideration. The coefficient of restitution being the ratio of the rebound and initial velocities, it is thus a picture of the kinetic energy of the ball and of the overall energy dissipated (through plasticity) and stored (in residual stresses) in the impacted body. Being a single scalar, it is the most macroscopic indicator of the impact. Results plotted in Fig. 4.11 show

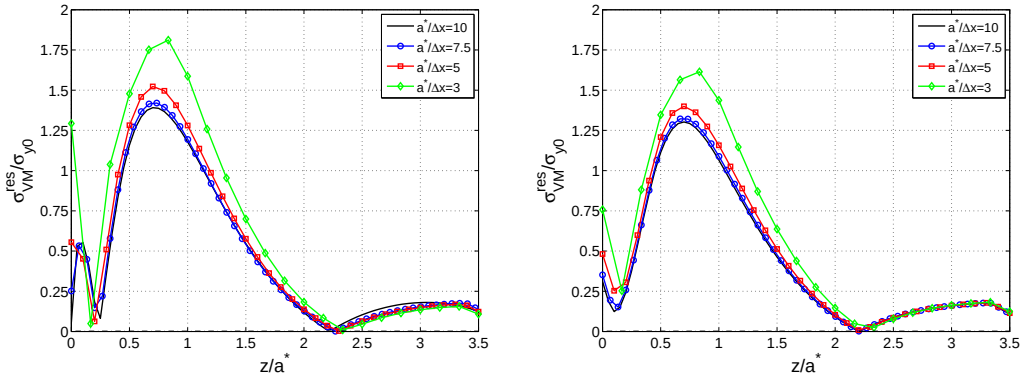

(a) SAM w/o large displacements (b) SAM w/ large displacements

Figure 4.10: Residual von Mises stress σ_{VM}^{res} along depth z at the center of the contact for the single impact benchmark case, evolution of the results with the mesh size Δx. SAM results without (a) and with (b) large displacement effect.

that the coefficient of restitution is not very sensitive to the mesh size. When the large displacements of the surface are considered, the error for the coarser mesh is lower than 2%, thus giving a fair image of the rebound velocity even with a very coarse modelling of the bodies in contact. As for the stresses and strain, the model without large displacement consideration is a bit more sensitive, showing an error reaching 3.5% when the mesh is the coarsest. Still this error is rather low and very coarse meshes can be used when the coefficient of restitution is the observed parameter.

At last, an interesting parameter to look at is the CPU time needed to perform these simulations. The decrease in computation time is very large. It is more or less inversely proportional to the cube of the mesh size (since proportional to the number of elements in the model). It is interesting to notice that relatively coarse meshes can lead to fairly accurate results in a largely reduce CPU time showing here the interest of such sensitivity studies and the velocity of the SAM.

$a^*/\Delta x$	Computation time [min]
10	≈100
7.5	≈45
5	≈15
3	≈10

Table 4.3: Evolution of the CPU time (computation on 3GHz desktop) with the mesh size normalized by the maximum area of contact radius

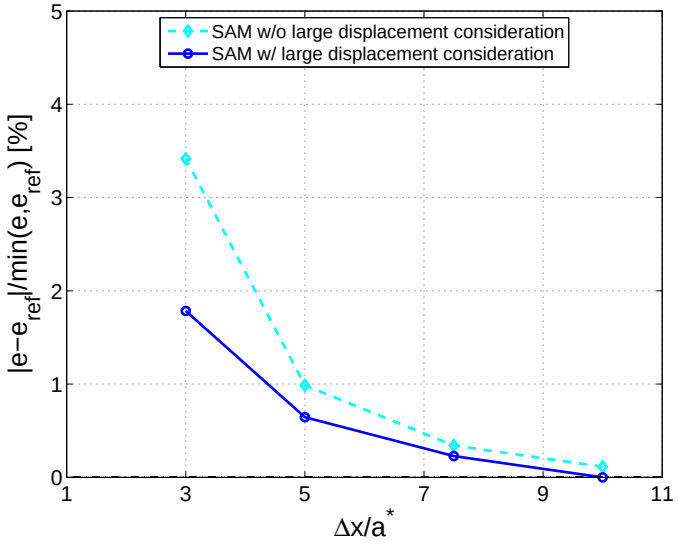

Figure 4.11: Evolution of the error on the coefficient of restitution for an impact with the mesh size Δx normalized by the maximum area of contact radius a^*. Effect of large displacement consideration. The error is measured as the normalized difference with the reference coefficient of restitution e_{ref} measured in the case of the single impact benchmark.

4.3 Effect of the impacting sphere size

Some interesting analytical expressions for impact problems can be derived from the Hertzian theory [JOH 85]. The theory of elastic normal contact between two spheres (here taken to be a sphere and a plane) gives, for any prescribed normal force or displacement, the maximum contact pressure and the contact radius. One may easily find that at the maximum load during impact i.e. when the velocity of the impacting sphere drops to zero, the values of the load, maximum (elastic) contact pressure p_{Hertz}, contact radius a^* and elastic deflection δ^* are given by:

$$F^* = \frac{4}{3}E^*R^2\left(\frac{5}{4}\rho.\pi.\frac{v^2}{E^*}\right)^{\frac{3}{5}} \tag{4.1}$$

$$p_{Hertz} = \frac{2E^*}{\pi}\left(\frac{5}{4}\rho\pi\frac{v^2}{E^*}\right)^{\frac{1}{5}} \tag{4.2}$$

$$\frac{a^*}{R} = \left(\frac{5}{4}\rho\pi\frac{v^2}{E^*}\right)^{\frac{1}{5}} \tag{4.3}$$

$$\frac{\delta^*}{R} = \left(\frac{5}{4}\rho\pi\frac{v^2}{E^*}\right)^{\frac{2}{5}} \tag{4.4}$$

From theses equations, it can be seen that both the maximum rigid body approach δ^* and maximum contact radius a^* are proportional to the radius R of the impacting sphere. Meanwhile, the maximum contact pressure p_{Hertz} is independent of the dimension of the impacting sphere. That is to say, for an impact at a given velocity v, with given material properties, a modification of the impactor's dimensions will only change the scale of the problem, in a proportional manner, but the maximum pressure to which the bodies in contact are subjected during impact will remain the same.

This was proven for the elastic case, simulations performed with the semi-analytical method show that similar behaviour is observed in the elastic-plastic regime. Four simulations have been performed, for each of them the initial velocity of the impacting sphere, as well as all material parameters are kept constant, the radius R of the sphere being the only variable. The simulations are conducted for a reference radius R_{ref} and values of radius equal to $0.5R_{ref}$, $1.5R_{ref}$ and $2R_{ref}$. The accumulated plastic strain profile along depth at the center of the impact is plotted in Fig. 4.12 for each impact.

As in the elastic case, the maximum contact pressure was constant, here the maximum accumulated plastic strain is constant as well. Similarly, it has been shown that in the elastic case, the dimensions of the problem, e.g. the maximum rigid body approach and the area of contact, are scaled by the radius. Here, in the same way, the dimensions of the plastic zone, e.g. both its dimension and the location where the plastic strain is found maximum, are scaled by the sphere radius. So, whenever an impact problem is to be considered, the dimensions should not be an issue, considering that the problem is completely scaled by the radius of the impacting sphere.

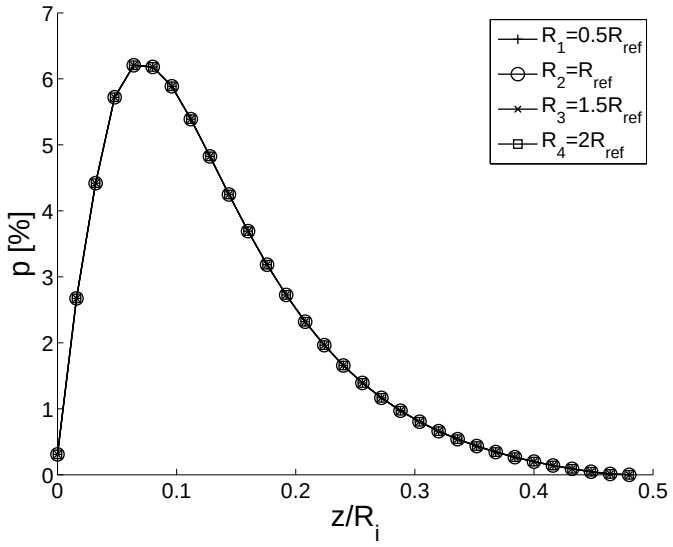

Figure 4.12: Accumulated plastic strain p along depth at the center of the impact $(x,y) = (0,0)$ for several sphere radii R_i

4.4 Predicting the coefficient of restitution

The purpose of this section is to investigate the coefficient of restitution resulting from the impact of a rigid (or elastic) sphere on an elastic-plastic body considering an isotropic hardening. By the use of semi analytical methods, a parametric study of repeated 3D impacts becomes affordable and numerical results will be analysed as well and analytical expressions derived.

In a first approach, the problem is considered to be quasi-static, i.e. no inertial effects are taken into account during computation. It means that the impact velocity should be much lower than the velocity of sound within the studied materials. The validity of this assumption has also been discussed by Johnson [JOH 85] and Yang [YAN 05] and similar conclusions have been reached.

The impact of a rigid sphere on an elastic plastic semi infinite body is here studied. Considering first a single impact, the evolution of the coefficient of restitution with the initial relative velocity as defined by Johnson [JOH 85] is described, validation of the model is made through comparisons with other models and analytical formulae derived. No inertial effects are taken into account. The effect of the hardening law parameters are then studied. Simplified equations are derived to predict the coefficient of restitution versus the dimensionless tangent modulus. That will allow to quickly predict the amount of energy dissipated during a single impact. Extension will be then made to repeated impacts, here again several equations are provided.

4.4.1 Coefficient of restitution for a single impact

4.4.1.1 Comparison with various authors

The accuracy of SAM to simulate the coefficient of restitution resulting from the impact of a rigid or elastic sphere on a semi infinite elastic perfectly plastic body is shown in this section. The coefficient of restitution e is defined as:

$$e = \left| \frac{v_r}{v} \right| \tag{4.5}$$

Johnson [JOH 85] gives an analytical expression for the evaluation of the coefficient of restitution for the impact of a rigid sphere on an elastic perfectly plastic body. Considering that the contact pressure is constant and equal to three times the yield limit σ_y in the fully plastic regime, the force displacement relation is given by:

$$\frac{F}{F_y} = 5.5 \frac{\delta}{\delta_y} \tag{4.6}$$

The rigid body approach, assuming neither sinking nor piling-up occurs, is given by:

$$\delta = \frac{a^2}{2R} \tag{4.7}$$

Under theses assumptions, the coefficient of restitution becomes:

$$e \simeq 3.8 \left(\frac{\sigma_y}{E^*} \right)^{\frac{1}{2}} \left(\frac{1}{2} \frac{mv^2}{\sigma_y R^3} \right)^{\frac{-1}{8}} \tag{4.8}$$

This equation suggests that for fully plastic regime the coefficient of restitution is proportional to $v^{-1/4}$. Thornton and Ning [THO 98] provided a similar equation for the coefficient of restitution considering initial velocity v at least 10 times higher than the yield velocity v_y at which plasticity appears, the coefficient of restitution can then be expressed as follows:

$$e = 1.185 \left(\frac{v_y}{v} \right)^{\frac{1}{4}} \tag{4.9}$$

The yield velocity v_y being, in the case of a sphere impacting a half-space, expressed as:

$$v_y = \sqrt{\frac{26\sigma_y^5}{\rho E^{*4}}} \tag{4.10}$$

It is interesting to note that this velocity is independent of the radius of the impacting sphere. Note also that the coefficient of restitution provided by Eq. 4.9 does not tend to unity when the initial velocity v approaches the yield velocity v_y. Indeed, this is an approximated expression for the coefficient of restitution, considering that v is significantly higher than v_y. For more details the reader may refer to [THO 98]. Note also that this

representation accounts for a fully plastic impact. On the contrary, for values of velocity close to the onset of plasticity, the elastic part plays an important role and this formulation is no more valid. Jackson et al. [JAC 10] provided two sets of equations to describe the evolution of the coefficient of restitution. These equations are defined for specified ranges of yield strain $\varepsilon_y = \sigma_y/E$ and Poisson's ratio ν which correspond to the values used in this paper. A different definition of the yield velocity is used in these equations, however in the current range of application this difference is negligible, being lower than 2.5%. Using the residual interference after impact as defined by Etsion et al. [ETS 05], Jackson et al. predict the evolution of the coefficient of restitution as defined in Eq. 4.11. However this equation is limited to relatively low velocity, up to $1000v_y$. Such a range of velocity is often too low compared to those encountered in shoot peening processes. Note that other models have been proposed in the literature, see for example Wu et al. [WU 03].

$$e = 1 - 0.0361\,(\varepsilon_y)^{-0.114}\, ln\left(\frac{v}{v_y}\right)\left(\frac{v}{v_y} - 1\right)^{9.5\varepsilon_y} \tag{4.11}$$

Several simulations are now performed using the semi-analytical method for various initial velocities and the coefficient of restitution derived. Results are plotted in Fig. 4.13 showing the coefficient of restitution e as a function of the initial velocity v normalized by the yield velocity v_y. The analytical solutions from Johnson [JOH 85] and Thornton and Ning [THO 98] are plotted as well. As it can be seen, the results provided by the semi-analytical method are close to the Johnson's results, whereas the Thornton's solution, due to a different force displacement relation predicts lower values of the coefficient of restitution. The difference between the analytical solution of Johnson and the numerical results based on SAM is attributed to the pressure distribution which differs notably. It leads to different contact stiffness at very high plasticity levels. The difference between the Thornton and Ning analytical solution and the present SAM numerical results is attributed to the fact that the former seems to consider implicitly two identical elastic-plastic bodies in contact whereas here as well as in the Johnson's solution only one of the two bodies behaves elastic-plastic.

Zhang and Vu-Quoc [ZHA 02] performed FEM simulations to estimate the coefficient of restitution, but in a range of lower impact velocities compared to the yield velocity. Their FE results are plotted in Fig. 4.14 as well as the Thornton's and Johnson's analytical solutions along with the results by SAM for a lower range of velocity. The Jackson solution as described in Eq. 4.11 is also provided. A very good agreement between FE, half-numerical half-analytical solution of Jackson et al. and SAM numerical results is observed. This prove that SAM is efficient to predict elastic-plastic impact in a wide range of velocity, as far as inertia effects can be neglected.

Based on Eq. 4.11, a master curve has been derived from curve-fit of the analytical results with the present model assuming an elastic perfectly-plastic material. The coefficients of this equation 4.12, given in Table 4.4, differ slightly from those proposed by Jackson et al.. Note that these results were fitted on a range of velocity about 3.5 times higher than the one used by Jackson et al.. They proposed equations for velocities up to

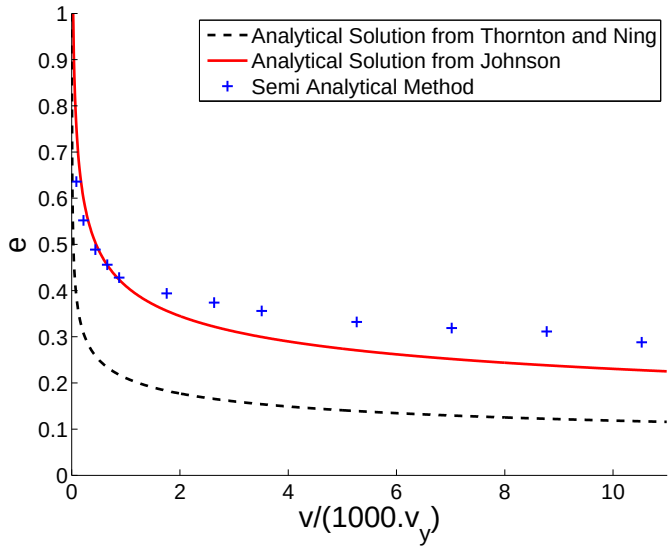

Figure 4.13: Coefficient of restitution e as a function of normalized velocity v/v_y for elastic perfectly plastic impacts: Comparison of semi-analytical results and analytical solutions from Johnson [JOH 85] and Thornton and Ning [THO 98]

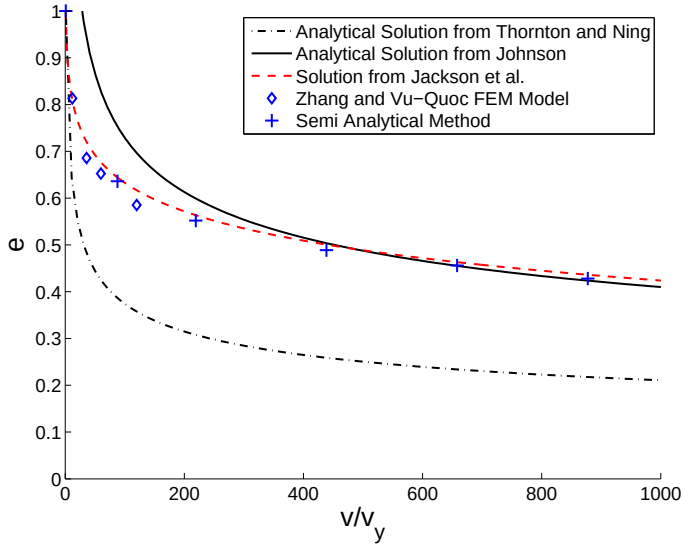

Figure 4.14: Coefficient of restitution e as a function of normalized velocity v/v_y for elastic perfectly plastic impacts: Comparison of semi-analytical results, analytical solutions from Johnson [JOH 85] and Thornton and Ning [THO 98], equation by Jackson et al. [JAC 10], and FEM results from Zhang and Vu-Quoc [ZHA 02]

$1000v_y$ as plotted in fig. 4.14 while the SAM results are presented for results reaching $3500v_y$, see fig. 4.15. The slight difference between the two solutions is attributed to the methods: the method proposed by Jackson et al. combines FEM results and analytical expressions whereas the present investigation is fully numerical based on SAM. The fitted curve of SAM results and the raw numerical results show an average difference of 4.7% with a maximum of 11.1%, as seen in Fig. 4.15.

4.4.1.2 Effect of large isotropic hardening

The analysis is now extended to elastic-plastic materials with a linear isotropic behaviour and different dimensionless tangent modulus E_T/E ranging from 5% to 80%. A master equation in the form of Eq. 4.12 can be derived for each ratio between the hardening slope and the Young modulus. A set of parameter f_{e1}, f_{e2} and f_{e3} can be estimated for each material, see Table 4.4. Finally a general expression is proposed in the form of Eq. 4.13 for a quick estimation of the restitution coefficient. The results of Eq. 4.12 are plotted in dash lines in Fig. 4.15. The approximation provided by Eq. 4.13 corresponds to the full line curves, with the constants a_{eij} given in Table 4.5. The results from this second set of equations show an average difference of 2.9% with the SAM results, with a maximum of 11.1%, over a wide range of impact velocity ranging from 1 to 3500 times the yield velocity.

$$e \simeq 1 - f_{e1}\,(\varepsilon_y)^{f_{e2}}\, ln\left(\frac{v}{v_y}\right)\left(\frac{v}{v_y} - 1\right)^{f_{e3}\varepsilon_y} \tag{4.12}$$

E_T/E	f_{e1}	f_{e2}	f_{e3}
0	0.0347	−0.114	8.8224
0.05	0.0306	−0.114	8.6554
0.1	0.0273	−0.114	8.5150
0.2	0.0219	−0.114	8.4741
0.4	0.0143	−0.114	8.3205
0.6	0.0085	−0.114	8.2962
0.8	0.0039	−0.114	8.3043

Table 4.4: Curve-fitted parameters for the expression of the coefficient of restitution by Eq. 4.12 for various dimensionless tangent moduli

$$f_{e1} = a_{e11}\left(\frac{E_T}{E}\right)^2 + a_{e12}\frac{E_T}{E} + a_{e13} \tag{4.13a}$$

$$f_{e3} = a_{e31}\left(\frac{E_T}{E}\right)^2 + a_{e32}\frac{E_T}{E} + a_{e33} \tag{4.13b}$$

It is graphically shown in Fig. 4.15 that the restitution coefficient increases with the tangent modulus and decreases with the impact velocity. These two trends could be explained by the contribution of plasticity. An increase of the kinetic energy leads to more energy dissipated by plasticity, resulting in lower rebound kinematic energy and velocity. Conversely a behaviour with higher hardening contributes to lower plastic strain which in turn increases the coefficient of restitution and then the rebound velocity.

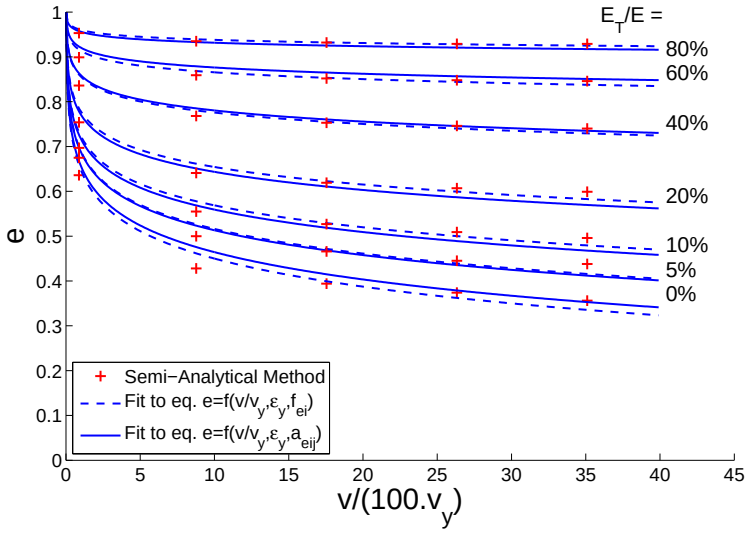

Figure 4.15: Evolution of the coefficient of restitution as the function of normalized initial velocity for different hardening laws with best fit to Eqs. 4.12 and 4.13

Parameters in Eq. 4.13	
a_{e11}	0.0321
a_{e12}	-0.0626
a_{e13}	0.0338
a_{e31}	1.4371
a_{e32}	-1.6811
a_{e33}	8.7514

Table 4.5: Curve-fitted parameters for the expression of the coefficient of restitution by Eq. 4.13

4.4.2 Coefficient of restitution for multiple impacts

4.4.2.1 Coefficient of restitution for repeated impacts

The study is here extended to repeated impacts. It is important to notice that repeated impacts have here the same initial velocity v which is representative of cases such as shot-peening but differs from the free rebound of a sphere on a semi infinite body. Various studies of repeated impacts show that after a given number of impacts the coefficient of restitution tends to a fixed value. This asymptotic value is equal to 1 in cases where dissipation through inertial effects can be neglected. This is explained by the fact that, after some repeated impact, a steady-state regime is reached and the behaviour becomes fully elastic. Therefore the whole initial kinetic energy is restored to the impacting sphere [WEI 05] during its rebound. When inertial effects play an important role, the saturation value differs from 1 depending on the amount of dissipated energy as can be seen in [SEI 05] or [MIN 10]. The global evolution of the coefficient of restitution is similar, tending more or less rapidly to an asymptotic value depending on the initial velocity of the sphere and the yield velocity of the body.

Weir and Tallon [WEI 05] proposed an analytical expression, see Eq. 4.14, to determine the coefficient of restitution e_n of the n-th impact of an elastic or rigid sphere on an elastic perfectly plastic sphere as a function of the coefficient of restitution of the former impact e_{n-1}. This equation takes into account the so-called seismic dissipation i.e. the inertial effects, represented by the term v/c_0 where c_0 is the wave velocity in the body. While neglecting the effect of wave dissipation this equation fits well the semi-analytical results.

Weir and Tallon proposed another expression giving the coefficient of restitution of n-th impact directly as a function of the coefficient of restitution of the first impact e_1 if inertial dissipation is neglected. This expression, provided in Eq. 4.15, allows to calculate directly the coefficient of restitution for any impact number and to estimate the number of impacts to saturation, which here logically occurs for $e = 1$. In this equation, the exponent $8/3$ comes from the analytical force-displacement relation for the contact of elastic-perfectly plastic bodies.

An extension of this formula is proposed here, thus adapting this exponent when the plastic behaviour is no more perfectly plastic but with linear isotropic hardening. This gives the relation provided in Eq. 4.16 where the exponent f_m depends linearly on the dimensionless tangential modulus E_T/E as shown in Eq. 4.17 with coefficients given in Table 4.6. Several simulations have been performed with tangent modulus ranging from 0 to 50% of the elastic modulus. The initial velocity v is taken equal to $10m/s$ which here corresponds to approximately 1750 times the yield velocity v_y. Semi analytical results as well as results from Eqs. 4.16 and 4.17 are presented in Fig. 4.16.

$$e_n^{\frac{8}{3}} = e_{n-1}^{\frac{8}{3}} + e_1^{\frac{8}{3}} \left(1 - 2.7 \left(\frac{v}{c_0} \right)^{\frac{3}{5}} - e_n^2 \right) \tag{4.14}$$

$$1-e_n^{\frac{8}{3}} \simeq \left(1-e_1^{\frac{8}{3}}\right) exp\left(-(n-1)\,e_1^{\frac{8}{3}}\right) \tag{4.15}$$

$$1-e_n^{f_m} \simeq \left(1-e_1^{f_m}\right) exp\left(-(n-1)\,e_1^{f_m}\right) \tag{4.16}$$

$$f_m = a_{f1}\frac{E_T}{E} + a_{f2} \tag{4.17}$$

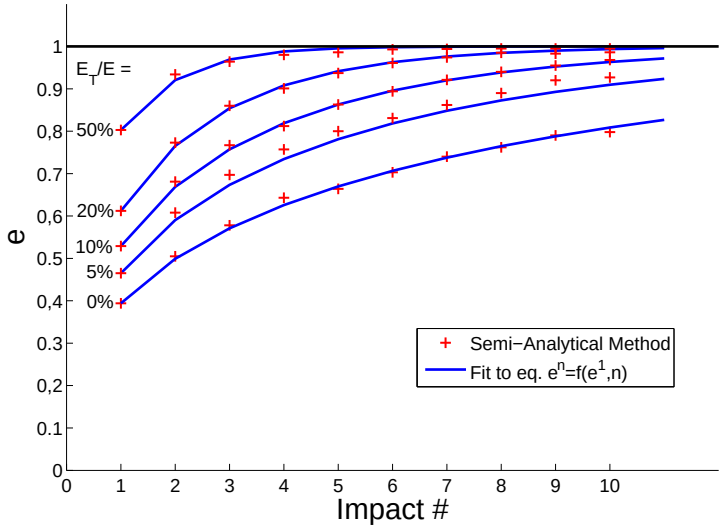

Figure 4.16: Evolution of the coefficient of restitution as the function of the number of impacts for different hardening laws with best fit to Eq. 4.12

The semi analytical results and fitted results show a remarkable correlation with an average difference of 1.3% with a maximum of 5.9%. The number of impacts to saturation decreases with the isotropic tangent modulus. Indeed, the higher the tangent modulus, the more plasticity occurs at each impact reaching faster a stabilized state. For low values of hardening, or without hardening, the steady state regime requires more impacts to be reached. It could be explained by the fact that, for low hardening, more plastic flow occurs during each impact producing also spreading of the plastic zone.

4.4.2.2 Coefficient of restitution for translated impacts

The coefficient of restitution for a first impact can be predicted as a function of material parameters and impact velocity. Formulae allow to predict the coefficient of restitution for repeated impacts. A last study is proposed here, considering a second impact occurring

Parameters in Eq. 4.17	
a_{m1}	-5.016
a_{m2}	8/3

Table 4.6: Curve-fitted parameters for the expression of the coefficient of restitution for repeated impacts by Eq. 4.17

at a different position than the center of the first impact. Here again, the initial impact velocity is considered constant. The impacted body is considered elastic perfectly plastic and distances are normalized by the contact radius of the first impact a^*. Several "second" impacts are simulated at different distances from the first center of impact, denoted by the distance x from the center of the first impact. The objective here is to provide insights on the behaviour of impacts between the two limit cases that are repeated impacts and impacts on a virgin surface.

Results are presented in Fig. 4.17. The normal residual displacement u_z^{res} and the subsurface accumulated strain profile are depicted in the same figure for understanding purposes. An increase (up to 25%) of the coefficient of restitution between the first and second impact is observed for low values of x (typically below a^*). The value of the coefficient of restitution e_2 for the second impact then decreases slightly (by up to 4%) and logically tends to the value of e_1 as x increases and the impacted body gets closer to a virgin surface.

The evolution of the coefficient of restitution can be linked to the value of the residual displacement, that is itself a direct consequence of the plastic strain profile. The coefficient of restitution increases when the second impact occurs in an area with negative residual displacement and decreases when the residual displacement on the impacted point is positive. The trends are similar, although no clear link between the two values can be established. This evolution is clearly consistent with the subsurface plastic strain distribution and the value of the coefficient of restitution can be linked to the amount of plastic work that remains to be done in the impacted area before elastic shakedown. Furthermore, in this case, only the value of the residual displacement along the radius was observed. An averaged value of the residual displacement over the expected contact area of the second impact might provide a more direct link to the evolution of the coefficient of restitution.

4.5 Conclusions

This chapter showed the capability of the SAM to simulate single impacts at high strain levels. Taking into account the large displacements of the surfaces in contact, results of excellent quality were obtained and validated through comparison with FEM results. It is to notice that the method is rather unstable at these strain levels. A significant sensitivity to the convergence parameters (error thresholds and relaxation coefficients mainly) was

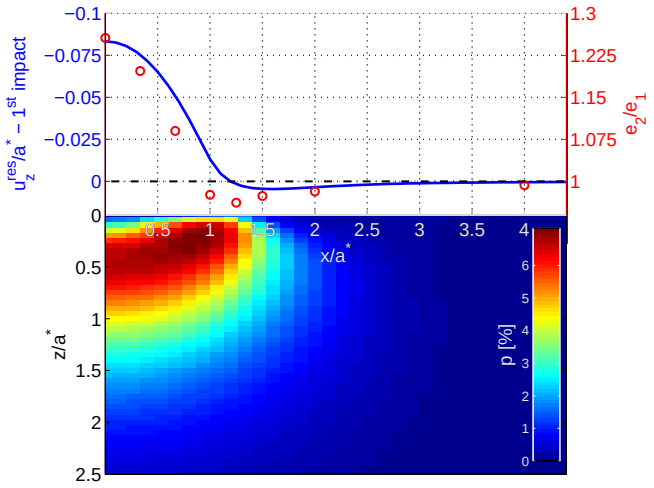

Figure 4.17: Evolution of the coefficient of restitution e_2 for a second impact as a function of the distance with the first impact, value normalized by the coefficient of restitution of the first impact e_1, both impacts with same initial velocities. Superimposition with the normal residual displacement u_z^{res} and accumulated plastic strain p generated by the first impact.

observed. The method has thus be proven potentially efficient but its robustness can be improved. These instabilities are most certainly linked to the strain calculation. In the current method, the compatibility of the strain field is not ensured during the computation which may be the source of instabilities when the plastic strain levels involved become relatively high. Furthermore, a slight gap was observed on the residual displacement field issued from the SAM and the FEM in the region of pile-up. Further investigation on this phenomena should be necessary.

Computation velocity of the method was studied, along with the effect of the mesh size. For a single impact, fairly good results are obtained even with relatively coarse meshes. Three dimensional impact simulations can be performed in reduced time, typically less than a half hour while conserving an excellent quality of results. Less computation time can even be obtained for the observation of macroscopic parameters like the coefficient of restitution. The current computations were performed on a single processor so even lower computation times can be expected with upcoming parallelization of the method.

A large focus was made on the study of the coefficient of restitution. Formulae were provided to predict the coefficient of restitution resulting from the impact of an elastic sphere over a semi infinite body. These formulae account for the material parameters, the initial velocity and potential isotropic hardening of the impacted body. The establishment of formulae for repeated impacts brings equations to consider multiple impacts occurring at the same point. Insights to consider the evolution of the coefficient of restitution when

impacts occur between two limit cases that are repeated impacts and impacts on virgin surfaces are given. Computational velocity of the method might allow to determine simple empirical models for any situation and thus evaluate the coefficients of restitution for more complicated engineering problems, like the simulation of ultrasonic shot peening.

Single Impact experiments

This chapter presents experimental results of single impacts on three different materials. An impact device was used to throw ceramic balls at velocities ranging from 20 to 40m/s. Coefficients of restitution are measured and compared with analytical expressions. A measurement of the impacts dimensions is made both with a contact profilometer and via digital image stereo correlation. A comparison with simulation results is made and extended to a comparison of residual surface strain with stereo correlation results.

Contents

5.1 Introduction

The development of new methods implies to put in place validations to ensure the quality of the results. Three possibilities are then available when developing a computation code: (i) compare results to analytical solutions in a known case, (ii) compare a test case to results from other validated computation codes and (iii) compare computation results to experiments.

A comparison of the semi analytical method results with analytical solutions has been made in the very simple case of an elastic case. It is obvious that this case validation is insufficient since it does not imply the effect of plasticity. This effect can be very critical but no satisfactory analytical solutions exist for the case of impact considering plasticity.

A benchmark was performed with two different Finite Elements codes on a test case. Obtained results were rather satisfactory and the test case parameters matched common industrial applications. This allowed to guarantee the quality of the semi analytical method for the simulation of impacts. Certain hypotheses were assumed for the different models such as frictionless contact and no inertial or viscous effects. Finally numerical simulations will be compared to the results of single impact experiments.

Several kinds of experimental set-ups exist to generate single impacts. Dropping balls from a high height shows very simple to execute but the impact velocity obtained is extremely limited. Simple pendulum-type devices exists and can produce impacts reaching 4 or $5 m/s$ [SEI 10, MIN 10]. Higher velocities can be reached using air guns. Minamoto and Kawamura [MIN 11] produced impacts with velocities reaching $20 m/s$ to study coefficients of restitution resulting from the impact of two identical spheres. These velocities correspond clearly to the range of velocity of peening processes. Impact at higher velocities will come to the field of ballistics or high velocity processes like cold spray for which the projectile is very strongly deformed. In the case of shot peening the impactor hardness compared to the one of the impacted surface and the range of velocity are such that the deformation of the projectile is negligible or at least lower than that of the impacted surface. Air guns set-ups look then like a good choice to perform impact experiments.

The laboratory *Mécasurf* located at the AMPT in Aix-en-Provence, France, developed an air gun type set-up being able to produce impacts ranging from about 10 to $40 m/s$ with shots of radii up to $12 mm$. Experimentations were performed in collaboration with this laboratory and the results will be compared to those of the semi analytical impact model.

The aim of these experiments was to produce experimental results to validate the model. It is then necessary to perform impacts under controlled or at least known conditions to feed numerical simulations and to extract results from these experiments able to confirm the validity of the corresponding numerical results.

The difficulty of knowledge of the experimental conditions remains in two main characteristics: the impact velocity and the impacted material behaviour. The balls were Si_3N_4 ceramic balls which elastic properties are known and their yield limit is high enough so that their behaviour during impact is purely elastic. Furthermore, this hypothesis can be checked afterwards.

The impact velocity is probably the most critical parameter needed to perform realistic simulations corresponding to experiments. The impact velocity measurements were performed by two methods. Laser barriers were put on the ball's trajectory to obtain a first measure of the impact initial velocity. Secondly, a high speed camera was used to film the impacts thus being able to measure both the initial and rebound velocity of the ball. An evaluation of the impacts initial and rebound angle is also possible this way. Several experimental problems led unfortunately to rather poor velocity measurements. Nevertheless, coefficient of restitution measurements were performed for several impacts.

The knowledge of the elastic and hardening behaviours of the impacted materials is also of very high importance for the experimental validation. Three materials were chosen for the experiments:

- An aluminium alloy 7010 (AA 7010). This material was available in great quantities for preliminary tests and its hardening behaviour was first assumed to be known. It was later suspected that the initially assumed stress-strain curve did not correspond to the real response due to ageing of this material. The results will however be presented since trends have been found coherent with what was expected.

- A stainless steel 316L. A large number of experimental data of the hardening behaviour under cyclic and monotonic loading of this specific casting are available. Thus data for this material also exist for the behaviour at high strain rate and elevated temperatures. This material was thus chosen for the interesting insights it could provide for a finer modelling of impacts.

- An Inconel 600 nickel alloy. This material is used for the industrial application of the collaborative PhD by Li [LI 11] The hardening behaviour of this material can present large differences from one casting to another and only monotonic tensile curves data were available for the specific casting. Cyclic experiments were specifically performed to identify its hardening behaviour. Indentation results, see chapter 3 and simple analytical considerations showed that the kinematic part of hardening plays only a minor role for indentation and in extension for single impacts. However a thorough full identification of the cyclic response has been found useful for the simulation of multiple impacts presented later in chapter 6. Experimental results along with hardening law identification are given in appendix B.

The choice of experimental data to correlate with numerical results is of great importance. The measurement of the surface profile after impact is relatively easy to perform and will be used first. The surface profiles were measured using two methods: a classical contact profilometer and optical stereo correlation method. The aim being to validate stereo correlation results through profiles obtained through contact. Full impact profiles, including impact radius and maximum depth of the imprint can be done. This measure might prove insufficient. The surfaces profiles are only a two dimensional post impact data, they provide rather poor information upon the complexity of the subsurface three dimensional elastic plastic contact problem. Numerical simulations showed that the sur-

face geometry post impact is not highly sensitive to several parameters or approximation in the modelling.

Stereo correlation measures were thus used. Combining pre and post impact measures, it is possible to measure the surface residual strain profiles and consequently extend the quality of comparisons. These measurements were proven difficult by the highly traumatic loading applied on the samples that causes difficulties for the correlation measures themselves and speckle generation necessary for the measures. The small dimensions of impacts (about 2*mm* in radius), limited by the capability of the experimental impact device, also made the measurements difficult. The correlation material had to be used to its maximum capability and a rather poor representation of the large gradients in the impacted surface has been obtained.

Other experimental measures are in sight though not performed. Residual stresses measures, performed a priori by x-ray diffraction, might be performed at the surface and in depth of the samples. The residual stress shows as the perfect parameter to analyse the results of subsurface plastic phenomena. These measures would prove rather difficult due to the very high gradients involved in very limited size areas compared to the measurement zones. Micro graphic analysis and nano indentation tests, to characterize the materials changes during impact and the plastic zone expense were also considered.

The experimental devices will first be presented. A quick explanation on the stereo correlation device is made. The measurement difficulties and actual capabilities of the final set-up are presented along with their impact on the experimental results. The impact set-up is then described. It should be here recalled that the design and fabrication of this set-up was not part of this work. The mechanism is presented along with its capabilities and drawbacks in the actual version. The device these experiments have been made on is a first version and several improvements are in process.

The final plan of experiments comes next. The range of velocities studied, impact angle, choice of balls, impacted materials and dimensions of the samples are presented. Part of the experimental results won't actually be analysed but are here presented as an opening to future analysis.
Three different materials were impacted. A presentation of the hardening behaviour of these materials is made in section 5.3. The choice of hardening laws to simulated these behaviours is discussed in the corresponding section.

The whole experimental results are finally presented. Starting with the basic macroscopic measure of the coefficient of restitution, a first comparison is made with the empirical laws developed for the coefficient of restitution accounting for the hardening of the material in chapter 4. The dimensions of the impacts are then analysed. A focus is made on the residual imprint depth and radius and comparisons between profilometer and stereo correlation measures are made. A comparison with numerical results is performed on some representative cases and basic tendencies in the evolution of an impact dimension with the velocity are observed. Finally, the contribution of the stereo correlation is exploited through the analysis of the residual strain measures at the surface of the impacted materials. Once again, comparisons are made with numerical results.

At last, a large part is dedicated to openings regarding these experiments and future extended exploitation of the results.

5.2 Experimental procedure

5.2.1 Experimental set-up

5.2.1.1 Stereo-Correlation set-up

Digital image correlation is nowadays a classical experimental technique for the measurement of shapes, displacement or strains [SUT 09]. It allows to measure a sample's dimensions without physical contact and the technique is extended to the measure of strain fields. The basic principle of the method lies in the recognition of patterns drawn on the sample. The principle is similar to the grid method but the randomness of the patterns brings a higher precision in correlation. Furthermore the random pattern has the advantage to deliver results independent of a given reference coordinate system. The use of one camera allows then to monitor the positions of points of the sample's surface and follow their displacements in a plane perpendicular to the camera's axis. Post-treatment of the obtained displacement field allows to determine the corresponding strain (and stress if elastic) fields.

The use of a second camera, called stereo correlation, offers the possibility to follow the displacement of the surface's points in all three spatial dimensions and, by taking several pictures during an experiment, in the time dimension as well. Results obtained by stereo correlation are then similar to profilometer measures except that the history of displacements, and strains, of any point of the surface is known through all the experiment. Yet this full measure implies the capability of taking picture with a correctly calibrated correlation system throughout the experiment.

Stereo correlation was used for these measurements to obtain a three dimensional profile of the impacts and the residual surface strain fields. Only two pairs of pictures are taken for each impact, one before and one after the impact. Two major problems were encountered for these measurements: first the realization of speckle that would withstand the impact of the sphere and still be exploitable on the post impact pictures and secondly to produce pictures of sufficiently high definition to be able to capture the high displacement and strain gradients within and around the impact area.

A speckle pattern for stereo correlation will prove efficient if: (i) the speckle size is coherent with the pixel size of the cameras taking the pictures and (ii) a sufficient contrast exists between the speckles and the background of the sample. The use of classical black speckles on white painting background is inappropriate for two reasons. The background painting thickness is difficult to control and considering the reduced depth of material having an effect on the rebound behaviour, the actual effect of the painting on the impact behaviour is hard to quantify. Furthermore, a full painting coat usually endures badly the impact and in the best cases, all painting is removed from the impact crater. Meanwhile, in the worst cases, a full patch of painting is torn down by the energy of the impact.

This behaviour depends highly on the quality of the painting and the freshness of the coat. These problems are solved by first sandblasting the surface with particles small enough to produce a roughness compared to the impact dimensions that it won't affect its behaviour. This produces a grey surface that does not reflect light. A black painting speckle is then applied to the surface to produce the patterns. The contrast between the background and the surface is not as good as with classical white painting background but all-sufficient for correlation if the lighting of the surface is powerful. The roughness of the surfaces produces small craters for the painting. The integrity of the pattern is then fully conserved during the impact, at least at the studied impact velocities. A picture of one sample is shown in Fig. 5.1 before and after impact.

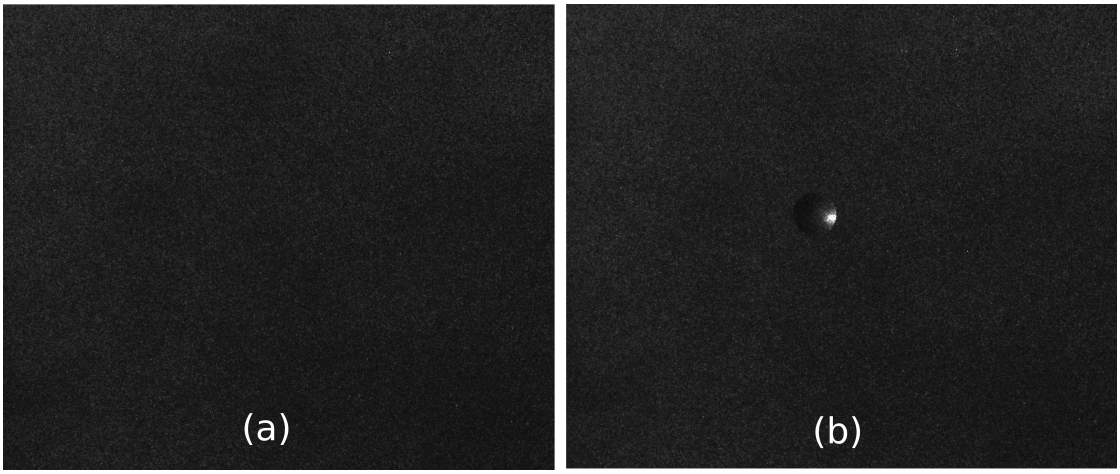

Figure 5.1: Stainless steel sample Ix09 before (a) and after (b) impact. Conservation of speckle integrity.

As explained before, the quality of pictures is crucial for the quality of the correlation results. Two cameras of definition 4872×3248 pixels were used. The large definition of these cameras authorized catching a picture of the full sample and ensuring that the impact position will be captured, independently of the precision of the impacting device. Lenses with a large opening were chosen to get the maximum exposure of the picture. The problem is to ensure both the sharpness of the whole picture and its brightness. The opening of the lenses allows to increase the brightness but at the same time it reduces the depth of field. The opening is thus chosen as the maximal value for which the full picture is sharp. A rather long shutter speed is selected to increase the brightness of the picture but reasonable. At last, a very powerful lighting is provided by two sets of bright white LEDs.

The picture results were not fully satisfactory for several reasons, despite the optimization of the set-up. The position of the lenses in relation to the sample has a direct influence on the magnification of the pictures and so on the accuracy of the results. This

parameter was limited by the cluttering of the material and is finally not fully adapted to the needs of these experiments. A satisfactory brightness was obtained but the impact creates a reflecting area in the crater. The post impact picture thus present very high brightness changes in localized area (see Fig. 5.1). Correlation is impossible in these areas and large parts of data are consequently missing. Finally, the sandblast of the surface, absolutely necessary for these measurements, has the drawback to create bright points. The exact position of these points can differ slightly in the pictures before and after impact and so generate errors in the measurements that are not accounted by the correlation software. Despite these drawbacks, satisfactory measures were made and an interesting insight through the capability of stereo correlation measures in impact experimentation was made. The stereo correlation set-up is presented in Fig. 5.2. The whole set-up is fixed on an optical table to avoid vibrations and relative movement of the elements between each picture. Indeed, stereo correlation measures and impact experiments were performed in different locations.

Figure 5.2: Stereo correlation set-up - Sample holding and positioning system, lenses, cameras and LEDs racks.

The correlation picture are post treated with the digital image correlation commercial software VIC-3D ©.

5.2.1.2 Impact set-up

Impact experiments were performed on an air gun system. This set-up was designed and manufacture by the laboratory *Mécasurf*. Experiments were made in collaboration with this laboratory. This set-up allows to shoot balls of diameter ranging from a few millimetres up to around $12mm$ in diameter at velocities typically ranging from $15m/s$ to $45m/s$. Normal and tangential impacts can be made by tilting the sample. The device is presented in Figs. 5.3 and 5.4.

Energy is brought to the ball by compressed air. The air is stocked in a tank and brought to the needed pressure. The air pressure in the tank is the actual monitored parameter that will determine the impact velocity. The impact is triggered by the opening of the solenoid valve of the tank. The compressed air is guided to a piston. The ball stands on conical hourglass shape shell. The diameter of the shell is equal to the inside diameter of the piston to limit air leaks during the impact. The compressed air propels the shell and the ball. The first one is stopped by shock absorbers at the end of the piston while the balls continues and hits the sample. Laser barriers are mounted at the output of the piston to measure the velocity of the ball. The sample is mounted close to the piston's end (about 20*cm*) to limit the deceleration of the ball between the measure and the impact. This measure also helps to limit the dispersion in the impact position.

Figure 5.3: Air gun impact set-up from the laboratory *Mécasurf*. Laser barriers are not assembled on the photography.

The impact velocity is driven by the air pressure in tank. The lower limit is fixed by the minimum amount of energy needed to actually put the shell in motion (the mass of the ball being negligible in comparison). The upper velocity limit is governed by the friction between the shell and the tube that is not measured and causes a great dispersion in the

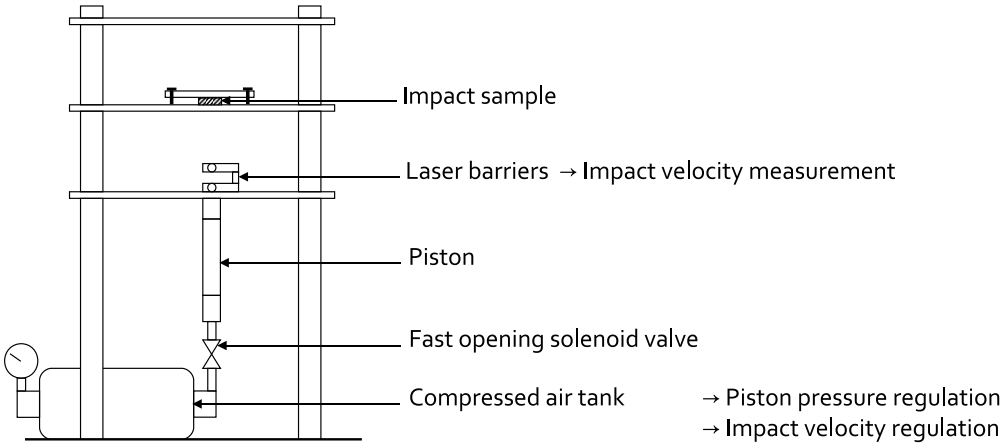

Figure 5.4: Air gun impact set-up from the laboratory *Mécasurf*.

impact velocities. A first analytical estimation of the velocity can be made by neglecting the friction between the different elements and with the air and considering the piston and the shell to be perfectly adjusted. The velocity v at distance x from the initial point is given in Eq. 5.1 as a function of the air pressure P, the diameter of the piston $D = 2R$, the air density ρ_{air}, the mass m of the set (shell+ball) and C_x the drag coefficient of the former defined set.

$$v(x) = \tanh^{-1}\left(\cosh^{-1}\left(e^{\frac{\pi D^2 \rho_{air} C_x}{8m} x}\right)\right)\sqrt{\frac{2P}{\rho_{air} C_x}} \tag{5.1}$$

Several limitations exist on this device that is currently in an optimization process. First as indicated before, the shell and thus the ball velocity is highly governed by the friction in the piston. The piston presents a slight ovoid distortion that increases these friction effects and sometimes causes the blocking of the shell in the piston. This leads to a very large scattering of the impact velocity for a given air pressure. Figure 5.5 shows the velocities measured by laser barriers for pressures ranging from 1 to 4 bars, the large scattering of data is there obvious. Some points show a very low velocity compared to the applied pressure, this is to relate to the blocking of the shell in the piston, these points are not accounted in the average calculation. As a consequence, the monitoring of velocity is difficult with this device. A saturation effect is observed nevertheless for pressures higher than three bars.

The friction in the piston has for secondary effect to generate vibrations of the shell during its path. The effect of these vibrations are reduced by the damping system at the end of the piston but interfere with the ball's trajectory. As a consequence, it is impossible to predict the position of the impacts with precision. The impact position cannot be estimated out of an area of dimensions $35 \times 35 mm^2$. These dimensions are low enough to

ensure that the impact will occur on the samples but causes difficulties for the measurements with high speed camera as explained further.

The measurement of the velocity is a also problem. The laser barrier's sample rate is rather high, about $25kHz$ while the typical time between the two barriers measurements range from 200 to $500\mu s$. Thus, the measurement error resulting from the barriers is non negligible. Velocity measurements are completed with high speed camera videos of the impacts. The definition of the camera is not optimized compared to the dimensions of the problems and thus obtaining several sharp images of the ball during its impacts to perform a satisfactory measure of the velocity was difficult. The ball is sometimes blurred, or out of the picture, due to the low precision of the position. Yet it was often possible to measure the impact and rebound velocities of the ball but the measurement error, difficult to estimate on the videos remains rather high. Comparison between the two methods offers supplementary information.

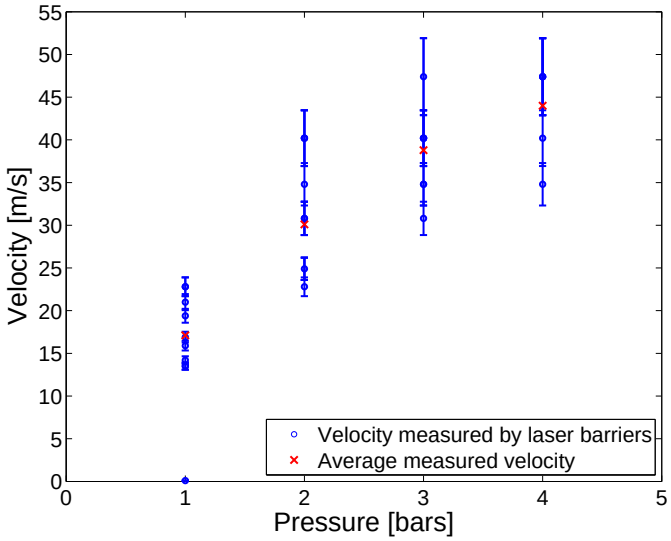

Figure 5.5: Impact velocity measured by laser barriers as a function of air pressure for the impact set-up.

In summary, this device offers the possibility to perform impacts at velocities from about $15m/s$ to $45m/s$. The impact position and velocity are not accurately controlled and significant measurement errors are made on the velocity. The repeatability of the measures is rather poor and the velocity measurements were doubled to reduce uncertainty of the results.

5.2.2 Plan of experiments

Impact experiments are performed on three materials. The choice of the material was described in this chapter's introduction and is the following : an aluminium alloy 7010, a stainless steel 316L and a nickel alloy Inconel 600. 316L and Inconel 600 samples were heat treated after cutting-out. The heat treatment procedure is the same as for the cyclic behaviour on Inconel 600 experiments, see section B.2. The samples were heated at 600^oC for three hours with controlled heating and cooling temperatures to avoid temperature gradients in the pieces. This heat treatment is expected to reduce the residual stress level in the samples but not to remove it completely. The full analysis of the heat treatment effect, residual stress level and effective consideration of these stresses on the numerical simulation was studied by Li [LI 11]. The samples are then sandblasted and speckled after cleaning of the surface. As a first step here, the samples are considered free of pre-existing residual stresses and strains.

The samples surface is considered planar but taking of correlation picture before and after impact allows to check this hypothesis. The in-plane dimensions of the samples are large enough to apply the hypothesis of semi-infinite body and the impact position is checked a posteriori to validate this hypothesis. The samples thickness varies between 10 and $12mm$. The effective thickness of samples is not crucial as a semi infinite body hypothesis is made. The samples were impacted on only one side to guarantee no interaction between several impacts.

The full range of velocity is obtained with pressure from 1 to 3 bars. As shown before, an accurate evaluation of the corresponding velocity is not possible a priori. The impacting balls are made out in Si_3N_4 ceramic, which yield limit is high enough to guarantee a fully elastic behaviour of the balls during impact. This hypothesis is checked by visual observation of the balls after impact. The Young modulus of the ceramic balls is taken equal to $305GPa$ from the bibliography and its density is equal to $3200kg/m^3$. The diameter of the ball is equal to $10.31mm$. This diameter was chosen as the higher diameter (to provide better measurements of the dimensions through stereo correlation and of residual stresses through x-ray diffraction) respecting the limit dimension of the set-up and the semi infinite body hypothesis considering the thickness of the samples.

As indicated before, the impacted body is considered semi infinite and the rigidity of the whole system is considered infinite, which is a priori consistent with the dimensions of the set-up and the samples relatively to the ball. At last, impacts were performed perpendicular to the surface for the majority and a few sets of impacts were made with an incidence angle (defined in Fig. 5.6) equal to 30^o to provide some information on the effect of a tangential component of the velocity. The full experimental conditions are recalled in tab. 5.1. Due to the lack of repeatability of the experiments, several impacts are made for each set of experimental conditions.

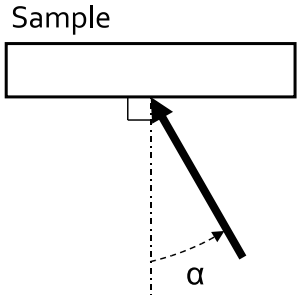

Figure 5.6: Definition of the incidence angle α.

Impacted material	Pressure [bars]	Incidence angle	Number of impacts
Aluminium 7010	1	0^o	6
	2	0^o	6
	3	0^o	6
	2	30^o	4
	1	30^o	1
Stainless Steel 316L	1	0^o	4
	2	0^o	4
	3	0^o	4
	2	30^o	2
Inconel 600	1	0^o	6
	2	0^o	6
	3	0^o	7
	2	30^o	4

Table 5.1: Plan of experiments

5.3 Material parameters

The comparison between experimental and numerical results requires representative hardening laws to describe the hardening behaviour of the impacted materials. Hardening laws can present several complexity levels depending on the kind of behaviour the material actually has and on the actual behaviour that is modelled. Single impact experiments are here performed. Neither inertial nor viscous effects are considered here. Consequently the knowledge of the quasi-static behaviour of the materials is all-sufficient. Simulations have shown that considering either kinematic or isotropic behaviour has no effect on simple indentation, see chapter 3 or [ZAI 10]. A simple isotropic behaviour could be considered but kinematic or mixed hardening behaviour might be necessary for multiple impact experiments that have been performed by Jun Li [LI 11] and which results are partly presented in chapter 6. Kinematic behaviour is then considered for 316L and Inconel 600 samples.

For all three materials, a simple linear hardening law, as defined in Eq. 2.44 is also identified for application of the estimation of the coefficient of restitution as in Eqs. 4.12 and 4.13. Two parameters regarding plasticity influence the evolution of the coefficient of restitution: the initial yield limit σ_{y0} and the tangent modulus E_T. The initial yield stress has the most critical effect on the coefficient of restitution since it triggers the decrease of e from its unit value in the elastic case. The tangent modulus acts on the evolution of the coefficient of restitution but its effect is of lesser order. These two parameters could be adjusted for an optimal fit but for a better representation of the effect of hardening on the coefficient of restitution the yield limit should be kept equal to the experimentally measured value. Only the tangent modulus is thus modified despite leading to a worse fit.

5.3.1 Aluminium alloy 7010

Cyclic experiments were made at the laboratory *Mécasurf* on AA 7010 samples. Stress strain curves were made for monotonic tension up to 4.5% total strain providing an isotropic hardening law described in Eq. 5.2. Cyclic experiments were also performed up to 200 cycles with strain extrema equal to $+/-0.9\%$. A fit is made of this material hardening law on a linear isotropic hardening law as described in Eq. 2.44. Resulting hardening parameters for AA 7010 are given in tab. 5.2 and the hardening laws are plotted in Fig. 5.7 for an accumulated plastic strain ranging from 0 to 10%. As indicated before, the eventual part of kinematic behaviour of this material was not analysed and experimental results show a critical gap with the numerical results. The material hardening parameters and especially the initial yield limit of the material are assumed to be wrong here and supplementary experiments would be necessary.

$$\begin{array}{c} \sigma_y = K_p p^{n_p} \mid p \geq 0 \\ \sigma_{y0} \mid p = 0 \end{array} \tag{5.2}$$

Elastic parameters		
E	GPa	70800
ν		0.3
Power law parameters		
σ_{y0}	MPa	500
K_p	MPa	608
n_p		0.027
linear hardening law parameters		
σ_{y0}	MPa	500
E_T/E	%	1.33

Table 5.2: AA 7010 material parameters. Elastic parameters, power law 5.2 parameters and linear isotropic hardening law parameters.

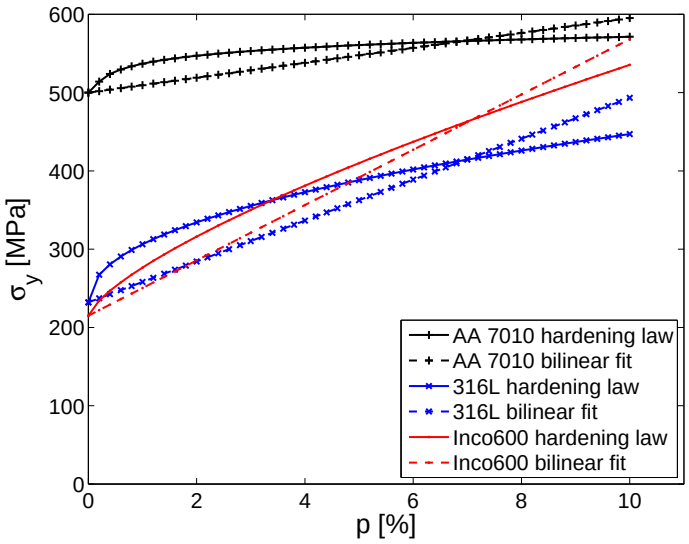

Figure 5.7: Experimentally identified hardening laws for AA 7010, Stainless steel 316L and Inconel 600. Monotonic tensile curves and linear isotropic hardening fit.

5.3.2 Stainless Steel 316L

Cyclic tension-compression experiments were performed at different temperatures by AREVA and a material hardening law has been identified at the ambient temperature on the software Systus. This hardening law is defined as an Armstrong-Frederick type hardening law (see Eq. 5.3) with an isotropic hardening part, here equal to 25%. At each load step, the plastic flow increment is computed and the actual part of kinematic and isotropic hardening are determined. The corresponding evolution of the isotropic hardening variable r is numerically deduced but no law is identified for the isotropic hardening. The yield function is then defined as a function of the kinematic hardening variables X_1 and X_2 and of the part of isotropic hardening p_{ISO} as indicated in Eq. 5.3. The corresponding identified material parameters are given in tab. 5.3.

$$f = J_2\left(\underline{\underline{\sigma}} - (1-p_{ISO})\left(\underline{\underline{X_1}} + \underline{\underline{X_2}}\right)\right) - r \tag{5.3}$$

σ_{y0}	MPa	232
C_1	MPa	1072
C_2	MPa	8500
γ_2		80
p_{ISO}		0.25

Table 5.3: Steel 316L hardening parameters for the Systus©type mixed hardening law (Eqs. 2.46 and 2.47).

This hardening law present the drawback of not being completely defined, part of the hardening being numerically calculated at each load step. Furthermore, as it can be seen in Eq. 2.47, the actual value of the internal hardening variables is not consistent with their effective consideration for the yield function calculation. An identification of a conventional mixed hardening law has thus been made.

The identification is made on a monotonic tensile curve based on the kinematic parameters given in tab. 5.3. The partition between kinematic and isotropic hardening plays no role for the simple tension curve. From this evolution of the total stress σ, it is assumed that a part, denoted σ_{ISO} and equal to p_{ISO} is due to isotropic hardening and the rest, denoted σ_{CIN}, is due to kinematic hardening. The split between the two parts is made according to Eq. 5.4.

$$\begin{aligned} \sigma - \sigma_{y0} &= \sigma_{ISO} + \sigma_{CIN} \\ \sigma_{ISO} &= p_{ISO}\,(\sigma - \sigma_{y0}) \\ \sigma_{CIN} &= (1-p_{ISO})\,(\sigma - \sigma_{y0}) \end{aligned} \tag{5.4}$$

A kinematic hardening law, based on Armstrong-Frederick model as defined in Eq. 2.47, is fitted to σ_{CIN}. A hardening law with two hardening variables is here necessary to

fit with satisfactory precision the hardening law. For similar reason, a Ramberg-Osgood power law (Eq. 2.46) is chosen for the isotropic hardening part and fitted to σ_{ISO}. An excellent fit with the original identified hardening law is obtained and corresponding hardening curves are presented in Fig. 5.8. Material parameters for the stainless steel, completed with the simplified linear hardening law are presented in tab. 5.4. The linear hardening law is presented in Fig. 5.7.

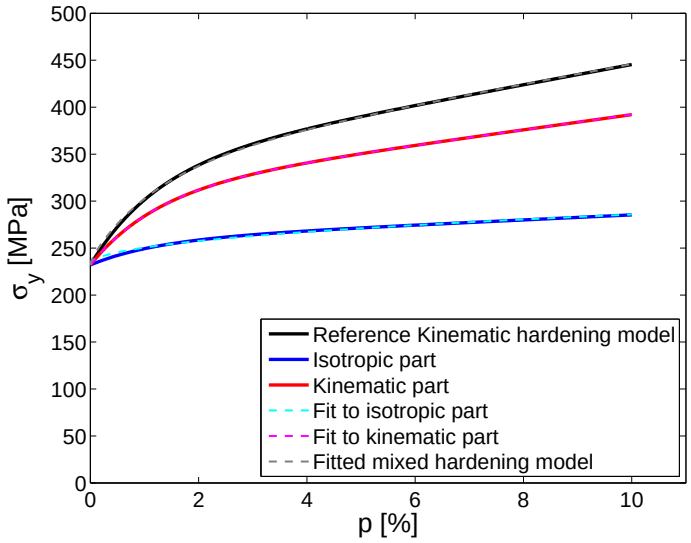

Figure 5.8: Fit of kinematic and hardening parts of hardening laws for the stainless steel 316L.

5.3.3 Inconel 600

The hardening behaviour of Inconel 600 can present significant variations from a casting to another according to internal industrial bibliography from industrial partners. Cyclic tension-compression experiments were made on Inconel600 samples from the same casting as the impact samples. Results, analysis and discussion on the choice of the hardening law are available in annex B. A fully kinematic non linear hardening law with a unique hardening variable, described in Eq. B.8, can be used to describe the kinematic hardening behaviour of Inconel 600. The consideration of the kinematic hardening behaviour would allow to apply this hardening law both for mono and multiple impacts experiments. Yet the kinematic hardening parameters were defined only up to 2% of plastic strain and give a rather poor definition of the yield limit beyond this value. An isotropic Ramberg-Osgood (see Eq. 2.46) hardening law, fitted on a simple tensile curve but for larger plastic strains is best suited here due to the studied range of plastic strains. A simple fit with a linear hardening law is made once again, results of the fitting for a simple tensile curve up to

Elastic parameters		
E	GPa	193.87
ν		0.3
Mixed hardening law parameters		
σ_{y0}	MPa	232.0
K	MPa	155.8
n		0.46
C_1	MPa	804.0
C_2	MPa	6375.0
γ_2		80.07
linear hardening law parameters		
σ_{y0}	MPa	232
E_T/E	%	1.33

Table 5.4: Steel 316L parameters. Elastic parameters, mixed hardening law 2.47 2.46 parameters and linear isotropic hardening law parameters.

10% accumulated plastic strain is given in Fig. 5.7. Material parameters for Inconel 600 are recalled in Tab. 5.5.

Elastic parameters		
E	GPa	195.2
ν		0.3
Ramberg-Osgood isotropic hardening law parameters		
σ_{y0}	MPa	215
K	MPa	1670
n	MPa	0.72
γ		110.0
linear hardening law parameters		
σ_{y0}	MPa	215
E_T/E	%	1.78

Table 5.5: Inconel 600 material parameters. Elastic parameters, Ramberg-Osgood isotropic hardening (Eq. 2.46) parameters and linear isotropic hardening law parameters.

5.4 Velocity measurements - Coefficient of restitution

Impact experiments were performed with two velocity measurements. The impact velocity is measured by laser barriers while the whole impact is filmed with a high-speed

camera. The laser barrier measurements, as indicated in section 5.2.1.2, present a large measurement error due to its sample rate. Furthermore, the cutting of the lasers by the ball is often incomplete due to its vibrations when it leaves the piston. For these reasons, the laser barrier measurements are often incomplete or absurd.

The impact videos are unusable when the impact occurs out of the window or out of focus. In the other cases, the velocity measurement is made by determining the position of the center of the ball for each picture and calculating its displacement between each picture. The final impact and rebound velocities are taken as the averages of the measured velocities upon all available pictures. Several parameters then influence the quality of measures. The movement of the ball out of the plane of the camera is considered negligible and is impossible to measure here. The exact position of the center of the ball is delicate to determine at the higher velocities since the ball creates a blur on the pictures. The velocity measured from two adjacent pictures can thus present significant variations. The measurement error is thus defined as the standard deviation of the measured velocities.

The high speed camera measurements are more precise and allow the measurement of the rebound velocity and are so taken as the reference velocity for the presentation of results. The average relative error between the two sets of measurements is equal to 15% which mainly indicates that the velocity measurements should be considered with precaution.

The coefficient of restitution has been measured for all impacts when possible. Results are presented for all materials in Fig. 5.9. The impact velocities studied here are far above the yield velocities of the studied materials. Thus the evolution of the coefficient of restitution in the range of studied velocities is rather low. A slight decrease of the coefficient of restitution is observed with the velocity which correlates with the observations made in chapter 4. At a given velocity, the coefficient of restitution increases with the yield limit of the material. Stainless steel 316L and Inconel 600 have very close Young moduli and initial yield limit which appears clearly in the measures of the coefficients of restitution that are very close for both materials.

Based on the experimental measures of the initial yield limits of the impacted materials, a first fit is made to Eq. 4.11. A perfectly plastic (P.P.) hardening law is assumed and the coefficient of restitution is fitted to the empirical equation given by Jackson et al [JAC 10]. A more accurate fit is made using the linear hardening laws defined in the former section and using equations 4.12 and 4.13. Fitting results are presented for all three material in Fig. 5.9.

Results are presented independently for each material in Figs. 5.10, 5.11 and 5.12. Error bars for the coefficient of restitution are plotted in these figures. This error is deduced from the standard deviations of the measurements of the impact velocity Δv and the rebound velocity Δv_r as: $\Delta e/e = \Delta v/v + \Delta v_r/v_r$. The impact velocities are presented normalized by the yield velocity of each material as defined in Eq. 4.10.

The equation providing the coefficient of restitution in the case of impacts on AA 7010 shows a very poor correlation. Material hardening data for these samples were issued from rather ancient experiments and the material is assumed to have been ageing.

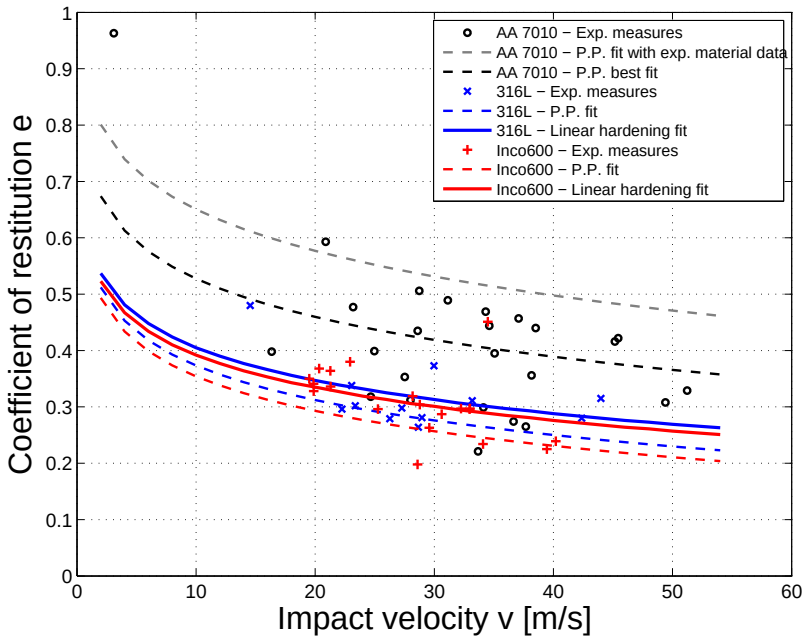

Figure 5.9: Experimental measurements of the coefficient of restitution as a function of the impact velocity. Fit to empirical equation 4.11 considering a perfectly plastic behaviour (P.P.) and to Eqs. 4.12 and 4.13 considering a linear hardening behaviour.

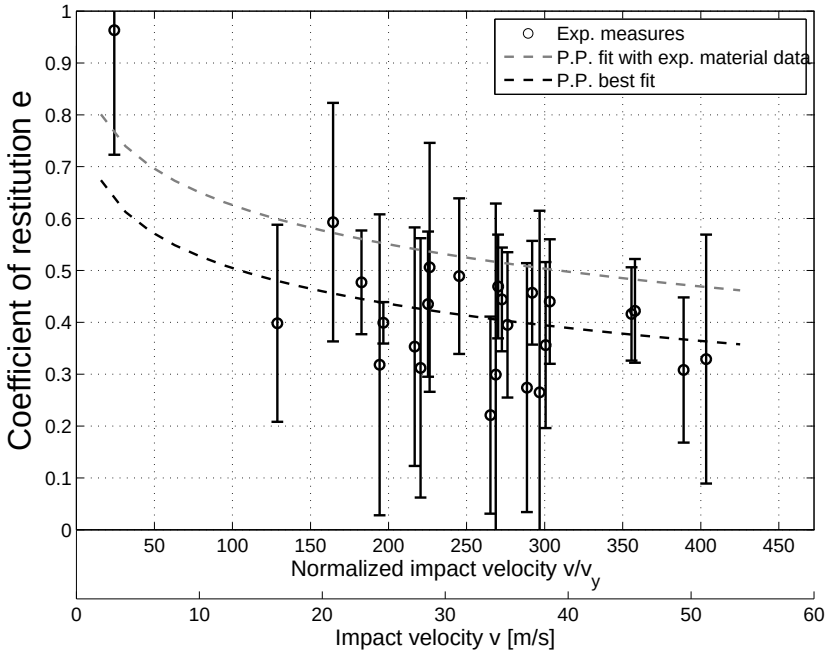

Figure 5.10: Experimental measurements of the coefficient of restitution for impacts on AA 7010 as a function of the normalized impact velocity. Fit to empirical equation 4.11 considering a perfectly plastic behaviour (P.P.) using original experimental data and best fist to experimental data for estimation of the current yield limit.

According to this hypothesis a decrease of the yield limit would be observed which correlates with the experimental results here. Furthermore this ageing process can be expected to be irregular among all the samples which could explain the large scattering of the coefficient of restitution measures observed for the aluminium samples compared to the other materials. Complementary experiments to determine the actual hardening parameters of the aluminium could not be made. The original hardening behaviour of AA 7010 being almost nil (see Fig. 5.7) a perfectly plastic behaviour is assumed and a best fit is made with the experimental values of the coefficient of restitution to provide a raw estimate of the current yield limit of the aluminium alloy. The best fitted curve is provided in Figs. 5.9 and 5.10. The current yield limit is found to be equal to approximately 270*MPa* while the original material data indicated a yield limit equal to 500*MPa*. Due to the large error bars and to the bias on the material parameters no clear conclusion can be drawn from these results. It is still clear that the global trends of the analytical law are consistent with the experimental results for velocities ranging here from 100 to 400 times the yield velocity v_y (value calculated with the initial value of the yield limit) of the AA 7010.

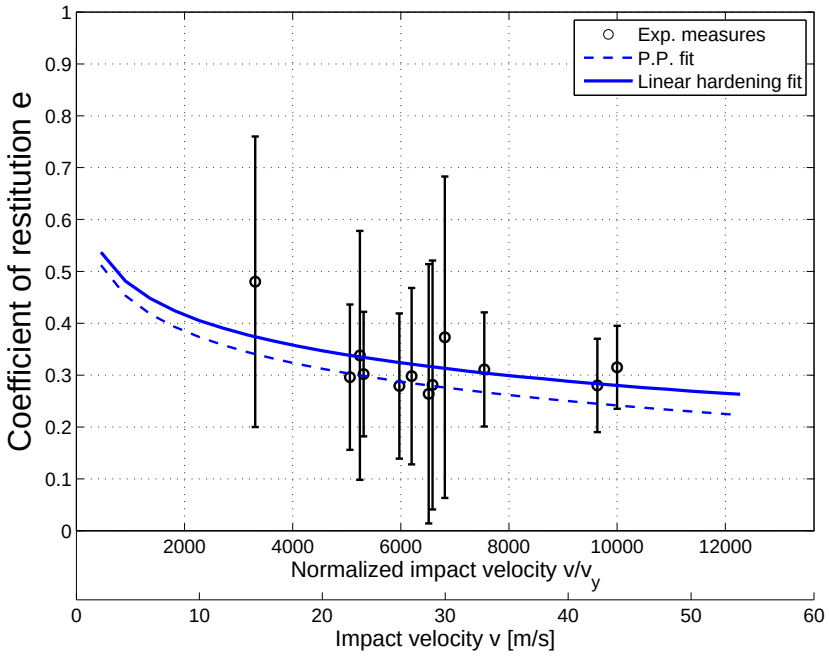

Figure 5.11: Experimental measurements of the coefficient of restitution for impacts on Steel 316L as a function of the normalized impact velocity. Fit to empirical equation 4.11 considering a perfectly plastic behaviour (P.P.) and to Eqs. 4.12 and 4.13 considering a linear hardening behaviour.

Coefficients of restitution for impacts on 316L and Inconel 600 show a good consistency between experimental results and analytical laws. The range of normalized veloci-

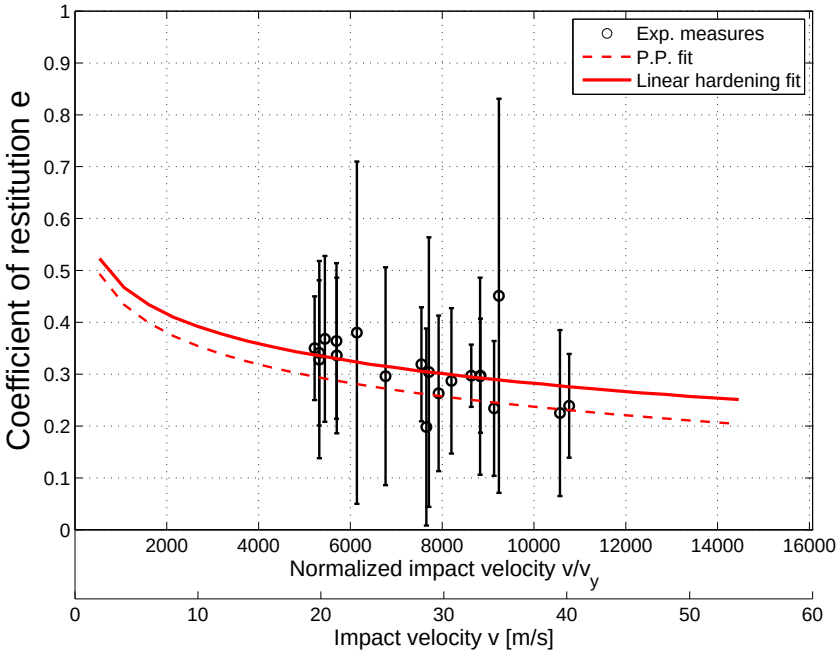

Figure 5.12: Experimental measurements of the coefficient of restitution for impacts on Inconel 600 as a function of the normalized impact velocity. Fit to empirical equation 4.11 considering a perfectly plastic behaviour (P.P.) and to Eqs. 4.12 and 4.13 considering a linear hardening behaviour.

ties are rather similar for both materials, around 6000 times their respective yield velocities. Considering the error bars on the experimental results, the influence of hardening cannot be clearly observed. For Inconel 600 that presents a relatively large hardening, a significantly better correlation with the experimental results is observed when considering a linear hardening than for a simple perfectly plastic behaviour. This shows the importance of considering hardening for the prediction of the coefficient of restitution and somehow validates the formulae defined in the former chapter.

5.5 Surface profile measurements

5.5.1 Comparison between profilometer and stereo correlation measurements

Surface profile measurements have been performed on impacted samples. Stereo correlation measurement of the surface displacements in all three directions were made on all impacted samples. Complementary measurements on a contact profilometer were made on some of the samples, the measurement time prevented to perform it on all samples.

The sandblasting of the surface was necessary for the stereo correlation measures but it generates high luminosity points and irregularities on the measured profiles. Furthermore, the impact of the ball on the samples generates a large change in surface orientation. Reflections are thus observed in this area that could not be fully avoided during stereo correlation measurements, even with changes in the light orientation. Data can not be measured in the areas of reflection and are thus interpolated with the data from the surroundings. These interpolated areas are present in all stereo correlation measurements and therefore results should be considered carefully. At last, the small size of the impacts compared to the measurement capabilities makes that the obtained measures are not optimum.

On available samples, surface profiles passing by the center of the impacts obtained by the profilometer and by stereo correlation were compared. A full set of results is presented for one sample. Global macroscopic parameters for all measurable samples will be presented further. The sample presented here is a stainless steel 316L sample. The average impact velocity was measured at $44 m/s$ with a standard deviation of the measures equal to $2.5 m/s$. Two lighting orientations were used to perform the stereo correlation measurement before and after the impact, allowing to move the location of the reflection area on the impacted sample. Results are presented in Figs. 5.13 and 5.14. The raw stereo correlation results are presented in Figs 5.13(a) and 5.14(a) illustrating the areas in which results are non-existent due to the reflections. The displacement along the Z direction, in mm, is here presented. The pattern size used for digital image correlation was optimized as a function of the quality of the results and with respect to the gradients of the data measured. On each picture, the point of minimum altitude is depicted along with the x and y parallel lines along which profiles will be measured. It appears first that a lot of measurement noise is captured at the surface of the sample, this is due to the bright

points generated by the sandblasting of the surface.

An interpolation of the data in the reflection areas is made on the raw data using the software Matlab. Several interpolation algorithms were tested giving similar results. The full surface position profile are presented in Figs. 5.13(b) and 5.14(b). The profiles of the interpolated data are then plotted along the x and y directions. The interpolated data are depicted in blue rectangles on these figures to interpret the results correctly. At last, the profilometer measures along two perpendicular directions are plotted in Figs. 5.13(e) and 5.14(e) and all measured profiles are superimposed in Figs. 5.13(f) and 5.14(f). All profiles are aligned along the minimum surface value for comparisons of the impact shapes.

The first set of results (Fig. 5.13) presents a very good agreement between the two measurement methods. For this impact case, the radii R_0 at $z = 0$ altitude are very similar (about $1.45mm$) for all four profiles. The depth of the impact is quite well measured by the stereo correlation technique despite a slight overestimation. The optical measures does not describe properly here the curvature at the bottom of the impact. At last, the measurement noise is too high at the surface of the body to be able to measure the dent's height. An area of higher height is yet observable around the impact in Figs. 5.13(a) and 5.13(b) and macroscopic parameters can be roughly estimated using the stereo correlation.

The second set of results (Fig. 5.14) presents measurements for the same sample but with different orientations of the lightings. Notably, the reflection area slightly overlaps here the point of minimum altitude z_{min} of the impact. Consequently, the minimum measured value is overestimated by the correlation software that lacks data and extrapolates the value at the border of the reflection zone as a function of the gradient of data, that is rather high since considering the sides of the impact. The impact radius values R_0 are roughly the same than in the former case and still consistent with the profilometer measurements.

This last case is representative of the overall stereo correlation measurements performed here. A correct measurement of the impact radius is made but the depth of the impact is overestimated by the correlation and results should be considered with care. The error made here is somehow proportional to the depth of the impact and still gives an estimate of the real value. The global trends can still be estimated and stereo correlation results were kept in all cases for a larger number of measurement.

5.5.2 Numerical results

Profilometer and stereo correlation measurements are here studied as a function of the impact velocity on each material. Three macroscopic measures are selected to describe the impacts. Figure 5.15 defines the geometry of the imprint. For both the profilometer and the stereo correlation measures, the plane of altitude $z = 0$ is defined as the average altitude plane. The impact radius R_0 is defined here at altitude $z = 0$ where the contact radius a^* is identified. Measures of R_0 are very close for both methods. The impact depth z_{min} is simply the lowest measure altitude. It was shown previously that the stereo correlation method tends to overestimate slightly this depth. At last the dent height h_d is measured as the highest altitude value. Only the profilometer allows this measure and so a

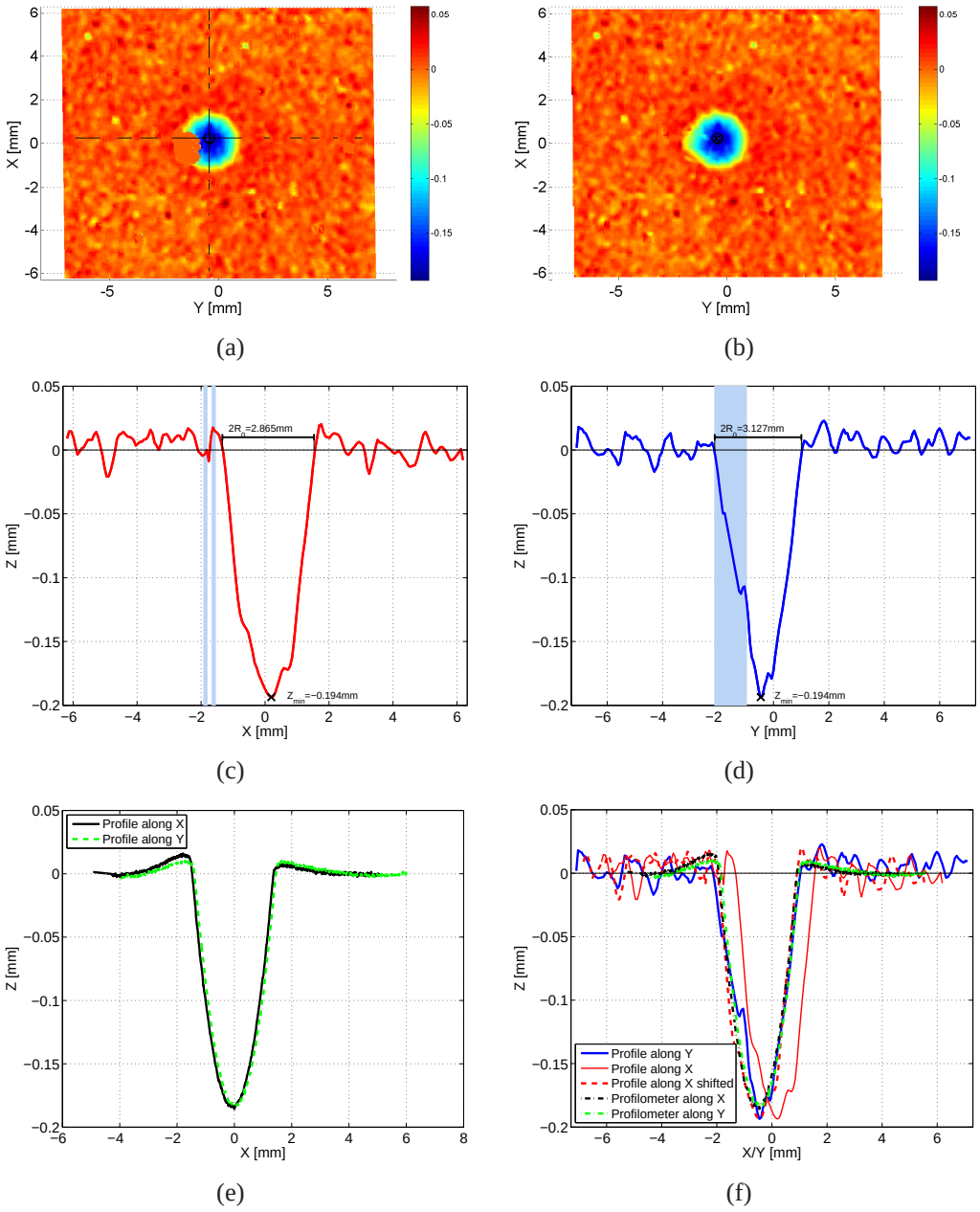

Figure 5.13: Profile measurements on a stainless steel 316L sample, impact velocity measured at $44 m/s$, first lighting orientation. (a) Raw stereo correlation normal displacement measure (in mm). (b) Interpolated displacement measure (in mm). Measured profiles along the x (c) and y (d) directions, interpolated zones in light blue. (e) Profilometer measures along the x and y directions. (f) Superimposition of all profiles.

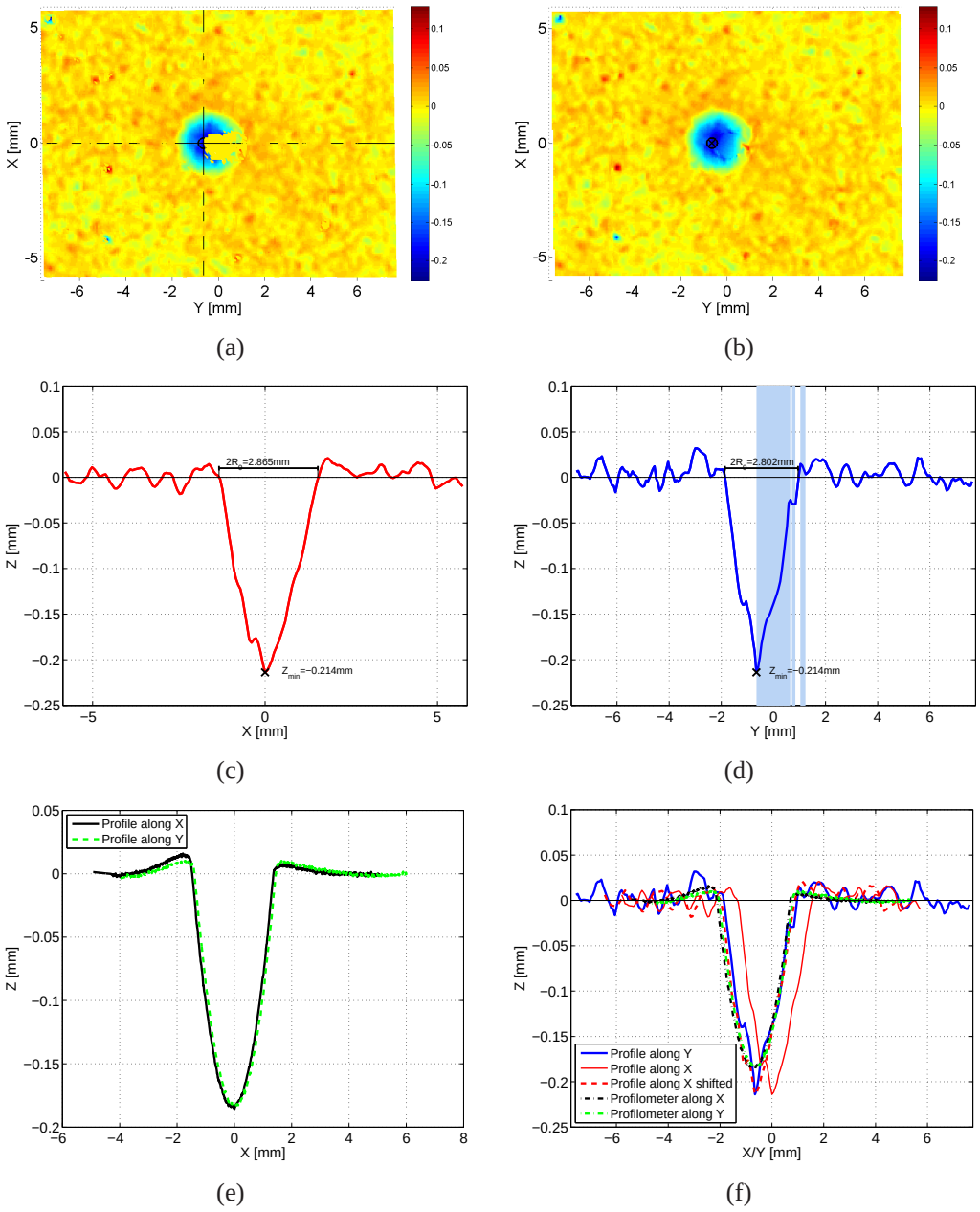

Figure 5.14: Profile measurements on a stainless steel 316L sample, impact velocity measured at $44 m/s$, second lighting orientation. (a) Raw stereo correlation normal displacement measure (in mm). (b) Interpolated displacement measure (in mm). Measured profiles along the x (c) and y (d) directions, interpolated zones in light blue. (e) Profilometer measures along the x and y directions. (f) Superimposition of all profiles.

lower set of results is presented for the dent height. The dent height can experimentally be highly different if the impact is not purely normal to the surface. Consequently measures of the impact dent height are often different depending on the direction of the measure or on the size of the dent considered. Four measures are made on each dent, the average value is plotted along with the minimum and maximum value for each set of measure.

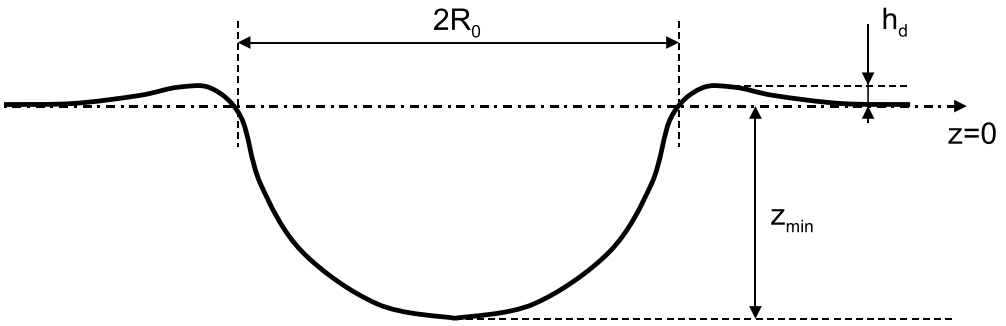

Figure 5.15: Definition of surface profiles measured parameters: radius of dent at zero altitude R_0, dent height h_d and dent depth z_{min}

A first full surface profile is presented for an impact at measured velocity $v = 25m/s$ on an Inconel 600 sample. Corresponding simulation results from the SAM and the Abaqus model used in the benchmark are presented in Fig. 5.16. The Inconel material parameters used here differ slightly from those described in section 5.3.3 and the results are so slightly different. Contrary to the single impact benchmark a poor correlation is observed between the SAM and FE results, this is due to the high level of strains involved in this case. The match between FE simulation and experiments is rather good for this particular impact case but experimental imprecisions, especially in the velocity measurement decrease the quality of the correlation and more global observations are made afterwards. Interestingly, the SAM results at $v = 25m/s$ correlate very well with profile measure made at an averaged impact velocity of 21m/s. The large strain levels involved in these cases make that the SAM results don't correlate well with the experimental results but as indicated in the further figures, the global trends are well reproduced and a simple shift in the velocity range seems to be made.

For each material a set of simulations is performed. The ball is taken elastic with ceramic Si_3N_4 material parameters. The samples are considered semi infinite, which is consistent with their dimensions. The depth is the most critical dimension, it is about $12mm$ for all the samples while the sphere diameter is equal to $10.31mm$. The material parameters are those defined in section 5.3 with the correction proposed for the yield stress of the aluminium alloy. For all simulations, the velocity is considered purely normal and no friction between the bodies is considered. Similar simulations with a coefficient of friction equal to 0.4 have been performed and no significant effect on the residual displacement profiles was observed. Recent results by Fulleringer [FUL 11] showed a

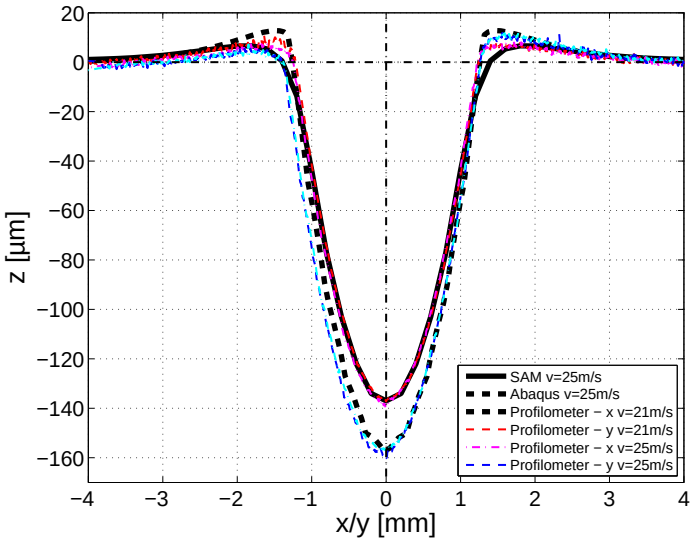

Figure 5.16: Comparison between surface profile measures and simulated residual displacement from SAM and Abaqus. Impact at measured velocity $v = 25m/s$ on an inconel 600 sample.

significant sensibility of the SAM method for frictional indentation. These results were issued from simulations at very low plastic strain amplitude and with a very fine mesh in the contact area to correctly describe the stick and slip zones. Similar results were not obtained at high strain levels and a detailed study of the effect of friction was not done here. It should be noticed that the influence of friction can be significant when the coefficient of friction if large (higher than 0.3). The radial displacements in the contact area especially are influenced by the history of slip-stick situation during the indentation/impact. These effects were not accounted for the comparisons with simulation here and will be part of future work.

Five impact velocities are considered, ranging from 10 to $50m/s$ to cover the experimental velocity range and compare the trends on the impact shapes between simulation and experiments. Results are presented as a function of the impact velocity, with indication of the normalization by the material's yield velocity v_y. For the profilometer measurements, the error on the velocity measure is depicted to illustrate the possible variation of the results with this parameter. Similar data is available for the stereo correlation measurements but is not depicted for readability. At last, the maximum accumulated plastic strain issued from the simulation is plotted. This is an important parameter to estimate the quality of the simulation results (for plastic strain higher than typically 10% some numerical error may occur due to the assumption of small strains).

Results are presented in Figs. 5.17, 5.18, and 5.19 for AA 7010, stainless steel 316L and Inconel 600, respectively. For all materials, that have relatively close yield limits and

thus present close levels of plasticity for similar velocities, the maximum level of accumulated plastic strain is around 10% or more, which is about the limits of the capabilities of the current code. A large scatter can sometimes be observed in the stereo correlation measurements of the impacts' depths (blue diamonds in Figs. 5.17(c), 5.18(c) and 5.19(c)). This is due to the overestimation of the depth by the correlation process in areas were data are not defined as described in the former section.

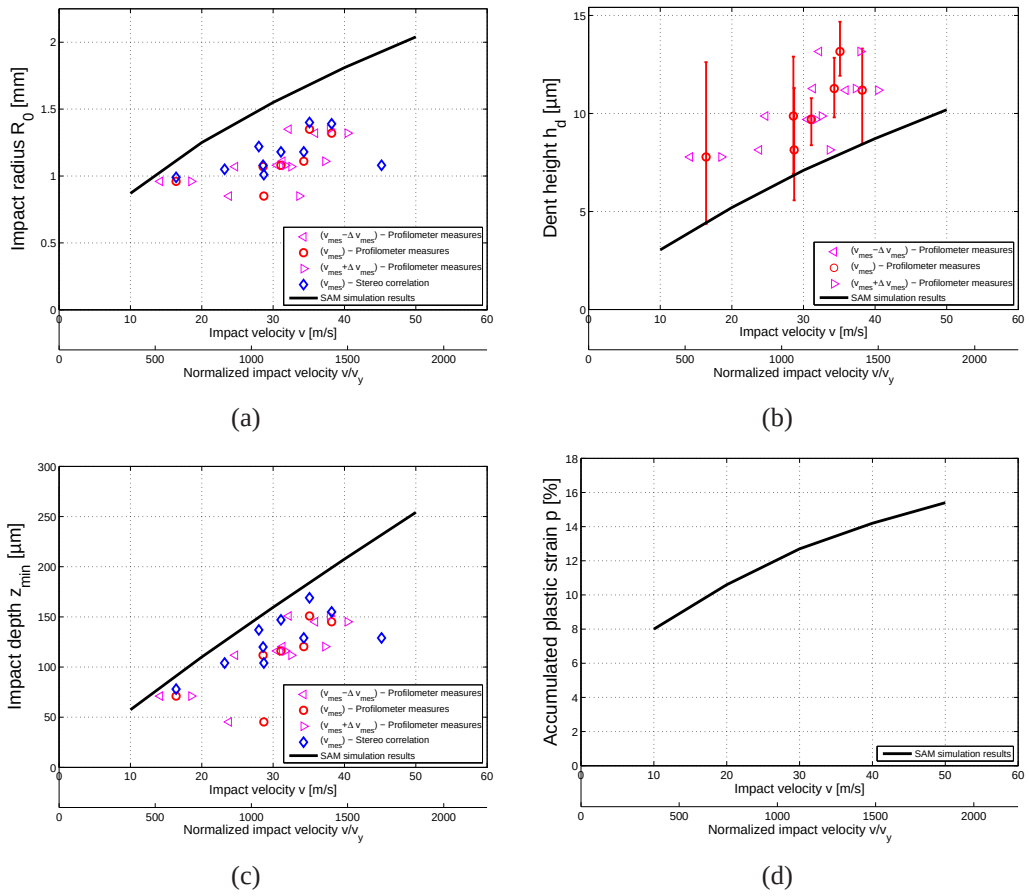

Figure 5.17: Comparison of experimental profile measurements and results from simulation as a function of impact velocity for impacts on AA 7010 samples. Comparison of impact radius R_0 (a), dent height (b), dent depth (c) ; maximum accumulated plastic strain obtained by simulation (d).

Results for impacts on AA7010 are presented in fig. 5.17(a). These results should be considered with care since the yield limit of the material was estimated with the coefficient of restitution results in the former section. As a consequence, the comparison between simulations and experiments is quantitatively poor. Qualitatively, it can be seen that the trends are the same. In the current range of velocity and for plastic strain that can

reach 14% the evolution of all measured dimensions is almost linear with the velocity. The impact depth z_{min} are overestimated which can be attributed to the poor knowledge of the hardening law. For similar reasons, the dent height is underestimated and the impact radius overestimated. It was observed in section 4.2 that the residual displacement predicted by the SAM differs from the FE prediction around the limits of the contact zone. This correlates with the underestimation of the dent height observed here. Furthermore, the residual displacement predicted by the SAM (see Fig. 4.1) being underestimated around $x = +/- a^*$ it leads to an overestimation of the radius of impact at $z = 0$ which here again correlates with the experimental observations.

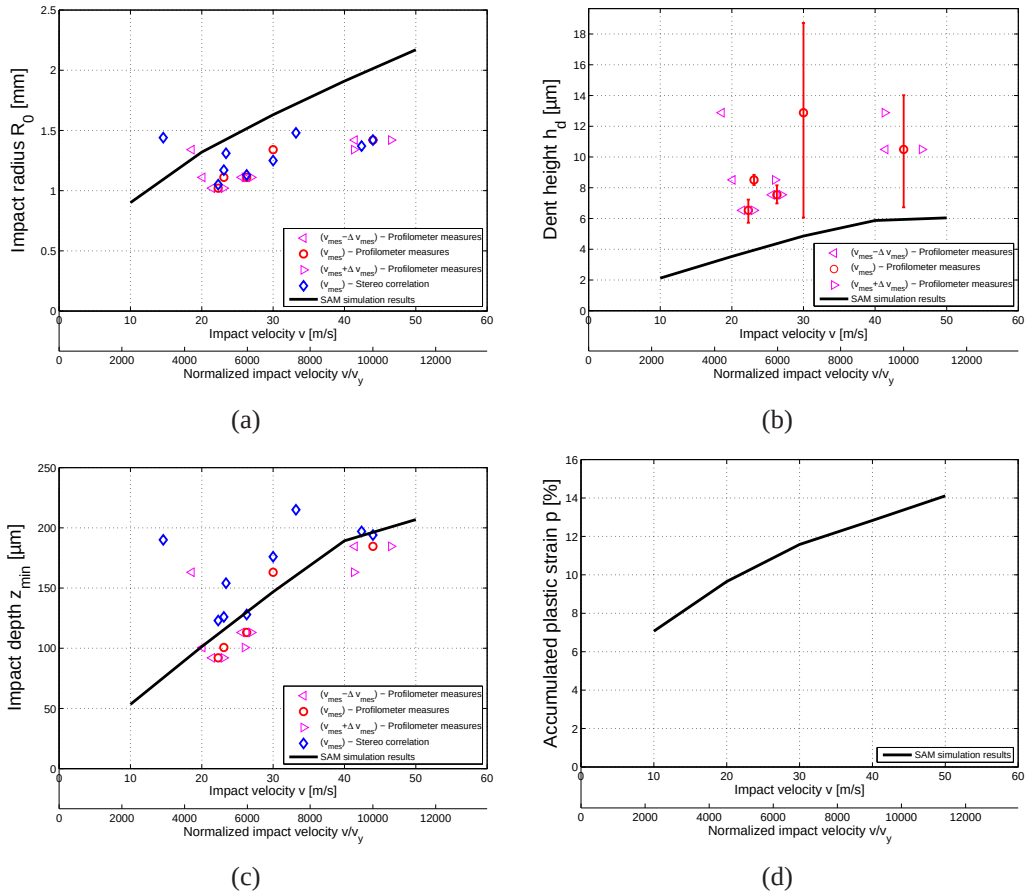

Figure 5.18: Comparison of experimental profile measurements and results from simulation as a function of impact velocity for impacts on stainless steel 316L samples. Comparison of impact radius R_0 (a), dent height (b), dent depth (c) ; maximum accumulated plastic strain obtained by simulation (d).

Results for impacts on the stainless steel 316L and Inconel 600, presented respectively in Figs. 5.18 and 5.19, show a better correlation due to a good knowledge of the hardening

law. An excellent fit between simulation and experimental results is obtained for the maximum depth of impact (Figs. 5.18(c) and 5.19(c)). For both cases the global trends are perfectly reproduced by the simulation.

An effect of saturation for values of impact velocity above $40m.s$ is observed both for the experimental and simulation results for 316L. Complementary experimental points, coupled with simulation results would be necessary to confirm this trend.

As for impacts on AA7010 samples, the prediction of the impacts' radii and maximum depth by the SAM is not perfect. The dent height are largely underestimated by the simulation but this was shown to be a significant point of improvement on the SAM, yet once again, the global trend is fairly described. For the impact radii R_0, a good correlation is observed for "low" velocities, i.e. about 10% of maximum plastic strain and the gap between simulation and experiments increases with the impact velocity. This clearly shows the limits of the SAM for the simulation of large strains, at least in the current state of the method. As the maximum plastic strain increases, the description of the effects on the borders of the contact, where the maximum plastic strain is measured and gets closer to the surface, by the SAM gets worse. This bias of the method is illustrated here by the measure of the impact radius that directly depends on these effects.

5.6 Surface residual strain

A significant interest of the stereo correlation is the possibility to measure strains at the surface of the impacted body, which simple profilometer measurements do not allow. It was shown here that a significant noise disturbs the measures around the impacts and that light reflections limit the measures in the impact dent. Despite this, the stereo correlation measures done here allow to measure the residual strains ε_{xx}^{res}, ε_{xy}^{res} and ε_{yy}^{res} (x and y being the directions along the surface) in and around each impact.

Similarly, the surface residual strain can be calculated from simulation results as a function of the surface residual displacements in the x and y directions, see Eqs. 5.5, 5.7 and 5.6. More interestingly, a measure of the residual strains outside of the plastic zone can give a direct measure of the surface residual stresses. The capability of this method is presented here on an example.

$$\varepsilon_{xx}(i,j) = \frac{u_x^{res}(i+1,j) - u_x^{res}(i-1,j)}{2\Delta x} \tag{5.5}$$

$$\varepsilon_{yy}(i,j) = \frac{u_y^{res}(i,j+1) - u_y^{res}(i,j-1)}{2\Delta y} \tag{5.6}$$

$$\varepsilon_{xy}(i,j) = \frac{1}{2}\left(\frac{u_x^{res}(i,j+1) - u_x^{res}(i,j-1)}{2\Delta y} + \frac{u_y^{res}(i+1,j) - u_y^{res}(i-1,j)}{2\Delta x}\right) \tag{5.7}$$

$$\varepsilon_{eq}(i,j) = \sqrt{\frac{2}{3}\left(\varepsilon_{xx}(i,j)^2 + \varepsilon_{yy}(i,j)^2 + 2\varepsilon_{xy}(i,j)^2\right)} \tag{5.8}$$

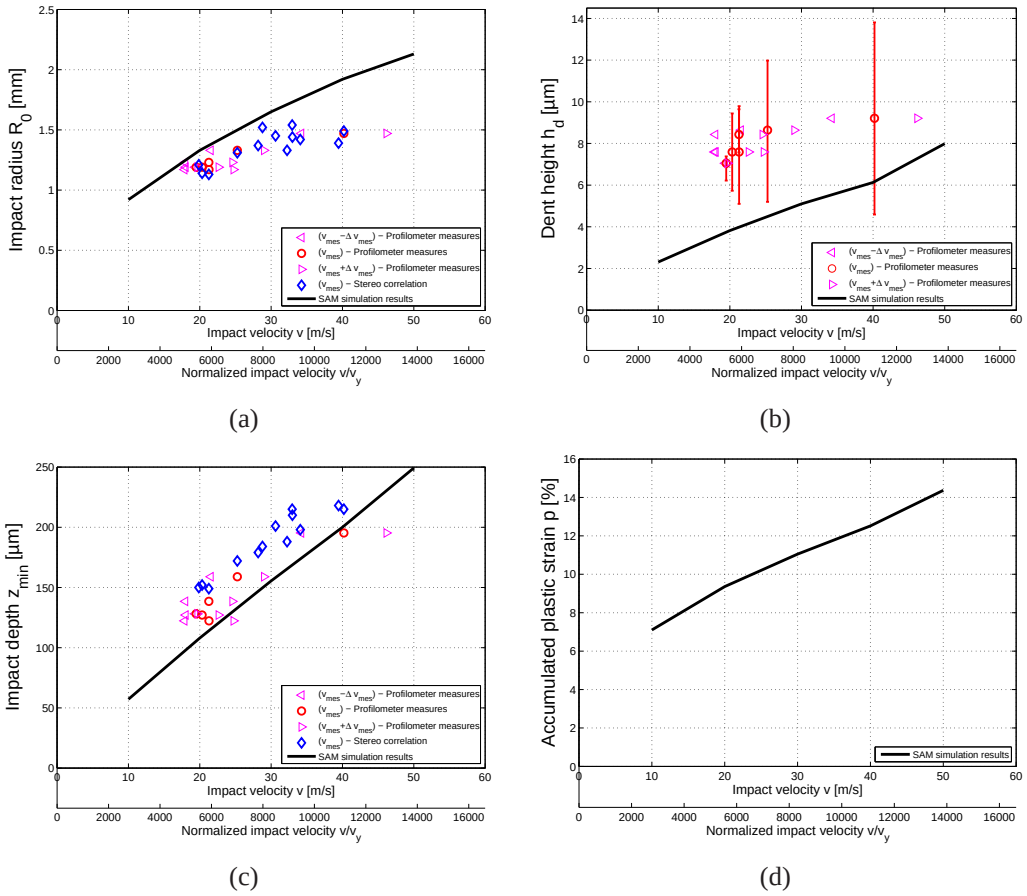

Figure 5.19: Comparison of experimental profile measurements and results from simulation as a function of impact velocity for impacts on Inconel 600 samples. Comparison of impact radius R_0 (a), dent height (b), dent depth (c) ; maximum accumulated plastic strain obtained by simulation (d).

The stainless steel 316L sample impacted at $44m/s$ presented in the former section is presented here again. Stereo correlation strain results are analysed with the same method that the surface normal displacement measures. Raw data are interpolated and profiles are extracted along the x and y directions around the maximum impact depth. The interpolated data are marked and the position of the measured impact radius is also depicted for analysis. Figures 5.20, 5.21, 5.22 and 5.23 present the measured residual strains for this specific impact, for the first orientation of lighting (Fig. 5.13).

Experimental results are compared with simulation along the x and y-axis passing by the center of the impact, when significant. Overall, the results correlate very well out of the dent for all strain components, confirming the quality of the SAM results. An interesting insight of these results is the measurement of residual stresses. Surface points outside the dent being fully elastic, or almost, the strain measurement can be directly related to the residual stress tensor by the classical theory of elasticity and so the surface strain measurement can be seen as a direct measure of surface residual stresses.

In the impact dent, corresponding to the contact zone during the impact, significant differences are observed between experiments and simulation,except for the equivalent residual strain. Two facts may explain these differences. First, although frictional simulations were performed as a first step, no specific care was taken for the description of the stick and slip zones during the impact. As indicated before, recent work by Fulleringer [FUL 11] showed that indentation simulation results might be significantly influenced by the coupled effect of both friction and plasticity. The radial residual displacement in the contact zone is highly influenced. Secondly, the quality of the results in the dent zone is clearly lowered by the lack of data due to the reflections and the interpolation. This clearly explains the peaks on the experimental values (see in particular Figs. 5.20(d), 5.22(c) and 5.23). Yet the signs of the residual strains ε_{xx}^{res} and ε_{yy}^{res} in the contact area differ between simulation and experiments, although some global trends are similar. Frictional effects along with the limits of the SAM at large strain levels might explains this important differences but further investigation would here be necessary.

5.7 Conclusions

This chapter presented a first set of experimentations meant to validate impact models. Thanks to a collaboration with the Mécasurf Laboratory at AMPT Aix-en-Provence, single impact experiments were performed on a impact test-rig prototype. Impacts were performed on three different materials, with balls of the maximum possible diameter and over the whole range of impact velocity the rig could provide.

The impact velocity was measured by two methods: laser barriers and fast speed camera measurements. Despite this, the precision obtained on the velocity measurement was not optimal which is a first important bias of these experiments.

Results were analysed through three kinds of measures:

- the coefficient of restitution. A good correlation was observed between the experimental results and formulae provided in chapter 4. Results of the coefficient of

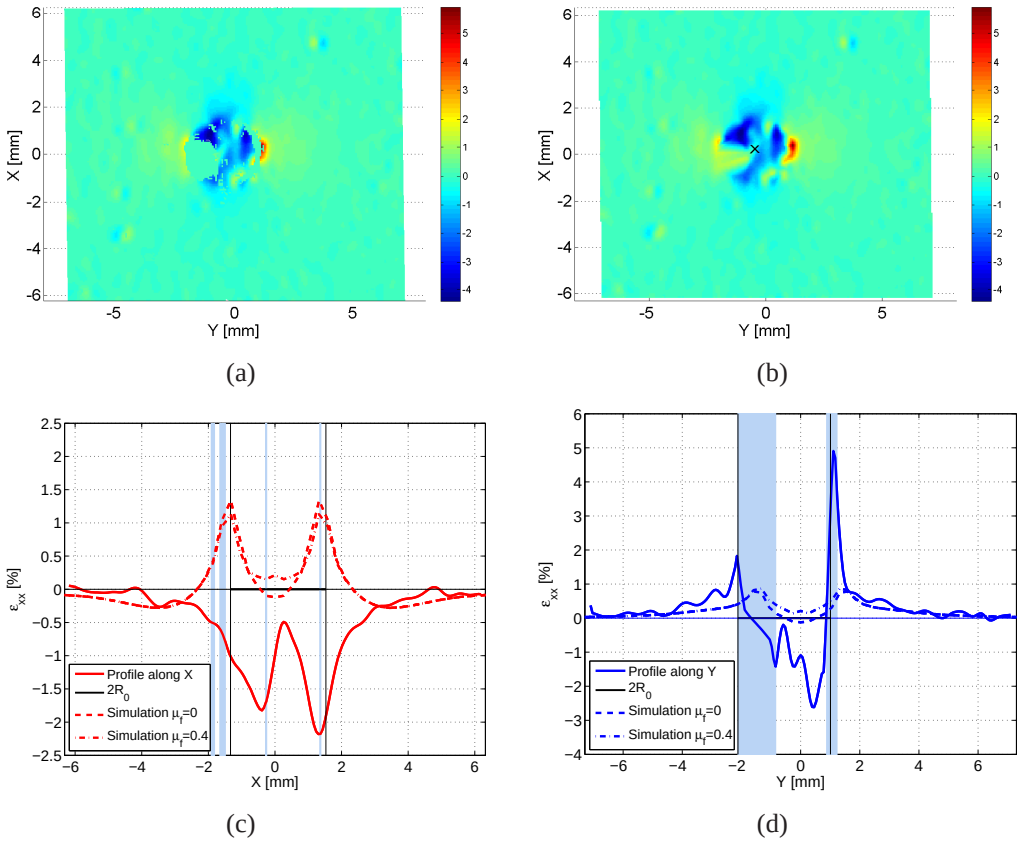

Figure 5.20: Residual strain ε_{xx}^{res} measurements on a stainless steel 316L sample, impact velocity measured at $44m/s$, first lighting orientation. (a) Raw stereo correlation strain measure (in mm/mm). (b) Interpolated strain measure (in mm/mm). Measured profiles in x (c) and y (d) directions, interpolated zones in light blue, superimposition with results from frictional and frictionless simulations.

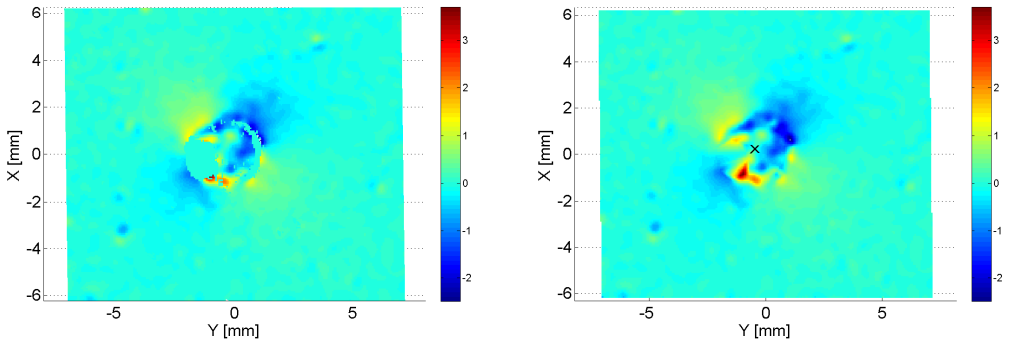

(a) (b)

Figure 5.21: Residual strain ε_{xy}^{res} measurements on a stainless steel 316L sample, impact velocity measured at $44m/s$, first lighting orientation. (a) Raw stereo correlation strain measure (in mm/mm). (b) Interpolated strain measure (in mm/mm).

restitution were also used to determine roughly hardening parameters for the AA 7010 for which no fair data was available due to ageing of the material.

- surface profile by contact profilometer and stereo correlation. Optical measures were interesting for the short time they require, yet the small size of the impacts and the difficulty to establish a good contrast on the impacted surfaces strongly limited the quality of the stereo correlation results. These results showed a good capability of the SAM to predict the depth of impacts and confirmed the limitations observed at the border of the contact zones and for high strain levels observed in the former chapters.

- surface residual strain by stereo correlation. Though limited by the quality of the correlation results and subject to discussion in the impacted zone for reasons that still need to be clarified, very encouraging results were found in the zones out of the impact and for the von Mises equivalent residual strain.

This first set of experimental results so validates the SAM method while also confirming its currents limitations. Complementary analysis on the effect of friction and in the consideration of large displacement in the SAM may provide fairly better fit between simulations and experiments. As improvements in the simulations are to be considered, improvements in the experimental results are to be expected as well. The experience acquired through these experiments provided interesting knowledge for further impact experiments and a large range of possibilities is observed by the stereo correlation measures.

Complementary measures have also been considered on the actual samples. Residual stress measurements might be performed on these samples and compared with simulations

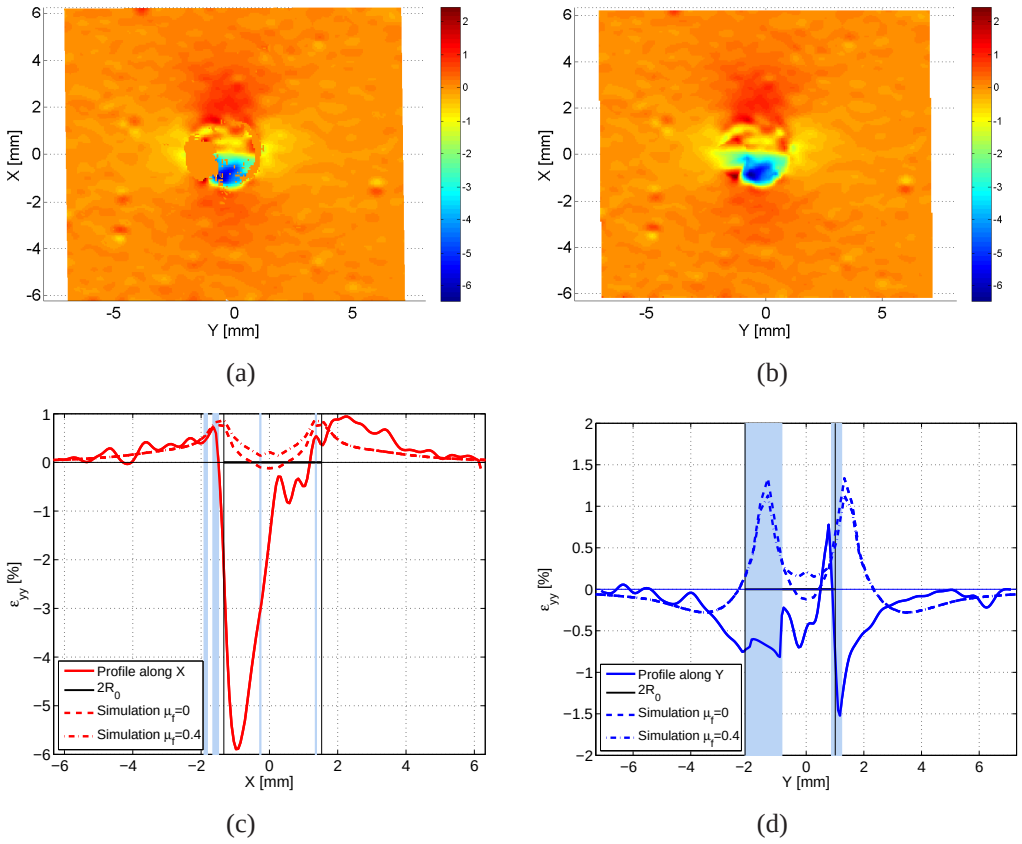

Figure 5.22: Residual strain ε_{yy}^{res} measurements on a stainless steel 316L sample, impact velocity measured at $44m/s$, first lighting orientation. (a) Raw stereo correlation strain measure (in mm/mm). (b) Interpolated strain measure (in m/mmm). Measured profiles in x (c) and y (d) directions, interpolated zones in light blue, superimposition with results from frictional and frictionless simulations.

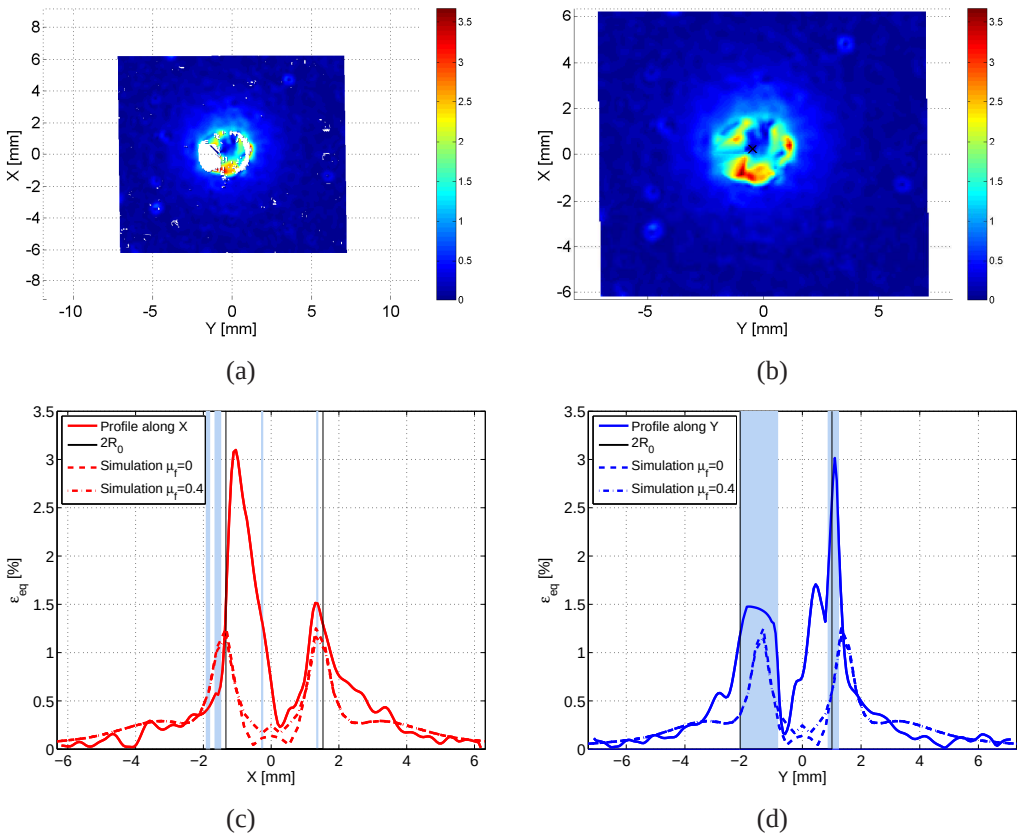

Figure 5.23: Residual strain ε_{VM}^{res} measurements on a stainless steel 316L sample, impact velocity measured at $44 m/s$, first lighting orientation. (a) Raw stereo correlation strain measure (in mm/mm). (b) Interpolated strain measure (in m/mmm). Measured profiles in x (c) and y (d) directions, interpolated zones in light blue, superimposition with results from frictional and frictionless simulations.

results. The relatively small size of the impacted zone as compared to a classical averaging area for residual stress measurements may provide results difficult to interpret and it is expected that the gradient of residual stresses in the measured area would be high enough to interfere with the measurements. A second set of planed measurements is the definition of the micro structure of the impacted sample and the analysis of its evolution through the impact. Although not considered in the current SAM model, eventual change in the material micro structure might be integrated in the model, at least in a phenomenological manner.

Modelling of Multiple Impacts

This last chapter deals with the use of the semi analytical method for the simulation of multiple impacts. A full methodology is proposed to model the plastic strains and residual stresses generated by a large number of impacts in a reduced number of semi analytical simulations. A benchmark with finite element codes is first performed and the influence of several impact parameters is studied (velocity, coverage rate, impact repartition,...). The simulation of a full ultra sonic shot peening process is then proposed and the results compared to an experiment within a thin plate.

Contents

6.1 Introduction

The previous chapters have provided results mainly for single impacts or impacts occurring at a constant position. Numerical and experimental validations were provided for these cases. The study of the literature provided several ways to model multiple impacts, mainly based on analytical or FE models. Analytical models are usually highly simplified. A huge number of FE models exist, the current calculation powers allowing the simulation of large number of impacts. Nevertheless, the size of the models remains an important problem.

A method for the simulation of multiple impacts is proposed in this chapter. Based on several hypotheses on the residual state of a peened piece a model to represent a large number of impacts in a reduced number of simulations is proposed. The main advantage of this model is its very fast computation time. As for the single impact, a benchmark with finite elements codes has been performed to validate numerically the results obtained by the SAM for multiple impacts.

Using the fast computation speed of the SAM, several sets of simulation were performed to analyse the influence of various parameters on multiple impact results. Several models, and the effect of material and process parameters are thus analysed providing a good understanding of the phenomena involved in multiple impacts.

The multiple impact model being defined and studied two complementary model and methods are proposed to simulate a complete ultrasonic shot peening process. A macroscopic ultrasonic shot peening is proposed to determine the impacts velocities from the process and material parameters. The SAM multiple impact model then allows to calculate residual strains from the impact velocities and material parameters. At last a methodology is proposed to determine residual stresses and macroscopic deflections in finite size structures from the SAM results, allowing so to model a complete ultrasonic shot peening process.

6.2 Multiple Impact scheme and reference area

It is assumed that after a uniform shot peening treatment on a surface, the residual stress and strain state has specific characteristics. The strain state is considered uniform in planes parallel to the surface and isotropic, i.e. independent on the x and y coordinates of the point at which its value is observed and on the chosen coordinate system.

The impacts are supposed to occur on regular positions. These positions are located on the angles of equilateral triangles which side length is noted d. The coverage rate c is then calculated as the ratio between the surface covered by the impacts over the total surface. Taking the triangle formed by the center of three impacts, a reference area A_r is defined. The covering rate can then be calculated over the reference area as follows:

$$c = \frac{2\pi}{\sqrt{3}} \left(\frac{a^*}{d} \right)^2 \tag{6.1}$$

Where a^* is the contact radius for a single elastic plastic impact. A faster estimation of the coverage rate could be made here by taking into account the contact radius for an elastic impact a_e^*, since this quantity can be calculated analytically. Yet for large velocity impacts and low hardening materials, commonly involved in shot peening, the difference between a_e^* and a^* can be very high thus leading to a wrong estimation of the coverage rate.

When studying shot peening experimentally, the coverage rate is defined as the surface covered by the impacts over the total treated surface, for a given time of process. This measure is usually made visually and is thus quite inaccurate. It is possible to define a 100% covering rate when the whole surface has been covered by at least one shot. Simple analytical formulae allow then to estimate the time of processing leading to a specific covering rate.

For simulations, the covering rate can easily be defined as shown in Eq. 6.1. This definition of the simulated covering rate depends on the relative impact positions and is slightly different from the experimental definition. With balls impacting the surface at a regular distance on a triangular pattern, the surface is completely covered when the impact radius is equal to $2/3$ of the altitude of the triangle which corresponds to a covering rate equal to approximately 121%. This difference between experimental and simulated covering rate might seem significant yet it is beyond the accuracy of the experimental measure and can be expected to be negligible compared to the effective sensitivity of the results to the covering rate.

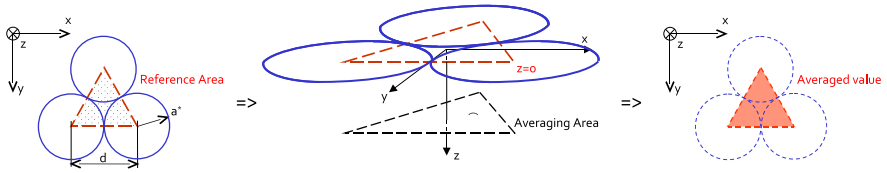

(a)

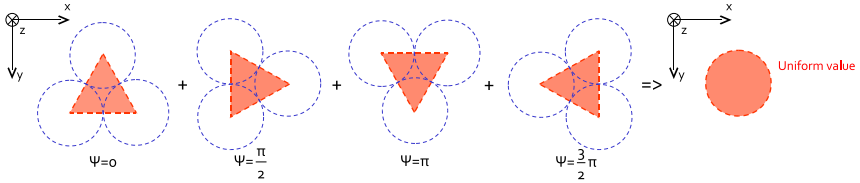

(b)

Figure 6.1: Reference area definition and averaging process for impacts occurring in a triangular scheme. (a) Definition of the averaging area along the depth z of the impacted body. (b) Averaging for 4 distributions to remove the influence of the coordinate system.

For each depth z, the values of results are averaged over the reference area as indicated in Eq. 6.2:

$$\bar{C}_{ij}(z) = \frac{1}{N_r} \sum_{(x,y)\in A_r} C_{ij}(x,y,z) \mid C = (\varepsilon^p, \sigma^{res}) \tag{6.2}$$

Where N_r is the number of elements in the reference area A_r.

A triangular distribution of the impacts has been chosen to minimize the number of simulations. It allows with only three impacts to obtain a fair representation of the full shot peened state. A drawback of this distribution is that is presents only one plane of symmetry. A square distribution of the impacts, for example, would have led to a system with two planes of symmetry. Simulations have been performed to ensure that the choice of distribution had a low effect on the results. The residual stress and plastic strain tensors averaged in the reference area won't here be diagonal. That is to say that the shear components won't be nil in the reference coordinate system and thus the choice of this coordinate system will have some effect. It is expected that for an isotropic fully shot peened state, the results taken at any point of the surface would be constant, independent of the coordinate system and without off-diagonal terms. This hypothesis is commonly assumed when modelling residual stresses produced by plastic strains or nitriding [ROU 97].

In the case of simulation, the off-diagonal terms, or shearing terms aren't totally nil due to the order of impacts but their magnitude is significantly lower than that of the diagonal terms. For impacts occurring simultaneously and with a symmetrical distribution, their value would be zero. To neglect this effect of the number of impacts, it is assumed that four simulations are performed, one reference, and three others, with a rotation of the coordinate system with an angle ψ equal to $\pi/2$, π and $3\pi/2$. The final results, considered representative of the fully shot peened state are taken as the average of these four simulations.

$$\underline{\underline{\bar{C}}}_{\psi} = \underline{\underline{\bar{C}}} + \underline{\underline{\bar{C}}}_{+\pi/2} + \underline{\underline{\bar{C}}}_{+\pi} + \underline{\underline{\bar{C}}}_{+3\pi/2} \mid \underline{\underline{C}} = \left(\underline{\underline{\varepsilon^p}}, \underline{\underline{\sigma^{res}}}\right) \tag{6.3}$$

Considering the change in the local coordinate system this finally leads to :

$$\underline{\underline{\bar{C}}}_{\psi} = \begin{bmatrix} \frac{\bar{C}_{xx}+\bar{C}_{yy}}{2} & 0 & 0 \\ 0 & \frac{\bar{C}_{xx}+\bar{C}_{yy}}{2} & 0 \\ 0 & 0 & \bar{C}_{zz} \end{bmatrix} \mid \underline{\underline{C}} = \left(\underline{\underline{\varepsilon^p}}, \underline{\underline{\sigma^{res}}}\right) \tag{6.4}$$

The final values C_{ψ} of the tensors will know simply be noted C. After this process, a residual stress, and more specifically a plastic strain field is obtained. The value of this field only depends on the depth z and its values are constant in every coordinate system $(\vec{x}, \vec{y}, \vec{z})$ where $\vec{x}$ and $\vec{y}$ are parallel to the surface and $\vec{z}$ in the depth of the body. This field is then coherent with the hypothesis made on the residual strain field in a fully shot peened body. An other advantage of this method is that it deletes the effect of the order of impacts. Simple simulations made by varying the order of the impacts showed that the post processed results are almost exactly the same. The effect of the random order of impacts is then somehow considered by this method.

All following results of multiple impacts are presented averaged following this process. For each set of simulations the distance between the impacts is calculated based on

the desired value of coverage rate and the contact radius a^* value issued from the first impact simulation.

6.3 Multiple Impact Benchmark

6.3.1 Codes and Impact parameters

As for a single impact (see chapter 4), a benchmark has been conducted between the SAM and three finite element codes. The aim of this benchmark was to validate the numerical results issued from several computational methods. Three impacts are simulated and results are post-processed as indicated in the former section to work on final averaged values independent of the coordinate system and of the order of impacts. The impacts of elastic 100Cr6 shots on a Inconel 600 flat with isotropic hardening properties are simulated to match a real engineering case. A reference coverage rate of 100% is simulated and the impact velocity of the shots is considered constant and equal to $8m/s$ here again to be close to the experiments presented further. A first analysis of the results showed that the level of plastic strain reached is relatively high compared to the demonstrated current capabilities of the SAM and a certain care is brought to the analysis of the results. The benchmark simulation parameters are presented in Tab. 6.1.

	Body 1	Body 2
Geometry	Sphere $R = 2mm$	Flat
Material	100Cr6	Inconel 600
Density	$\rho_1 = 7800kg/m^3$	N.A.
Elastic properties	$E_1 = 207GPa$ $\nu_1 = 0.3$	$E_2 = 218.2GPa$ $\nu_2 = 0.3$
Plastic properties	Purely elastic	Ramberg-Osgood $\sigma_{y0} = 274MPa$ $K = 1450MPa$ $n = 0.8$
Initial velocity	$v = 8m/s$	
Number of impacts	3	
Distance between impacts	$e = 0.619mm$	
Coverage rate	$c = 100\%$	

Table 6.1: Material parameters for the multiple impact benchmark between the Semi Analytical Method, Abaqus, code_ASTER and Systus.

The numerical parameters used by each code are presented in Tab. 6.2. The finite elements used by each model are the same, with complete integration, while the SAM cuboids have only one central calculation point which is closer to a reduced integration element. The elements size in the contact areas are the same for the SAM, Systus and

Code_Aster with similar depth. The abaqus simulation was made with much smaller elements in the surface directions but with a depth similar to the other models. This would allow somehow to analyse the influence of the mesh size in the contact area on the results but the difference is here negligible compared to the discrepancies of the several codes. As for the single impact benchmark, the evolution of the mesh out of the contact areas is let at the discretion of each code user. The CPU time taken for the simulation of three impacts are indicated. The CPU frequencies used for each code are similar and thus the indication of the CPU time is a direct measure of the velocity of the code. The Abaqus simulation took a much longer time than the other ones due to a significant larger number of nodes. The difference of CPU time between Code_Aster and Systus might be due to the same reason. The SAM and Systus models were of similar size but the SAM simulation was more than 10 times faster. The natural velocity of the method is mainly responsible for this but an other interesting source of reduced computation time is the structure of the SAM. Indeed for the first and second impact, only the plastic zone generated by these impacts is to be meshed and so the model size for these impacts is highly reduced.

	Finite Element codes			Semi Analytical Method
	Abaqus	Code_Aster	Systus	
Element size in contact areas	$\Delta x = \Delta y = 16\mu m$ $a^*/\Delta x \approx 20$	$\Delta x = \Delta y = 50\mu m$ $a^*/\Delta x \approx 6.5$		
	$\Delta z = 2\Delta x$	$\Delta z = 30\mu m$		$\Delta z = \Delta x/2$
Element type	Linear hexahedra with full integration			Cuboids with a central calculation point
Number of nodes	1075340	218942	161149	150920[1]
CPU time	$\approx 120h$	$\approx 90h$	$\approx 60h$	$\approx 5.2h$
[1] Number of cuboids in the largest (final) computation zone				

Table 6.2: Numerical parameters for the multiple impact benchmark between the Semi Analytical Method, Abaqus, code_ASTER and Systus.

6.3.2 Results and analysis

The post processed results of the benchmark are presented in details in this section. As usual, distances are normalized by the contact radius a^* calculated for the first impact by the SAM (the variation of a^* for the 2^{nd} and 3^{rd} impacts is actually lower than the mesh size and is thus not measurable) and each stress component is normalized by the initial yield limit of the material, given in Tab. 6.1 and here equal to $274MPa$.

Figure 6.2 shows the plastic strains results. Due to the post-processing of the results the components in the x and y directions are equal and represent the radial component. For all four methods, the results are extremely similar for a depth higher than $0.5a^*$. In the subsurface area (between 0 and $0.5a^*$) a divergence between the different methods is

noticed. This difference makes it impossible to choose one of the solutions to be the good one. The SAM is the only method to show a change in the slope close to the surface. The von Mises equivalent plastic strain, depicted in Fig. 6.2(b), is a direct consequence of these components and shows thus a similar behaviour. The fundamental difference between the SAM and the finite element method might explain this difference. The high level of strain involved in these simulations, that are not completely considered by the SAM may also explain this difference, the maximum plastic strain being located at the surface. The accumulated plastic strain, plotted in Fig. 6.2(c) that describes roughly the history of the strains during the three impacts is highly different between the SAM and the FE codes. If the three FE codes don't give the same results, thus indicating a high sensitivity of this variable to the model, the SAM results are significantly lower than the other ones. Explanations for this difference is the same than for the strain components. It should be noticed here that more than 10% of averaged accumulated plastic strain are observed, indicating that much more higher local values of strain have been reached which corresponds to level of strains for which the SAM still has to be improved. Despite this, the residual strain components, that will generate the residual stresses, are similar between all four methods. The difference in the accumulated plastic strain will have a significant effect in the consideration of the final yield limit of the impacted material.

Results for the stresses are presented in Fig. 6.3. The averaged radial (xx/yy) and in depth (zz) stress components are presented. As a consequence of the plastic strains, the stresses show a rather similar behaviour. The overall results are close between all three methods, the SAM being slightly different than the three FE codes. Interestingly, the results from Code_Aster and Systus are extremely similar for the stresses with a small difference for Abaqus while it was not the case for the strains. The differences on the stresses components somehow compensates for the von Mises equivalent residual stress giving remarkably similar results for all four methods.

Overall the SAM gives slightly different results from the FE methods but a very good fit is observed over all the results. Considering the significant gain in computation time of the SAM, this clearly confirms the interest of the method despite the fact that some improvements for the consideration of large strains remain to be done.

The hydrostatic pressure calculated in the multiple impact benchmark case is presented in Fig. 6.4. Figure 6.4(a) presents the hydrostatic pressure averaged over the reference area. For each value of depth, the value of all points located inside the reference area is also plotted. The hydrostatic pressure calculated along the center of the first impact completes this representation. The averaged value after three impacts is very similar to the value at the center of the first impact. For both cases, the stress is almost nil at the surface and the body is under compression until $3.25a^*$, small tensile stresses beyond this depth but up to a very large depth balance the effect of compression to ensure the equilibrium. The representation of the scattering around the averaged value shows that for a depth higher than $0.5a^*$ all points located in the reference area are under compression. Close to the surface, few points are under tension, certain to a very large value. These points are located in the borders of each impact's contact area as visible in the following figures. Figures 6.4(b), 6.4(b) and 6.4(b) represent the residual hydrostatic pressure in

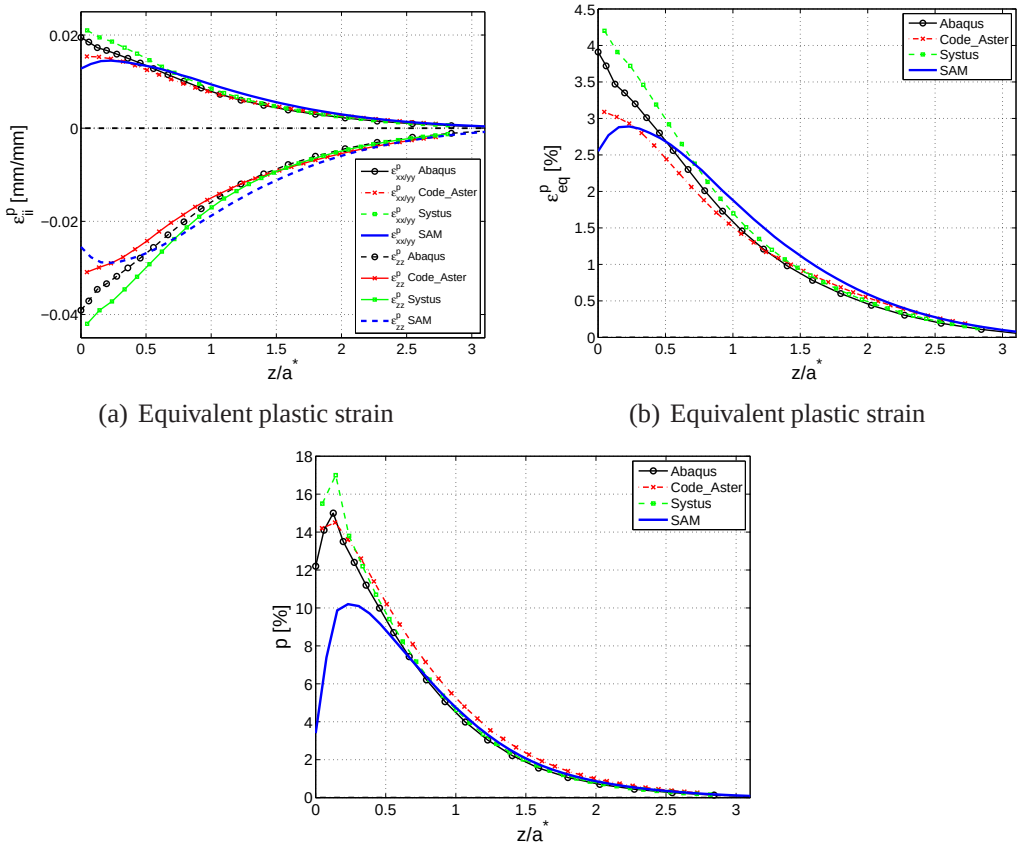

(a) Equivalent plastic strain

(b) Equivalent plastic strain

(c) Accumulated plastic strain

Figure 6.2: Plastic strain components ($\varepsilon^p_{xx} = \varepsilon^p_{yy}$ and ε^p_{zz}) (a), von Mises equivalent plastic strain (b) and accumulated plastic strain (c) along depth z averaged over the reference area for the multiple impact benchmark case.

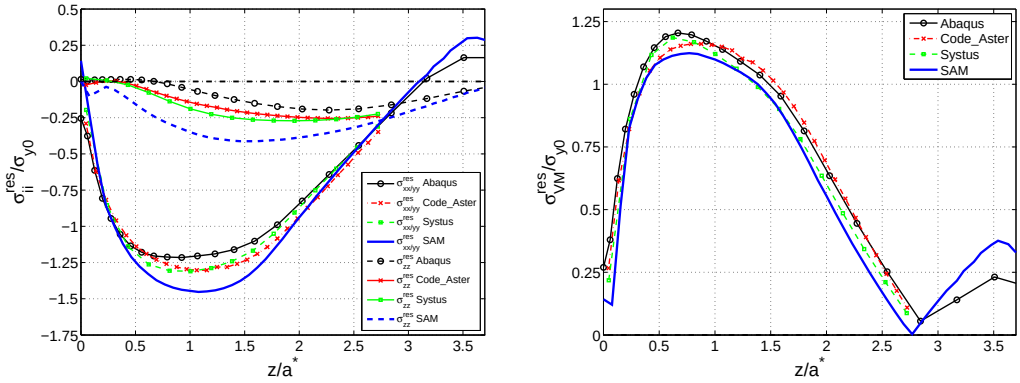

(a) Averaged residual stress components (b) Von Mises equivalent residual stress

Figure 6.3: Residual stresses components (a) and their von Mises equivalent value (b) along depth z averaged over the reference area for the multiple impact benchmark case.

planes parallel to the surface and respectively at the surface for the first impact, at the surface after the three impacts and at the Hertzian depth. The effect of the order of impacts is visible when three impacts are involved, yet the global trends are the same after one or three impacts: the body is in compression in a very large surface except in a small annulus around the impacts, corresponding to the zone where the residual displacement is positive and where the matter is pushed outside the contact area during the impacts. At the Hertzian depth, all the reference area and the surrounding zone is in compression.

Overall, impacts generate, as expected, a layer of compressive residual stresses. The equilibrating tensile stresses are rejected far below the Hertzian depth, as long as it is semi infinite. Localized areas of tensile stresses are located at the surface (see also Fig. 4.8) around each impact but can be expected to be annihilated by subsequent impacts occurring directly on the dent's borders during a full peening treatment.

6.4 Process, model and material parametric study

Several sets of simulations, involving various numbers of impacts have been performed to analyse the influence of several parameters on the multiple impact model proposed here. These various parameters are described in Tab. 6.3. Three kinds of parameters are observed: process, model and material parameters.

The process parameters, though difficult to set experimentally in the way they are proposed here, are analysed. The influence of the coverage rate is analysed in sections 6.4.1 and 6.4.2. This study aims at observing how results evolve with the coverage rate but also how an incorrect knowledge of the experimentally measured coverage rate might change the corresponding simulation results. A second experimental parameter which is difficult to measure is the impact velocity. A method will be proposed further for the estimation of the impact velocity but firstly the influence of a variation of the impact

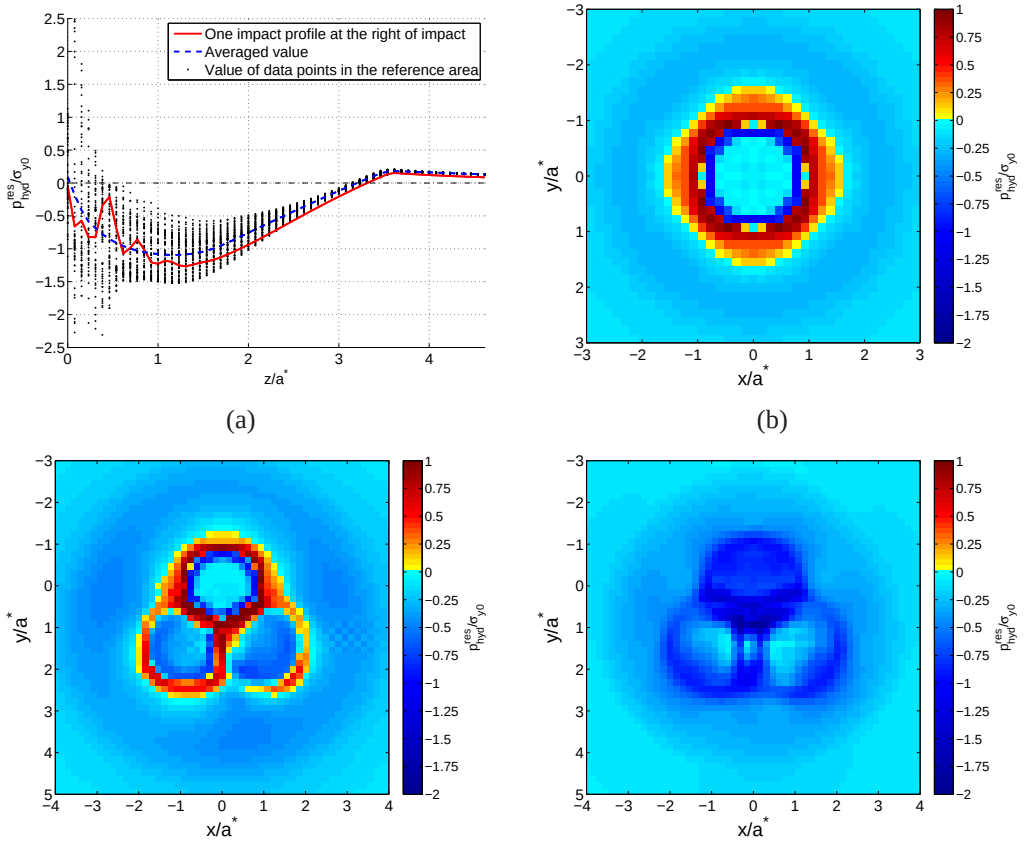

Figure 6.4: Residual hydrostatic pressure for the multiple impact benchmark case. (a) Averaged hydrostatic pressure in the reference area along the depth axis z with all values for points located in the reference area in black dots. (b) Hydrostatic pressure in the surface plane ($z = 0$) after the first impact. (c) Hydrostatic pressure in the surface plane ($z = 0$) after the third impact. (d) Hydrostatic pressure at the Hertzian depth ($z = 0.48a^*$) after the third impact.

velocity around its average value is observed in section 6.4.3. It is expected that the impact velocity would vary a lot in the real case.

Two parameters linked to the model are also analysed. The randomness in the distribution of the impacts is neglected by the model proposed here. Part of this effect is considered by averaging the results over a reference area which size is linked to the coverage rate. The choice of the reference area might affect the results. Section 6.4.2 proposes a study of the effect of the reference area definition on the results. A second important model parameter is the number of impacts considered. A study of the evolution of the results as a function of the number of impacts is proposed in section 6.4.4.

At last, the influence of the hardening model of the impacted material is proposed. Similar sets of simulations of impacts on a purely isotropic, purely kinematic and mixed hardening flat are studied and compared to give insights on the influence of the hardening model on the results.

For all simulations the shots impacting the surface are considered rigid and the impact velocity is purely normal to the surface. The contact is considered frictionless and no computation of the tangential contact problem is made. The range of normalized velocity varies for each simulation as indicated by the impact velocity and the initial yield limit in Tab. 6.3. All considered impacted materials have the same Young's modulus and Poisson's ratio, respectively equal to $200Gpa$ and 0.3. For the majority of results, four data are plotted for each simulation case. First the von Mises equivalent plastic strain calculated with the averaged plastic strain values over the reference area is presented as a picture of the level of remaining plastic strains. The averaged accumulated plastic strain is given to complete the former data with a picture of the history of strains. Averaged residual stresses are given through two data: the von Mises equivalent value of the averaged residual stress components, to provide a representation of the amount of residual stress and the residual hydrostatic pressure, to visualize the tension or compression state of the considered areas. As usual, distances are normalized by the contact radius of the first impact (used to calculate the coverage rate), stresses and strains are normalized by the corresponding initial yield values σ_{y0} and ε_{y0}

6.4.1 Application of reference

A first set of simulations for which parameters are indicated in Tab. 6.3 is presented here. Three sets of simulations are performed with all parameters but the coverage rate taken constant. The coverage rate varies from 75% to 125% which is estimated to be a large range of imprecision in an experimental measurement of a 100% coverage rate.

Resulting plastic strains (Figs. 6.5(a) and 6.5(b)) indicate a slight saturation effect beyond 100% of coverage rate. Both the residual and the accumulated plastic strain show a very small evolution between 100 and 125% of coverage rate. A saturation effect is thus observed on the strain, indicating that beyond a certain threshold the evolution of the residual strain might become negligible. This threshold might vary a lot with the material and hardening parameters and with the considered velocity, as some further simulations indicate.

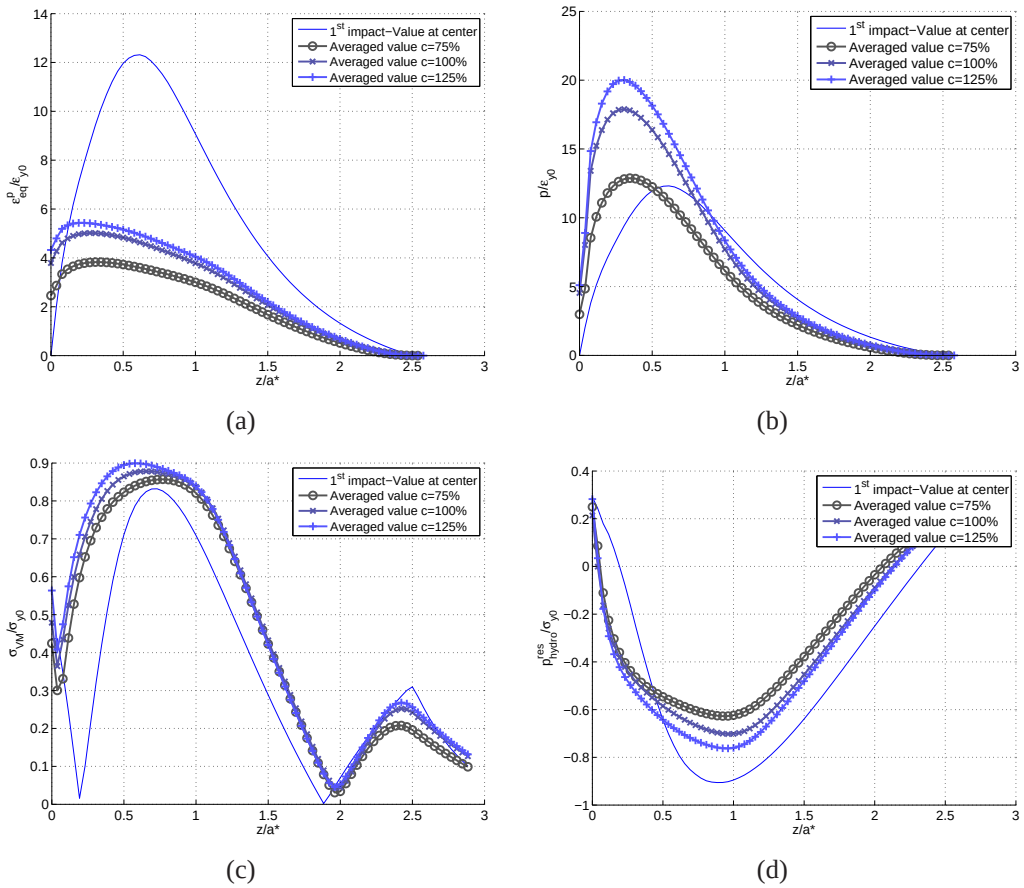

Figure 6.5: Influence of coverage rate on averaged results for 3 impacts on a linear isotropic hardening body ($E_T/E = 10\%$). (a) Equivalent plastic strain of averaged plastic strain components. (b) Averaged accumulated plastic strain. (c) Von Mises equivalent of averaged residual stress components. (d) Averaged hydrostatic pressure.

Section	Number of impacts	Impact Velocity [m/s]	Yield limit σ_y [MPa]	Tangent modulus E_T/E	Coverage rate c [%]
6.4.1	3	20	800	10	[75;100;125]
6.4.2	3 4 6	2.5	400	10	[50;100;150;200] 100[1] 200[2]
6.4.3	3	$[20+/-20\%E_{kin}]$	800	10	100
6.4.3	3	$[20+/-50\%E_{kin}]$	800	10	100
6.4.5	3	2.5	400	10[3]	100
6.4.4	6	10	400	0	150
6.4.4	6	10	400	10	[50;100;150]

[1] Square distribution of the impacts
[2] Doubling of the impacts of the $c = 100\%$ simulation
[3] Isotropic, kinematic and mixed hardening

Table 6.3: Multiple impact simulations parameters

For the stresses, values are almost constant for all coverage rates. The von Mises stress clearly saturates at a value linked to the initial yield limit, while a slight increase in the hydrostatic pressure level is observed. The differences between all observed results are clearly below the accuracy of residual stress measurements and might be taken constant for comparison with experiments. The trends and shapes are very similar to those observed in the multiple impact benchmark case. The levels of strains are close and in both case, the hardening effect is rather low compared to the initial yield limit. Further simulations in section 6.4.2 will show slightly different von Mises stress distribution when the amount of hardening is higher.

For this set of simulations, the corresponding data values taken in the depth at the center of the first impact are also indicated. It should be noted that the level of averaged residual plastic strain is significantly lower than the one taken only at the center of the impact while the amount of accumulated plastic strain is higher. When three impacts are involved and the coverage rate is high enough, the points in the reference area will be strongly influenced by each impact and a lot of plastic flow will occur. A difference is observed in the depth of the maximum value of p at the center of the first impact and after averaging of the results. Figure 6.6 shows the typical accumulated plastic strain distribution in the plane passing by the center of impact. It can be observed that the zone of maximum plastic strain has its higher depth at the center of the impact and goes closer to the surface around $x = a^*$. So the maximum value of p at the center of the first impact is taken at the maximum depth, while the averaged value considers the areas closer to the surface in which the strain level is the highest. Consequently a shift towards the surface is observed when the plastic strain values are averaged over the reference area.

For the stresses the global shapes and level are similar at the center of the first impact

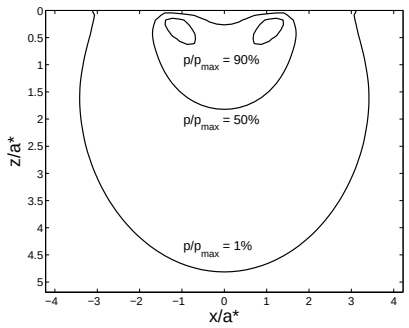

Figure 6.6: Typical accumulated plastic strain profile in the (x,z) plane after one impact.

and over the reference area. Yet, as for the equivalent residual strain a spreading in the depth of the area of the maximum is observed when three impacts are involved.

The residual strain and stress gradients are of great importance when the results are confronted to experiments since (stress) measurements are always averaged over a reference area.

6.4.2 Impact schemes

The effect of the coverage rate is here investigated from a different manner. Compared to the former section results, the initial yield limit is lower while the hardening and elastic properties are the same. Consequently, a higher amount of hardening is involved. The coverage rate ranges from 50 to 200% and two particular cases are proposed: the comparison between a triangular and square distribution of the impacts for a 100% coverage rate, and two representation of a 200% coverage rate. The first one is made by considering three very close impacts for which the coverage rate calculate with Eq. 6.1 equals the desired value. The second one uses the distance between impacts obtained for a 100% coverage rate but the three impacts are doubled to obtain a final 200% coverage rate. This second case might be closer to an experimental 200% case for which the processing time is doubled compared to the 100% case but it involves a higher number of impacts on a larger zone and is thus longer to simulate. Remaining simulation parameters are recalled in Tab. 6.3 and the distribution of impacts for all simulations is presented in Fig. 6.7. Results for all these simulations are plotted in Fig. 6.8.

Global trends are the same than for the previous case. The saturation effect is less clear for this velocity and strain level, yet the evolution of accumulated plastic strain is reduced over 150% coverage rate. The residual strain distribution is slightly less concentrated than for the former case due to the different amount of hardening.

The saturation of the von Mises residual stress with the coverage rate is obvious, while the hydrostatic pressure, as in the former case evolves slightly with the coverage rate. The stress distribution is here closer to what is observed at the center of a single impact. From

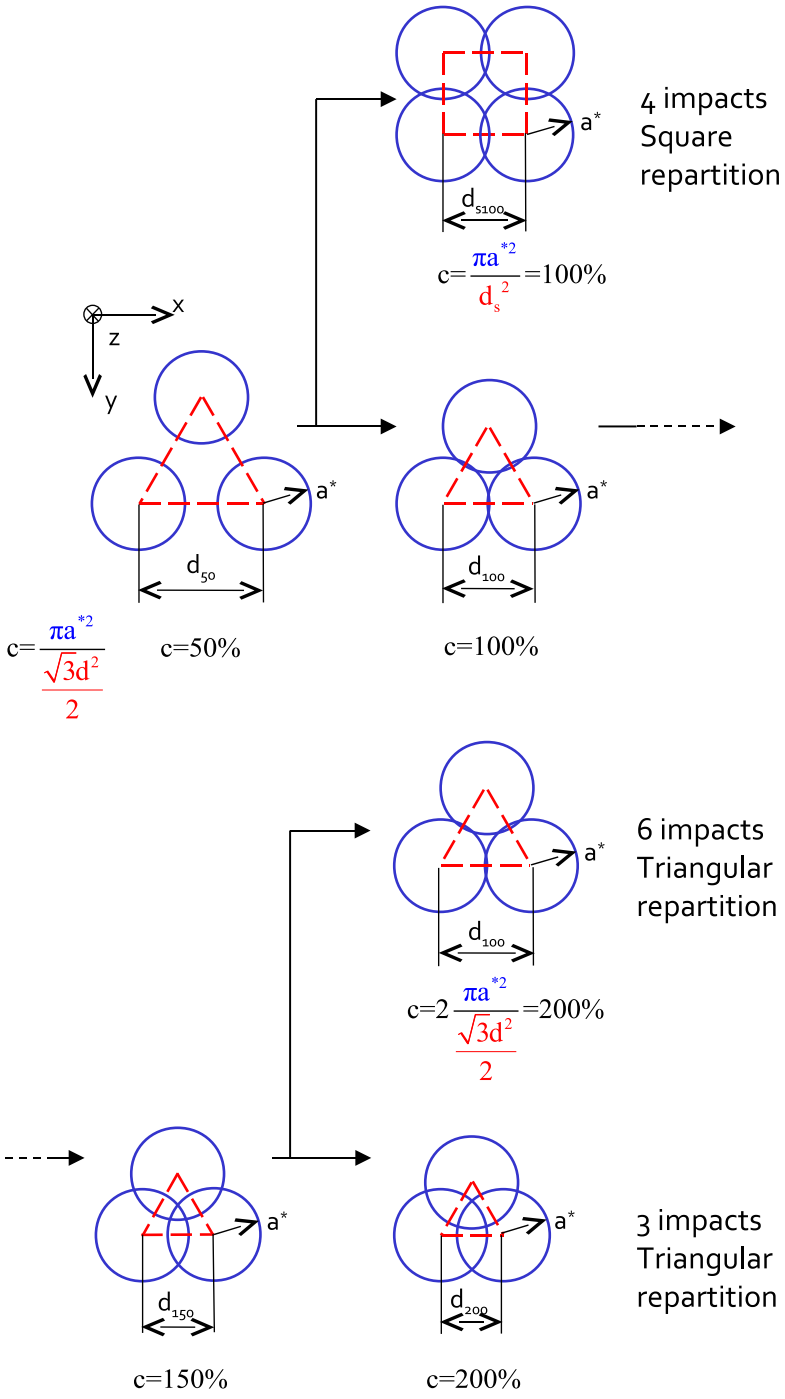

Figure 6.7: Impact distribution schemes for several cases. Calculation of the coverage rate c as a function of the distribution, the contact radius a* and the distance d between impacts. Subscript s denotes the case of a square distribution and the number in subscripts references the coverage rate.

this might be concluded that: (i) a saturation effect on the von Mises stress in a semi infinite body appears very fast with an increasing coverage rate, (ii) the saturation on residual strains depends on the material properties and velocity level , (iii) the residual stress and strain distribution and the value of coverage rate at the saturation is highly dependent on the hardening and velocity levels.

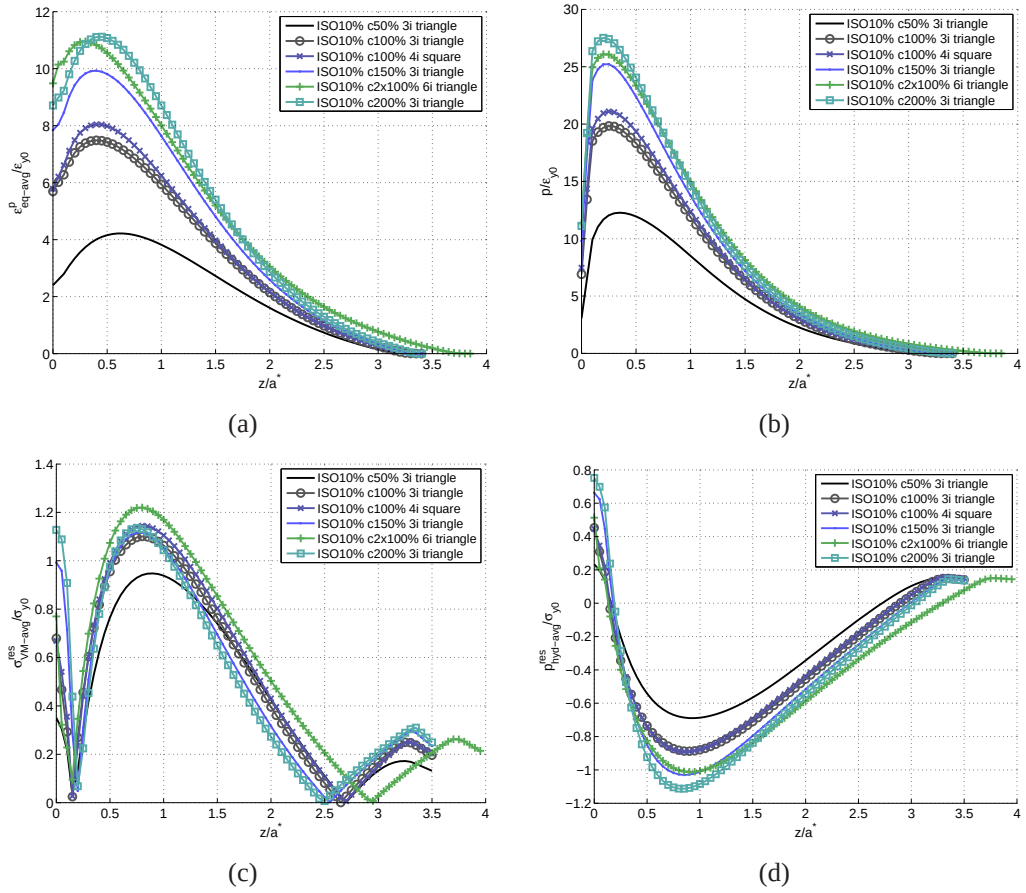

Figure 6.8: Influence of coverage rate on averaged results for 3 impacts on a linear isotropic hardening body ($E_T/E = 10\%$), comparison of the effect of the impact distribution scheme (triangle vs. square at $c = 100\%$ and $c = 200\%$ vs. $c = 2 \times 100\%$). (a) Equivalent plastic strain of averaged plastic strain components. (b) Averaged accumulated plastic strain. (c) Von Mises equivalent of averaged residual stress components. (d) Averaged hydrostatic pressure.

Considering the effect of the impact distribution, results show first than a square distribution of the impacts gives results very similar to a triangular distribution. For the studied case, averaged residual stresses are exactly the same for both cases and the difference in the averaged strains are very low, especially compared to the effect of the coverage

rate. Complementary simulations on different cases, though not indicated here, indicate the same trends. Consequently the influence of the impact distribution can be considered negligible.

At last, the two simulations sets of a 200% coverage rate give results of similar shapes and amplitude. Accurate conclusions would require more complete simulations but these first trends tend to indicate that the residual and accumulated plastic strains are close enough in both case for the model to be considered equivalent. The scattering in the stress distribution is higher, especially compared to the other simulations results. Yet these data are for simulation in a semi infinite domain and more complete results in a finite structure might draw different conclusions.

6.4.3 Influence of velocity variation

The influence of a variation of the impact velocity is studied here. It is convenient, and commonly done, to perform simulation of multiple impacts with a constant impact velocity. This allows to remove one parameter of randomness from the models. In shot peening processes, the impact velocity is never constant. It is possible to determine an average velocity from model of the process (see for example sec. 6.5) but becomes then necessary to determine how results from simulations of multiple impacts with a constant velocity differ from the reality in which the impact velocity varies. Preliminary answers are proposed here on some sets of simulations for which the impact velocity of the three impacts considered varies around an average reference value.

For each case, three simulations of three impacts are made. The first simulation considers three impacts at a constant reference velocity v_{ref}, corresponding to a reference kinetic energy E_{kinref}. For the second simulation, the first impact velocity is lower than the reference velocity and so that the kinetic energy of the first impact is 20% lower than E_{kinref}; the second impact velocity is equal to v_{ref} and the last impact velocity is higher than v_{ref} with a kinetic energy 20% higher than E_{kinref}. The third simulation considers the same impact velocities but this time the impact velocity decreases for each impact. For each simulation the total kinetic energy brought to the body through the three impacts is constant and equal to $3E_{kinref}$. The remaining impact parameters are indicated in Tab. 6.3 and the results post-processed as usual are presented in Fig. 6.9.

Results for this three sets of simulation are almost the same. Slight but negligible differences can be observed in the accumulated plastic strain and in the von Mises residual stress at very large depth. A similar set of simulations is performed with a larger kinetic energy variation (up to 50%) between each impact, results are plotted in Fig. 6.10.

For this larger variation case, the difference between the three cases is again very small. The differences in residual stresses are negligible, a slight increase in the von Mises stress and hydrostatic pressure is observed with the increase of the first impact velocity. The accumulated plastic strain and thus the history of plastic strain is lower when the velocity varies but the residual level of plastic strain (Fig. 6.10(a)) is almost constant.

From these simulations it can be concluded that a variation of the impact velocity

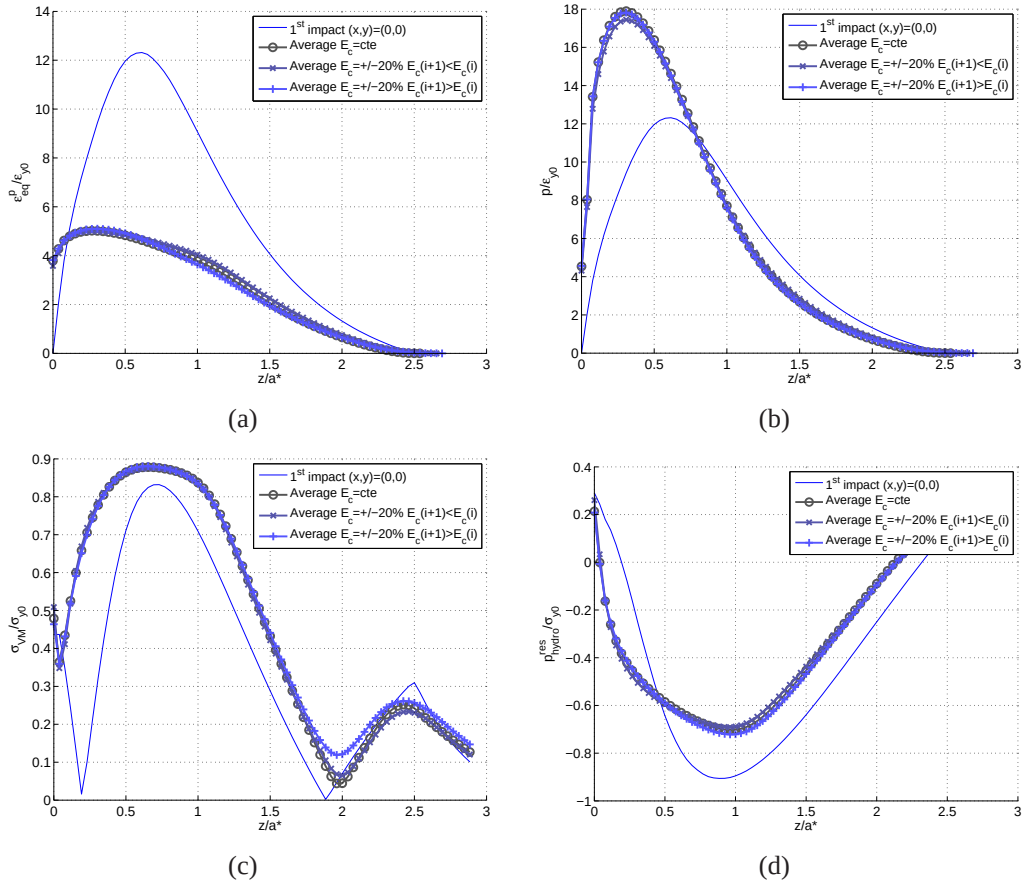

Figure 6.9: Influence of a variation of 20% of the impact's kinetic energy on averaged results for 3 impacts on a linear isotropic hardening body ($E_T/E = 10\%$). (a) Equivalent plastic strain of averaged plastic strain components. (b) Averaged accumulated plastic strain. (c) Von Mises equivalent of averaged residual stress components. (d) Averaged hydrostatic pressure.

has a negligible effect on the results as soon as the total kinetic energy brought to the system is constant. Complementary simulations applied to most specific cases might be performed but it is already possible to validate the hypothesis of a constant impact velocity for multiple impact velocity as soon as this velocity is representative of the average kinetic energy of the shots. Remains now to determine this average velocity which will addressed further.

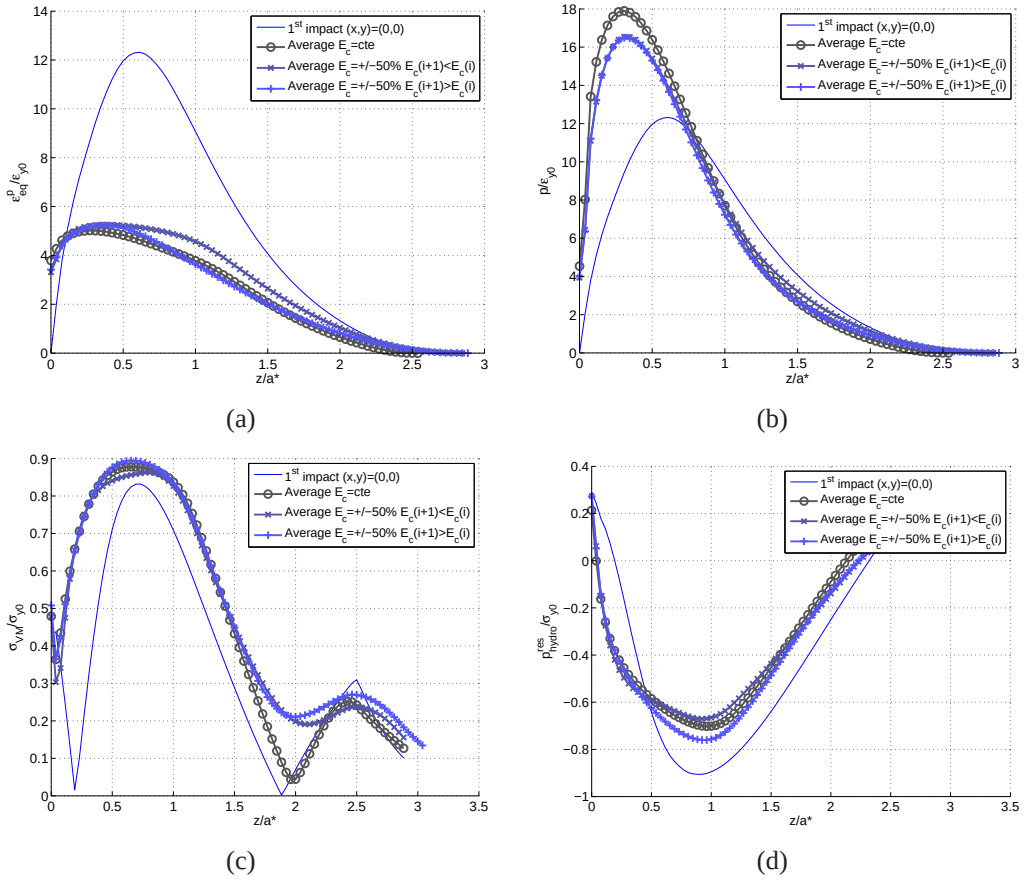

Figure 6.10: Influence of a variation of 50% of the impact's kinetic energy on averaged results for 3 impacts on a linear isotropic hardening body ($E_T/E = 10\%$). (a) Equivalent plastic strain of averaged plastic strain components. (b) Averaged accumulated plastic strain. (c) Von Mises equivalent of averaged residual stress components. (d) Averaged hydrostatic pressure.

6.4.4 Number of impacts to shakedown

All simulations presented were considering only three impacts before averaging the results in the reference area. This value is the minimum necessary to define correctly the reference area but might seem insufficient to correctly define the results in this reference area. The analysis of results was made on the residual stresses and strains but it is important to remind that the stresses are only a consequence of the plastic strains and were calculated in a semi-infinite body. They will differ depending on the boundary conditions and size of the body in which the plastic strains are generated. When considering more than three impacts, up to 6 in this case, as defined in Fig. 6.11, the correct number of impacts is reached when the strain averaged over the reference area does not evolve any more with further impacts. To determine this critical number of impacts, simulations of 6 impacts are made and the accumulated plastic strain averaged over the reference area is observed.

Two cases are observed: impacts on a 10% isotropic hardening body with 50, 100 and 150% coverage rate and a more critical case of a perfectly plastic body with a 150% coverage rate. This second case can be considered as a limit case. As no hardening is involved the evolution of plastic strain from one impact to the other is the highest. In the case of a 150% coverage rate, the contact radius a^* is approximately equal to $2/3$ of the distance between impacts. With very large overlapping of the impacts, the influence of each impact on the previous impact's plastic strain is about the highest.

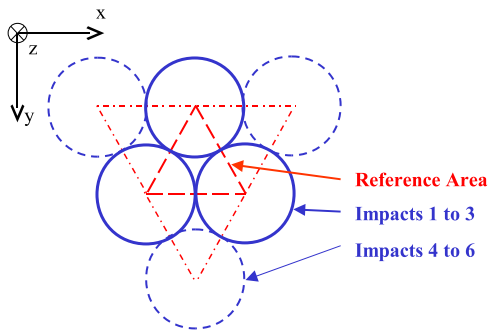

Figure 6.11: Distribution of impacts in a triangular scheme. Definition of the reference area with the center of the three first impacts and subsequent impact positions.

For the three cases of isotropic hardening (Fig. 6.12(a)) the accumulated plastic strain averaged in the reference area is exactly the same after 3 and 6 impacts. The second set of impacts (4 to 6) has absolutely no effect on the evolution of plastic strain in the reference area, the stresses, though not represented here, are reorganized by the subsequent impacts but simply as the effect of changes in the boundary conditions around the reference area.

For the second case (Fig. 6.12(b)), only a slight increase of the accumulated plastic strain is observed between the 3^{rd} and 6^{th} impacts. Three impacts are then considered as

a very reasonable value to determine a converged state of plastic strain over the reference area. A very low number of simulations is thus needed to determine a state of plastic strains representative of a full shot peening process. Remains the problem of the determination of stresses. The stresses calculated here are obtained in a semi infinite body that remains predominantly elastic. The study of the number of impacts giving a stabilized stress state has not been done here. It is expected that beyond a certain number of impacts, the stresses in the reference area would show no more evolution, the change in the boundary conditions being too far from the considered zone to affect the stress distribution. This number of impacts can be expected to be significant, implying simulations on a very large computation zone while the only operation done would be to reproduce the plastic strains of the reference area over the surroundings areas and compute the stresses over the obtained domain. A faster and much more simple method to do this operation will be proposed further.

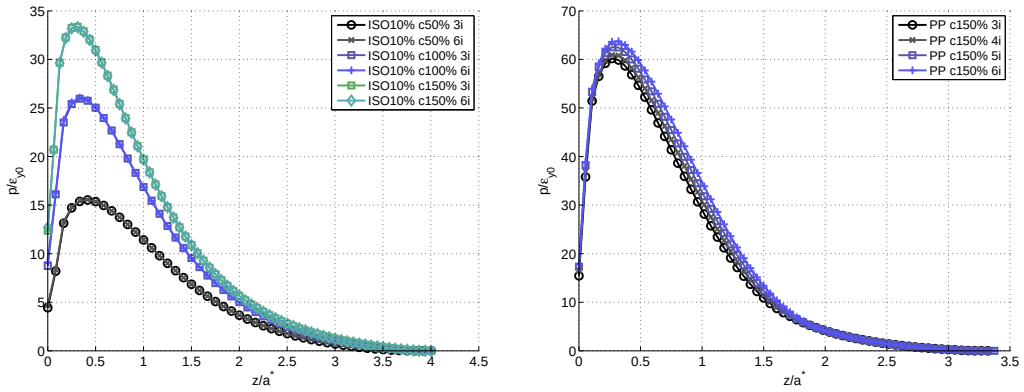

(a) (b)

Figure 6.12: Evolution of the accumulated plastic strain p normalized by the yield strain for 6 impacts on (a) an isotropic hardening body ($E_T/E = 10\%$; coverage rates $c = [50\%; 100\%; 150\%]$) and (b) a perfectly plastic body (coverage rate $c = 150\%$).

6.4.5 Hardening model influence

For many applications, material properties are only given by a simple tensile curve and the kinematic part of the hardening is not necessarily known. When multiple impacts are considered the sign of radial stresses in some parts of the reference area might change sign and cyclic effect might be involved. It might be then of great importance to consider kinematic effects when modelling multiple impact processes. It is proposed here to observe the influence of the hardening model. Several simulations, which parameters are given in Tab. 6.3, are done varying the hardening model. The typical 10% isotropic

hardening case is presented with simulations for cases of a perfectly kinematic hardening body with equivalent tensile curve and an intermediate mixed hardening body with 50% of isotropic and kinematic hardening. Definition of the hardening models can be found in section 2.4.2 and in Fig. 2.7.

Results, presented in Fig. 6.13, show almost no difference between the isotropic and mixed hardening cases.

For a purely kinematic hardening body though, very large differences are observed. Both the residual stresses and strains profiles are highly modified up to $1.75a^*$ depth. The phenomenon observed here is the same than the one described in chapter 3. When the second and third impacts occur, the sign of the radial stresses in some parts of the reference area changes. Up to a certain depth, the amplitude of stresses is large enough to produce reverse plasticity and thus decrease the equivalent residual plastic strain level (see Fig. 6.13(a)). At the same time, the accumulated plastic strain logically increases, see Fig. 6.13(b). This reorganization of the plastic strains expresses as a strong modification of the residual stresses. Both the levels of von Mises equivalent stress and hydrostatic pressure are decreased between the surface, at which they are nil, and $z = 1.75a^*$. These profiles of stresses are very specific and due to the specific boundary conditions involved in a three impacts modelling. Kinematic effects can so have strong effects in the strain and stress results.

The cyclic effects in a multiple impact loading are so negligible if the kinematic effects are not large enough but their influence can become significant if they are activated.

6.5 Shot peening process modelling

Previous results showed that fast and efficient simulations of multiple impacts can be performed with the SAM. Simulation results also showed that the model is not highly sensitive to a variation of the velocity around a reference average value or to different definitions of the coverage rate. A correctly estimated average impact velocity and coverage rate are thus the only necessary process parameters necessary as input to the model. The presented model was only considering impacts normal to the surface. The influence of a tangential component of the velocity can be considered negligible for impact angles lower than 30. Two main problems are addressed here for the case of ultrasonic shot peening: how can the average impact velocity be linked to the process parameters that are the sonotrode amplitude and frequency of vibration and is the hypothesis of impacts normal to the work piece valuable.

6.5.1 Model and simulation parameters

A simplified model of ultrasonic shot peening is proposed here. The peening chamber is defined in a simple Matlab software as a rectangular box in which several shots are moving, bouncing against the walls, the sonotrode and the work piece (see Fig. 6.14). The sonotrode is vibrating following a sine curve.

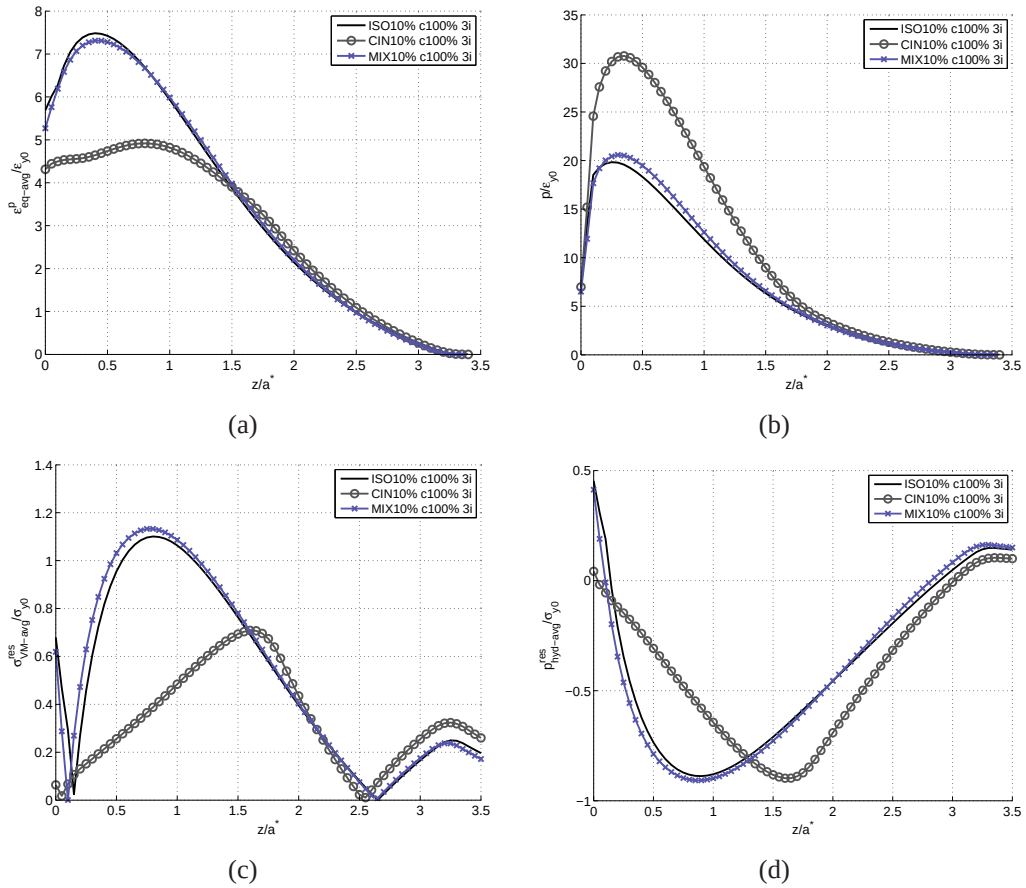

Figure 6.13: Influence of the impacted material hardening model on averaged results for 3 impacts at a coverage rate $c = 100\%$. (a) Equivalent plastic strain of averaged plastic strain components. (b) Averaged accumulated plastic strain. (c) Von Mises equivalent of averaged residual stress components. (d) Averaged hydrostatic pressure.

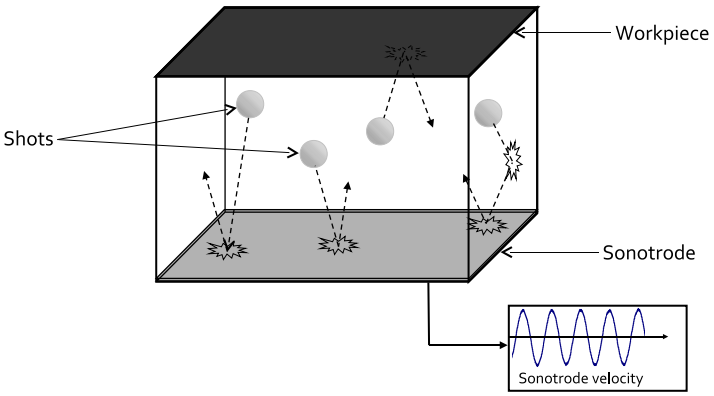

Figure 6.14: Ultra sonic shot peening process model.

From a prescribed initial step of the shots in the chamber, the evolution of the position $\vec{x}$ and velocity $\vec{v}$ of the shots at each time t_i is computed as follows, the shots being under the unique influence of the gravity.

$$\vec{v}(t_i) = \vec{v}(t_{i-1}) + \vec{g}\Delta t \tag{6.5}$$

$$\vec{x}(t_i) = \vec{x}(t_{i-1}) + \vec{v}(t_{i-1})\,\Delta t + \vec{g}\frac{\Delta t^2}{2} \tag{6.6}$$

where Δt is the time step at the current time. The value of Δt is taken the largest to accelerate the computation but limited by the value avoiding overlapping of the shots with other elements. The values of time steps are significantly higher than the typical time of an impact in ultrasonic shot peening, which of the order of $1\mu s$. The impacts are thus considered instantaneous.

For each time step, the minimum distance of the shots with their neighbours and with the chamber parts is calculated to determine if an impact is occurring or not. Where an impact between two elements occurs, the normal $\vec{n}$ between them and their relative velocity v (that differs from the shot velocity only when it impacts the sonotrode) is calculated. The velocity is decoupled in a normal and a tangential value defined by the normal $\vec{n}$ as indicated in Fig. 6.15. The rebounds velocities are calculated using a coefficient of restitution e_N for the normal velocity and e_T for the tangential velocity.

The tangential coefficient of restitution suffers from a lack of knowledge, few literature data exist about it and the current version of the model does not allow to study correctly the tangential effects of impacts. Furthermore, no good knowledge of the coefficients of friction between the different elements of the shot peening chamber was available. Considering here elastic impacts between the shots, and with the walls and the sonotrode, only impacts between the shots and the work piece are elastic plastic. These

impacts being close to normal, the tangential coefficient of restitution is considered constant and equal to 1 for all impacts.

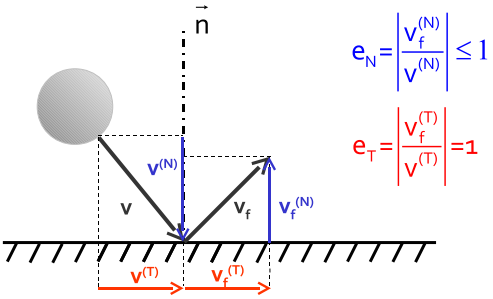

Figure 6.15: Decoupling of the normal and tangential velocities and corresponding coefficients of restitution definition. The tangential coefficient of restitution e_T is considered equal to 1.

The normal coefficient of restitution e_N is considered equal to 1 for impacts between shots and impacts of shots with the walls and the sonotrode. At last, the coefficient of restitution for impacts of shots on the work piece is defined using the formulae proposed in chapter 4. Simulations performed up to this point involve only a limited number of impacts so the influence of the former impacts on the coefficient of restitution is neglected and e_N is calculated for each impact as for a shot impacting a virgin surface. Further investigation might propose an evolution of the coefficient of restitution with the increasing number of impacts to account for existing plasticity, up to a point at which the whole surface is saturated in plastic strains and behaves elastically.

6.5.2 Results - Coverage rate and impact velocity

Results from the ultrasonic shot peening model presented in the previous section are presented here. A relatively long simulation of the shot peening processing of an Inconel 600 sample is performed. Dimensions, material and process parameters are presented in Tab. 6.4. The simulations parameters are taken to match the experiments performed in Li's PhD thesis [LI 11]. A small number of shots was chosen to limit the impacts between shots and keep the impact velocity as normal as possible. Longer processing time to obtain saturation results from this choice. The model's results here allow to validate this hypothesis.

A major difference between the model and the experiments is the size of the sample, that was smaller than the chamber in the case of the experiments and is supposed to have the size of the chamber's top wall for the simulation. The bolts holding the sample, on which the ball can experimentally bounce and then acquire a large tangential velocity components are not modelled neither. At last, in the model, the surface of the sample

and the wall is supposed to stay perfectly flat which is an additional parameter helping keeping a normal impact velocity though being a strong hypothesis.

Initially, the shots are dropped into the box with a velocity close to the sonotrode's maximum velocity with a slight tangential component to introduce a minimum randomness in the model. No detailed study on the effect of the initial conditions on the model results was performed, yet is was observed that the model reaches a stabilized state in very few time steps.

Chamber material	PEHD
Chamber dimensions	$80 \times 40 \times 50 mm^3$
Shots material	Inconel 718
Number of shots	6
Shots radius	3mm
Number of shots	6
Shots initial velocity	Close to sonotrode max. velocity Almost normal to the work piece
Sonotrode material	Ta6V
Sonotrode amplitude of vibration	$75 \mu m$
Sonotrode frequency	20kHz
Sample material	Inconel 600
Simulation time	4200 ms

Table 6.4: Ultrasonic shot peening simulations parameters

For this particular simulation, as indicated in the previous section, the coefficients of restitution are calculated using Eqs. 4.12 and 4.13.

Figure 6.16 presents the evolution of the impact velocity on the work piece during the time of the simulation. All normal impact velocities are represented showing a very large scattering. The absolute, normal and tangential velocities are plotted averaged over $500 ms$ periods of time and over the whole simulation. It can be seen that the transition period of the model is negligible and that the evolution of the velocities is extremely stable over time. The tangential impact velocity appears clearly negligible compared to the normal impact velocity, validating the normal impacts hypothesis, at least when a few number of shots are considered. The normal (or absolute) impact velocity appears to be very close to twice the root mean square (RMS) value of the sonotrode velocity.

Figure 6.17 shows the distribution of the normal impact velocities on the sonotrode and on the work piece over the whole simulation. A relatively large scattering of the data is observed but the averaged value give can directly be related to the process parameters. As indicated before the average normal impact velocity on the work piece is close to twice the RMS of the sonotrode velocity, while the average normal impact velocity on the sonotrode is close to its maximum velocity. The tangential components of the velocities, impacts between shots and with the walls having second order effects here, the shots

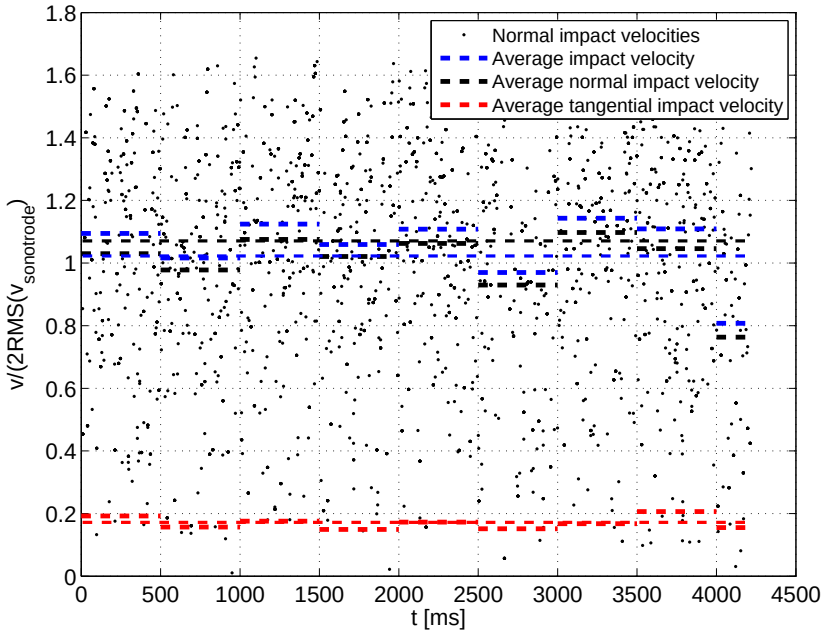

Figure 6.16: Evolution of the velocities of impacts on the work piece. Illustration of the normal and tangential components normalized by twice the sonotrode root mean square velocity.

roughly accelerate when hitting the sonotrode and decelerate by dissipating energy in impacts with the work piece.

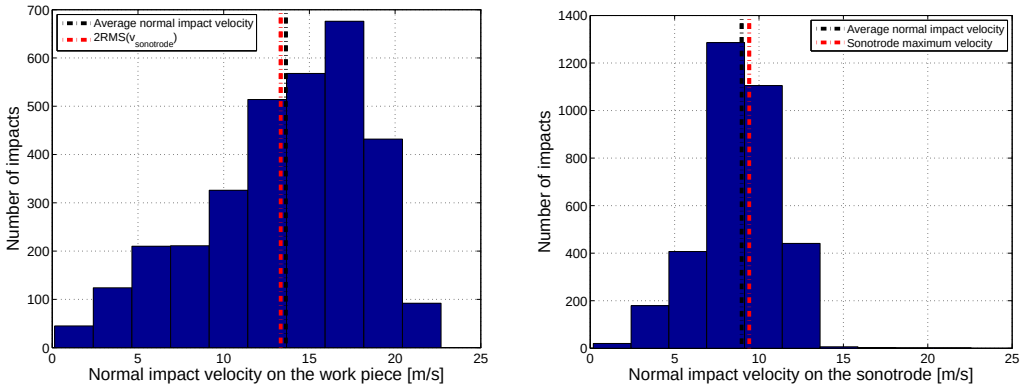

(a) (b)

Figure 6.17: Distribution over a given simulation time of the normal impact velocities on the work piece (a) and on the sonotrode (b).

As indicated in section 6.2, the experimental determination of the coverage rate might largely differ from its value determined in the simulations. A relatively low influence of the coverage rate over a certain threshold value was deduced from the simulation results. A comparison between the two methods of determination is proposed here. The two methods to determine the coefficient of restitution are defined in Fig. 6.18(a). From the simulation results, the coverage rate is calculated as a function of time using the two definitions. For this calculation the value of the impact radius a^* is estimated analytically as a function of the velocity with formulae proposed by Johnson [JOH 85]. Results are presented in Fig. 6.18(b).

In the beginning of the simulation, almost no overlapping of the impacts occurs and both definition give the same coverage rate. But this two sets of results quickly diverge. The average velocity of the shots being almost constant the evolution of the "simulation" coverage rate (1) with time is almost linear. The second definition gives results with a significantly lower slope due to the non consideration of the overlapped zones. This evolution is closer to the experimental one. This difference between the different methods to calculate the coverage rate can have a very strong effect when considering the process in its entirety and should be considered with care. This simulation results should nevertheless consider with some care for the incomplete physic they depend on and by the fact that the small number of shots that don't interact too much with each others, generating highly deterministic impact zones with very strong overlapping.

The obtained velocities are highly dependent of the physic considered for the coefficients of restitution. Similar simulations were performed for purely elastic impacts for which the rebound velocity equals the impact velocity, giving highly different results. It

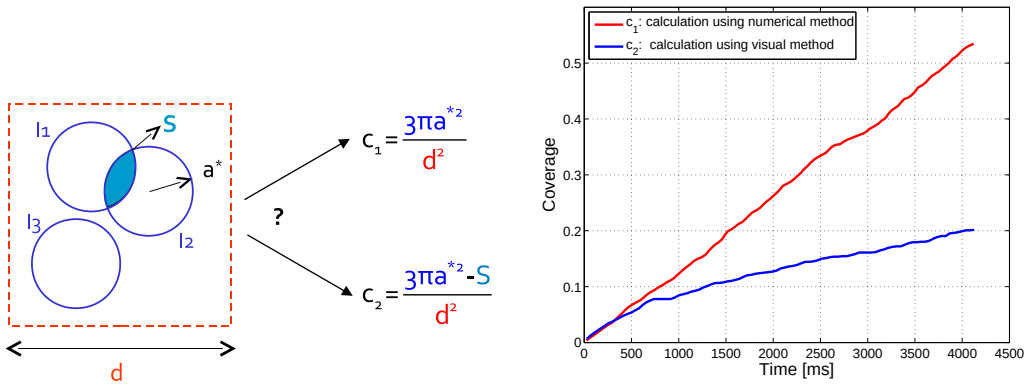

(a) (b)

Figure 6.18: (a) Methods for the experimental determination of the coefficient of restitution: (1) considering the whole surface covered by the impacts, with overlapping, (2) considering only once each part of the covered surface (visual observation). (b) Evolution of the coverage rate as a function of time. Comparison of the two calculation methods presented.

will be necessary then to increase the physical reality of the model by accounting for the plasticity of the work piece in the determination of the coefficient of restitution to obtain more realistic results and eventually see saturation effects in the results. Rotation and damage of the shots was not considered here neither and might affect the results. From these more complete results, a correlation with experimentations, in the saturation time and the evolution of the coverage rate might be performed. Influence of the process parameters, like the number, density and size of the shots, sonotrode amplitude and frequency will also most certainly affect the results and should be observed in future work.

6.6 Modelling residual stresses in a real finite size structure

The most restrictive hypothesis made by the multiple impact model proposed in this chapter is the half-space hypothesis. If the calculated plastic zone has finite dimensions that can be consistent with finite size structures, the stresses resulting from these inelastic strains are strongly affected by the boundary conditions. When considering bodies of finite size, results from the SAM need to be post processed to account for the finite dimension of the structure. A method for obtaining residual stresses in a finite size structure from the residual strains in the semi infinite body is proposed in this section. It is recalled here that from the multiple impact model is obtained a diagonal strain tensor which value varies only with the depth of the considered point.

This method, using the SAM to calculate residual strains and transferring them to a FE finite structure was applied by Li [LI 11] and compared to experimental results that are partly presented here.

6.6.1 Strains transfer to finite structure

To determine the residual stresses generated by the final plastic strain field, a model based on an equivalent approach using thermo-elastic properties is used. The strain field $\varepsilon^p(z)$ determine by the SAM multiple impact model is imported in a finite structure using the commercial software Systus as thermal strains. This method was previously applied by Fulleringer et al [FUL 10]. A finite element structure representing the real shot peened structure is meshed. Each plane of elements is taken to have the same size in depth that the SAM elements. The FE elements are defined in a different material at each depth. These materials are attributed anisotropic thermal expansion properties corresponding to the plastic strain in the current depth as described in Eq. 6.7.

$$\alpha_i^{th}(z) = \varepsilon_{ii}^p(z) \mid i = (x,y,z) \tag{6.7}$$

Where α_i^{th} is the material's thermal expansion coefficient in the i direction. A uniform unit temperature field is applied then applied to the structure. The boundaries of the model are considered free of any constraint. Under this temperature field, the structure will deform and its equilibrium give the residual stress field for a finite structure. These residual stresses are observed at a center point of the structure far from the boundaries where it is assumed that side effects will influence the results.

The whole multiple impact model is recalled in Fig. 6.19 from the three impacts modelled by the SAM on a semi infinite body to the final residual stress field in a structure of finite size.

6.6.2 Comparison with experimental results

Ultrasonic shot peening experiments were performed by Li [LI 11] to validate the multiple impact model proposed here. These experiments are close to the Almen experiments typically used to validate the repeatability of the processes.

Inconel 600 samples were peened in an ultrasonic shot peening chamber containing only 10 shots of $4mm$ diameter to keep the impacts normal to the samples. Several sonotrode amplitudes with a vibration frequency of $20kHz$ were tested. Only the results for a maximum vibration of the sonotrode equal to $4m/s$ are presented here. The time needed to obtain a 100% coverage rate was determined by visual observation of the samples, and doubled to obtain a 200% coverage rate. Other process parameters are similar to those presented in Tab. 6.4. The sample dimension are $60 \times 18 \times 2mm^3$

During the shot peening process, the sample is bolted to the chamber and assumed to behave as a semi infinite body at each impact's scale. At the end of the peening, a slight deflection of the sample is noticed (see Fig. 6.20 (b)), showing that the semi infinite body hypothesis does not perfectly hold. The sample is then released, generating

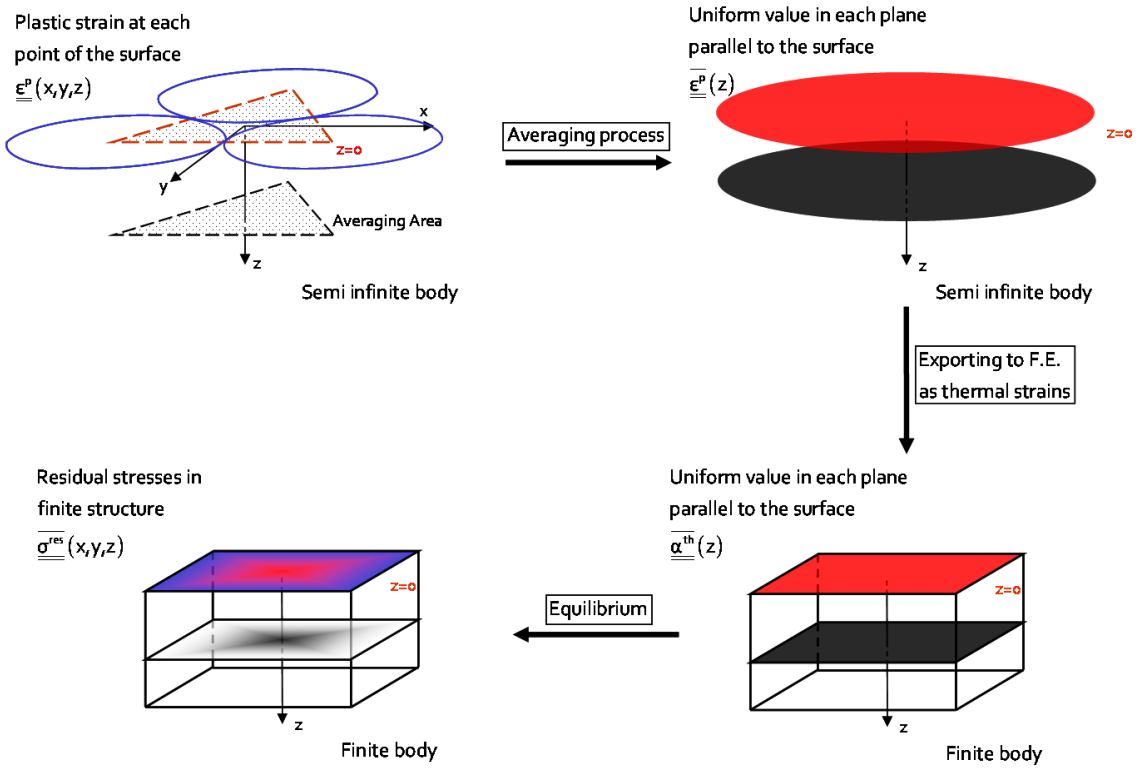

Figure 6.19: Averaging and transfer to finite structure process. Averaging of results over the semi infinite body reference area, exportation as thermal strains in a finite element model of a finite size structure and computation of residual stresses by resolving the equilibrium.

a large deflection that is measured by a three-dimensional measuring machine (Fig. 6.20 (c)). Experimental results are completed with residual stresses measurements by x-ray diffraction, plotted in Fig. 6.21. The residual stresses are measured at different depth (reached by electro erosion) starting from the peened surface. The change in stiffness of the sample with the electro erosion is assumed negligible and not accounted for in the residual stress measures. The stresses are measured in the two directions, x being the longitudinal direction of the sample and y the transversal direction. The measurement error is estimated around $50MPa$.

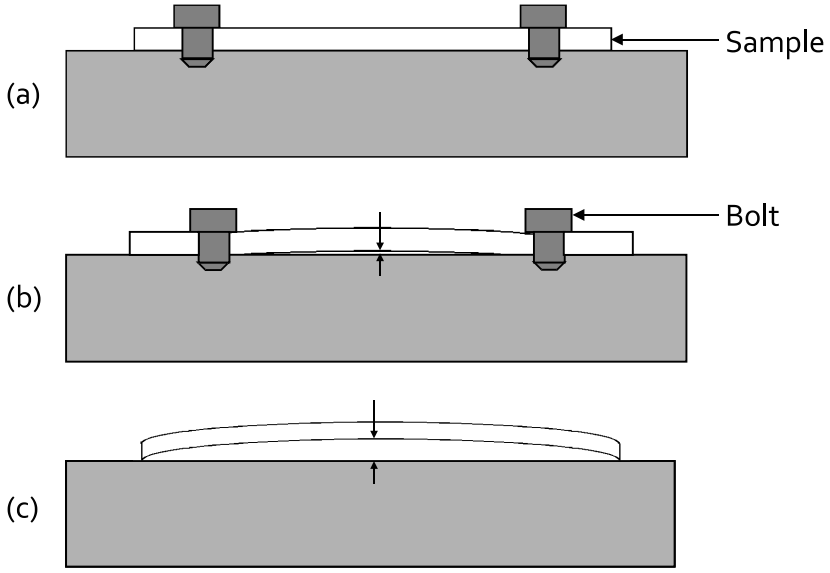

Figure 6.20: Definition of the residual arc height on peened sample. (a) Clamped sample before ultrasonic shot peening treatment. (b) Clamped sample after peening. (c) Released sample with residual arc.

Experimental results are compared with simulation results. For each set of simulation three impacts are performed. The shots velocity is assumed constant equal to the maximum velocity of the sonotrode ($4m/s$). The 100Cr6 properties are considered for the shots that are assumed to behave elastically. The impacted body is assumed elastic plastic with material properties equal to those used for the multiple impact benchmark. The coverage rate is calculated using the method proposed in section 6.2 with values equal to those determined experimentally (despite the assumed bias). Simulation results are the averaged following the multiple impact method. Averaged residual stresses in the semi infinite body are plotted as indication in Figs. 6.21(b), 6.21(c) and 6.21(d).

The averaged plastic strain are then exported in a FE model of the samples as thermal strains to determine the residual stresses in the finite structure and the deflection of the samples. FE results in the finite structure are plotted in Fig. 6.21. The deflection along

the longitudinal x direction of the plate is plotted while the residual stresses are plotted along the depth of the plate at its center.

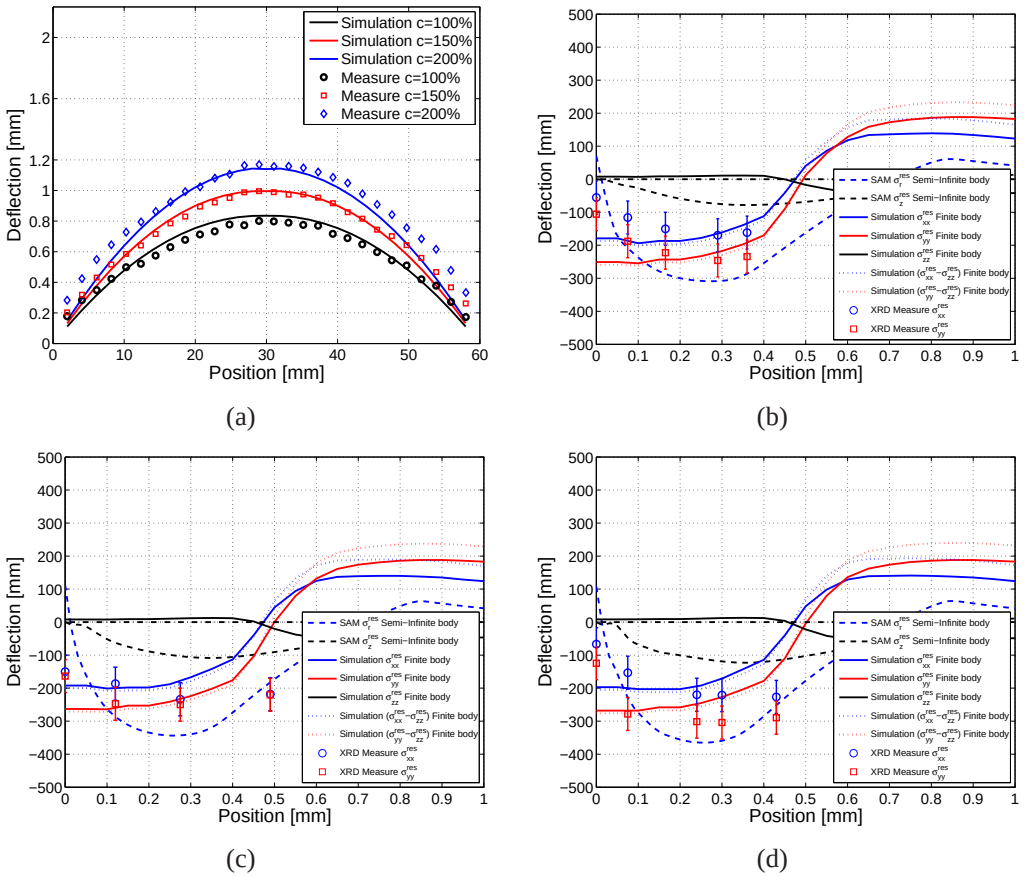

Figure 6.21: Almen-type experimental results for a maximum sonotrode velocity $v = 4m/s$. (a) Comparison of the deformed shape by simulation and after experiments for 3 coverage rates. Comparison of simulated and XRD measured residual stresses for $c = 100\%$ (b), $c = 150\%$ (c) and $c = 200\%$ (d).

An excellent fit is obtained in this case between simulation and experimental results for the deflection of the plate. The maximum measured value is perfectly reproduced by the model. Results tend to diverge at the border of the plate were the actual boundary conditions logically differ from those used in the simulations. For this case, no saturation of the deflection is observed for the three values of coverage rate.

The residual stresses values are quite similar for all three cases, both for the experimental and simulation values. The actual measured stresses being the difference the radial and depth components, these stresses are plotted for the simulation results but with negligible effect due to the low amplitude of the depth stress σ_{zz}^{res}. A significant reorganization

of the stresses is observed between the semi infinite and finite bodies. The radial stresses become almost symmetric while stresses in the depth σ_{zz}^{res} are almost nil in the plastic zone and of very low amplitude beyond. A good fit is observed between both sets of results, validating roughly the method. Some points present important differences. First the value measured at the surface is highly different between the three sets of experimental results while it is almost constant in the simulation. This value was proven to be very sensitive in the numerical models and especially the SAM behaviour close to the surface is different than what the FE model predict. Next, values at deep depth tend to diverge between simulation and experiments.

Results from these experiments are encouraging despite a certain number of divergences. A significant number of hypotheses remains to be released. The SAM model needs to be improved at high strains. The impact velocity was here roughly estimated and might be ripened with ultrasonic shot peening model such as the one presented previously if the physics involved in the model is fine enough. At last, kinematic hardening effects might be involved in this case and were not accounted in the model, indeed the difference in trends between simulation and experiments correlates with the simulation results from section 6.4.5.

6.7 Conclusions

A fast and versatile model for the simulation of multiple impacts using the SAM was proposed. It allows to simulate the effect of an infinite number of impacts in a reduced number of simulation. The methodology proposed allows to erase the effect of various randomness parameters by averaging the results over a reference area. From this model the influence of a large number of parameters was observed. Only three impacts are sufficient to obtain a representative residual strain state in most applications. The relative independence of the model to the impact distribution, velocity variation and coverage rate in some cases was observed.

Numerical validation was made by a benchmark with three finite element codes. Results obtained by the SAM are encouraging showing a good correlation with the FE codes but the high level of strains involved implies instabilities in the SAM and improvement remain to be done. The gain in computation allowed by the SAM is about one order of magnitude. Comparison with experimental results was made giving again encouraging results although a large number of hypotheses need to be addressed.

A full methodology was proposed for the complete modelling of the ultrasonic shot peening process. Some strong hypotheses need to be released to obtain physically satisfying models and a complete coupling of all three models has not been performed yet. A coupling with accurate experiments was started, trying to obtain representative and measurable experimental data to validate the model. Complementary work by Li [LI 11] goes in that way.

At last, it should be noticed that the method proposed here can easily be adapted to any process generating residual stresses. A change in the geometry or loading type would

present no difficulty and conventional shot peening, roto peening, hammering or laser peening might be simulated as long as the loadings can be correctly defined.

Conclusions and prospects

The prediction of residual stresses is of crucial importance in the development of high technology applications. Residual stresses cannot be completely relieved from mechanical parts and more than that they appear to have a fundamental role in the extension of the fatigue life of components. The development of fast and reliable tools to predict residual stresses should be useful to improve the fatigue life of mechanical parts and avoid costly experiments.

The development of Semi Analytical Methods (SAM) in the past years has proven to be an efficient and especially fast way to simulate mechanical contacts, including when various physical phenomena such as plasticity, thermal effects, or friction are involved. The fast computation speed of the SAM becomes a precious advantage when many simulations are required. The large number of parameters involved is an obstacle to the mastering of the link between the process parameters, the knowledge of the mechanical properties of the materials and the results in terms of residual stresses and damaging of the material. This work tried to offer possibilities of modelling those processes using the capabilities of the SAM.

A semi analytical model has been extended, based on previous work and knowledge, for the simulation of mechanical processes such as burnishing or shoot peening. The calculation of residual strains and stresses does now consider large displacements of the surfaces, pushing away the limits of the method. A better computation speed was obtained by the use of the 3DFFT technique. The numerical model was validated on these specific aspects. The method is now able to account for any kind of hardening and to consider impacts up to moderate velocities, as far as the equivalent plastic strain remains below 10% and internal inertial forces can be omitted.

The method was first applied to a frictionless contact, with and without rolling as a first comprehensive model of the low plasticity burnishing process. The effects of the geometry and of the material properties on pressure and plastic strain were outlined. These conclusions would provide interesting data for the estimation of rolling contact life. The ratcheting phenomenon was observed when considering the case of an elastic ball rolling on a kinematic hardening elastic plastic flat while very fast stabilization is observed when isotropic hardening is considered.

The SAM was then applied to the modelling of single and multiple impacts. Vali-

dations of the model were performed through benchmarks in collaboration with several finite element code users and experiments on single impacts. These validations emphasized the limits of the method in its actual level of development when the level of plastic strain becomes higher than 10% but also indicated the strong potential of the SAM.

Two applications were investigated in greater details: the prediction of the coefficient of restitution through the definition of simple empirical formulae and the modelling of multiple impacts processes from the original process parameters to the final residual stresses through the coupling of several models.

The experiments performed were a first step to the experimental validation of impact models. Behaviour trends were obtained on the surface displacement after impacts on several materials and successfully correlated with SAM results. The digital image correlation technique was tentatively used to measure the surface displacements and subsequent strains. More work in this area is now needed. For example the evolution of the material micro-structure during impacts might provide interesting data to better understand the physics involved when large strains are observed. Residual stresses measurements will also be useful to compare with numerical results. The specific structure of the impacted materials and especially the small areas in which very high stress gradients are located should be carefully considered in future works.

The model was extended to large displacements but small strains are still assumed. The extension of the SAM to large strains is therefore one of the main prospects. Encouraging results were obtained on benchmark results when plastic strains are ranging from 10 to 12%, approximately. The benchmark with multiple impacts and the associated experimental results showed the limits of this approach beyond these strain levels. If the SAM results remain consistent, approximations and numerical instabilities were noticed. Several points of improvements have already been identified: (i) the continuity of strain fields should be ensured and might stabilize the convergence for strain level above 10%, (ii) analytical solutions considering large strains might be applied or developed, and (iii) using Lagrangian type formulation to solve the equilibrium. This type of formulation would allow to consider large strains while still solving the equilibrium of the reference underformed configuration, which is a necessary condition for the application of the FFT methods.

A multiple impact model was proposed to simulate with a reduced number of impacts the shot peening process. The use of a reference area and an averaging method allowed to obtain representative results with the simulation of only three impacts, representing only a few hours of computation on a standard desktop. It was observed that the computed plastic strain field is almost independent of the order of impacts, and hardly affected by the variation of the impact velocity around a mean value. A fast and simple method was coupled with this model to obtain the residual stress fields generated in a finite size body. The method is applicable to any kind of structure. Preliminary experimental validations of the full method were presented. The method can be applied to most mechanical processes

that generate residual stresses as soon as the loading and the contact geometry are known, such as roto peening, laser peening or hammering for example.

The definition of the loading is one important and delicate part of the processes modelling. In the case of shot peening, the impact velocity and coverage rate are the parameters needed. Thanks to a careful analysis carried out to estimate the restitution coefficient for single or multiple impacts, a simple ultrasonic shot peening model was proposed. From this model, the impact velocity and the evolution of the coverage rate with time becomes now predictable and can be linked to the global process parameters offering direct industrial applications. The results have been found to be highly dependant on the quality of the estimation of the restitution coefficient needed in the simulation.

However, several physical effects have not been yet considered. First the coupling between the normal and tangential contact problems has not been investigated. However recent work by [FUL 11] suggested that the presence of plasticity may completely change the distribution of shears and slips in a stick-slip contact. The effect of friction on the rotation of the impacting sphere when the impact is oblique has either not been yet considered.

Visco-elasticity and visco-plasticity may also play a significant role at certain temperatures, depending on the material, or at very high impact velocities. Finally body forces have been neglected but it is obvious that, at high strain rates or when the deformed particle or the impacted body starts to flow, this assumption does not hold any more. These effects should require more attention in the future.

Acknowledgement

Thanks go to AREVA and EDF for their financial and technical support. The author also thanks the laboratory Mécasurf from the AMPT Aix-en-Provence for the use of their experimental devices and their useful help and discussions.

Influence Coefficients

A.1 Elastic stresses generated by a uniform pressure

The influence coefficients giving the elastic stresses in a semi infinite body generated by a uniform pressure are here recalled. Love [LOV 52] first developed the solution for the displacement of the surface. The development of the solution to obtain the stresses was made by Vergne [VER 85].

The pressure is applied on a rectangular surface of size $\Delta x \times \Delta y$ centered in $(x,y) = (0,0)$. The coefficients are given as a function of the position of the calculation point (x,y,z), x and y being the directions parallel to the surface and z the depth, directed towards the body. ν is the Poisson's ratio of the body.

$$\frac{\sigma_{IJ}}{p} = C^p_{IJ}(x,y,z,E,\nu) = S^p_{IJ}(x+\frac{\Delta_x}{2},y+\frac{\Delta_y}{2},z,E,\nu) + S^p_{IJ}(x-\frac{\Delta_x}{2},y-\frac{\Delta_y}{2},z,E,\nu) - S^p_{IJ}(x+\frac{\Delta_x}{2},y-\frac{\Delta_y}{2},z,E,\nu) - S^p_{IJ}(x-\frac{\Delta_x}{2},y+\frac{\Delta_y}{2},z,E,\nu), \quad \text{(A.1)}$$

with

$$S^p_{xx}(x,y,z,E,\nu) = \frac{\nu}{\pi}\arctan\left(\frac{z^2+y^2-y\rho}{zx}\right) + \frac{1-2\nu}{\pi}\arctan\left(\frac{\rho-y+z}{x}\right) + \frac{z}{2\pi}\frac{xy}{(x^2+z^2)\rho}, \quad \text{(A.2)}$$

$$S^p_{yy}(x,y,z,E,\nu) = \frac{\nu}{\pi}\arctan\left(\frac{z^2+y^2-y\rho}{zx}\right) + \frac{1-2\nu}{\pi}\arctan\left(\frac{\rho-x+z}{y}\right) + \frac{z}{2\pi}\frac{xy}{(y^2+z^2)\rho}, \quad \text{(A.3)}$$

$$S^p_{zz}(x,y,z,E,\nu) = \frac{1}{2\pi}\arctan\left(\frac{z^2+y^2-y\rho}{zx}\right) - \frac{z}{2\pi}\frac{xy}{\rho}\left(\frac{1}{x^2+z^2}+\frac{1}{y^2+z^2}\right), \quad \text{(A.4)}$$

$$S^p_{xy}(x,y,z,E,\nu) = -\frac{z}{2\pi}\frac{1}{\rho} - \frac{1-2\nu}{2\pi}\ln(\rho+z), \quad \text{(A.5)}$$

$$S^p_{yz}(x,y,z,E,\nu) = \frac{z^2}{2\pi}\frac{x}{(y^2+z^2)\rho}, \tag{A.6}$$

$$S^p_{xz}(x,y,z,E,\nu) = \frac{z^2}{2\pi}\frac{y}{(x^2+z^2)\rho}. \tag{A.7}$$

A.2 Elastic stresses generated by a uniform shear in the x direction

The influence coefficients giving the elastic stresses in a semi infinite body generated by a uniform shear are here recalled. Love [LOV 52] first developed the solution for the displacement of the surface. The extension of the solution to obtain the stresses generated by a uniform shear was made by Vergne [VER 85].

The shear are applied on a rectangular surface of size $\Delta x \times \Delta y$ centered in $(x,y) = (0,0)$. The coefficients are given as a function of the position of the calculation point (x,y,z), x and y being the directions parallel to the surface and z the depth, directed towards the body. ν is the Poisson's ratio of the body.

$$\begin{aligned}\frac{\sigma_{IJ}}{q_x} = C^{q_x}_{IJ}(x,y,z,E,\nu) = S^{q_x}_{IJ}(x+\frac{\Delta_x}{2},y+\frac{\Delta_y}{2},z,E,\nu) + S^{q_x}_{IJ}(x-\frac{\Delta_x}{2},y-\frac{\Delta_y}{2},z,E,\nu) \\ - S^{q_x}_{IJ}(x+\frac{\Delta_x}{2},y-\frac{\Delta_y}{2},z,E,\nu) - S^{q_x}_{IJ}(x-\frac{\Delta_x}{2},y+\frac{\Delta_y}{2},z,E,\nu),\end{aligned} \tag{A.8}$$

with

$$S^{q_x}_{xx}(x,y,z,E,\nu) = -\frac{z}{2\pi}\frac{1}{\rho}\left(1+\frac{-x^2+zy}{(\rho+z)(\rho-y)}\right) + \frac{\nu}{\pi}\frac{y}{\rho+z} - \frac{1}{\pi}\ln(\rho-y), \tag{A.9}$$

$$S^{q_x}_{yy}(x,y,z,E,\nu) = -\frac{z}{2\pi}\frac{y}{\rho(\rho+z)} - \frac{\nu}{\pi}\left(\frac{y}{\rho+z}+\ln(\rho-y)\right), \tag{A.10}$$

$$S^{q_x}_{zz}(x,y,z,E,\nu) = \frac{z^2}{2\pi}\frac{y}{\rho(x^2+z^2)}, \tag{A.11}$$

$$S^{q_x}_{xy}(x,y,z,E,\nu) = -\frac{z}{2\pi}\frac{x}{\rho(\rho+z)} - \frac{\nu}{\pi}\frac{x}{\rho+z} - \frac{1}{2\pi}\ln(\rho-x), \tag{A.12}$$

$$S_{yz}^{q_x}(x,y,z,E,\nu) = -\frac{z}{2\pi}\frac{1}{\rho}, \tag{A.13}$$

$$S_{xz}^{q_x}(x,y,z,E,\nu) = \frac{z}{2\pi}\frac{xy}{\rho(x^2+z^2)} + \frac{1}{2\pi}\arctan\left(\frac{z^2+y^2-y\rho}{zx}\right). \tag{A.14}$$

For the case of a shear in the y or 2 direction, the solutions for $S_{ij}^{q_y}$ can be found easily by circular permutation of the indices.

A.3 Residual surface displacement generated by a cuboid of uniform strain

The influence coefficients giving the residual displacement at the surface of a semi infinite body generated by a cuboid of uniform strains are recalled here. The solution for the displacement normal to the surface was developed by Chiu [CHI 78] and Jacq [JAC 01]. The extension to the tangential displacement in the x and y directions was made by Fulleringer [FUL 10] to couple plasticity and tangential effects in the semi analytical models.

The source of the displacements is a cudoid of uniform strain of dimensions $\Delta x \times \Delta y \times \Delta z$ with its center C at (x,y,z). The calculation point A is located at the surface of the body, at the origin of the coordinate system $(x,y,z) = (0,0,0)$. ν is the Poisson's ratio of the body.

A.3.1 Residual displacement in the z direction

The residual displacement in the direction normal to the surface (z or 3) is given by:

$$u_z^{res}(A) = \varepsilon_{ij}^p D_{3ij}(A,C) \,|\, (i,j) = 1,2,3 \tag{A.15}$$

The function D_{3ij} was analytically integrated by Jacq et al. [JAC 01] and is given by:

$$\begin{aligned} D_{3ij}(A,C) = {} & F_{3ij}\left(x+\frac{\Delta x}{2},y+\frac{\Delta y}{2},z+\frac{\Delta z}{2}\right) - F_{3ij}\left(x+\frac{\Delta x}{2},y+\frac{\Delta y}{2},z-\frac{\Delta z}{2}\right) \\ & - F_{3ij}\left(x+\frac{\Delta x}{2},y-\frac{\Delta y}{2},z+\frac{\Delta z}{2}\right) - F_{3ij}\left(x-\frac{\Delta x}{2},y+\frac{\Delta y}{2},z+\frac{\Delta z}{2}\right) \\ & + F_{3ij}\left(x+\frac{\Delta x}{2},y-\frac{\Delta y}{2},z-\frac{\Delta z}{2}\right) + F_{3ij}\left(x-\frac{\Delta x}{2},y-\frac{\Delta y}{2},z+\frac{\Delta z}{2}\right) \\ & + F_{3ij}\left(x-\frac{\Delta x}{2},y+\frac{\Delta y}{2},z-\frac{\Delta z}{2}\right) - F_{3ij}\left(x-\frac{\Delta x}{2},y-\frac{\Delta y}{2},z-\frac{\Delta z}{2}\right) \end{aligned} \tag{A.16}$$

with:

$$F_{311}(x,y,z) = \frac{1}{\pi}\left(-\nu x \ln(y+R) - (1-2\nu) z \arctan\left(\frac{y+z+R}{x}\right)\right) \tag{A.17}$$

$$F_{322}(x,y,z) = \frac{1}{\pi}\left(-\nu y \ln(x+R) - (1-2\nu) z \arctan\left(\frac{x+z+R}{y}\right)\right) \tag{A.18}$$

$$F_{333}(x,y,z) = \frac{1}{\pi}\left((1-2\nu)\left(2z\arctan\left(\frac{x+y+R}{z}\right) + x\ln(R+y) + y\ln(R+x)\right) + \frac{z}{2}\arctan\left(\frac{xy}{zR}\right)\right) \tag{A.19}$$

$$F_{312}(x,y,z) = \frac{1}{\pi}\left(-2\nu R - (1-2\nu) z \ln(z+R)\right) \tag{A.20}$$

$$F_{313}(x,y,z) = \frac{1}{\pi}\left(2x\arctan\left(\frac{y+z+R}{x}\right) + y\ln(z+R)\right) \tag{A.21}$$

$$F_{323}(x,y,z) = \frac{1}{\pi}\left(2y\arctan\left(\frac{x+z+R}{y}\right) + x\ln(z+R)\right) \tag{A.22}$$

with $R = \sqrt{x^2+y^2+z^2}$.

A.3.2 Residual displacement in the x direction

The residual displacement in the direction parallel to the surface (x or 1) is given by:

$$u_x^{res}(A) = \varepsilon_{ij}^{p} D_{1ij}(A,C) \,|\, (i,j) = 1,2,3 \tag{A.23}$$

The function D_{1ij} was analytically integrated by Fulleringer et al. [FUL 11] and is given by:

$$\begin{aligned} D_{1ij}(A,C) = {} & F_{1ij}\left(x+\frac{\Delta x}{2}, y+\frac{\Delta y}{2}, z+\frac{\Delta z}{2}\right) - F_{1ij}\left(x+\frac{\Delta x}{2}, y+\frac{\Delta y}{2}, z-\frac{\Delta z}{2}\right) \\ & - F_{1ij}\left(x+\frac{\Delta x}{2}, y-\frac{\Delta y}{2}, z+\frac{\Delta z}{2}\right) - F_{1ij}\left(x-\frac{\Delta x}{2}, y+\frac{\Delta y}{2}, z+\frac{\Delta z}{2}\right) \\ & + F_{1ij}\left(x+\frac{\Delta x}{2}, y-\frac{\Delta y}{2}, z-\frac{\Delta z}{2}\right) + F_{1ij}\left(x-\frac{\Delta x}{2}, y-\frac{\Delta y}{2}, z+\frac{\Delta z}{2}\right) \\ & + F_{1ij}\left(x-\frac{\Delta x}{2}, y+\frac{\Delta y}{2}, z-\frac{\Delta z}{2}\right) - F_{1ij}\left(x-\frac{\Delta x}{2}, y-\frac{\Delta y}{2}, z-\frac{\Delta z}{2}\right) \end{aligned} \tag{A.24}$$

with:

$$F_{111}(x,y,z) = \frac{1}{2\pi}(z\ln(R+y)+y\ln(R+z)+2x\arctan\left(\frac{y+z+R}{x}\right)+x\arctan\left(\frac{yz}{xR}\right) + (1-2\nu)\left(2x\arctan\left(\frac{y+z+R}{x}\right)+z\ln(R+y)+\frac{1}{2}y\ln(R+z)-\frac{zy}{2(R+z)}\right)) \tag{A.25}$$

$$F_{122}(x,y,z) = \frac{1}{2\pi}\left(-y\ln(R+z)+(1-2\nu)y\left(\frac{z}{2(R+z)}+\frac{1}{2}\ln(R+z)\right)\right) \tag{A.26}$$

$$F_{133}(x,y,z) = \frac{1}{2\pi}\left(-2\nu z\ln(R+y)+(1-2\nu)y\left(2x\arctan\left(\frac{R+y+z}{x}\right)+y\ln(R+z)\right)\right) \tag{A.27}$$

$$F_{112}(x,y,z) = \frac{1}{\pi}\left(2y\arctan\left(\frac{x+z+R}{y}\right)+z\ln(R+x)+\frac{1-2\nu}{2}\left(x\ln(R+z)+\frac{xz}{R+z}\right)\right) \tag{A.28}$$

$$F_{113}(x,y,z) = \frac{1}{\pi}\left(2z\arctan\left(\frac{x+y+R}{z}\right)+y\ln(R+x)\right) \tag{A.29}$$

$$F_{123}(x,y,z) = \frac{-R}{\pi} \tag{A.30}$$

with $R=\sqrt{x^2+y^2+z^2}$.

For the case of the residual displacement in the y or 2 direction, the solutions for F_{2ij} can be found easily by circular permutation of the indices.

A.4 Residual stresses in an infinite body

The influence coefficients giving the residual stresses generated in an infinite body by a cuboid of uniform strains ε^p_{ij} $(i,j=1,2,3)$ are recalled here. Thess solutions were developed by Chiu [CHI 77].

The source of the displacements is a cudoid of uniform strain of dimensions $\Delta x\times\Delta y\times\Delta z$ with its center located at the origin of the coordinate system $(x,y,z)=(0,0,0)$. The calculation point M is at (x,y,z). Recall here that the body is considered infinite, thus the origin of the coordinate system has no importance. ν is the Poisson's ratio of the body. The vectors linking the corners of the cuboid to the observation point are first defined as follows:

$$C_1 = \left(x-\frac{\Delta x}{2},y-\frac{\Delta y}{2},z-\frac{\Delta z}{2}\right) = \left(c_1^1,c_2^1,c_3^1\right) \tag{A.31}$$

$$C_2 = \left(x + \frac{\Delta x}{2}, y - \frac{\Delta y}{2}, z - \frac{\Delta z}{2}\right) = \left(c_1^2, c_2^2, c_3^2\right) \tag{A.32}$$

$$C_3 = \left(x + \frac{\Delta x}{2}, y + \frac{\Delta y}{2}, z - \frac{\Delta z}{2}\right) \tag{A.33}$$

$$C_4 = \left(x - \frac{\Delta x}{2}, y + \frac{\Delta y}{2}, z - \frac{\Delta z}{2}\right) \tag{A.34}$$

$$C_5 = \left(x - \frac{\Delta x}{2}, y + \frac{\Delta y}{2}, z + \frac{\Delta z}{2}\right) \tag{A.35}$$

$$C_6 = \left(x - \frac{\Delta x}{2}, y - \frac{\Delta y}{2}, z + \frac{\Delta z}{2}\right) \tag{A.36}$$

$$C_7 = \left(x + \frac{\Delta x}{2}, y - \frac{\Delta y}{2}, z + \frac{\Delta z}{2}\right) \tag{A.37}$$

$$C_8 = \left(x + \frac{\Delta x}{2}, y + \frac{\Delta y}{2}, z + \frac{\Delta z}{2}\right) \tag{A.38}$$

For a cuboid with constant unit normal plastic strain, i.e. $\varepsilon_{11}^p = 1$ and $\varepsilon_{ij}^p = 0 | (i,j) \neq (1,1)$, the elastic strains at the observation point M are given by:

$$\varepsilon_{1111} = \frac{1}{8\pi^3} \sum_{m=1}^{8} \left[D^m_{,1111} + \frac{2-\nu}{1-\nu} \left(D^m_{,1111} + D^m_{,1133} \right) \right] - H(M) \tag{A.39}$$

$$\varepsilon_{2211} = -\frac{1}{8\pi^3} \sum_{m=1}^{8} \left[-D^m_{,1122} \right] + \frac{\nu}{1-\nu} \left(D^m_{,2222} + D^m_{,2233} \right) \tag{A.40}$$

$$\varepsilon_{3311} = -\frac{1}{8\pi^3} \sum_{m=1}^{8} \left[-D^m_{,1133} \right] + \frac{\nu}{1-\nu} \left(D^m_{,2233} + D^m_{,3333} \right) \tag{A.41}$$

$$\varepsilon_{1211} = \frac{1}{8\pi^3} \sum_{m=1}^{8} \left[\frac{\nu}{1-\nu} D^m_{,1112} \right] + \frac{1+\nu}{1-\nu} \left(D^m_{,2221} + D^m_{,3312} \right) \tag{A.42}$$

$$\varepsilon_{1311} = \frac{1}{8\pi^3} \sum_{m=1}^{8} \left[\frac{\nu}{1-\nu} D^m_{,1113} \right] + \frac{1+\nu}{1-\nu} \left(D^m_{,3331} + D^m_{,2213} \right) \tag{A.43}$$

$$\varepsilon_{2311} = \frac{1}{8\pi^3} \sum_{m=1}^{8} \left[\frac{\nu}{1-\nu} \left(D^m_{,2233} + D^m_{,3332} \right) \right] \tag{A.44}$$

For a cuboid with constant unit shear plastic strain, i.e. $\varepsilon_{12}^p = \varepsilon_{21}^p = 1$ and $\varepsilon_{ij}^p = 0 | (i,j) \neq (1,2),(2,1)$, the elastic strains at the observation point M are given by:

$$\varepsilon_{1112} = \frac{1}{8\pi^3}\sum_{m=1}^{8}\left[\frac{-2\nu}{1-\nu}D^m_{,1112}\right] + 2\left(D^m_{,2221} + D^m_{,3312}\right) \tag{A.45}$$

$$\varepsilon_{2212} = \frac{1}{8\pi^3}\sum_{m=1}^{8}\left[\frac{-2\nu}{1-\nu}D^m_{,1222}\right] + 2\left(D^m_{,1112} + D^m_{,3312}\right) \tag{A.46}$$

$$\varepsilon_{3312} = \frac{1}{8\pi^3}\sum_{m=1}^{8}\left[\frac{-2\nu}{1-\nu}D^m_{,3312}\right] \tag{A.47}$$

$$\varepsilon_{1212} = \frac{1}{8\pi^3}\sum_{m=1}^{8}\left[\frac{-2\nu}{1-\nu}D^m_{,1122} + D^m_{,1111} + D^m_{,2222} + D^m_{,1133} + D^m_{,2233}\right] - H(M) \tag{A.48}$$

$$\varepsilon_{1312} = \frac{1}{8\pi^3}\sum_{m=1}^{8}\left[-\frac{1+\nu}{1-\nu}D^m_{,1123}\right] + D^m_{,2223} + D^m_{,3332} \tag{A.49}$$

$$\varepsilon_{2312} = \frac{1}{8\pi^3}\sum_{m=1}^{8}\left[-\frac{1+\nu}{1-\nu}D^m_{,2213}\right] + D^m_{,1113} + D^m_{,3331} \tag{A.50}$$

If the point M is located inside the cuboid, $H(M) = 1$ and $H(M) = 0$ otherwise. The function $D^m_{,ijkl}$ $(m = 1\ldots8)$ are defined as follows :

$$\begin{aligned} D^m_{,1111} =& 2\pi^2\Big(\arctan\left(\frac{c_2^m c_3^m}{c_1^m R}\right) \\ & - \frac{c_1^m c_2^m c_3^m}{2R}\left(\frac{1}{\left(c_1^m\right)^2 + \left(c_2^m\right)^2} + \frac{1}{\left(c_1^m\right)^2 + \left(c_3^m\right)^2}\right)\Big) \end{aligned} \tag{A.51}$$

$$\begin{aligned} D^m_{,1112} =& -\pi^2\Big(sign\left(c_3^m\right) \\ & \times ln\left(\frac{R + \left|c_3^m\right|}{\sqrt{\left(c_1^m\right)^2 + \left(c_2^m\right)^2}} - \frac{\left(c_1^m\right)^2 c_3^m}{\left(\left(c_1^m\right)^2 + \left(c_2^m\right)^2\right)R}\right)\Big) \end{aligned} \tag{A.52}$$

$$D^m_{,1122} = \frac{\pi^2 c_1^m c_2^m c_3^m}{\left(\left(c_1^m\right)^2 + \left(c_2^m\right)^2\right)R} \tag{A.53}$$

$$D^m_{,1123} = -\frac{\pi^2 c_1^m}{R} \tag{A.54}$$

where

$$R = \sqrt{\left(c_1^m\right)^2 + \left(c_2^m\right)^2 + \left(c_3^m\right)^2} \tag{A.55}$$

The other $D^m_{,ijkl}$ functions are obtained by circular permutation of the subscripts. Similar permutation allows to determine the elastic strains at the observations point M generated by other plastic strains. At last the use of the traditional Hooke's law allows to calculate the elastic stresses generated by the plastic strain from the elastic strains.

Experimental characterization of the cyclic behaviour of inconel 600

B.1 Purpose

To perform simulations of shot peening of inconel 600 samples, an experimental characterization of this material is made. The shot peened surface encounters several successive impacts, thus an identification of the cyclic hardening behaviour of this material, and especially of its kinematic part, is wanted. Cyclic experiments have been conducted on this purpose. Those experiments are carried at ambient temperature.

B.2 Experimental procedure

B.2.1 Samples preparation

Experiments are done on a hydraulic tensile test device with a capacity of $200kN$ on inconel 600 samples machined in a solid piece provided by AREVA (casting #157984). The blueprint is available at the end of this annex. Strain is measured using a clip-on extensometer (absolute measurement error on strain measurement: $+/-0.005\%$). The ambient temperature, measured at the beginning of each experiment, is equal to $20\,\mathrm{deg}C$.

A stress relaxation heat treatment has been made on the samples by heating them up to $600\,\mathrm{deg}C$ during 3 hours with controlled heating and cooling velocities. These velocities are fixed at $150\,\mathrm{deg}C/s$ to avoid large temperature gradients in the samples. A characterization of the efficiency of this treatment, by x-ray measurement of the residual stresses before and after the operation, is also made. The following results come from a collaborating work with Jun Li. [LI 11]. Results presented here were made on plate samples of thickness equal to $2mm$. These samples were shaped by electro-erosion while the cyclic experiment samples were machined. Differences in the surface stress distribution and amplitude between the two kinds of samples can thus be expected.

Measurements of residual stresses made on specimens before and after heat treatment show a significant decrease of the residual stresses amplitude, see Figs. B.1. The average sub surface residual stress level is a about $-100MPa$ in both directions parallel to the

surface and is reduced to a bit more than $-50MPa$ after stress relaxation heat treatment (SRHT). Just below the surface, tensile residual stresses were observed before SRHT. The heat treatment switches these stresses to compressive stresses of similar amplitude. Finally, tensile residual stresses are observed at both surfaces of the samples, before and after SRHT. Here again, the stress amplitude is reduced by half by the treatment.

The SRHT thus reduces the amplitude of residual stresses but does not remove them. Surface residual stresses on the actual cyclic experiment samples can be expected to be different. Nevertheless, the influence of these initial residual stresses will be neglected in the following work.

The results show that the surface residual stresses is around $100MPa$ in tension before heating and lowers of about half after treatment. Yet the difference in these measurement is lower than the measurement error, thus no great efficiency of the treatment can be noticed. Inside the samples, the residual stress state is in compression with a stress amplitude averaging around $-100MPa$, no clear effect of the treatment is here shown. Finally is can be seen that the stress state is rather independent of the direction of measure, showing an uniform and isotropic stress state.

B.2.2 Initial data

Simple traction curves were previously made on this casting by AREVA (samples 1.1 and 3.1). The results are displayed in fig B.2 and will be use to extrapolate the results obtained during cyclic experiments.

B.2.3 Strain cycles

Two tension-compression cyclic experiments were performed. Both are strain-driven.

Experiment #	Strain rate $[s^{-1}]$	Strain amplitude [%]	Number of cycles
C_1	10^{-4}	0.3	5
C_2	5.10^{-4}	0.4	10
		1	10
		2	10
		1	10
		0.4	10
		2	5

Table B.1: Experimental cycles on Inconel 600 samples, number of cycles, strain rate and strain amplitude

N.B.: Due to a fault in the equipment, the experiment C_1 is incomplete. The workable part of the results is here present. It notably allows to check for the repeatability of the experiments.

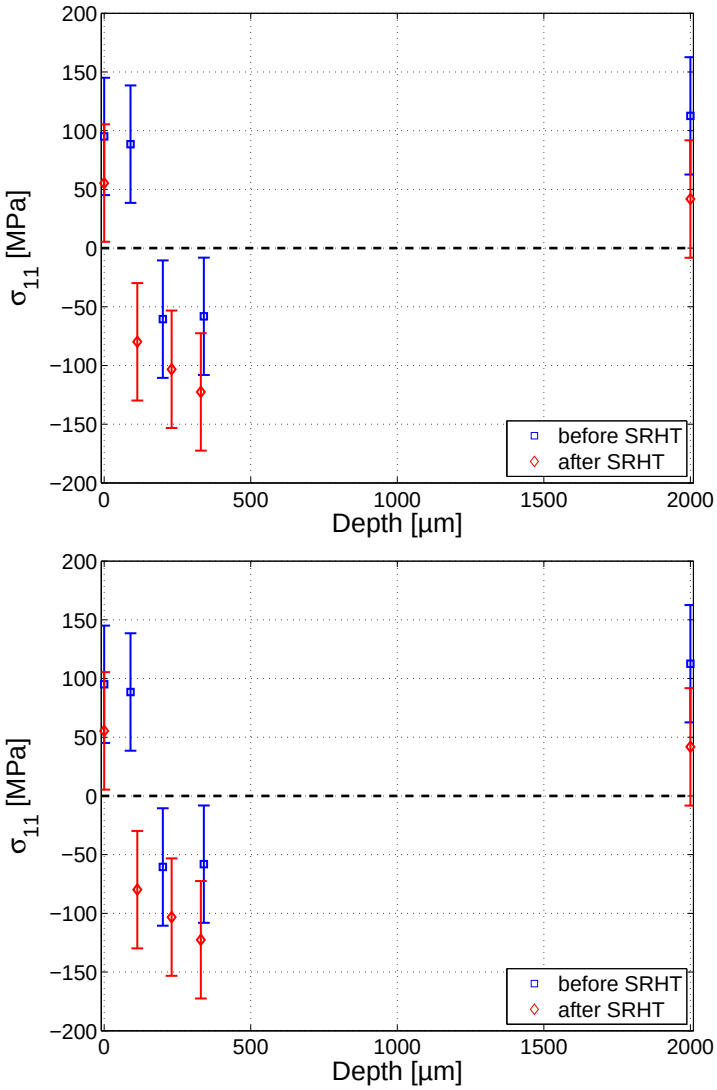

Figure B.1: Residual stresses on the inconel 600 samples measured before and after stress relaxation heat treatment (SRHT). Measurements have been performed by x-ray diffraction. 1 and 2 are the directions parallel to the surface of the sample.

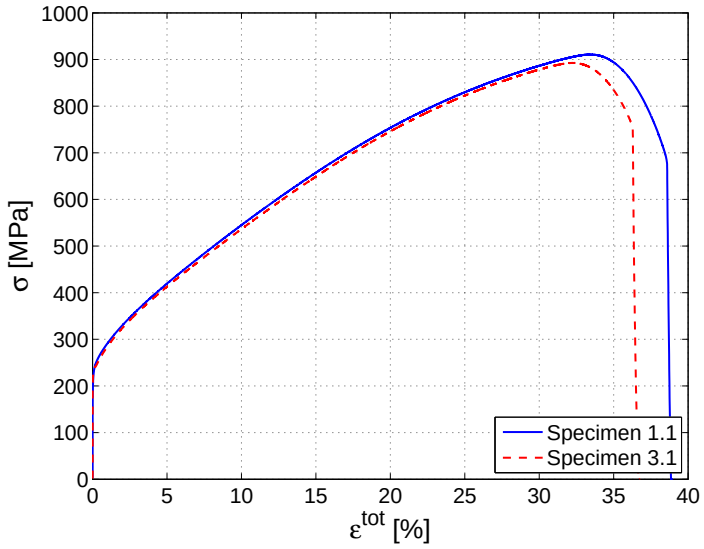

Figure B.2: True stress vs. total strain curves for specimens 3.1 and 3.3. Inconel 600 at 23řC. Monotonic traction curves until rupture.

The cycles realised on sample C_2 would allow to determine the cyclic behaviour of inconel 600. Small amplitudes cycles are made after larger amplitude cycles to observe a possible memory effect of the material. The experiment on sample C_1 showed a rather slow stabilization of cycles. Ten cycles are performed for each amplitude on sample C_2. A second set of cycles at 2% amplitude is made at the end to confirm that the behaviour at "large" deformation is independent of the return to small deformation cycles. Cycles at higher amplitude (5%) were planned but were impossible to perform due to the buckling of the sample.

B.3 Results

The complete stress/strain curves of the experiments are here presented. The strain is that measured by the extensometer, the initial error inherent in the positioning of the device has been corrected.

The engineer stress σ^{eng} is calculated from the measured effort F and the initial diameter d_0 of the samples. The true stress σ^{true} is calculated by considering the strain to be fully plastic and incompressible.

$$\sigma^{eng} = \frac{F}{S_0} = \frac{F}{\pi\frac{d_0^2}{4}} \tag{B.1}$$

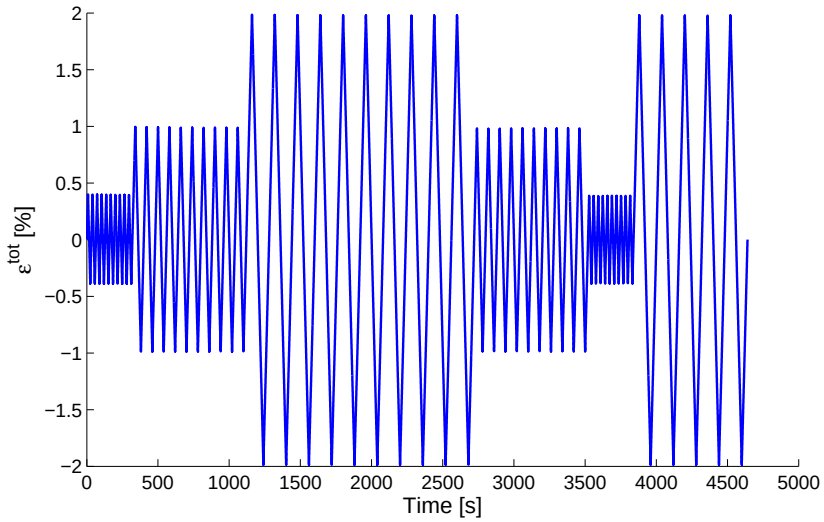

Figure B.3: Full strain loading path for experiment on inconel 600 sample C_2

$$\sigma^{true} = \frac{F}{S} = \frac{F}{\frac{S_0}{1+\varepsilon^{tot}}} = \sigma_{eng}\left(1+\varepsilon^{tot}\right) \tag{B.2}$$

Both stresses are plotted and compared for the first cycle on sample C_2 (strain amplitude $+/-0.4\%$) and the 51^{th} cycle (strain amplitude $+/-2\%$) on Fig. B.4. Differences between the two stress measures appear to be negligible for low amplitude cycles and very small for large amplitude cycles. In the following, the true stress will be used.

Figures B.5 and B.6 show the full stress/strain curves for experiments C_1 and C_2. Only the exploitable part of experiment C_1 is presented as well as the 50 first cycles of experiment C_2.

N.B. : A slight discontinuity in the slope appears on the curves (from the third set of cycles for experiment C_2 in Fig. B.6). This discontinuity corresponds to a slight looseness in the jaws when the load becomes too high. The reason for this is the small diameter of the sample's head that causes a very high pressure on the surface in contact with the jaws. A better adjustment of the jaws between experiments C_1 and C_2 allowed a clear improvement of this inconvenient.

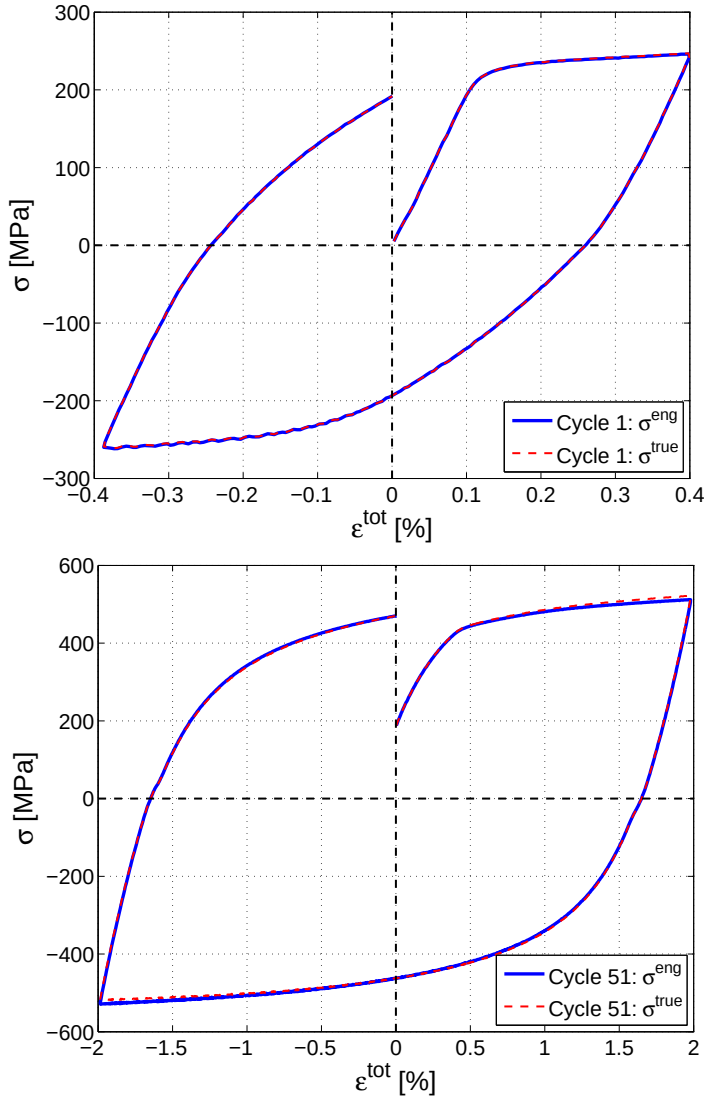

Figure B.4: Comparison of true stress σ^{true} and engineer stress σ^{eng} for low and large strain amplitude cycles for sample C_2

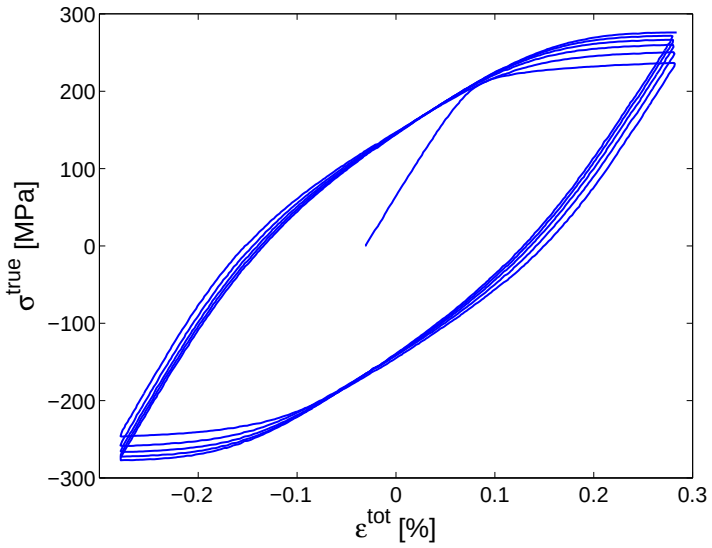

Figure B.5: Exploitable part of stress/strain curve of experiment C_1 - True stress σ^{true} vs. measured total strain ε^{tot}

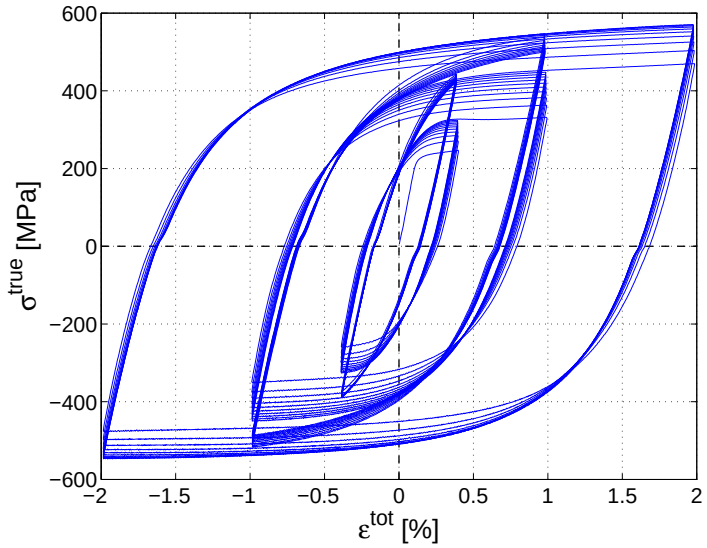

Figure B.6: Stress/strain curve of experiment C_2 - True stress σ^{true} vs. measured total strain ε^{tot}

B.4 Analysis

B.4.1 Tensile test

From the first part of the data curves obtained through experiments and those given by AREVA, it is possible to extract the basic material properties of inconel 600. These tension data come from two specimen, 1.1 and 1.3, made out of the same inconel 600 casting that the samples C_1 and C_2. The complete traction curves of these specimen are displayed in Fig. B.2.

The superimposition of experiments C_1 and C_2 shows the perfect repeatability of the experiments, see Fig. B.9. From experiment C_2, the elastic modulus of inconel 600, as well as the yield limits at 0% and 0.2% plastic strain, are measured. The yield limit at 0% plastic strain is determined from the linear part of the loading curve, accounting for the measurement error on the total strain. The yield limit at 0.2% plastic strain is measured conventionally, following the norm procedures.

E	GPa	195.2
σ_{y0}	MPa	215
$\sigma_{y0.2}$	MPa	242.5

Table B.2: Measured material properties on sample C_2 in inconel 600 from casting #157984

It appears that the traction curve of specimen 3.1 corresponds perfectly to the first part of the cyclic experiments, see Fig. B.9. The different between both curves corresponds to an initial shift in the strain measurement, that was probably made by displacement measures for the monotonic tension curves. A compensatory shift is made to the specimen 3.1 curve to allow using the full monotonic tensile curve with the more precise date from experiments C_1 and C_2 on the first part of the curves.

Neglecting the kinematic part of the hardening behaviour of the samples, an isotropic hardening law is fitted to these sample results providing a hardening behaviour law for the inconel 600 up to very large strains. A ramberg-osgood type hardening law is selected and the parameters are computed by best fit to the specimen 3.1 tension curve shifted to be superimposed with the C_1 and C_2 experiments and for a plastic strain ranging from 0 to 15%. The hardening behaviour of the inconel 600 can thus be described as follows :

$$\sigma_y = \sigma_{y0} + Kp^n \tag{B.3}$$

where p is the accumulated plastic strain, σ_{y0} the initial yield limit, equal to $215MPa$ and K and n the hardening parameters respectively equal to $1670MPa$ and 0.72.

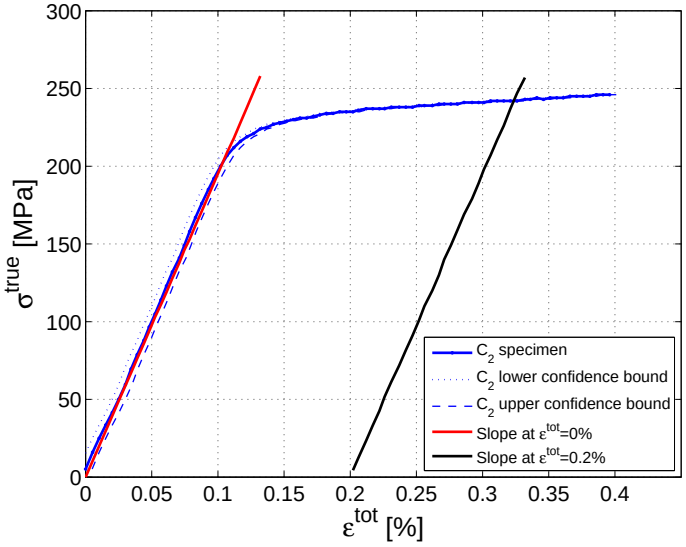

Figure B.7: Measurement of yield limits at 0% and 0.2% plastic strain on inconel 600 C_2 sample. Upper and lower confidence bounds are indicated on strain measurement, measurement error on stress is negligible.

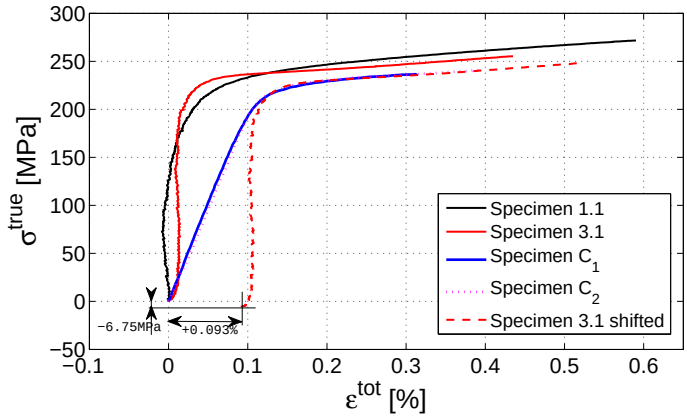

Figure B.8: Comparison of the stress/strain curves from experiments C_1, C_2, 1.1 and 3.1

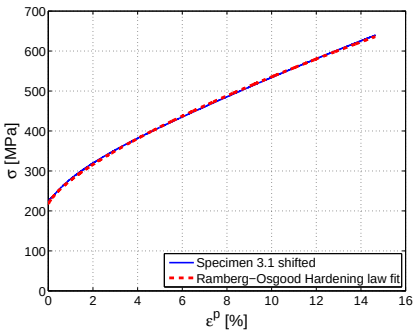

Figure B.9: Ramberg-Osgood isotropic hardening law fit to specimen 3.1 shifted to superimpose with the first part of cyclic experiments.

B.4.2 Cycles Stabilization

The experiment C_1 showed that the cycle stabilization was rather long on inconel 600. Ten cycles of each amplitude have been performed during experiment C_2. The cycle stabilization is evaluated from the percentage of stress evolution on the last cycles, based on the following criterion :

$$max\left(\left|\frac{\sigma^{max}_{10^{th}cycle}-\sigma^{max}_{9^{th}cycle}}{\sigma^{max}_{10^{th}cycle}}\right|;\left|\frac{\sigma^{min}_{10^{th}cycle}-\sigma^{min}_{9^{th}cycle}}{\sigma^{min}_{10^{th}cycle}}\right|\right)\leq 1\% \tag{B.4}$$

Based on this rule, all cycles are stabilized except from the last set of cycles for which a gap of 1.16% is still measured for the minimum stress reached at each cycle.

B.4.3 Identification of a non linear hardening law

A first simple identification of a non linear kinematic hardening law is here proposed [LEM 90]. This hardening law allows to model the stabilized behaviour of the material without accounting for the memory effect. Thus only the last cycles of each three first sets of cycles are taken into account, i.e. cycles 10, 20 and 30.

The kinematic hardening variable X evolution is express as follows :

$$\underline{\underline{dX}} = \frac{2}{3}C\underline{\underline{d\varepsilon^p}} - \gamma\underline{\underline{X}}dp \tag{B.5}$$

Where p is the accumulated plastic strain. The unidimensional traction-compression law then expresses as follows, the parameter k, C and γ remaining to identify :

$$f = |\sigma - X| - k = 0 \tag{B.6}$$

$$d\varepsilon^p = \frac{1}{h}\left\langle \frac{\sigma - X}{k} d\sigma \right\rangle \frac{\sigma - X}{k} = \frac{d\sigma}{h} \; if \; (\sigma - X)\, d\sigma > 0 \tag{B.7}$$

$$dX = \frac{2}{3} C d\varepsilon^p - \gamma X dp \tag{B.8}$$

$$h = C - \gamma X Sgn(\sigma - X) \tag{B.9}$$

As a first step, k is determined approximately from the elastic domain size on stabilized cycles at 0.2%, 1% and 2% total strain. Then, the coefficient C/γ is determined as the asymptotic value of the curve $\frac{\Delta\sigma}{2} - k = f\left(\frac{\Delta\varepsilon^p}{2}\right)$, see Fig. B.10.

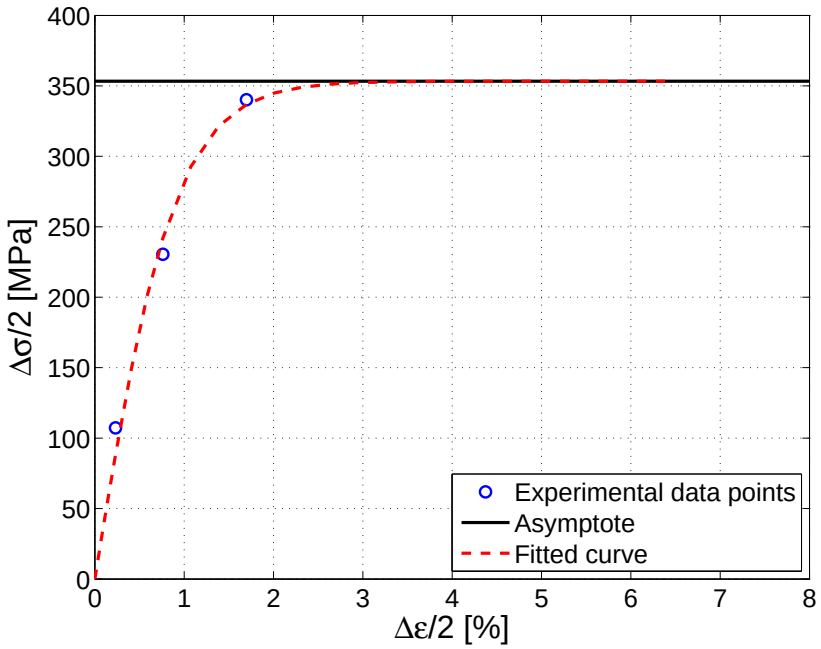

Figure B.10: Non linear hardening law parameters identification - Half stress cycles amplitude $\Delta\sigma/2 - k$ vs. half strain cycles amplitude $\Delta\varepsilon/2$

Giving the following parameters :

The identified hardening law is not a perfect representation of the true hardening behaviour of the material. Indeed, only the behaviour of the stabilized cycles is accounted and the memory effect is lacking too. The extremal values of the cycles are well represented, yet the evolution of data between the extrema is poorly represented. Still, it allows a simplified approach of the hardening behaviour for a first study with a rather simple hardening law. The memory effect is not accounted but its influence on a single

k	MPa	218.17
C	MPa	38879.27
γ		110.0

Table B.3: Non linear hardening law parameters

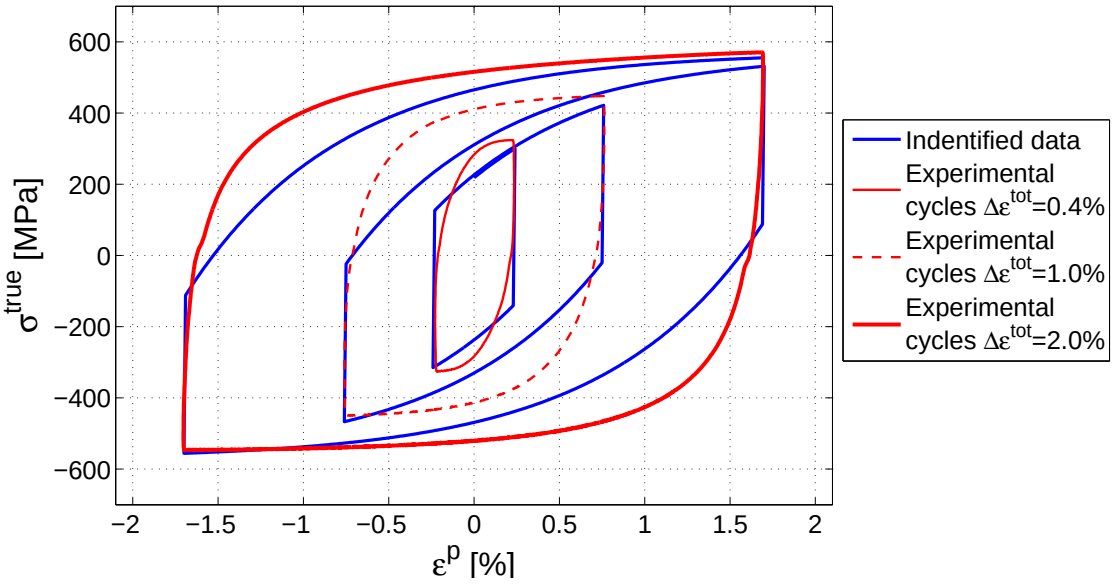

Figure B.11: Comparison of the identified non linear kinematic hardening law with the stabilized experimental cycles. Plastic strain vs. true stress.

impact mechanics is considered negligible since only one cycle will be represented. Actually, this effect might have a large influence only for successive impacts with a decrease in the load (i.e. the velocity) amplitude. Due to the variations on the inconel 600 material properties noticed in the literature , the error made by considering only the stabilized cycles behaviours is rather small. Finally, the error made on the path of the loading can be considered not fundamental as long as the extrema are well represented.

For values of strain beyond 2% the fitted kinematic hardening law might prove insufficient for it does not consider the increase of the yield limit beyond this values. In such cases, the ramberg-osgood isotropic hardening law will provide better results as long as kinematic effects can be neglected.

In a second time, an identification of a more complete law, with two hardening variables and a mixed hardening behaviour to account for the low evolution of the parameter k might be planed.

B.5 Sample blueprint

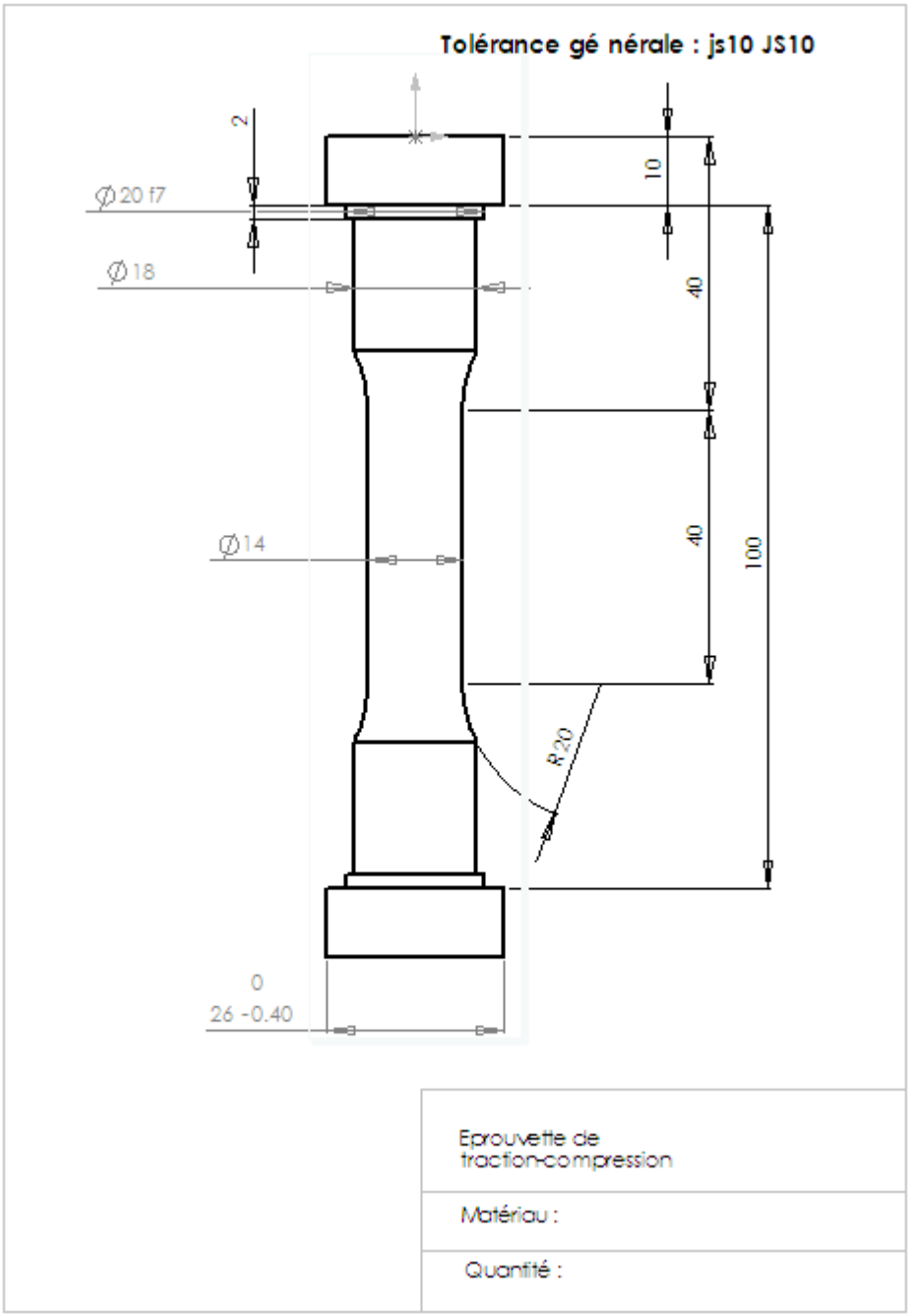

Figure B.12: Blueprint of the samples C_1 and C_2

Bibliography

[ANT 04] ANTALUCA E., NÉLIAS D., CRETU S.
A Three-Dimensional Friction Model for Elastic-Plastic Contact - Application to Dented Surfaces. *Proceedings of the ASME/STLE International Joint Tribology Conference*, Long Beach, CA, USA, 2004.

[ANT 05] ANTALUCA E.
Contribution à l'Etude des Contacts Elasto-Plastiques - Effet d'un Chargement Normal et Tangentiel. PhD thesis, INSA Lyon, 2005.

[ANT 06] ANTOINE J.-F., VISA C., SAUVEY C., ABBA G.
Approximate Analytical Model for Hertzian Elliptical Contact Problems. *ASME Journal of Tribology*, vol. 128 (3), 2006, p. 660-664.

[ANT 08] ANTALUCA E., NELIAS D.
Contact Fatigue Analysis of a Dented Surface in a Dry Elastic-Plastic Circular Point Contact. *Tribology Letters*, vol. 29 (2), 2008, p. 139-153.

[ASS 03] ASSADI H., GARTNER F., STOLTENHOFF T., KREYE H.
Bonding Mechanism in Cold Gas Spraying. *Acta Materiala*, vol. 51 (15), 2003, p. 4379-4394.

[BAS 10] BASKARAN B., M.SRINIVASAN S., MAFFEO B.
Optimzation of the Fatigue Strength of Materials Due to Shot Peening: A Survey. *International Journal of Structural Changes in Solids*, vol. 2, 2010, p. 33-63.

[BEN 67] BENTALL R. H., JOHNSON K. L.
Slip in the Rolling Contact of Two Dissimilar Elastic Rollers. *International Journal of Mechanical Science*, vol. 9 (6), 1967, p. 389-404.

[BHU 10a] BHUVARAGHAN B., SRINIVASAN S. M., MAFFEO B., PRAKASH O.
Analytical Solution for Single and Multiple impacts with Strain-rate Effects for Shot Peening. *Computer Modeling in Engineering and Sciences*, vol. 57 (2), 2010, p. 137-158.

[BHU 10b] BHUVARAGHAN B., SRINIVASAN S., MAFFEO B., MCCLAIN R. D., POTDAR Y., PRAKASH O.

Shot Peening Simulation Using Discrete and Finite Element Methods. *Advances in Engineering Software*, vol. 41 (12), 2010, p. 1266-1276.

[BIJ 97] BIJAK-ZOCHOWSKI M., MAREK P.
Residual Stress in Some Elasto-Plastic Problems of Rolling Contact with Friction. *International Journal of Mechanical Sciences*, vol. 39 (1), 1997, p. 15-32.

[BOS 11a] BOSMAN R., SCHIPPER D. J.
Running-in of Systems Protected by Additive Rich Oils. *Tribology Letters*, vol. 41 (1), 2011, p. 263-282.

[BOS 11b] BOSMAN R., SCHIPPER R. J.
Transition from Mild to Severe Wear Including Running-in Effects. *Wear*, vol. 270 (7-8), 2011, p. 472-478.

[BOU 85] BOUSSINESQ J.
Application des Potentiels à l'Etude de l'Equilibre et du Mouvement des Solides Elastiques. Gauthiers-Villars, Paris, 1885.

[BOU 04] BOUCLY V.
Modélisation Semi-Analytique du Contact Thermo-Elasto-Plastique. Master's thesis, INSA Lyon, 2004.

[BOU 05] BOUCLY V., NÉLIAS D., LIU S., WANG Q. J., KEER L. M.
Contact Analyses for Bodies with Frictional Heating and Plastic Behavior. *ASME Journal of Tribology*, vol. 127 (2), 2005, p. 355-364.

[BOU 07] BOUCLY V., NÉLIAS V., GREEN I.
Modeling of the Rolling and Sliding Contact Between Two Asperities. *ASME Journal of Tribology*, vol. 129 (2), 2007, p. 235-245.

[BOU 08] BOUCLY V.
Semi-Analytical Modeling of the Transient Thermal-Elastic-Plastic Contact and its Application to Asperity Collision, Wear and Running-in of Surfaces. PhD thesis, INSA Lyon, 2008.

[BRA 90] BRANDT A., LUBRECHT A. A.
Multilevel Matrix Multiplication and Fast Solution of Integral Equations. *Journal of Computational Physics*, vol. 90 (2), 1990, p. 348-370.

[BUC 05] BUCAILLE J.-L., GAUTHIER C., FELDER E., SCHIRRER G.
The Influence of Strain Hardening of Polymers on the Piling-up Phenomenon in Scratch Tests: Experiments and Numerical Modelling. *Wear*, vol. 260 (7-8), 2005, p. 803-814.

[CAI 05] CAI S., BHUSHAN B.
A Numerical Three-Dimensional Contact Model for Rrough, Multi-Layered Elastic/Plastic Solid Surfaces. *Wear*, vol. 259 (7-12), 2005, p. 1408-1423.

[CAT 38] CATTANEO C.
Sul contatto di due corpi elastici: distribuzione locale degli sforzi. *Accademia Nazionale Lincei, Rendiconti, Ser. 6*, vol. XXVII, 1938, p. 342-348 434-436 474-478.

[CHA 09] CHAO K. K., SABA C. S.
Pretreatment of Steel Racetracks by using Sand-Blasting Technique with a special Emphasis on Si3N4 Powder-Part two. *STLE Tribology Transactions*, vol. 52 (5), 2009, p. 632-642.

[CHE 08a] CHEN W., LIU S., WANG Q. J.
Fast Fourier Transform Based Numerical Methods for Elasto-Plastic Contacts of Nominally Flat Surfaces. *ASME Journal of Applied Mechanics*, vol. 75 (1), 2008, p. 011022-1-11.

[CHE 08b] CHEN W., WANG Q.
Thermomechanical Analysis of Elasto-Plastic Bodies in a Sliding Spherical Contact and the Effects of Sliding Speed, Heat Partition, and Thermal Softening. *ASME Journal of Tribology*, vol. 130 (4), 2008, p. 041402-1-10.

[CHE 08c] CHEN W., WANG Q., WANG F., KEER L., CAO J.
Three-dimensional Repeated Elasto-Plastic Point Contact, Rolling and Sliding. *ASME Journal of Applied Mechanics*, vol. 75 (2), 2008, p. 021021-1-12.

[CHE 09a] CHEN W. W., WANG Q. J., W. K.
Transient Thermomechanical Analysis of Sliding Electrical Contacts of Elastoplastic Bodies, Thermal Softening, and Melting Inception. *ASME Journal of Tribology*, vol. 131 (2), 2009, p. 021406-1-10.

[CHE 09b] CHEN W., WANG Q.
A Numerical Static Friction Model for Spherical Contacts of Rough Surfaces, Influence of Load, Material, and Roughness. *ASME Journal of Tribology*, vol. 131 (2), 2009, p. 021402-1-8.

[CHE 10] CHEN W. W., ZHOU K., KEER L. M., WANG Q. J.
Modeling Elasto-Plastic Indentation on Layered Materials Using the Equivalent Inclusion Method. *International Journal of Solids and Structures*, vol. 47 (20), 2010, p. 2841-2854.

[CHI 77] CHIU Y.
On the Stress Fiels due to Initial Strains in a Cuboid Surrounded by an Infinite Elastic Space. *ASME Journal of Applied Mechanics*, vol. 44 (4), 1977, p. 587-590.

[CHI 78] CHIU Y.
On the Stress Fiels and Surface Deformation in a Half Space with a Cuboidal Zone in which Initial Strains are Uniform. *ASME Journal of Applied Mechanics*, vol. 45 (2), 1978, p. 302-306.

[CIA 98a] CIAVARELLA M.
The Generalized Cattaneo Partial Slip Plane Contact Problem. I-Theory. *International Journal of Solids and Structures*, vol. 35 (18), 1998, p. 2349-2362.

[CIA 98b] CIAVARELLA M.
The Generalized Cattaneo Partial Slip Plane Contact Problem. II-Examples. *International Journal of Solids and Structures*, vol. 35 (18), 1998, p. 2363-2378.

[COC 06] COCHENNEC F., ROUHAUD E., RESTRAINT D., ROUQUETTE S., ROOS A.
Analysis of the Impact of a Shot at Low Velocity Using the Finite Element Method. Application to the Ultrasonic Shot-peening Process. *Materials Science Forum*, vol. 524-525, 2006, p. 337-342.

[DAV 48] DAVIES R.
The Determination of Static and Dynamic Yield Stresses using a Steel Ball. *Proceedings of the Royal Society of London*, vol. 197 (1050), 1948, p. 416-432.

[DER 68] DERESIEWICZ H.
A Note on Hertz Impact. *Acta Mechanica*, vol. 6, 1968, Page 110.

[DES 00] DESLAEF D.
Modélisation Numérique du Grenaillage de Précontrainte. PhD thesis, Université de technologie de Troyes, 2000.

[DIN 04] DINI D., NOWELL D.
Flat and Rounded Fretting Contact Problems Incorporating Elastic Layers. *International Journal of Mechanical Sciences*, vol. 46 (11), 2004, p. 1653-1657.

[ETS 05] ETSION I., KLIGERMAN Y., KADIN Y.
Unloading of an Elastic-Plastic Loaded Spherical Contact. *International Journal of Solids and Structures*, vol. 42 (13), 2005, p. 3716-3729.

[FOT 96] FOTIU P. A., NEMAT-NASSER S.
A Universal Integration Algorithm for Rate-Dependant Elastoplasticity. *Computers and Structures*, vol. 59 (6), 1996, p. 1173-1184.

[FRA 09] FRANCHIM A. S., DE CAMPOS V. S., TRAVESSA D. N., DE MOURA NETO C.
Analytical Modelling for Residual Stresses Produced by Shot Peening. *Materials and Design*, vol. 30 (5), 2009, p. 1556-1560.

[FUL 10] FULLERINGER B., NELIAS D.
On the Tangential Displacement of a Surface Point Due to a Cuboid of Uniform Plastic Strain in a Half-Space. *Journal of Applied Mechanics - Transactions of the ASME*, vol. 77 (2), 2010, Page 021014.

[FUL 11] FULLERINGER B.
Semi-Analytical Modeling of Complex Mechanical Contacts: Application to Inclusions and Wear of Coated Surfaces. PhD thesis, INSA Lyon, 2011.

[GAL 53] GALIN L.A. E. T. B. H. M.
Contact Problems in the Theory of Elasticity. North Carolina College, Departments of Mathematical and Engineering Research, NSF Grant No. G16447, 1953.

[GAL 06] GALLEGO L., NELIAS D., JACQ C.
A Comprehensive Method to Predict Wear and to Define the Optimum Geometry of Fretting Surfaces. *ASME Journal of Tribology*, vol. 128 (3), 2006, p. 476-485.

[GAL 07a] GALLEGO L.
Fretting et Usure des Contacts Mécaniques : Modélisation Numérique. PhD thesis, INSA Lyon, 2007.

[GAL 07b] GALLEGO L., NÉLIAS D.
Modeling of Fretting Wear Under Gross Slip and Partial Slip Conditions. *ASME Journal of Tribology*, vol. 129 (3), 2007, p. 528-535.

[GAL 10a] GALLEGO L., FULLERINGER B., DEYBER S., NÉLIAS D.
Multiscale Computation of Fretting Wear at the Blade/Disk Interface. *Tribology International*, vol. 43 (4), 2010, p. 708-718.

[GAL 10b] GALLEGO L., NÉLIAS D., DEYBER S.
A Fast and Efficient Contact Algorithm for Fretting Problems Applied to Fretting Modes I, II and III. *Wear*, vol. 268 (1-2), 2010, p. 208-222.

[GAL 10c] GALLEGO L., NÉLIAS D., DEYBER S.
A Fast and Efficient Contact Algorithm for Fretting Problems Applied to Fretting Modes I, II and III. *Wear*, vol. 268 (1-2), 2010, p. 202-222.

[GLA 80] GLADWELL G.
Contact Problems in the Classical Theory of Elasticity. sijthoff & Noordhoff, 1980.

[GRE 66] GREENWOOD J., WILLIAMSON J. B. P.
Contact of Normally Flat Surfaces. *Proc. R. Soc. London, Ser. A*, vol. 295 (1442), 1966, p. 300-319.

[GUO 04] GUO Y., BARKEY M.
FE-Simulation of the Effects of Machining-Induced Residual Stress Profile on Rolling

Contact of Hard Machined Components. *International Journal of Mechanical Sciences*, vol. 46 (3), 2004, p. 371-388.

[HER 82] HERTZ H.
On the Contact of Elastic Solids. *J. Reine Angrew. Math.*, vol. 92, 1882, p. 156-171.

[JAC 01] JACQ C.
Limite d'Endurance et Durée de Vie en Fatigue de Roulement du 32CrMoV13 Nitruré en Présence d'Indentations. PhD thesis, INSA Lyon, 2001.

[JAC 02] JACQ C., NÉLIAS D., LORMAND G., GIRODIN D.
Development of a Three-Dimensional Semi-Analytical Elastic-Plastic Contact Code. *ASME Journal of Tribology*, vol. 124 (4), 2002, p. 653-667.

[JAC 10] JACKSON R. L., GREEN I., B. M. D.
Predicting the Coefficient of Restitution of Impacting Elastic-Perfectly Plastic Spheres. *Nonlinear Dynamics*, vol. 60 (3), 2010, p. 217-229.

[JAE 04] JAEGER J.
New Solutions in Contact Mechanics. Witpress, Southampton, Boston, 2004.

[JIA 02] JIANG Y., XU B., SEHITOGLU H.
Three-Dimensional ElasticŰPlastic Stress Analysis of Rolling Contact. *ASME Journal of Tribology*, vol. 124 (4), 2002, p. 699-708.

[JOH 85] JOHNSON K. L.
Contact Mechanics. Press syndicate of the university of Cambridge, 1985.

[JU 96] JU Y., FARRIS T. N.
Spectral Analysis of Two-Dimensional Contact Problems. *ASME Journal of Tribology*, vol. 118 (2), 1996, p. 320-328.

[KAL 90] KALKER J. J.
Three Dimensional Elastic Bodies in Rolling Contact. kluwer Academic Publishers, Dordrecht, 1990.

[KAT 09] KATTA R. R., POLYCARPOU A. A., HANCHI J. V., ROY M.
Analytical and Experimental Elastic-Plastic Impact Analysis of a Magnetic Storage Head-Disk Interface. *ASME Journal of Tribology*, vol. 131 (1), 2009, p. 011902-1-10.

[KAT 10] KATTA R. R., POLYCARPOU A. A.
Impact of a Fixed-Length Rigid Cylinder on an Elastic-Plastic Homogeneous Body. *ASME Journal of Tribology*, vol. 132 (4), 2010, p. 041402-1-11.

[KER 07] KERMOUCHE G., KAISER A., GILLES P., BERGHEAU J.
Combined Numerical and Experimental Approach of the Impact-Sliding Wear of a Stainless Steel in a Nuclear Reactor. *Wear*, vol. 263, 2007, p. 1551-1555.

[KIM 10] KIM T., HAENG LEE J., LEE H., CHEONG S.-K.
An Area-Average Approach to Peening Residual Stress Under Multi-Impacts using a Three-Dimensional Symmetry-Cell Finite Element Model with Plastic Shots. *Materials and Design*, vol. 31 (1), 2010, p. 50-59.

[KLE 05] KLEMENZ M., HOCHRAINER T., DELONNOY L., SCHULZE V., VOHRINGER O., GUMBSCH P.
Similarity Rules for the Shot Peening Process Based on Finite Element Simulations. *International Conference on shot Peening 9*, Marne la Valle, France, 2005.

[KLE 09] KLEMENZ M., SCHULZE V., ROHR I., LÖHE D.
Application of the FEM for the Prediction of the Surface Layer Characteristics after Shot Peening. *Journal of Materials Processing Technology*, vol. 209 (8), 2009, p. 4093-4102.

[KOG 02] KOGUT I., ETSION I.
Elastic-Plastic Contact Analysis of a sphere and a rigid flat. *ASME Journal of Applied Mechanics*, vol. 69 (5), 2002, p. 657-662.

[LEE 10] LEE A., KOMVOPOULOS K.
Dynamic Finite Element Analysis of an Elastic-Plastic Half-Space Indented by a Rigid Sphere. *ASME/STLE International Joint Tribology Conference*, San Francisco, CA, USA, 2010.

[LEM 90] LEMAITRE J., CHABOCHE J.-L.
Mechanics of Solid Materials. Cambridge University Press: Cambridge, 1990.

[LEQ 10] LE QUILLIEC G., DRISSI-HABTI M., MAUVOISIN G., INGLEBERT G., LIEURADE H.-P., MACQUET P.
Analyse par Indentation Instrumentée du Martelage à Haute Fréquence des Assemblages Soudés. *Matériaux*, Nantes, France, 2010.

[LEQ 11] LE QUILLIEC G., DRISSI-HABTI M., MAUVOISIN G., INGLEBERT G., LIEURADE H.-P., MACQUET P.
Application de l'Indentation Instrumentée Sphérique à l'Estimation des Courbes Locales de Traction d'un Matérieu Métallique. *Matériaux et Techniques*, vol. 99, 2011.

[LER 10] LEROUX J., FULLERINGER B., NÉLIAS D.
Contact Analysis in Presence of Spherical Inhomogeneities within a Half-Space. *International Journal of Solids and Structures*, vol. 47 (22-23), 2010, p. 3034-3049.

[LI 02] LI L.-Y., WU C.-Y., C. T.
A Theoretical Model for the Contact of Elastoplastic Bodies. *Proceedings of the Institution of Mechanical Engineers, Part C: Journal of Mechanical Engineering Science*, vol. 216 (4), 2002, p. 421-431.

[LI 07] LI Y. W., F., LU J., XU K.
Finite Element Analysis for Shot Peening Models of Single Shot Impact and Multiple Impingement. *Hsi-An Chiao Tung Ta Hsueh/Journal of XiŠan Jiaotong University*, vol. 41 (3), 2007, p. 348-352.

[LI 09] LI F., PAN J., SINKA C.
Contact Laws Between Solid Particles. *Journal of the Mechanics and Physics of Solids*, vol. 57 (8), 2009, p. 1194-1208.

[LI 11] LI J.
Simulation des Réparations par Soudage et Billage d'un Alliage à Base Nickel. PhD thesis, INSA Lyon, 2011.

[LIU 00] LIU S., WANG Q., LIU G.
A Versatile Method of Discrete Convolution and FFT (DC-FFT) for Contact Analyses. *Wear*, vol. 243 (1-2), 2000, p. 101-111.

[LIU 01] LIU G., WANG Q., LIU S.
A Three-Dimensional Thermal-Mechanical Asperity Contact Model for Two Nominally Flat Surfaces in Contact. *ASME Journal of Tribology*, vol. 123 (3), 2001, p. 595-602.

[LIU 03] LIU S., WANG Q.
Transient Thermoelastic Stress Field in a Half-Space. *ASME Journal of Tribology*, vol. 125(1), 2003, p. 33-43.

[LIU 05] LIU S., WANG Q.
Elastic Fields Due to Eigenstrains in a Half-Space. *ASME Journal of Applied Mechanics*, vol. 72 (6), 2005, p. 871-878.

[LOV 52] LOVE A. E. H.
A Treatise on the Mathematical Theory of Elasticity. Cambridge University Press, London, 4th edition edition, 1952.

[LUB 91] LUBRECHT A. A., IOANNIDES E.
A Fast Solution of the Dry Contact Problem and the Associated Sub-Surface Stress Field Using Multilvel Techniques. *ASME Journal of Tribology*, vol. 113 (1), 1991, p. 128-133.

[MAH 07] MAHMOUD C. O. M.
Analyse des Contraintes Résiduelles Générées lors du Grenaillage : Approches Analytique, Numérique et Expérimentale des Impacts de Billes. PhD thesis, Université de Technologie de Troyes, 2007.

[MAJ 05] MAJZOOBI G. H., AZIZI R., ALAVI NIA A.
A Three-Dimensional Simulation of Shot Peening Process Using Multiple Shot Impacts. *Journal of Materials Processing Technology*, vol. 164-165, 2005, p. 1226-1234.

[MAW 76] MAW N., BARBER J., FAWCETT J. N.
The Oblique Impact of Elastic Spheres. *Wear*, vol. 38 (1), 1976, Page 101.

[MAW 81] MAW N., BARBER J., FAWCETT J. N.
The Role of Tangential Compliance in Oblique Impact. *Journal of Lubircation Technology*, vol. 103 (1), 1981, Page 74.

[MEG 07] MEGUID S., G. S., STRANART J. C.
Development and Validation of Novel FE Models for 3D Analysis of Peening of Strain-Rate Sensitive Materials. *Journal of Engineering Materials and Technology*, vol. 129 (2), 2007, p. 271-283.

[MEI 68] MEIJERS P.
The Contact Problem of a Rigid Cylinder on an Elastic Layer. *Applied Science Research*, vol. 18 (5), 1968, Page 353.

[MIA 09] MIAO H., LAROSE S., PERRON C., LEVESQUE M.
On the Potential Applications of a 3D Random Finite Element Model on the Modeling of Shot Peening. *Advances in Engineering Software*, vol. 40, 2009, p. 1023-1038.

[MID 53] MIDLIN R. D., DERESIEWICZ H.
Elastic Spheres in Contact Under Varying Oblique Forces. *ASME Journal of Applied Mechanics*, vol. 20 (3), 1953, p. 324-344.

[MIN 49] MINDLIN R. D.
Compliance of Elastic Bodies in Contact. *ASME Journal of Applied Mechanics*, vol. 16 (3), 1949, p. 259-268.

[MIN 50] MINDLIN R. D., CHENG D. H.
Thermoelastic Stress in the Semi-Infinite Solid. *Journal of Applied Physics*, vol. 21 (9), 1950, p. 931-933.

[MIN 10] MINAMOTO H., SEIFRIED R., EBERHARD P., KAWAMURA S.
Analysis of Repeated Impacts on a Steel Rod with Visco-Plastic Material Behavior. *European Journal of Mechanics / A Solids*, vol. 30 (3), 2010, p. 336-344.

[MIN 11] MINAMOTO H., KAWAMURA S.
Moderately High Speed Impact of Two Identical Spheres. *International Journal of Impact Engineering*, vol. 38 (2-3), 2011, p. 123-129.

[MUS 53] MUSKHELISHVILI N.
Singular Integral Equations. P. Nordhoff N. V., 1953.

[NéL 05] NÉLIAS D., JACQ C., LORMAND G., DUDRAGNE G., VINCENT A.
A New Methodology to Evaluate the Rolling Contact Fatigue Performance of Bearing Steels with Surface Dents - Application to 32CrMoV13 (Nitrited) and M50 Steels. *ASME Journal of Tribology*, vol. 127 (3), 2005, p. 611-622.

[NéL 06] NÉLIAS D., BOUCLY V., BRUNET M.
Elastic-Plastic Contact Between Rough Surfaces: Proposal for a Wear or Running-In Model. *ASME Journal of Tribology*, vol. 128 (2), 2006, p. 476-485.

[NéL 07a] NÉLIAS D., ANTALUCA E., BOUCLY V.
Rolling of an Elastic Ellipsoid Upon an Elastic-Plastic Flat. *ASME Journal of Tribology*, vol. 129 (4), 2007, p. 791-800.

[NéL 07b] NÉLIAS D., ANTALUCA E., BOUCLY V., CRETU V.
A 3D Semi-Analytical Model for Elastic-Plastic Sliding Contacts. *ASME Journal of Tribology*, vol. 129 (4), 2007, p. 761-771.

[NOG 97] NOGI T., T. K.
Influence of a Hard Surface Layer on the Limit of Elastic Contact-Part I: Analysis Using a Real Surface Model. *ASME Journal of Tribology*, vol. 119 (3), 1997, p. 493-500.

[NOW 98] NOWELL D., DAI D. N.
Analysis of Surface Tractions in Complex Fretting Fatigue CycLe Using Quadratc Programming. *ASME Journal of Tribology*, vol. 120 (4), 1998, p. 744-749.

[OUL 06] OULD C., ROUHAUD E., FRANCOIS M., CHABOCHE J.
A Kinematic Hardening Finite Elements Model to Evaluate Residual Stresses in Shot-Peened Parts, Local Measurements by X-ray Diffraction. *Mater. Sci. Forum*, vol. 524-525, 2006, p. 161-166.

[PAU 81] PAUL B., HASHEMI J.
Contact Pressure on Closely Conforming Elastic Bodies. *ASME Journal of Applied Mechanics*, vol. 48 (3), 1981, p. 543-548.

[PEN 00] PENG W., BHUSHAN B.
Modelling of Surfaces with a Bimodal Roughness Distribution. *Proceedings of the institution of mechanical engineers, Part J: Journal of Engineering Tribology*, vol. 214 (5), 2000, p. 459-470.

[PEN 01] PENG W., BHUSHAN B.
Three Dimensional Contact Analysis of Layered Elastic/Plastic Solids with Rough Surfaces. *Wear*, vol. 249 (9), 2001, p. 741-760.

[PEN 02] PENG W., BHUSHAN B.
Sliding Contact Analysis of Layered Elastic: Plastic Solids With Rough Surfaces. *ASME Journal of Tribology*, vol. 124 (1), 2002, p. 46-61.

[PIL 05] PILE C., FRANCOIS M., RESTRAINT D., ROUHAUD E., LU J.
Modelling of the Ultrasonic Shot Peening Process. *Materials Science Forum*, vol. 490-491, 2005, p. 67-72.

[POL 99] POLONSKY I., KEER L. M.
A Numerical Method for Solving Rough Contact Problems Based on the Multi-Level Multi-Summation and Conjugate Gradient Techniques. *Wear*, vol. 231 (2), 1999, p. 206-219.

[POL 00] POLONSKY I. A., KEER L. M.
Fast Methods for Solving Rough Contact Problems: a Comparative Study. *ASME Journal of Tribology*, vol. 122 (1), 2000, p. 36-40.

[POP 06a] POPESCU G., GABELLI A., MORALES-ESPEJEL G. E., WEMEKAMP B.
Micro-Plastic Material Model and Residual Fields in Rolling Contact. *Journal of ASTM International*, vol. 3, 2006, p. 1-12.

[POP 06b] POPESCU G., MORALES-ESPEJEL G. E., WEMEKAMP B., GABELLI A.
An Engineering Model for Three-Dimensional Elastic-Plastic Rolling Contact Analyses. *STLE Tribology Transactions*, vol. 49 (3), 2006, p. 387-399.

[REN 10] REN N., ZHU D., CHEN W. W., WANG Q. J.
Plasto-Elastohydrodynamic Lubrication (PEHL) in Point Contacts. *ASME Journal of Tribology*, vol. 132 (3), 2010, Page 031501.

[ROU 97] ROUHAUD E., MILLEY A., LU J.
Introduction of Residual Stress Fields in Finite Element Three-Dimensional Structures. *Proceedings of the 5th International Conference on Residual Stresses*, Oxford, UK, 1997.

[ROU 02] ROUHAUD E., DESLAEF D., LU J., CHABOCHE J.-L.
Modeling of Residual Stress, Shot Peening. *Handbook on Residual Stress, vol. 2. Society of Experimental Mechanics*, 2002.

[ROU 09] ROUQUETTE S., ROUHAUD E., FRANCOIS M., ROOS A., CHABOCHE J.-L.
Coupled Thermo-Mechanical Simulations of Shot Impacts: Effects of the Temperature on the Residual Stress Field Due to Shot-Peening. *Journal of Material Processing Technology*, vol. 209 (8), 2009, p. 3879-3886.

[SAI 02] SAINSOT P., JACQ C., NELIAS D.
A Numerical Model for Elastoplastic Rough Contact. *Cmes-Computer Modeling in Engineering & Sciences*, vol. 3 (4), 2002, p. 497-506.

[SAN 10] SANDA A., GARCIA NAVAS V., GONZALO O.
Surface State of Inconel 718 Ultrasonic Shot Peened: Effect of Processing Time, Material and Quantity of Shot Balls and Distance From Radiating Surface to Sample. *Materials and Design*, vol. 32 (4), 2010, p. 2213-2220.

[SCH 99] SCHIFFNER K., HELLING C. D. G.
Simulation of Residual Stresses by Shot Peening. *Computers and Structures*, vol. 72 (1), 1999, p. 329-340.

[SCH 02] SCHULZE V.
Characteristics of Surface Layers Produced by Shot Peening. *International Conference on Shot Peening 8*, Munich, Germany, 2002.

[SEI 05] SEIFRIED R., SCHIEHLEN W., EBERHARD P.
Numerical and Experimental Evaluation of the Coefficient of Restitution for Repeated Impacts. *International Journal of Impact Engineering*, vol. 32 (1-4), 2005, p. 508-524.

[SEI 10] SEIFRIED R., MINAMOTO H., EBERHARD P.
Viscoplastic Effects Occuring in Impact of Aluminium and Steel Bodies and Their Influence on the Coefficient of Restitution. *ASME Journal of Applied Mechanics*, vol. 77 (4), 2010, p. 041008-1-7.

[SHE 06] SHEN S., ALTURI S. N.
An Analytical Model for Shot Peening Induced Residual Stresses. *Computers, Materials and Continua*, vol. 4 (2), 2006, p. 75-85.

[SIM 85] SIMO J., TAYLOR R. L.
Consistent Tangent Operator for Rate-Independant Elastoplasticity. *Computer Methods in Applied Mechanics and Engineering*, vol. 48 (1), 1985, p. 101-118.

[SNE 51] SNEDDON I.
Fourier Transforms. McGrawHill, New York, 1951.

[SOC 06] SOCHTING S., SHERRINGTON I., LEWIS S., ROBERTS E. W.
An Evaluation of the Effect of Simulated Launch Vibrations on the Friction Performance and Lubrication of Ball Bearings for Space Applications. *Wear*, vol. 260 (11-12), 2006, p. 1190-1202.

[STO 06] STOLTENHOFF T., BORCHERS C., GÄRTNER F., KREYE H.
Microstructures and Key Properties of Cold-Sprayed and Thermally Sprayed Copper Coatings. *Surface and Coatings Technology*, vol. 200 (16-17), 2006, p. 4947-4960.

[SUT 09] SUTTON M. A., ORTEU J.-J., SCHREIER H.
Image Correlation for Shape, Motion, and Deformation Measurements: Basic Concepts, Theory and Applications. 2009.

[THO 77] THOMPSON J. C., ROBINSON A. R.
An Exact Solution for the Superseismic Stage of Dynamic Contact Between a Punch and an Elastic Body. *ASME Journal of Applied Mechanics*, vol. 44 (4), 1977, Page 583.

[THO 97] THORNTON C.
Coefficient of Restitution for Collinear Collisions of Elastic-Perfectly Plastic Spheres. *ASME Journal of Applied Mechanics*, vol. 64 (2), 1997, p. 383-386.

[THO 98] THORNTON C., NING Z.
A Theoretical Model for the Stick/Bounce Behaviour of Adhesive, Elastic-Plastic Spheres. *Powder Technology*, vol. 99 (2), 1998, p. 154-162.

[TIA 96] TIAN X. F., BHUSHAN B.
A Numerical Three-Dimensional Model for the Contact of Rough Surfaces by Variational Principle. *ASME Journal of Tribology*, vol. 118 (1), 1996, p. 33-42.

[TIR 08] TIROSH J.
Extended Fatigue Life by Shot Peening Process via Shakedown Analysis. *ASME Journal of Applied Mechanics*, vol. 75 (1), 2008, p. 011005-1-8.

[VER 85] VERGNE F.
Calcul des Déplacements et des Contraintes dans un Demi-Espace Elastique Chargé en Surface par des Actions Distribuées Normales ou Tangentielles Quelconques. Master's thesis, INSA Lyon, 1985.

[VIN 06] VINCENT A., NÉLIAS D., JACQ C., ROBIN Y., DUDRAGNE G.
Comparison of Fatigue Performances of 32CrMoV13 and M50 Steels in Presence of Surface Dents. *Journal of ASTM International*, vol. 3 (2), 2006, p. 1-9.

[VUQ 99] VU-QUOC L., ZHANG X.
An Elastoplastic Contact Force-Displacement Model in the Normal Direction: Displacement-Driven Version. *Proc. R. Soc. Lond. A*, vol. 455, 1999, p. 4013-4044.

[WAN 05] WANG F., KEER L.
Numerical Simulation for three Dimensional Elastic-Plastic Contact with Hardening Behavior. *ASME Journal of Tribology*, vol. 127 (3), 2005, p. 494-502.

[WAN 10a] WANG Z.-J., WANG W.-Z., WANG H., ZHU D., HU Y.-Z.
Partial Slip Contact Analysis on Three-Dimensional Elastic Layered Half Space. *ASME Journal of Tribology*, vol. 132 (2), 2010, p. 021403-1-12.

[WAN 10b] WANG Z., WANG W., HU Y., WANG H.
A Numerical Elastic-Plastic Contact Model for Rough Surfaces. *STLE Tribology Transactions*, vol. 53 (2), 2010, p. 224-238.

[WEI 05] WEIR G., TALLON S.
The Coefficient of Restitution for Normal Incident, Low Velocity Particle Impacts. *Chemical Engineering Science*, vol. 60 (13), 2005, p. 3637-3647.

[WES 39] WESTERGAARD H. M.
Bearing Pressures and Cracks. *ASME Journal of Applied Mechanics*, vol. 6, 1939, Page 49.

[WIL 04] WILLNER K.
Elasto-Plastic Normal Contact of Three-Dimensional Fractal Surfaces Using Halfspace Theory. *ASME Journal of Tribology*, vol. 126 (1), 2004, p. 28-33.

[WIL 88] WILLNER K.
Fully Coupled Frictional Contact Using Elastic Halfspace Theory. *ASME Journal of Tribology*, vol. 130 (3), 2088, p. 031405-1-8.

[WU 03] WU C.-Y., LI L.-Y., THORNTON C.
Rebound Behaviour of Spheres for Plastic Impacts. *International Journal of Impact Engineering*, vol. 28 (9), 2003, p. 929-946.

[WU 05] WU C., LI L., THORNTON C.
Energy Dissipation During Normal Impact of Elastic and Elastic-Plastic Spheres. *International Journal of Impact Engineering*, vol. 32 (1-4), 2005, p. 593-604.

[YAN 05] YANG J., KOMVOPOULOS K.
Impact of a Rigid Spehre on an Elastic Homogeneous Half-Space. *ASME Journal of Tribology*, vol. 127 (2), 2005, p. 325-330.

[YIL 11] YILDIRIM B., MUFTU S., GOULDSTONE A.
Modeling of High Velocity Impact of Spherical Particles. *Wear*, vol. 270 (9-10), 2011, p. 70.-713.

[YU 91a] YU H. Y., SANDAY S. C.
Elastic Fields in Joined Half-Spaces Due to Nuclei of Strain. *Proceedings of the Royal Society of London, Series A*, vol. 434, 1991, p. 503-519.

[YU 91b] YU H. Y., SANDAY S. C.
Elastic Fields in Joined Semi-Infinite Solids With an Inclusion. *Proceedings of the Royal Society of London, Series A*, vol. 434, 1991, p. 521-530.

[ZAI 10] ZAIT Y., ZOLOTAREVSKY V., KLIGERMAN Y., ETSION I.
Multiple Normal Loading-Unloading Cycles of a Spherical Contact Under Stick Contact Condition. *ASME Journal of Tribology*, vol. 132 (4), 2010, p. 041401-1.

[ZHA 02] ZHANG X., VU-QUOC L.
Modeling the Dependence of the Coefficient of Restitution on the Impact Velocity in Elasto-Plastic Collisions. *International Journal of Impact Engineering*, vol. 27 (3), 2002, p. 317-341.

[ZHO 09] ZHOU K., WAYNE CHEN W., KEER L. M., WANG Q. J.
A Fast Method for Solving Three-Dimensional Arbitrarily-Shaped Inclusions in a Half Space. *Computer Methods in Applied Mechanics and Engineering*, vol. 198 (9-12), 2009, p. 885-892.

THÈSE SOUTENUE DEVANT L'INSTITUT NATIONAL DES SCIENCES APPLIQUÉES DE LYON

NOM: CHAISE DATE de SOUTENANCE : 5 septembre 2011

Prénoms: Thibaut, Pierre

TITRE: Mechanical simulation using a semi analytical method: from elasto-plastic rolling contact to multiple impacts

NATURE: Doctorat Numéro d'ordre: 2011-ISAL-0076

École doctorale: MEGA

Spécialité: Mécanique - Génie Mécanique - Génie Civil

Cote B.I.U. - Lyon : T 50/210/19 / et bis CLASSE:

RÉSUMÉ:
La durée de vie en fonctionnement des pièces mécaniques peut être augmentée par la présence de contraintes résiduelles de compression. Inhérentes à la plupart des procédés de fabrication, les contraintes résiduelles jouent un rôle sur la tenue en service des éléments mécaniques. La connaissance et la maîtrise de ces contraintes résiduelles et des procédés associés sont donc fondamentales. La mise en place de méthodes numériques performantes pour prédire ces contraintes résiduelles permettra à terme d'éviter de nombreux et coûteux essais et d'étudier l'influence des principaux paramètres.
Cette thèse présente le développement et l'application de méthodes de calcul semi analytiques (SA) à la modélisation de procédés mécaniques de mise en compression des surfaces. Les méthodes SA, initialement développées pour la simulation des contacts élasto-plastiques, ont l'avantage de temps de calcul très significativement réduits par rapport aux méthodes numériques conventionnelles. Cette méthode est d'abord utilisée pour la simulation d'un procédé connu sous le nom de galetage, avec un chargement de type contact roulant. Enfin elle est utilisée pour la simulation d'impacts uniques puis répétés, et les développements associés présentés.
Le contact roulant entre deux massifs élasto-plastiques, sans considération du frottement, est d'abord étudié. L'influence de la plasticité et du type d'écrouissage (isotrope ou cinématique), de la géométrie des massifs en contact (sphères ou ellipsoïdes) et du type de chargement (indentation ou roulement) sur la pression de contact et les déformations plastique sont analysés.
La simulation d'impacts est ensuite abordée. La méthode développée est tout d'abord validée numériquement, puis confrontée à l'expérience. Trois matériaux ont été plus particulièrement étudiés : 316L, AA 7010, et l'Inconel 600. Les dimensions des impacts ainsi que les déformations générées, mesurées par stéréo corrélation sont utilisées pour valider expérimentalement la méthode.
Le procédé de billage ultrasonore a été tout particulièrement étudié. Dans un premier temps nous nous sommes attachés à la décrire la cinématique des billes dans une chambre fermée, mises et maintenues en mouvement par une sonotrode. L'utilisation de formules analytiques pour l'estimation des coefficients de restitution, lors des nombreux chocs entre les billes ou avec les parois de la chambre, a permis d'affiner le calcul des vitesses moyennes d'impact en fonction des paramètres du procédé. La méthode SA est ensuite utilisée pour déterminer le champ de déformations plastiques induits par les impacts. Enfin une méthode de projection est proposée pour permettre in fine la prédiction des contraintes résiduelles pour des structures fines ou épaisses.

MOTS-CLÉS: Modélisation numérique, Méthode Semi Analytique, Plasticité, Impact, Grenaillage

Laboratoire(s) de recherche: Laboratoire de Mécanique des Contacts et des Structures
UMR CNRS 5259 - INSA de Lyon
20, avenue Albert Einstein
69621 Villeurbanne Cedex FRANCE

Directeur de thèse: Monsieur le Professeur Daniel Nélias

Président du jury: Prof. Jean-Louis Chaboche

Composition du jury: Prof. Jean-Louis Chaboche
Prof. Etienne Barthel
Prof. Farshid Sadeghi
Dr. Frédéric Hasnaoui
Prof. David Hills
Dr. Philippe Gilles
Dr. Régis Kubler
Prof. Daniel Nélias